Design and Modeling of Millimeter-Scale Soft Robots for Medical Applications

A THESIS
SUBMITTED TO THE FACULTY OF THE GRADUATE SCHOOL
OF THE UNIVERSITY OF MINNESOTA
BY

Gillian Jo McDonald

IN PARTIAL FULFILLMENT OF THE REQUIREMENTS
FOR THE DEGREE OF
DOCTOR OF PHILOSOPHY

Timothy M. Kowalewski, Ph.D.
James D. Van de Ven, Ph.D.

April, 2021

Acknowledgements

I would like to express my gratitude to my co-advisors, Professor Timothy Kowalewski and Professor James Van de Ven for their guidance and support throughout my time in graduate school. They both devoted incredible amounts of time and energy to helping me grow as an engineer, but also encouraged my growth outside of my graduate education.

I would also like to thank my thesis committee, including Professor Will Durfee and Professor Daniel Keefe. Each member of my committee provided guidance in their respective areas of expertise that helped bolster both my dissertation and interests in new fields. I am extremely grateful for the time they committed to helping me shape the focus of my work. I would also like to thank Professor Emmanuel Detournay, who mentored me with unrivaled patience over this past year and championed my growth with kindness and sincerity. Professor Detournay's guidance helped form my work into a comprehensive story.

I have numerous labmates and colleagues to thank for helping me feel part of a community, including Mihai Duduta, John O'Neill, Rod Dockter, Anna French, Trevor Stephens, Mark Gilbertson, Jason Kelly, Rebecca Smith, Chaitanya Awasthi, Amer Safdari, Yusra Farhat Ullah, Mark Gotthelf, Brad Drahos, Matt Kubala, Faizan Malik, Emily Goldberg, Sarah Hanson, and John Huss. I would also like to thank the members of the MEPS Lab, including Nate Fulbright, Alek Gust, Steve Thomalla, Jeremy Simmons, Grey Boyce-Erickson, John Voth, Nitish Ponkshe, Garrett Bohach, Jenny Swanson, Kshitij Sonkar, and Jonatan Pozo Palacios for welcoming me, along with my pile of questions, into weekly meetings. Our daily interactions made work more enjoyable and undoubtedly expanded my breadth of knowledge.

Many of my contributions could not have been made without the help of various undergraduate researchers, including Gabe Korinek, Ben Hamlen, Khoi Nguyen, Daniel Ng, Kelly Pelicano, Riley Kaiser, and Charles Feng. Mentoring and learning from each of them taught me how to

become an effective leader, but more importantly brought a sense of fulfillment as they all grew into experts in their own fields of interests. I owe a special thank you to Ben Hamlen and Khoi Nguyen who displayed incredible work ethic and a dedication to learning that went far beyond what any graduate researcher could expect.

My education would not have been possible without the financial support of various organizations, including the University of Minnesota College of Science and Engineering, National Science Foundation Graduate Research Fellowship, and University of Minnesota Institute for Engineering in Medicine. Their generous support allowed me to focus on academics, mentorship, and collaboration without added financial stressors.

Finally, I would like to thank my family for all of their support. Although they may never be able to fully describe my research to those who ask, they provided unending encouragement, engagement, and, when necessary, distraction throughout my pursuit of a Ph.D. To Tara, thank you for keeping me in high spirits, always. To my siblings, I am incredibly proud to be part of a crew with such vast interests and achievements. To my parents, thank you for instilling commitment and determination in each of us and constantly pushing us to set and achieve new goals. None of this would have been possible without each of you.

Dedication

To my relentless supporter, Grandma Toni.

Abstract

The advancement of soft robotics and the inherent ability of soft robots to interact safely with delicate environments has created a host of opportunities for innovation in a wide range of disciplines, from pipe inspection to muscle rehabilitation. The compliance of soft robots has potential to be particularly valuable in medicine where robots are becoming increasingly present in clinical settings. However, developing medically relevant soft robots at millimeter size scales and accurately predicting how they will interact with their environments is a challenge that has yet to be overcome. This work investigates how soft robot behavior is affected as the size of the robot is reduced using both novel experimental prototypes and efficient modeling methods.

One core contribution of this work is a soft robot design that is capable of locomoting through tube-like environments, such as arteries or the intestinal tract. The overall robot is modeled using components of fluid power systems to enable the robot, comprised of multiple individual sections referred to as actuators, to move in sequence using just one control input. The experimental prototype was developed using custom fabrication methods to allow new designs and material combinations to be efficiently explored.

A second key contribution is an interaction model that predicts the actuator shapes and forces that develop as a result of soft robots interacting with environmental constraints. The model utilizes a combination of Hencky bar-chain and linear complementarity methods to create a simple, efficient contact model that does not require computationally expensive finite element modeling and estimates shapes with errors of 1.06% and forces on the order of grams-force.

A third major contribution is the determination of the factors controlling the underlying dependence of soft actuator bending stiffness on actuation pressure, which ultimately plays a role in how robots behave. The presented work introduces the free-fold test to soft robotics to empirically estimate the bending stiffness of soft actuators, whether composite or homogeneous.

This work concludes by tying together the proposed models and corresponding empirical studies to provide a design tool and overall understanding of how soft robot behavior is affected by size reduction. The work identifies fundamental challenges and performance limitations of producing increasingly smaller soft robots at the millimeter scale and provides a foundation on which to build in order to advance the viability of soft robots in medicine.

Contents

List of Tables

List of Figures

Chapter 1

Introduction

The use of robots in surgery began in 1985 when the Puma 560 was modified for precise control in neurosurgical biopsies [5]. Since then, medical robots have become more advanced and versatile, but their impact remains limited due to size and rigidity. The growing field of soft robotics provides an opportunity to overcome those limitations by offering robots that are soft, compliant, and inherently safe for use in intricate environments such as the human body. This thesis addresses the need to better understand how the behavior and performance of soft robots is altered as their size decreases to an anatomically relevant scale. The result of the work discussed throughout this thesis is a foundational design tool and improved fundamental understanding of the effects of scaling down for use in creating soft robots that provide solutions to prevalent health challenges. To better understand the motivations behind this thesis, the innovations and gaps in current soft robot technology will be discussed followed by an overview of the specific contributions of this work to address those gaps.

1.1 Background

1.1.1 Medical Motivation

Since the first laparoscopic appendectomy was performed in 1983, minimally invasive surgery has undergone rapid growth [6]. Due to smaller incisions and reduced trauma to the patient, minimally invasive surgery offers benefits to patients like shorter hospital stays, lower procedure

costs, and improved patient outcomes [7]. Robotic surgery has grown in tandem with minimally invasive surgery after the PUMA 560 robotic surgical arm was used in 1985 to perform a robot-assisted neurosurgical biopsy [8]. As of 2020, over 9.5 million robot-assisted procedures have been performed globally across a wide range of specialties [9]. One reason for this growth is the increase in surgical accuracy and repeatability provided by state-of-the-art technology, such as the da Vinci™ Surgical System (Intuitive Surgical®, Sunnyvale, CA) [10, 11], which continues to be used in today's operating rooms.

Although there are many compelling areas for the advancement of robotics within medicine, one of the areas that could particularly benefit from soft robots is stroke treatment. In the United States, a person has a stroke every 40 seconds; every four minutes, someone dies of stroke [12]. Approximately 87% of all strokes are ischemic strokes, meaning an artery that supplies blood to the brain is blocked by a clot [12]. The most effective way to treat an ischemic stroke is to have a highly trained neurointerventionalist use minimally invasive techniques to remove the clot as quickly as possible because the time to treatment is critical to patient outcomes, as shown in Fig. 1.1 [13, 14]. If clot removal, known as thrombectomy, is performed within three hours of a stroke, 64% of patients will be able to live independently three months later. Independence drops to 46% if performed eight hours after a stroke [14].

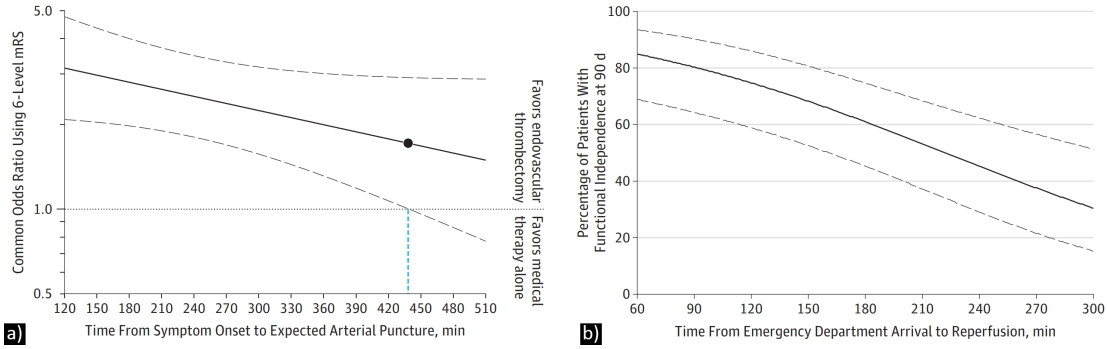

Figure 1.1: a) The odds ratio for less disability at three months in endovascular thrombectomy compared to medical therapy groups alone b) Functional independence of patients after 90 days based on time to reperfusion (clot removal) [14].

However, one of the largest hindrances to proper and timely stroke treatment is a lack of neurointerventionalists available to provide round the clock clinical service for interventional procedures [13]. The hospitals at which a qualified neurointerventionalist is available around

the clock to treat stroke patients are called stroke centers. In Minnesota and many other regions throughout the United States, stroke centers are concentrated around urban areas as shown in Fig. 1.2, making it more difficult for residents in rural areas to receive timely treatment [15].

Due to the minimal number of stroke centers, the median time from onset to arrival is between 165 and 342 minutes, depending on whether the patient needs to be transferred [16]. For every minute that passes without treatment, the patient loses approximately 1.9 million neurons [17].

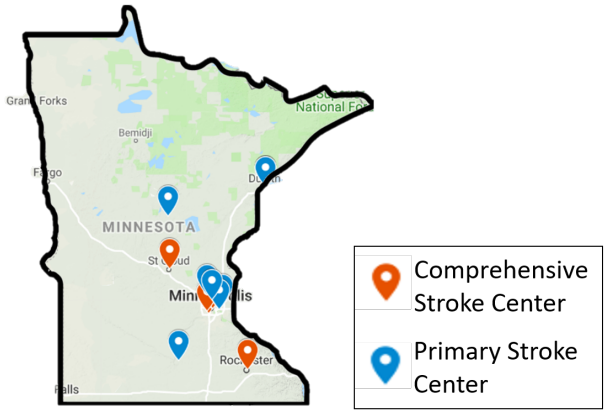

Figure 1.2: Map of Minnesota stroke centers. Data from [15].

The compliant and inherently safe nature of soft robots offers an opportunity to transform stroke treatment by automating thrombectomies. Instead of wasting precious hours while being transported to a stroke center, patients could be treated remotely or en route by a soft robot capable of propelling itself through the arteries to remove the clot using CT scanners within mobile stroke units as guidance.

Although the specific motivation discussed thus far has been focused on stroke treatment, a stronger understanding of soft robot behavior and interaction with the constraining environments at millimeter scales could create a foundation for soft robot design to bring innovation to many other areas, from transcatheter medical procedures to pipe inspection and construction.

1.1.2 Soft Robots: Necessary First Steps

The idea of soft robots navigating human vasculature while using CT scans as a "road map" would undoubtedly transform stroke treatment and medicine, but gaps within soft robotic technology must first be addressed. The term "soft robotics" was first adopted in 2008 and was used to describe the study of rigid-bodied robots with compliant joints, as well as robots made from soft material that could flex, deform, and adapt to large degrees [18, 19, 20]. More generally, soft robots can be thought of as any machine or device that is made of compliant material and controllable via an actuation method (e.g. fluids, electricity, magnetism, heat) such that it can safely interact with its environment. This adaptability allows the intelligence and benefits of robots to no longer be confined to safety cages, but instead accomplish tasks that would be nearly impossible for rigid robots made from hard materials, such as grasping unknown objects, locomoting through dynamic and congested environments, and interacting safely with humans [19, 20, 21, 22].

Because the field is relatively new, many fundamental modeling, design, and manufacturing challenges have yet to be understood. For example, what are the tradeoffs of various actuation methods based on the use case of the robot? How can we practically manufacture soft robots such that they are controllable, yet compliant – especially at smaller scales? How does a compliant machine interact with its environment? How small, or how large, can we make soft robots without compromising their efficacy — and how does the change in size affect their behavior? The list of questions the soft robotics community is working to address is expansive and critical to continued advancement of the field. This thesis addresses several of the fundamental soft robotics questions aimed at improving medical technology, specifically:

1. Can we design and control a soft robot that is capable of locomoting through structures similar to human anatomy (e.g. arteries)?

2. How does a soft robot quantifiably interact with its environment and what computationally tractable models capture this interaction?

3. Specific to fluid-powered soft robots, how does the pressure required to actuate the robot affect its properties and behavior?

4. What are the limitations imposed by scaling down a soft robot to a medically relevant scale, and how can we use the information to inform robot design?

1.2 Literature Review

1.2.1 Soft Robotics

Soft robotics covers a broad range of compliant systems, both active and reactive, and is categorized as a subset of hyper-redundant and continuum robots [22]. The applications of soft robotics are vast, and include soft actuators, artificial muscles, stretchable sensors and electronics, soft energy harvesting, and more [23]. The benefits of soft robots, however, do not come without trade-offs. Safe, soft-bodied robots are compliant and less rigid in their movements — requiring elastic components and lubricious tendons to move — but these natural and pliable movements introduce control and motion planning challenges due to their passive nature and potentially infinite degrees of freedom [24]. In other words, the behavior of the robot is no longer a simple kinematic solution to a chain of rigid links, but is dictated by the robot design, control, and its environment [25].

Soft robots must vary greatly in size in order to excel across such a wide range of application areas. Micro-tentacle robots reach 2 mm or less in diameter, while elephant trunk robots are more than an order of magnitude larger at over 100 mm in diameter [26, 27, 28]. Surgical applications for procedures within the human body, particularly in places that current technology cannot navigate effectively, require robots on the smaller end of the spectrum. Neurovascular catheters are typically below 3 mm in diameter and most diagnostic cardiovascular catheters are below 2 mm in diameter [29, 30]. Smaller robots also mean limited space for actuation mechanisms. As a result, precise control becomes more difficult and force from the robot's end effector becomes limited, yet both factors remain critical to surgical success.

The most common materials used as the core structure of soft robots are elastomers such as silicones, urethanes, natural rubbers, and hydrogels [31, 32]. A comparison between commonly used elastomers and biological tissue is shown in Fig. 1.3. The manufacturing methods used alongside the materials are quite diverse. A majority of robots are made by molding, where catalyzed polymer is poured or injected into a mold that dictates the shape of the actuator. One benefit of molding is that soft-rigid hybrid systems can be generated and support structures can be cast into the robot walls. Another method is thin-film manufacturing where multi-layered robots are created using a combination of etching, lamination, and cutting. A more recent development is in additive manufacturing with the ability to 3D print soft robots, which allows

the possibility to generate multi-material robots with smooth transitions, embed electronics, and create self-healing robots [32, 33, 34, 35]. Finally, both shape deposition manufacturing and bonding allow the ability to utilize the benefits of multiple manufacturing approaches by either using both additive and subtractive processes, or bonding several solutions together [36].

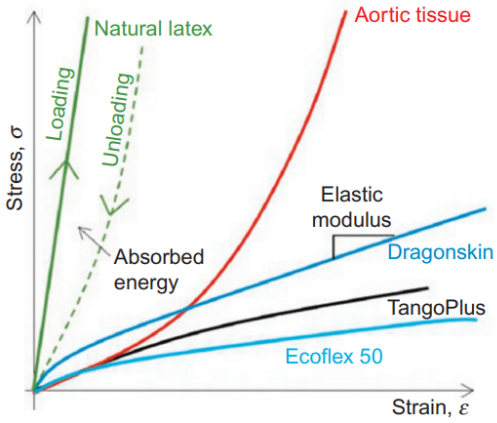

Materials	Young's modulus*
Biological tissue	
Human epithelial cells	10 kPa
Soft tissue	1 Mpa
Mammalian muscles	10 Mpa
Human bone	10 GPa
Artificial materials	
Hydrogels	< 10 kPa
PDMS	1 MPa
Vulcanized rubber	10 MPa
Polyurethane	10 MPa
Polyethylene	0.1 GPa
Carbon nanotubes	1 TPa

*Values are approximate and within an order of magnitude

Figure 1.3: Material comparison between commonly used elastomers and biological tissue. Image from [37].

Biological Inspiration

Many researchers are looking to mechanisms and organisms in nature to help solve the scalability, control, and force density problems [38, 39]. Biologically-inspired soft robots include robotic cephalopods that generate effective forces while remaining flexible [40, 41], snakes that slither on unstructured terrain [42, 43], insects that maintain traction in their environment to locomote [44, 45, 46, 47], fish that utilize non-rigid movements to navigate in water [48], elephant trunks capable of manipulating objects like a human arm [49, 50, 51], and vines that grow at their tip [52, 53, 54]. The biological foundations often guide robot designs to tackle problems in ways that traditional robots cannot. Each biological robotic inspiration moves in unique ways and, as such, requires distinctive mechanisms to produce and control each movement.

Actuation Mechanisms

To mimic the movement of these biological systems, soft robots can be actuated, meaning their movement controlled, by a host of actuation mechanisms. El-Atab et al. nicely summarize the

different classes of soft actuation mechanisms, comprising electrically-, magnetically-, thermally-, and photo-responsive, as well as pressure-driven, and explosive stimulation types [55]. Each actuation mechanisms can be further broken down into subgroups, all contributing to the controlled motion of soft robots that have benefits and downfalls for various use cases.

The proposed research primarily focuses on fluid-powered robots due to their high power density and compatibility with the human body if actuated using saline [56]. Suzumori et al. emphasized the benefit of fluid actuation in modeling and control, stating, "By measuring the volume and pressure of an operating fluid having been supplied, the operator can learn about the posture of the actuator and the acting force; that is, it is possible to control the posture and the acting force without equipping a sensor on the distal end of the actuator" [57]. Fluid-powered robots generate movement by controlling the flow of fluid between soft chambers. Fluid-powered soft robots can be broken down into two types: single-chamber and multi-chamber, as shown in Fig. 1.4.

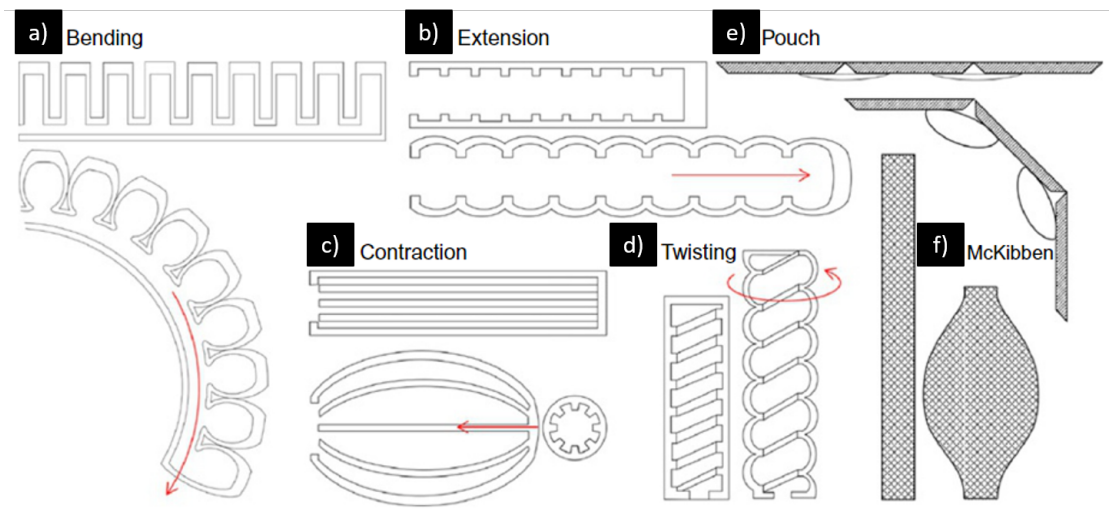

Figure 1.4: Different fluid-powered soft actuators generate different movements, including: a) bending, b) extension, c) contraction, d) twist, e) bending via fluid pouches acting on rigid elements and f) contraction via inextensible fibers (McKibben). Image from [37].

As the name implies, single-chamber, fluid-powered robots are comprised of one main bellows. Additive and subtractive manufacturing techniques are used to generate relief patterns or patterns of varying stiffness of material to control the behavior of the robot. Other components can also be embedded or incorporated into the single-chamber structure, such as fibers, valves,

and sensors to add functionality and control. One of the earliest versions of a soft robotic actuator is called a McKibben actuator, which was introduced as an artificial muscle in the 1950s [58]. The McKibben actuator has a single-chamber and utilizes inextensible fibers enclosing the elastomer to dictate extending or contracting movements. A majority of this thesis focuses on a subset of single-chamber, fiber-reinforced, fluid-powered robots called fiber-reinforced elastomeric enclosures (FREEs).

Alternatively, multi-chamber soft robots are typically produced with molding and casting techniques and are comprised of a series of connected chambers. As pressure is increased, fluid moves through the channels and generates varying motions based on the overall structure of the robot. One of the designs that helped soft robot become more accessible and affordable is PneuNets, or pneumatic networks, which were introduced in 2011 by the Whitesides Research Group at Harvard [31, 37, 59]. PneuNets created the foundation for advancing multi-chamber robots and soft robots in general, showing that by changing the layout of the fluid chambers or the material combinations used, a range of actuator behaviors could be generated.

The introduction of the McKibben actuator and PneuNets laid the foundation for others to build off of in the fluid-powered soft actuator space. One such innovation was the idea of varying the angles of the fibers reinforcing the actuator wall to dictate behavior.

Fiber-Reinforced Soft Actuators

As mentioned in the previous section, fiber-reinforced actuators utilize a single bellow and strategically placed fibers to add local rigidity along the actuator to produce displacement and forces [60, 61, 62, 63]. The major benefit of this style of soft actuator is that the inextensibility of the fibers allows the actuator to withstand high actuation pressures, and thus, exert larger forces on its environment while remaining compliant.

The McKibben actuator was the first actuator of this kind [58]. McKibben actuators consist of a soft tube with fibers placed at equal and opposite angles, as shown in Fig. 1.5. Variations of McKibben actuators go by many names, such as pneumatic air muscles, artificial muscles, hydraulic artificial muscles.

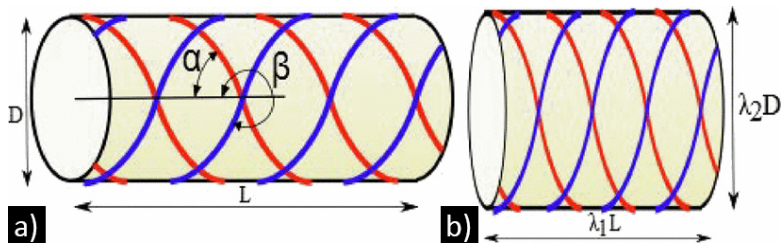

Figure 1.5: Pertinent dimension of a McKibben actuator. Note that $\alpha = -\beta$. Image from [64].

In 1996, Chou et al. developed a fundamental method for designing McKibben actuators by mapping input pressure to output force based on the wrap angle of the fibers [63]. Since then, more developed models have been introduce that incorporate material properties and the characterization of frictional forces relative to material properties into the model [62, 65, 66]. Additionally, actuator designs have moved from the equal and opposite fiber wrappings of McKibbens toward two pattern fiber weaves and varying fiber angles [67, 68, 69].

Since the introduction of the McKibben actuator, a generalization of fiber wrapped actuators has sprouted called Fiber-Reinforced Enclosed Elastomers (FREEs), of which McKibben actuators are a subset. FREEs utilize a soft, elastomeric tube encased with two or three fibers of varying orientation to generate movements that go beyond the extension and contraction of McKibben actuators [70, 71, 72, 73]. The FREE model focuses on creating kinematic models that map an internal volume to an output position. Various output positions, or actuation modes (e.g. twisting, bending, spiraling, extending), are generated by varying fiber wrap orientation combinations as shown in Figure 1.6 [71].

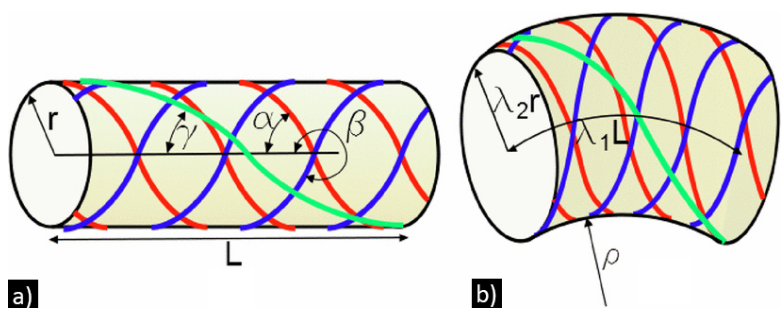

Figure 1.6: Fiber reinforced elastomeric enclosures (FREEs) utilize two or more fibers wrapped at controlled angles to generate motion from a) an initial configuration to b) a pressurized, deformed configuration [71].

These FREE actuators can be strategically combined to create entire robots that are controlled by fluid pressure. The objective of the robot discussed in this work is to locomote through structures comparable to human anatomy without the need to be pushed and controlled directly by a surgeon.

Locomoting Soft Robots

The ability to navigate within unknown environments is both a key challenge and benefit of soft robots. Whether the goal is to explore new and unknown territories or move through hazardous or restrictive areas that cannot be reached by humans, soft robots provide an opportunity to explore in a gentle, safe, and adaptable manner. Researchers have successfully implemented soft robotics to generate peristaltic crawling, walking, jumping, rolling, winged flight, swimming, vine-like navigation, and vibration based movement [53, 74, 75, 76].

The robot discussed in this work focuses on a two-anchor crawling approach in which the robot moves similarly to an inchworm. An example of a potential two-anchor robot is shown in Fig. 1.7.

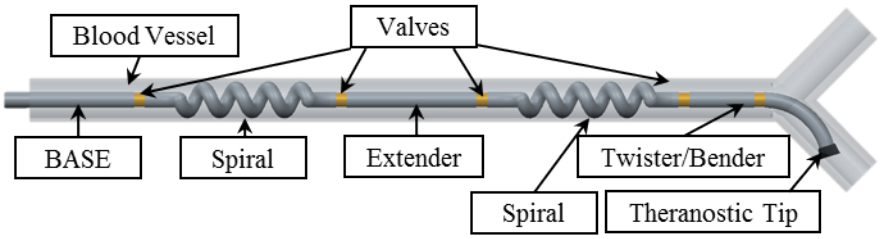

Figure 1.7: The proposed soft robot navigating through a tube. The robot consists of a tethered base, three segments for locomotion, each containing a valve and an actuator, and an end-effector made up of a bending and twisting actuators as well as a theranostic tip.

The specific sequence of movement involves anchoring into the environment, then extending and contracting the robot body to generate forward motion. Although this mode of locomotion is not novel to the field [74, 75], the specific design discussed in this work is unique in that it utilizes anchoring actuators that do not occlude its environment. This is particularly useful in medical applications when maintaining blood flow is critical.

Medical Soft Robots

The use of microrobots for minimally invasive medicine has been a major focus of medical technology for many years [77]. Soft robots, in particular, have been gaining popularity among medical professionals due to their soft feel, compliance, and compatibility with natural tissues for surgical and wearable applications [27]. While rigid equipment jeopardizes patient safety by increasing the possibility of causing damage or discomfort, medical soft robots conform to the body's natural and delicate surfaces. The increase in interest is not solely applicable to surgeons either. As shown in Fig. 1, research in soft robots for surgery has increased steadily since 2013 [78].

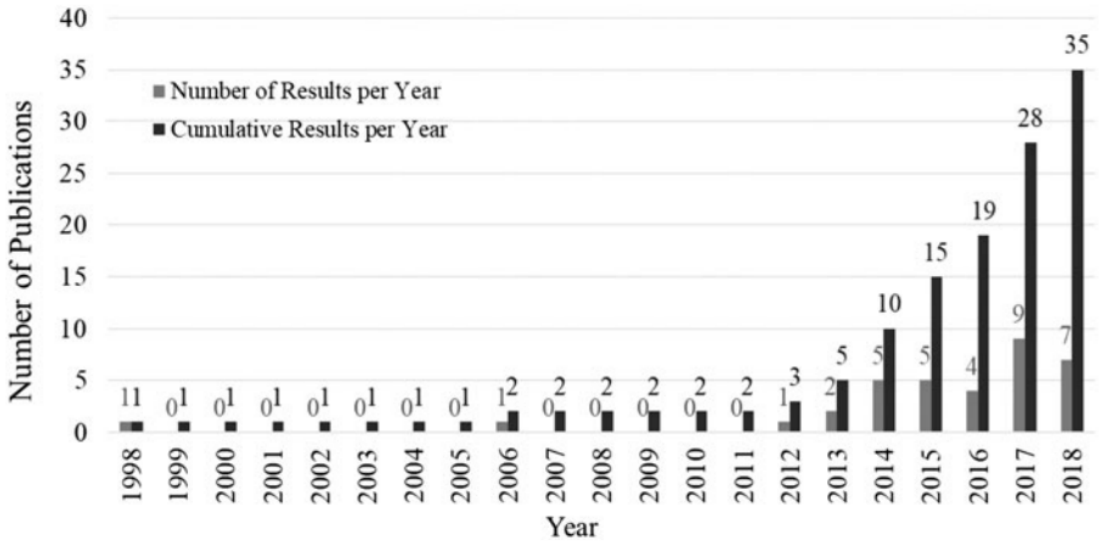

Figure 1.8: The interest in medical soft robots has grown in recent years, as shown by the increase in publications whose core focus was soft robots for surgery. Image from [78].

Applications for medical soft robots include rehabilitation [79, 80, 81], cardiac compression [82], steerable catheters [83, 84, 85], and colonoscopy tools [86, 87, 88].

Although many colonoscopy robots move in a similar self-propelled motion to the robot discussed in this thesis, they differ in their size, anchoring approaches, and control mechanisms [74, 89, 90, 91]. One of the main methods of inchworming through the body, specifically the GI tract, is with a double balloon approach comprised of three individual actuators combined [88, 92]. The two actuators on the ends expand like a balloon to provide anchoring force while

the middle actuator extends and contracts to provide extension and contraction to move the robot forward. However, these anchoring balloons completely occlude their environment. For the GI tract, which is filled with air, full occlusion is acceptable. In applications such as stroke treatment, it is less desired and more dangerous to block blood flow with anchoring balloon actuators.

Takeshima and Takayama used a unique approach for in-pipe locomotion that resembles the anchoring actuators in the robot proposed in this thesis [91]. The robot locomotes within pipes using pneumatics to deform a triple helix bundle of actuators. Once pressurized, the helices generate traction in the pipe, and periodic pressurization allows the bundle to travel. This design differs from the robot in this thesis in that the entire robot consists of one bundle of helical actuators, rather than the inchworming, double anchor approach previously described. The downside of the design presented by Takeshima and Takayama is that it requires multiple pressure lines to control each of the helices within the bundle, which would make the design more complicated to scale down to millimeter or sub-millimeter scale and also results in higher occlusion ($\sim$3x) of its environment. Additionally, the success of the locomotion relies solely on traction force and minute progress with each period of pressurization, which would likely cause challenges in slick environments or in situations where time is of the essence (e.g. surgery).

The other benefit of many inchworming robots published in the soft robotics community is their size. Endoscopic robots typically have outer diameters of approximately 15 mm or more [89, 92], whereas the work throughout this thesis focuses on the effects of scaling down to sizes much smaller than 15 mm. The larger size also makes the control of the robot simpler because multiple actuation lines can fit within the robot to control each actuator individually without hindering overall performance. As the size of the robot is decreased, however, the possibility of large deformations from anchoring actuators and space for multiple actuation lines disappears.

Ikuta et al. was one of the earliest researchers to develop a steerable catheter at millimeter scale. The design consisted of two serially-connected bending actuators separated by a bandpass valve and controlled by a pressure line [83, 84, 85]. The method of actuation is similar to the control mechanism discussed in Chapter 2 of this work in that multiple actuators are separated by a valve and controlled using a single pressure source. However, Ikuta et al. use a bandpass valve which is more difficult to scale down compared to completely passive components as used in this work. Ikuta's steerable catheter has successfully been manufactured to 3 mm, but is slow to

actuate and is limited in its movement by two degrees of freedom. This group has also worked on even smaller bending actuators that are 1 mm in diameter and extremely delicate [93]. Although the ability to create and control an actuator at that size is astounding, the manufacturing process is complex and not widely available. Additionally, steerable microcatheters are able to bend and manipulate an end effector efficiently, but are limited in the tasks they can perform due to their inability to carry a payload.

Perhaps the smallest soft robot for medical applications to date is a ferromagnetic continuum robot by Kim et al. [94]. The robot has an outer diameter of just 600 μm and is capable of active steering and navigation via magnetic actuation. The group has proven the robot's ability to deliver laser therapy within phantom vasculature, which could provide future treatment functionalities. The benefit of the robot is that it circumvents many of the miniaturization challenges of conventional soft robots and utilizes a hydrogel coating to reduce friction and assist with navigating in tight, tortuous cerebrovasculature. However, the robot requires magnetic fields of approximately 80 mT, creating a complicated control scheme that is not readily available. Furthermore, the robot does not contain an inner lumen to use as a working channel to deliver surgical tools to its tip, nor would it be capable of withstanding the forces that could be encountered by transporting non-laser tools or interacting with the body to deliver therapy or diagnostics. Nonetheless, the size of the robot and its steerability of along tortuous paths is a remarkable leap forward for soft robotic technology and medical technology as a whole.

1.2.2 Actuator Modeling

As discussed throughout previous sections, modeling has been applied to predict and describe the intricacies of soft robots across nearly all aspects of the field. Several groups have modeled the strain and force produced by McKibben actuators [66, 95, 96], although none have derived an explicit model for how the bending stiffness changes as a function of pressure, as will be discussed in Chapter 4. Others have emphasized the importance of a model to describe the pressure exerted by an anchoring balloon and the corresponding pressure from its environment and the strain of the elastomer [92].

A wide range of modeling methods have been utilized, although the finite element method (FEM) is perhaps the most prevalent across all categories of soft robots [61, 97, 98]. The downside of FEM is that it is computationally expensive, time consuming, and oftentimes require

advanced knowledge of all material properties of the actuator components. When manufacturing soft robots with diameters on the millimeter scale, small variations in manufacturing can lead to intractable differences between detailed finite element models and experimental robot behavior.

More specifically, portions of this thesis focus on the deformation of fluid-powered soft actuators as a function of pressure and the ensuing forces exerted by the actuators. The modeling of soft, bending actuators as a function of pressure has been sufficiently studied both with FEM and physics-based methods [61, 99, 100, 101, 102]. However, the models created to describe contact forces between a bending actuator and its environment typically utilize computationally expensive FEM or explicitly focus on point contact rather than a contact region [61, 98].

The unique aspect of the actuators discussed throughout this thesis is that they deform as a function of pressure and their construction rather than from external forces. This is referred to as eigenstrain ("eigen" in German means "inherent" or "self") which is discussed in detail in Chapter 3. Coevoet et al. focus on a non-FEM, optimization-based model to describe soft robots with contact handling of objects [103]. The group uses an approach used as part of the contact model in this work, the linear complementarity approach. However, one major difference between the work of Coevoet et al. and this thesis is that the robot in Coevoet's work uses cable actuation rather than an actuator that deforms by eigenstrains. Additionally, the modeling of the system performed before using quadratic program with linear complementary constraints differs, where Coevoet et al. describe the robot using piece-wise constant curvature and this work applies the Hencky Bar-Chain model to describe the continuous actuator as a discretized structure.

A review of all modeling approaches presented in soft robot literature is beyond the scope of this thesis. Rather, the following sections provide an overview of the two core methods used for modeling – and more specifically, contact modeling – in this work.

1.2.3 Hencky Bar-Chain

One of the key modeling approaches used throughout this thesis, specifically in Chapters 3 and 4, is the Hencky Bar-Chain model (HBM), which is comprehensively reviewed by Wang et al. [104]. The Hencky Bar-Chain model was first proposed in 1920 by Professor Heinrich Hencky as a method for describing continuous structures in a discrete manner, such as beams, elastica, and in this case, soft robotic actuators [104]. The premise behind HBM is to treat continuous

structures as a series of rigid links connected by frictionless hinges with elastic rotational springs, as shown in Fig. 1.9.

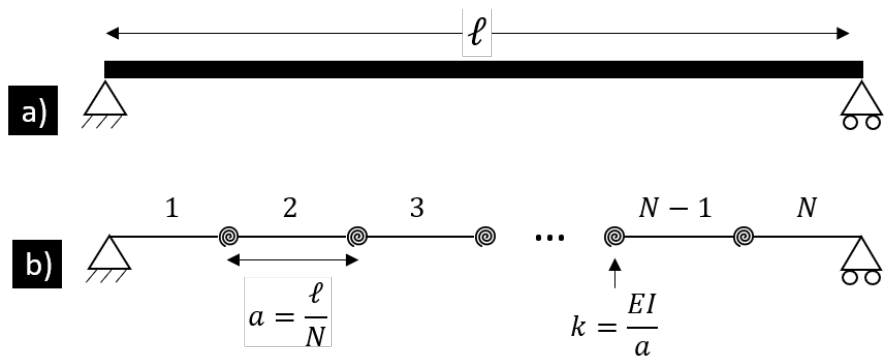

Figure 1.9: a) Continuous, simply supported Euler beam of length, ℓ, and stiffness, EI. b) Hencky Bar-Chain approximation of the continuous beam. The beam is comprised of N rigid links, each of length $a = \frac{\ell}{N}$, connected by a torsion spring of stiffness $\frac{EI}{a}$.

The stiffness, k, of each rotational spring can be described as

$$k = \frac{EI}{a} \tag{1.1}$$

where EI is the bending stiffness of the "beam" being modeled, where E is the elastic modulus of the beam and I is the beam's area moment of inertia. The length of each link is represented by a. The relationship between link length and the overall length, ℓ, of the beam is

$$a = \frac{\ell}{N} \tag{1.2}$$

where N is the number of links in the discretization.

The rotational spring stiffness is derived from a discretized adaption of the moment-curvature relationship, described by

$$M = EI\left(\frac{d\theta}{dx}\right) \approx \frac{EI}{a}\delta\theta = k\delta\theta \tag{1.3}$$

where $\delta\theta$ is the change in angle between two adjacent rigid links.

Mathematically, HBM is a physical structure equivalent to the first order central finite difference method (FDM). Computationally, the discretization displays advantages over numerical methods, primarily in the simplicity and speed of HBM, as will be shown in Chapters 3 and 4.

This is because the governing ordinary differential equation is discretized into a set of algebraic equations [104]. The solution accuracy and computational efficiency can be modified by adjusting the resolution of the discretization which is equivalent to changing the number of rigid links, N. As expected, a finer discretization produces a solution that is closer to the continuum Euler beam or structure which the Hencky Bar-Chain approach is modeling.

Interestingly, as the number of discretizations approaches infinity, HBM agrees with the discrete planar Cosserat rod model, which is a method commonly used in continuum robotics to model concentric tube robots [105]. However, HBM is a softer model in comparison to the discrete planar Cosserat rod model, meaning it underestimates the Euler's formula as opposed to the overestimation of the Cosserat rod model [104].

Although HBM has been used since the mid 1900s, its applications have primarily focused on structural engineering and vibration analysis. HBM has yet to be widely adopted within the soft robotics community and this work outlines how soft robot modeling can benefit from the computational simplicity and efficiency of approximating a continuous soft robot as a discretized Hencky Bar-Chain structure.

1.2.4 Linear Complementarity Method

Another key modeling approach used throughout this thesis to model the interaction between soft robots and their environments is the linear complementarity method, also commonly referred to as a linear complementarity problem (LCP). The linear complementarity method was first proposed in 1966 by Richard Cottle as a mathematical optimization problem that unifies linear and quadratic programs and bimatrix games [106]. LCPs have numerous applications beyond contact problems, including computing economic equilibria and solving systems of nonlinear equations [107, 108]. Additionally, LCPs can handle large scale linear programs that otherwise create numerical difficulties. The problem is stated as the following: given a real matrix $M \in \mathbb{R}^{n \times n}$ and vector $q \in \mathbb{R}^n$, find the vectors w and z that satisfy

$$w = Mz + q \tag{1.4}$$

$$w \geq 0 \tag{1.5}$$

$$z \geq 0 \tag{1.6}$$

$$z^T w = 0 \tag{1.7}$$

where $z^T w = 0$ is the complementarity condition that implies that for all $1 \leq i \leq n$, at most only one of w_i and z_i can be positive.

Because this thesis will focus on the use of LCPs to model interactions between soft robots and rigid environments, an example of a contact problem using LCP is shown. A simple system that can be used to gain a stronger understanding of Linear Complementarity Problems (LCPs) is the example of a weighted ball suspended above the ground by a spring, as shown in Fig. 1.10.

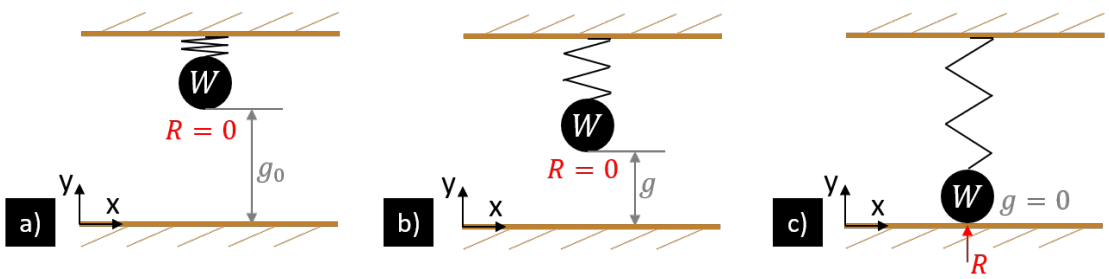

Figure 1.10: Example linear complementarity problem of a ball of weight, W, suspended above the ground by an initial distance, g_0, by a spring of stiffness, k. When the ball is released, depending on the ball weight, initial distance, and spring stiffness, the remaining gap, g, or the reaction force between the ball and the ground, R, can be solved using the linear complementarity system of equations.

We can describe the system as

$$R = kg + q; \tag{1.8}$$

where R is the reaction force that develops between the ball and the ground when in contact, k is the stiffness of the spring, and g is the gap or distance between the bottom of the ball and the ground. We can define a variable q such that

$$q = W - kg_0; \tag{1.9}$$

where g_0 is the initial distance between the bottom of the ball and the ground before the ball is released from its initial height. The system is subject to the constraints

$$g \geq 0 \tag{1.10}$$

$$r \geq 0 \tag{1.11}$$

$$g^T R = 0 \tag{1.12}$$

where $g^T R = 0$ is the complementarity condition. As shown by the complementarity condition, it is physically impossible to have both a gap and a reaction force between the weighted ball and the ground. Throughout this thesis, a similar method will be used to create a computationally efficient soft robot contact model without the need for intricate modeling methods such as Finite Element Modeling. Similar to the Hencky Bar-Chain model, linear complementarity problems are widely used throughout other fields, particularly in engineering, mathematics, economics, and computer science [108]. However, linear complementarity approaches to soft robot contact models have only been used by a small number of groups, none of which use the combination of HBM and LCP to model soft robots in a similar manner to this work [98, 103, 109]. Further detail is discussed in Chapters 3 and 4.

1.3 Overview

The remainder of this thesis consists of five chapters, first beginning with an overview of the robot design that is the focus of this research, followed by an in-depth analysis of how soft robotic properties, behavior, and performance are affected when the size of the robot is reduced to a medically-relevant scale. The summary and specific contributions of each chapter are as follows:

- **Chapter 2: Serial Locomotion in Tube-Like Environments and the Effects of Scaling Down -** This chapter discusses the design, modeling and control of a soft robot capable of locomoting within tube-like environments, including actuator and passive valve design and modeling. Following the overview of the robot design, the chapter investigates the challenges of maintaining locomoting capabilities while scaling down the size of the robot to the millimeter scale.

- **Chapter 3: Interaction Model Between Soft Robots and Rigid Environments -** This chapter contributes a model for the shape a robotic actuator assumes when constrained by an environment, as well as the forces that develop between the robot and its environment. Ultimately, the contributions of this chapter offer insight into how the force capability of soft robots is reduced as a function of the size of the robot.

- **Chapter 4: Pressure-Dependent Bending Stiffness -** This chapter examines how the stiffness of soft actuators, and elastomers in general, changes as a function of pressure.

- **Chapter 5: Extending Actuators and Scaling Down -** This chapter offers a characterization of extending, fiber-reinforced actuators at the millimeter scale and underscores the trade-offs between size reduction and performance.

- **Chapter 6: Conclusion -** This chapter ties all of the core contributions of this work together to offer a soft robotic design tool that can be used for medical-scale robots. An overview of the research of this thesis provides a vision for the future of soft robots, specific to medical applications.

Chapter 2

Serial Locomotion in Tube-Like Environments and the Effects of Scaling Down

This chapter consists of an IEEE Robotics and Automation Letters paper (Section 2.2) [1], a paper in the Proceedings of the 2019 Design of Medical Devices Conference (Section 2.3) [110], a presentation at the IEEE IROS Full-Day Workshop on Continuum Robots in Medicine (Section 2.4) [111], and a technical brief in the ASME Journal of Medical Devices (Section 2.5) [2].

2.1 Chapter Overview

This chapter contains multiple sections that lay the groundwork for the motivation of the succeeding chapters of this thesis. First, the motivating design for robots capable of locomoting within tight environments (e.g. arteries and other tube-like environments) is discussed in depth (Section 2.2) [1]. The results of the inchworm-like robot prototype prompted an exploration of a similar robot capable of the same movement, but at a smaller scale, to move closer to achieving medical relevancy (Section 2.3). Following the scale reduction, specific elements of the robot design and behavior were examined, including a study on anchoring force achieved by anchoring soft actuators (Section 2.4) [111] and an exploration of a new passive valve design to aid in

control of each individual actuator within the robot (Section 2.5) [2].

2.2 Serially Actuated Locomotion for Soft Robots in Tube-like Environments [1]

2.2.1 Introduction

As mentioned in Chapter 1, soft robotics research was spurred in the 1950s with the invention of the McKibben actuator which utilized the wrapping of inextensible fibers at equal and opposite angles around an elastomeric tube to generate extension or contraction as internal pressure was applied [58]. More recently, research has made substantial advances in the area of fluid-powered actuators by exploring the application of various wrap angles to produce novel bending, twisting, helical, and screw motions [60]. These actuators, along with the McKibben actuators, are known as fiber-reinforced elastomer enclosures (FREEs), which map an input volume to a specified motion to expand the movement capabilities of soft actuators [70, 71, 72, 73].

Several studies have focused on combining multiple soft robotic actuators that are individually controlled via a fluid drive line to each actuator. A majority of these robots consist of N soft actuators controlled using N pressure inputs, as shown in Fig. 2.1. However, multiple drive lines make it difficult to scale the robot for intravascular or small-channel environments. Moreover, multiple drive lines require numerous pumps or controlled valves at the source, adding both bulk and cost. This underscores a need for serially-actuated soft robots, with a single control line providing an actuation medium to each actuator of the robot. In addition to the need for serial actuation, actuators must undergo reshaping, like forming helices or extenders, that allows cannular flow to be maintained throughout locomotion.

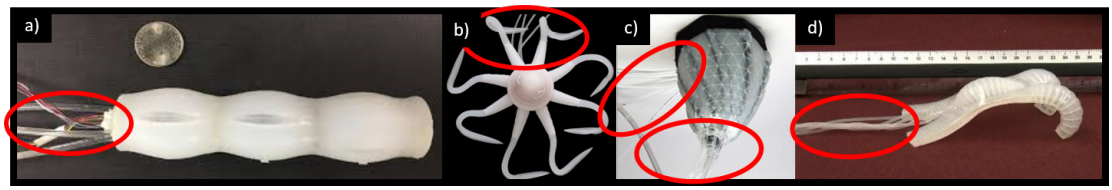

Figure 2.1: Soft robots with multiple input lines: a) Colonoscopy robot (13.9 cm length, 2.4 cm diameter) that utilizes a bio-mimetic peristaltic wave and shape memory alloy (SMA) springs to traverse the GI tract [112]. Each pneumatic pressure line provides forced convection to reduce cooling time in the SMA springs. b) Bio-inspired octopus robot with body diameter of 55 mm [113]. Pressurized air was supplied to each tentacle using multiple, 2 mm outer diameter, flexible tubes. c) Soft robotic sleeve of 16 mm overall thickness to assist in contraction of the heart [114, 115]. Contraction is achieved by using multiple input lines to pressurize soft actuators within the sleeve. d) Soft, quadrupedal robot (14 cm approximate length, 0.9 cm thickness) that can crawl using five actuators which are controlled using five pneumatic pressure lines connected to solenoid valves [116].

Prior work by Ikuta et al. has focused on creating band pass valves to serially actuate and control two soft bender actuators while traversing a blood vessel phantom [84, 85]. The band pass valves were constructed via micro stereolithography and consisted of two check valves that were able to open or close to the actuator based on the input pressure from the control line [83]. A second band pass valve by Napp et al. consisted of rubber flaps sandwiched between plastic orifice plates to create a two-way check valve [117].

The design of the actuators, along with the control of the dynamic response of each segment of the robot, plays an important role in achieving inherently safe, serially actuated locomotion throughout cannular networks. Previous work has focused on the serial control using complex valves, which can be difficult to scale and result in slower locomotion. However, this chapter aims to close the existing gap in current soft robots by producing a serially actuated, soft robot using passive elements (valves) while simultaneously allowing flow throughout locomotion in tube-like environments.

The novel contribution of this chapter section is a generalizable method for designing soft robots to locomote through a specific tube geometry that simultaneously: (1) uses only passive components with no moving parts (i.e. simple orifice valves, unlike [117]), (2) is serially actuated (i.e. requires only one power source, unlike [69]), and (3) utilizes a geometry that avoids blocking flow while maintaining high contact area for anchoring force (i.e. a helical actuator unlike a balloon [69] or bending actuator [83]). This includes experimental validation.

The layout of this chapter section is as follows. First, in the Methods, a design of the robot

based on ideal and theoretical models is discussed. The focus then shifts to the modeling the actuators and valves which make up the robotic segments. Objectives are set for the actuators and valves such that optimal robot locomotion is achieved. Next, the task of the robot including the desired geometry, pressures, and dynamic response is examined. Finally, the necessary actuator and valve designs needed to achieve the task are discussed. This portion of the chapter concludes with a discussion of the experimental results and future work.

2.2.2 Methods

Locomoting Robot Design

The goal of this chapter section was to produce a design method for a soft robot capable of traversing a cannula through serial actuation as shown in Fig. 2.2. The robot consisted of three segments, each including an actuator and a valve. The first and third segments contained helical actuators to anchor into the cannular wall, while the second segment utilized an extending actuator to produce locomotion. A helical geometry was chosen to generate anchoring force for locomotion while also making the robot adaptable to environments where flow through the cannula must be maintained (e.g. vasculature procedures, pipe inspection).

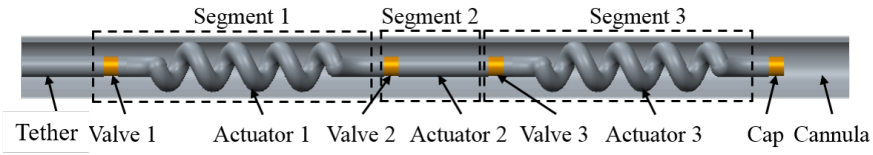

Figure 2.2: Soft robot locomoting through a cannula. The robot consists of a tethered base and three segments, each containing a valve and an actuator. The helical shapes prevent blockage of fluid flow. The cap represents the end effector.

The serial combination of multiple segments and the control of the flow into each actuator with the valves provided the rationale for the ideal locomotion sequence represented by the events labeled in Fig. 2.3. Within the ideal sequence, the robot starts in its nominal unactuated state (Fig. 2.3 event A), then the first segment actuates, forming a helix and anchoring into the wall of the cannula (Fig. 2.3 event B). While the first actuator remains anchored, the second segment actuates, causing extension along the cannula (Fig. 2.3 event C). This is followed by the actuation of the third segment (Fig. 2.3 event D). To move the robot along the cannula,

the actuators are deflated in the same order of actuation (Fig. 2.3 events E-G). This sequence is repeated until the robot reaches its destination.

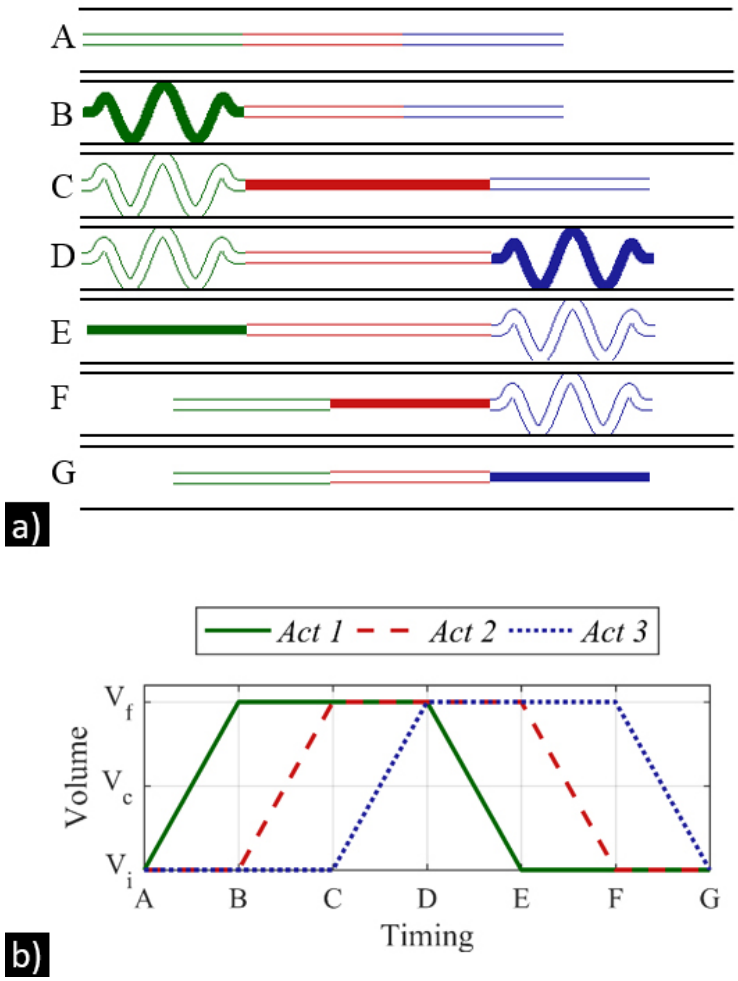

Figure 2.3: a) Ideal actuation and timing events of the soft robot actuators. b) Volume response of each actuator corresponding to the ideal actuation events (Events labeled A-G).

Fig. 2.3b shows the ideal timing of each actuator which corresponds to the states in Fig. 2.3a. The volume-time relationship is crucial because the volume of liquid within each actuator directly translates to the pose of that actuator. There are two important volumes for the actuators. The first is the contact volume, V_c, which is the volume at which the helical actuators (*Act 1*, *Act 3*) make contact with the cannula wall. The second important volume is the final volume, V_f, which represents fully anchored helices for *Act 1* and *Act 3*, and a fully extended actuator for

Act 2.

Theoretical System Model

For the purpose of modeling the pressures and volumes within the system, the valves were modeled as flow restricting orifices and the actuators were modeled as nonlinear, spring-loaded hydraulic accumulators (Fig. 2.4).

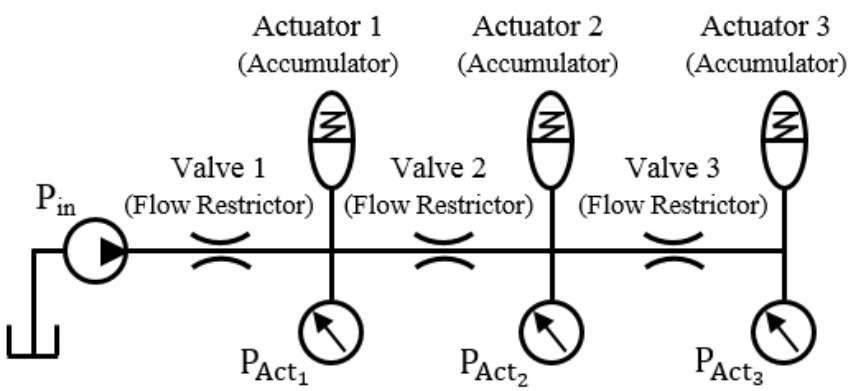

Figure 2.4: Theoretical model showing each segment modeled as a flow restrictor and a nonlinear, spring-loaded accumulator.

The robot was driven by a pressure source. The resulting volume change for each segment was described by the following system of differential equations for the flow rates:

$$\begin{aligned}
\dot{V}_1 &= f_{valve_1}(u, P_{Act_1}) - f_{valve_2}(P_{Act_1}, P_{Act_2}) \\
\dot{V}_2 &= f_{valve_2}(P_{Act_1}, P_{Act_2}) - f_{valve_3}(P_{Act_2}, P_{Act_3}) \\
\dot{V}_3 &= f_{valve_3}(P_{Act_2}, P_{Act_3})
\end{aligned} \tag{2.1}$$

where u is the pressure input, f_{valve_i} describes the flow through a restricted orifice, and P_{Act_i} is an equation to describe the behavior of the pressure in the ith accumulator based on its material properties.

Model Components

Actuator (Accumulator) Model The actuator was modeled as a nonlinear-spring-loaded accumulator. The volume coefficient, V, was the independent variable defined as the ratio of final actuator volume to initial actuator volume (eq. 2.2) and the internal pressure, P, was the dependent variable.

$$V = \frac{V_f}{V_i} \tag{2.2}$$

A polynomial function (eq. 2.3) modeled the nonlinear-spring-loaded accumulator where the coefficients, c_n, could be estimated using least squares from pressure-volume data for each actuator. The polynomial order, n_f, was increased until a residual, res (eq. 2.6), less than 2.5% was reached.

$$P_{Act_i} = \sum_{n=1}^{n_f} c_n (\hat{V})^n \tag{2.3}$$

for n_f such that $e < 2.5\%$ where

$$(\hat{V}) = V - 1 \tag{2.4}$$

$$e = |res(n) - res(n-1)|/res(n-1) \tag{2.5}$$

$$res = \left[\sum_{t=0}^{t_f} (P - [\hat{V} \ldots \hat{V}^n][c_1 \ldots c_n]^T)^2 \right]^{1/2} \tag{2.6}$$

The following assumptions were made: the loading on the rubber in the nonlinear-spring-loaded accumulator was time invariant, exhibited no creep, hysteresis effects were negated [118], and that derivations from such assumptions resulted in negligible error.

Valve (Flow Restrictor) Model The flow restrictors were modeled using the orifice equation (eq. 2.7), which described fluid flow through a restricted orifice and was governed by the valve coefficient, K_i (eq. 2.8), and pressure drop, ΔP [119].

$$f_{valve} = K_i \sqrt[*]{|\Delta P|} \tag{2.7}$$

where $\sqrt[*]{x} = sgn(x)\sqrt{|x|}$.

The valve coefficient, as determined by the orifice equation, was defined as:

$$K_i = C_d A_{orf_i} \sqrt{\frac{2}{\rho_f}} \tag{2.8}$$

where C_d is the discharge coefficient equal to 0.62, A_{orf_i} is the cross-sectional orifice area, ρ_f is the density of the fluid equal to 997.45 [kg m^{-3}] (at 23°C), and i indicates the valve index. Although the orifice equation is a steady state model, it was assumed this model holds true throughout actuation of the robot.

Physical Realization and Targeted Task

Task The specified task for the robot design was to locomote through a cannula ($D = 19$ mm) using a combination of segments that occluded the cannula by less than 50% and experienced pressures under 200 kPa (29 psi). The timing of the actuation needed to follow Fig. 2.3. This meant that *Act 1* must anchor before extension of *Act 2* contributed to locomotion. Additionally, *Act 2* must be near its final volume before *Act 3* anchored. This prevented *Act 2* from buckling or "wasting" extension.

Actuator Design To achieve the desired area occlusion ratio, the inner radii of the actuators were chosen as r=5 mm with 0.8 mm thickness, resulting in an area occlusion ratio of 37%, where the percent occlusion ratio calculation is shown in eq. 2.9.

$$\text{\% Occlusion Ratio} = 100 \left(\frac{r+t}{D/2} \right)^2 \tag{2.9}$$

To achieve the actuator shapes shown in Figs. 2.2 and 2.3, FREE actuators were used. FREE actuators utilize two or three varying wrap angles α, β, γ, as shown in Fig. 1.6, to create helical or extending actuators [60, 71]. The derivation of the FREE model relied on fiber inextensibility resulting in the geometric relations in eqs. 2.10-2.12. The following derivation of eqs. 2.10-2.17 are attributed to and detailed in [60]-[73].

$$\lambda_1^2 c_\alpha^2 + \lambda_2^2 s_\alpha^2 (\frac{\theta + \delta}{\theta}) = 1 \tag{2.10}$$

$$\lambda_1^2 c_\beta^2 + \lambda_2^2 s_\beta^2 (\frac{\zeta + \delta}{\zeta}) = 1 \tag{2.11}$$

$$\lambda_1^2 c_\gamma^2 + \lambda_2^2 s_\gamma^2 (\frac{\psi + \delta}{\psi}) = 1 \tag{2.12}$$

$$\theta = \frac{L\tan(\alpha)}{r}, \zeta = \frac{L\tan(\beta)}{r}, \psi = \frac{L\tan(\gamma)}{r}$$

where $c_\alpha = \cos(\alpha)$, $s_\alpha = \sin(\alpha)$, and L represents the overall length of the actuator.

The radial stretch parameter, λ_2, and axial twist, δ, were solved as functions of the axial stretch parameter, λ_1. This was done by substituting eq. 2.10 into eq. 2.11, resulting in eq. 2.13 and eq. 2.14, respectively.

$$\lambda_2 = \frac{\frac{\alpha}{|\alpha|} c_\beta \sqrt{1 - c_\alpha^2 \lambda_1^2} - \frac{\beta}{|\beta|} c_\alpha \sqrt{1 - c_\beta^2 \lambda_1^2}}{s_{\alpha-\beta}} \tag{2.13}$$

$$\delta = \frac{L}{r} \frac{\frac{\beta}{|\beta|} s_\alpha \sqrt{1 - \lambda_1^2 c_\beta^2} - \frac{\alpha}{|\alpha|} s_\beta \sqrt{1 - \lambda_1^2 c_\alpha^2}}{\frac{\alpha}{|\alpha|} c_\beta \sqrt{1 - \lambda_1^2 c_\alpha^2} - \frac{\beta}{|\beta|} c_\alpha \sqrt{1 - \lambda_1^2 c_\beta^2}} \tag{2.14}$$

The volume coefficient, V, was used to obtain a solution for λ_1 and was also an input to the system. V can be expressed in terms of stretch parameters:

$$V = \lambda_1 \lambda_2^2 \tag{2.15}$$

To solve for λ_1, the Newton Raphson method was applied to eqs. 2.13 and 2.15 with an initial condition of $\lambda_1 = 1$ [72]. For helical actuators consisting of three separate fiber angles, R (eq. 2.16) was defined as the radius of the helix. The helix radius as well as the helix angle, ϕ (eq. 2.17), are depicted in Fig. 2.5 and their derivation can be found in [71].

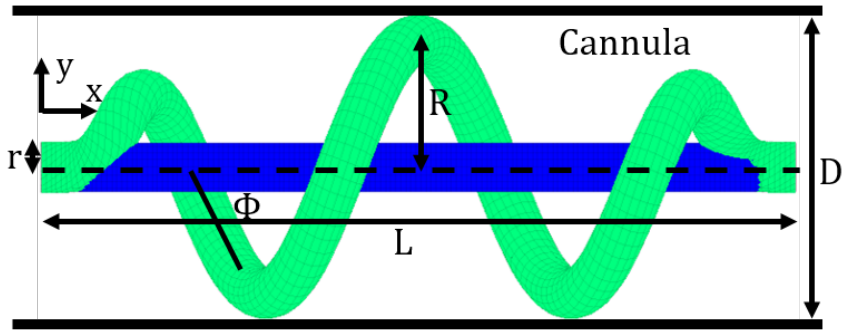

Figure 2.5: Pertinent dimensions for a FREE helix within a tube.

$$R = \frac{\rho}{1 + \left(\frac{(\delta+\psi)\rho}{L}\right)^2} \tag{2.16}$$

$$\phi = \arctan\left(\frac{(\delta+\psi)\rho}{L}\right) \tag{2.17}$$

where ρ is provided in [71].

Actuators capable of forming the desired helix in Fig. 2.2 were targeted as dictated by a specific task (i.e. traversing a $D = 19$ mm diameter tube). This informed the specific design criteria, which were fed into a cost function. The first constraint was to set the volume coefficient to $V = 1.30$ which was used for both helical actuators and the extending actuator. A $V = 1.30$ was chosen because it is large enough to produce the desired R and stable enough to obtain solutions before geometric lock (e.g. see [60]). For the actuator to successfully traverse a tube, R must be greater than or equal to $D/2$ (Fig. 2.5). The selection for this desired helix radius, $\hat{R}$, was $D/2$. This assumed anchoring forces large enough to anchor the actuator in the cannula since the helical actuator was able to compress twice the radius of the actuator on the cannular wall. Additionally, maintenance of a constant overall axial length of the helical actuator in the x-direction, λ_x, was desired, as shown by eq. 2.18. A constant value was chosen to achieve sufficient radial expansion while reducing a loss of forward motion by a helix that contracts axially. A constant overall axial length also prevents slip between the cannula and actuator between contacting and anchoring as a result of helical contraction or lengthening.

$$\lambda_x = \lambda_1 L \cos(\phi)\sqrt{\cos^{-2}(\phi) - 1} \tag{2.18}$$

The final objective of the cost function was to minimize the axial twist, δ, of the actuator (i.e. $\hat{\delta} = 0$) to minimize shear on the tube wall and maximize the efficiency of the robot. A simple grid search with a constant step size of 1.0° was performed over all α, β, γ permutations and the linear quadratic cost function (eq. 2.19) was evaluated with the design parameters in Table 2.1. The α, β, γ values that minimized cost were taken to be the optimal fiber wrap angles. The value for r was chosen based on the off-the-shelf latex tubing used to manufacture the actuators.

Table 2.1: Task-Specific Design Parameters for $D = 19$ mm

r (mm)	L (mm)	$\hat{R}$ (mm)	$\hat{\lambda_x}$	$\hat{\delta}$
5	300	$D/2$	1.0	0.0

$$\begin{aligned} \underset{\Phi}{\text{minimize}} \quad & \Phi^T Q \Phi \\ \text{subject to} \quad & \alpha, \beta, \gamma \in [-90°, 90°] \end{aligned} \tag{2.19}$$

where

$$\Phi = [\hat{R} - R, \hat{\lambda_x} - \lambda_x, \hat{\delta} - \delta] \tag{2.20}$$

$$Q = I_{3x3} \tag{2.21}$$

The second actuator was an extending McKibben actuator that was specified to consist of equal but opposite fiber wrappings greater than 54.7°. The goal of the second actuator was to maximize extension without buckling. The wrap angles of the extending actuator were determined through an empirical study, which examined the relationship between wrap angle, actuator buckling, and actuator extension. The volume coefficient for this actuator was the same as the helical design, $V = 1.30$.

To identify the parameters in eq. 2.3 for the kinematic actuator model using a pressure input, an experiment was performed. The nonlinear-spring-loaded accumulator model shown in eq. 2.3 was applied. Since the system was filled with water, incompressibility was assumed. The

relationship between P_{Act_i} and V was found experimentally by inputting a sine wave on volume using the characterization hydraulic test bench shown in Fig. 2.6. The test bench recorded the volume coefficient, V, and actuator pressure, P, at 100 Hz. Eq. 2.3 was then applied to determine the number of coefficients and their respective values with least squares.

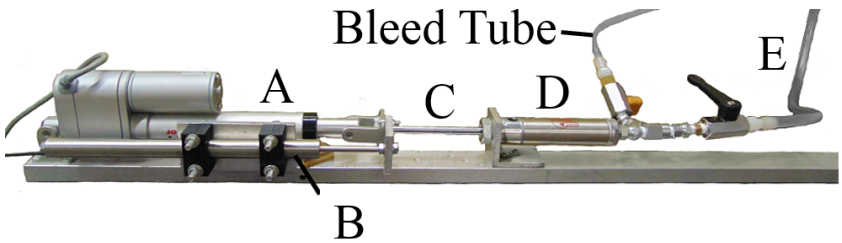

Figure 2.6: Closed hydraulic circuit test bench: A) linear actuator B) LVDT C) cylinder piston rod D) stroke cylinder E) tubing leading to the FREE actuator.

Actuator Construction The FREE actuators were constructed by turning fibers onto a latex tube (Kent Elastomer Products, Inc.) as shown in Fig. 2.7. A dipping process was used to secure the wrapped fibers in place. Each wrapped actuator was dipped three times into a 50/50 distilled water-latex (TAP Plastics Premium Liquid Latex Rubber) mixture with a two hour cure time between dips. The stretchability of the latex tubing allowed for sufficient motion of the actuators while keeping pressures under the task specification of 200 kPa.

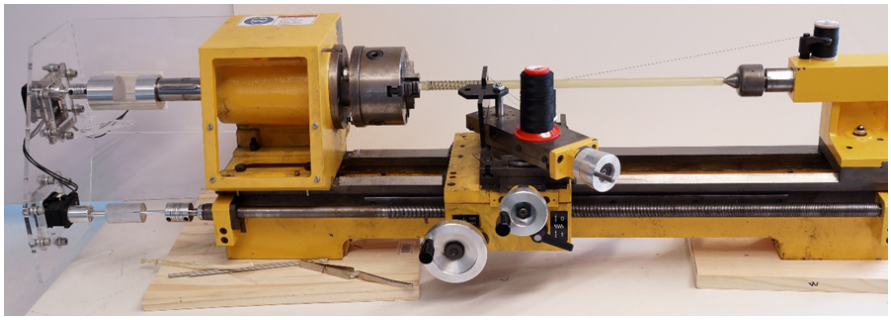

Figure 2.7: Computer-controlled lathe modified to wrap fibers at desired α, β, γ wrap angles onto a latex tubing.

Valve Design and Construction

Valve Design To create a model for the soft robot, eqs. 2.3 and 2.7 were substituted into eq. 2.1 to create the dynamic equations shown in eq. 2.22. The input pressure, u, was selected to be a pressure square wave between 0 and 83 kPa (12.04 psi) with a two second period.

$$\begin{aligned}\dot{V}_1 &= K_1 \sqrt[*]{u - P_1} - K_2 \sqrt[*]{P_1 - P_2} \\ \dot{V}_2 &= K_2 \sqrt[*]{P_1 - P_2} - K_3 \sqrt[*]{P_2 - P_3} \\ \dot{V}_3 &= K_3 \sqrt[*]{P_2 - P_3}\end{aligned} \tag{2.22}$$

Optimization of the resulting model (eq. 2.22) was performed with the design parameters being the valve coefficients, K_i, of the valves. The optimization had two objectives. The first was to maximize the volume change of Act_2 while Act_1 was anchored into the cannula, t_B, and before Act_3 had contacted the cannula, t_C, during the inflation phases, V_{fwd} (eq. 2.23). The second goal was to maximize the volume change of Act_2 between Act_1 releasing contact from the cannula, t_E, and Act_3 unanchoring, t_F, during the deflation, V_{rev} (eq. 2.24). V_{fwd} and V_{rev} were then combined into a single objective function which aimed to maximize their value while keeping their volume changes the same (eq. 2.25). See Fig. 2.3 for event time labels t_B, t_C, etc.

$$V_{fwd} = V_{Act_2}(t_B) - V_{Act_2}(t_C) \tag{2.23}$$

$$V_{rev} = V_{Act_2}(t_E) - V_{Act_2}(t_F) \tag{2.24}$$

$$\begin{aligned}\underset{K_2,K_3}{\text{maximize}} \quad & J_{vol} = [V_{fwd}^2 \;\; V_{rev}^2][c_1 \;\; c_2]^T - c_3|V_{fwd} - V_{rev}|^2 \\ \text{subject to} \quad & K_2, K_3 = [0, K_1]\end{aligned} \tag{2.25}$$

where $c_i = 1$ for $i = 1, 2, 3$.

The robot response to the chosen input was simulated using MATLAB and Simulink. The simulation utilized the nonlinear-spring-loaded accumulator model, P_{Act_i} (eq. 2.3), and the orifice equation, f_{valve} (eq. 2.7), to simulate the robot model in eq. 2.1. A square wave with an amplitude of 83 kPa gauge pressure and frequency of 0.5 Hz was used as the input. The pressure was chosen based on the material characteristics of the actuator to minimize the risk of actuator failure. The frequency was chosen because it was intuitive for human users and is on

the order of a resting heart rate, thus avoiding subjecting anatomy to foreign frequency content. The contact and anchoring volume coefficients were defined as 1.13 and 1.30 as dictated by the actuator design.

To ensure that *Act 1* actuated as quickly as possible, the cross-sectional orifice area, A_{orf_1}, was set to its maximum value dictated by the valve geometry. This maximized the valve coefficient through valve 1. The simulation performed a grid search over K_2 and K_3 for values less than or equal to K_1 using a constant step size of 5.0x10^{-7}m^2. An optimal value for K_1 was not incorporated into the objective function because valve 1 was made to allow as much flow into *Act 1* as possible, making K_1 the largest possible value determined by the valve's cross-sectional area. Eq. 2.25 was then evaluated and the K_2, K_3 combination which maximized J_{vol} was taken as the optimal dynamic response.

Valve Construction The desired valves were constructed by placing flexible tubing within a barbed fitting, inserting a set screw into the fitting wall, then setting the tubing with cast polyurethane (TAP Plastics, One-to-One Polyurethane Casting Resin) (Fig. 2.8). The set screw allowed for adjustments in the flow restrictor opening, changing the effective K_i.

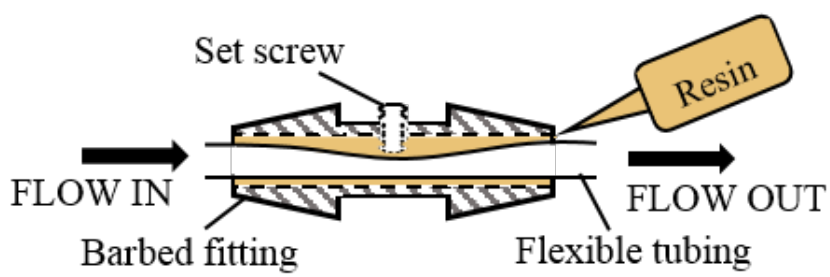

Figure 2.8: A manufactured passive valve. The process used to manufacture valves is as follows: begin with a barbed fitting compatible with actuator size; insert set screw into the fitting wall; back out set screw and insert flexible tubing; fill empty space with polyurethane resin.

To match the flow restrictor with the K_i's found by the simulation, the characterization hydraulic test bench (Fig. 2.6) was used with the flow restrictor placed between two pressure sensors. A cascading set of steps on voltage were inputted to the linear actuator, while the pressure drop, ΔP, and piston position were recorded. The data were then filtered with a fourth-order Butterworth filter with a cutoff frequency of 10 Hz. Next, the data were segmented for each voltage and transients were removed by attributing the data collected during the first

third of the stroke length to acceleration and evaluating the remaining data from the last two thirds of the stroke length. The flow rate was then calculated using a noise robust differentiation [120] based on the segmented piston position. Least squares was then applied to determine the K_i term of the flow restrictor. If the K_i found using the test bench was above (or below) the desired K_i, the set screw on the flow restrictor was tightened (or loosened). This process was repeated until the target K_i from the simulation was achieved within 2%.

Robot Locomoting Through a Tube

Once all the valves were tuned and the actuators were built, each segment was assembled and combined to form the robot. The locomotion hydraulic test bench was connected to the robot and used as a pressure source. A 0.5 Hz square wave input with an amplitude of 83 kPa was implemented with the locomotion hydraulic test bench. The robot was then placed in a cannula of diameter $D = 19$ mm and the segments were inflated and deflated to produce locomotion. A panel of reviewers ($N = 6$) identified key timing events over 5.5 cycles of locomotion recorded at 24 fps 1080P (Cannon EOS Rebel T6).

2.2.3 Results

Actuator (Accumulator) Models and Design Outputs

The α, β, γ wrap angles which optimized cost objectives specified by the design tasks and extender empirical study are shown in Table 2.2.

Table 2.2: Actuator Wrap Angles

	α	β	γ
Helix	72°	−72°	−14°
Extender	80°	−80°	–*

*wrap angle not used.

Fig. 2.9 shows the experimental results from the nonlinear-spring-loaded accumulator experiment for a single helical actuator. The same protocol was repeated for the other two actuators and the resulting coefficients are listed in Table 2.3. However, the pressure volume relationship for each actuator followed similar curves and values.

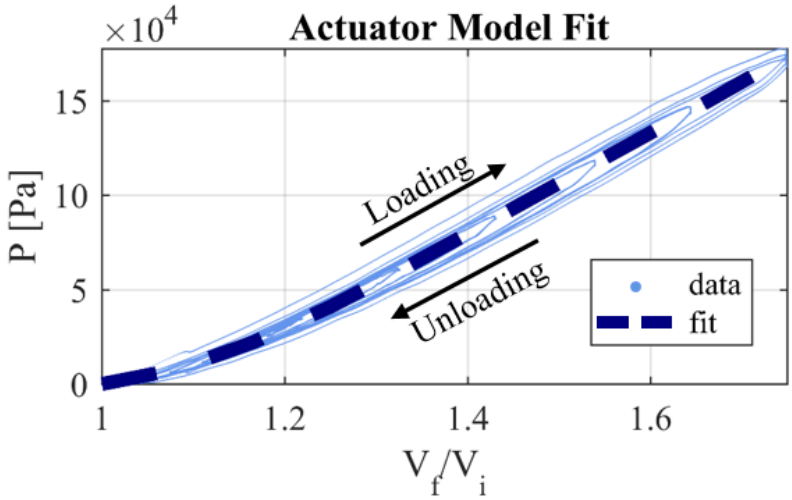

Figure 2.9: Nonlinear spring-loaded accumulator relationship shown with a hysteresis loop for Actuator 1.

Table 2.3: Pressure Volume Relationship found with eq. 2.3.

	c_1	c_2	c_3	c_4
P_{Act_1}	1.60	5.92	−11.14	7.18
P_{Act_2}	0.44	6.64	−8.79	4.28
P_{Act_3}	−0.28	10.61	−12.39	5.06

Valve Results

The simulation produced an objective function showing the values of J_{vol} (eq. 2.25) for each combination of K_i's in the grid search (Fig. 2.10).

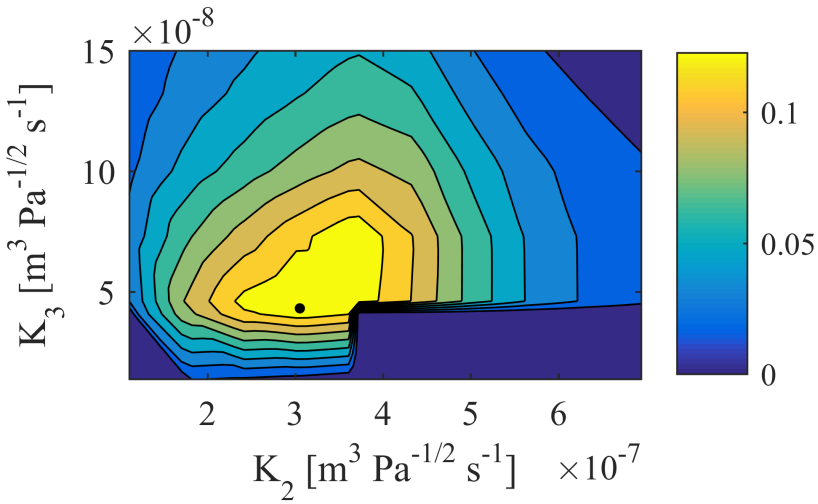

Figure 2.10: Objective function of grid search performed over K_i values, where the black dot represents the maximum of eq. 2.25.

The values of K_i correlating to the maximum of the objective function were matched experimentally. The experimental change in pressure versus flow data for each flow restrictor was compared to the optimal pressure versus flow data. An example of the experimental response versus optimal response can be seen in Fig. 2.11. The final values for both the optimal and experimental K_i values are shown in Table 2.4.

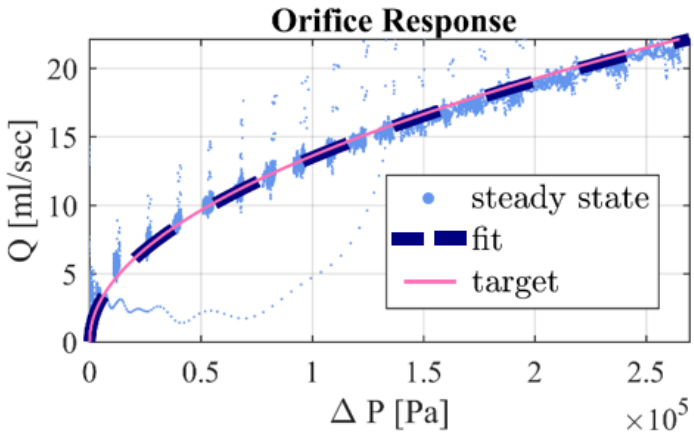

Figure 2.11: Flow restrictor testing and models shown for valve 3 (transparency for steady state data set to 15%; transient data excluded).

Table 2.4: Valve Resistance

K_i $[m^3 Pa^{-1/2} s^{-1}]$	Valve 1	Valve 2	Valve 3
Optimal	1.64x10^{-6}	3.05x10^{-7}	4.30x10^{-8}
Fit	–*	3.02x10^{-7}	4.26x10^{-8}
Error	–*	−1.04%	−0.84%

*determined by max cross section.

After finding the optimal K_i values using the objective function shown in Fig. 2.10, the values were entered into the simulation to produce the optimized volumetric response (Fig. 2.12) where V_{fwd} and V_{rev} both took 140 ms. Due to the different polynomial constants describing each accumulator, the final volume coefficients vary.

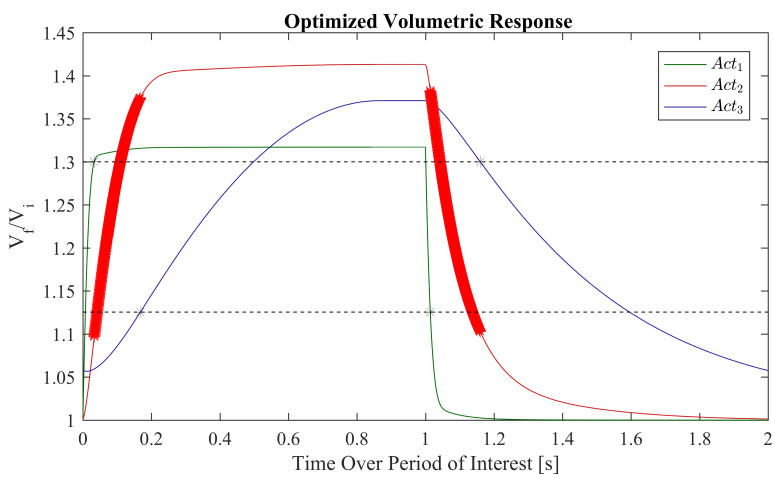

Figure 2.12: Optimized volumetric response for an actuation period. States corresponding to Fig. 2.3 (a,b) are shown, with the extender volume objective (eq. 2.25) highlighted in bold for *Act 2*. ($V_i = 1.00$, $V_c = 1.12$, $V_a = 1.30$); (Event timings: $t_A = 0.00s$, $t_B = 0.03s$, $t_C = 0.17s$, $t_D = 1.00s$, $t_E = 1.02s$, $t_F = 1.16s$, $t_G = 2.00s$).

Soft Robot Modeling

The soft robot successfully traversed the cannula as shown in Fig 2.13. The robot locomoted 27 ± 4 mm for each actuation cycle, which is within the deviation of the predicted locomotion of 28 mm found using the extension volume change (bold red in Fig. 2.12) and the empirical volume to extension behavior of Actuator 2. Fig. 2.14 shows the robot locomoting through the cannula at different time steps, allowing one to view the traversal. For both Fig. 2.13 and Fig. 2.14, a 5 mm×5 mm grid can be seen in the background. The images were cropped and

the image was shrunk to 35% of its original size in the horizontal direction. Additionally, the median timing of actuation was within the measurement resolution of the prescribed timing as shown in Fig. 2.15.

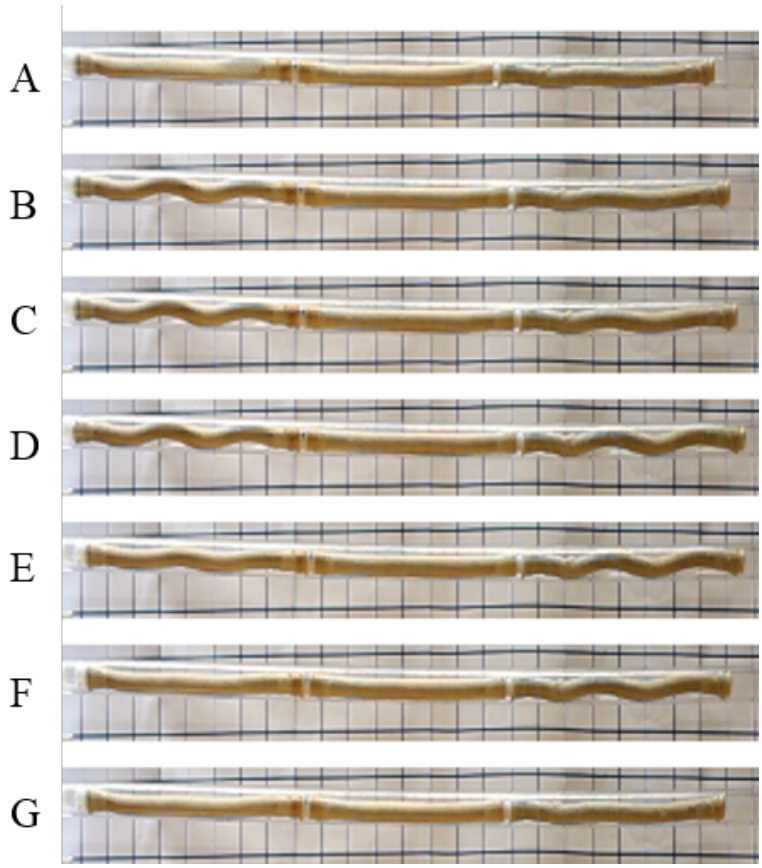

Figure 2.13: Soft robot at each event (Labeled A-G) in a cannula for a full cycle of 2 seconds. (Compare with Fig. 2.3) The grid markings in this figure and Fig. 2.14 are 5 mm×5 mm, the image was cropped and horizontally shrunk by 35%.

Figure 2.14: Soft robot locomotion through a cannula at different time steps. The images were captured at full anchoring, Event D (See Fig. 2.3a and Fig. 2.13).

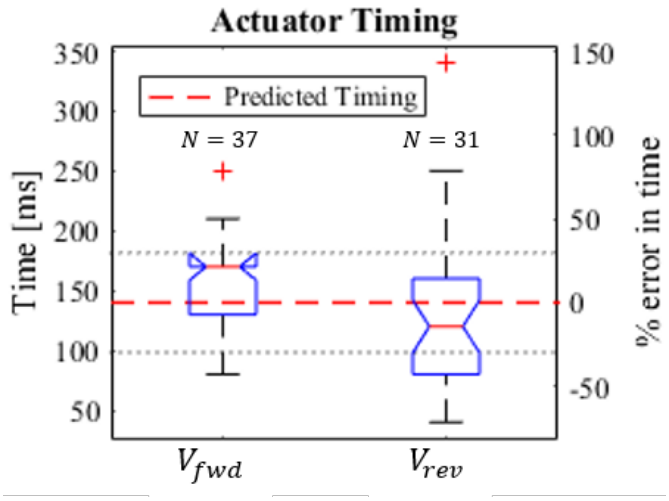

Figure 2.15: Experimental actuator timing for the forward, $(t_C - t_B)$, and reverse, $(t_F - t_E)$, direction. Results found with $(N = 6)$ independent reviewers timing all events for $(N = 37)$ and $(N = 31)$. The dotted black measurement lines represent the discrete measurement resolution with a video being recorded at 24 frames per second. Notches represent range in significant difference in median at $p = 0.05$.

2.2.4 Discussion

The methodology proposed in [71] was successfully utilized to provide ideal wrap angles for each actuator in the robot (Table 2.2). The helical actuator closely met the objectives described in Table 2.1. The actuator pressure-volume relationship (Fig. 2.9) was nonlinear and exhibited

some rate-independent hysteresis. This deviated from assumptions, but not substantially relative to the full pressure-volume range.

The optimization of the extension volume implies useful forward traversal locomotion. In general, the last orifice (K_3) has greater impedance than (K_2) meaning that optimal tuning is more sensitive to changes in (K_3) than (K_2).

The resulting optimization (Fig. 2.12) shows that well over 50% of the extension volume change results in extension as well as roughly equal and useful expansion and retraction stages. One thing to note is that *Act 3* always has a volume coefficient greater than one. This is due to the system reaching a cyclic steady state response and *Act 3* not being able to fully deflate. It is worth noting that all three actuators have different coefficients (see Table 2.3) and different final volumes ($V_f/V_i > 1.3$ in Fig. 2.12) because the dipping processes was not fully repeatable resulting in slightly different wall thicknesses.

The use of the orifice equation (eq. 2.7) to model the valves was mostly justified as seen in Fig. 2.11 with the exclusion of most transient data.

The experiment showed that the proposed design methodology succeeded at a) creating shapes and sequences proposed in Figs. 2.2 and 2.3, b) achieved the timing suggested in Fig. 2.3b and c) resulted in overall locomotion that was serially actuated and, by design, avoided full occlusion of the cannula cross section thus allowing fluid flow. The actuator timing, when accounting for measurement resolution, proved quite accurate since the mean timing for the forward and reverse direction fell within one frame of the specified timing. Errors in the timing could be attributed to the effect of external loading due to the contact and anchoring in the cannula. The effect on the system's dynamics can be seen in Fig. 2.15. During inflation, the actuator is fighting the reaction force generated due to contacting the cannula, thus extending the time period of V_{fwd}. Conversely, the time period of V_{rev} is shorter due to the reaction force assist the deflation gets from contact with the cannula. The model neglected this contact interaction. However, the resulting deviation was minimal (i.e. did not prevent locomotion).

2.2.5 Conclusion

A design methodology to realize task-specific, serially actuated soft robots to traverse tube-like environments without causing full occlusion of the tubular cross section was presented and experimentally verified. While this work was demonstrated for a specific case, it is generalizable

to other applications and environments. Such methodology can benefit multiple applications including pipe inspection and medical catheter robots.

Currently, the methodology does not include sensing and navigation control, but instead focuses on locomotion only. Consequently, the soft robot could locomote through bends, but would need an additional degree of freedom to choose a particular path upon coming to a junction.

The work presented has room for advancement and sets up the work presented throughout the rest of this thesis. First, this work presented a robot capable of locomoting within cannulas with diameters of 19 mm, but to make the robot applicable to a wider range of anatomy, a scaled down version of the robot presented in this chapter section should be developed (addressed in subsequent sections of this chapter). Second, the results from this chapter section set up the need for a traction model to predict the anchoring force between the helical actuator and cannula wall (addressed in subsequent sections of this chapter and in Chapter 3). Third, the optimization can expand to include actuation frequency (addressed in subsequent sections of this chapter) and actuator stiffness (addressed in Chapter 4) to tune robot designs for different environments and actuator timing. Finally, the effects of buckling or out-of-plane motion of the extender could be developed to greatly improve the accuracy and effectiveness of the predicted locomotion (addressed in Chapter 5).

2.2.6 Specific Contributions

This research was performed with Mark Gilbertson. My contributions to this section were developing the theoretical model for optimizing valve coefficients and modeling the combination of all system components. I was also responsible for the passive valve manufacturing method. Mark Gilbertson developed the initial version of the CNC lathe used in this section and worked on the FREE model optimization. The experimental work and results were a combined effort.

2.3 Scaling Down

2.3.1 Introduction

One of the core challenges that soft robots must overcome, especially to integrate into mainstream medical technology, is their controllability and force bearing capabilities at small scales.

As mentioned in Section 2.2, to achieve locomotion in anatomy or cannulas of smaller diameter like in cardio or neurovasculature, the size of the robot must be significantly reduced from a 11.6 mm diameter shown in Fig. 2.13 to approximately 3 mm in diameter [29, 30]. Although fluid power systems in particular are noted for their high power density compared to electromechanical systems, the force output of fluid-powered actuators decreases drastically with diameter ($F \propto D^2$) [66, 95, 96]. For example, a microhand finger with a diameter of 153 μm can hold 0.2 g of weight [121]. More generally, the force bearing capability of soft materials is low due to the Young's modulus modulus ranging from approximately $10^4 - 10^9$ Pa [27]. Although this contributes to the compliance of the robot, the low force capability is also a hindrance to performance in many cases.

The manufacturing of soft robots on the order of 3 mm in diameter poses an additional challenge on top of reduced force capabilities. Several groups have successfully manufactured fluid-powered actuators at or below 3 mm diameter, which is comprehensively summarized by Hines et al. and Gorissen et al. [122, 123]. Suzumori et al. were one of the earliest groups to begin manufacturing inflatable soft actuators capable of bending in 1989 using polymer molding [57]. Since then, the actuators have drastically decreased in size using a variety of manufacturing processes. These actuators include microtentacles (D = 153 μm) capable of holding delicate fish eggs manufactured using a direct peeling-based technique [121], pneumatically-actuated artificial cilia (D = 1 mm) for fluid propulsion made from molded silicone [124], and a four-fingered microhand capable of capturing electric components fabricated using anisotropic etching, conformal parylene deposition, and epoxy gluing [125]. However, many of these fabrication processes are complex, time consuming, and require expensive equipment that make them impractical for many researchers. The fabrication techniques can also lead to consistent failure due to the delicate structures of these robots [122].

Finally, the control complexity for fluid-powered robots comprising multiple actuators is greatly hindered with a reduction in size. Multiple pressure lines are not an option because of size restrictions and the materials that are used in the robot must be soft enough to create motion while being stiff enough to withstand forces and not fail due to over-pressurization. Because of this obstacle, many of the microactuators discussed in soft robotics literature are limited to single actuators connected to a larger overall system [123]. As mentioned in the previous section, Ikuta et al. have made significant contributions to controlling multiple microactuators using a

"pressure pulse drive" that controls the motion of bending actuators using valves containing high- and low-pass valves [83, 84, 85, 126]. However, the fabrication techniques and control methodology are complex, especially when the robot contains multiple actuators, and generating bending within a single actuator takes over 16 seconds [85]. For creating a locomoting, medical soft robot, motions generated on that timescale are too time consuming.

This section explores how the performance of the serially-actuated robot in Section 2.2 is affected when similar design methods are used and the overall diameter of the robot is reduced from 11.6 mm diameter to 3.3 mm in diameter. New fabrication processes are discussed, as well as a method to determine how closely the manufactured FREE actuators behave to the theoretical FREE behavior. Finally, the results of empirical traction studies are discussed to determine the anchoring force capabilities of soft actuators that do not fully occlude (e.g. unlike a balloon) the cannula.

2.3.2 Methods

Millimeter-Scale, Locomoting Robot Design

The goal of this chapter section was to determine whether a soft robot of 3.3 mm diameter could locomote in a tube using nearly identical methods from Section 2.2, with the exception of minor changes related to improving the fabrication methods. To avoid redundancy, overlapping elements of this section and the previous section were not re-introduced. Instead, this section referred back to elements of the previous section to explain the methods.

The overall design of the robot was the same as the design shown in Section 2.2, Fig. 2.2 where the first and third segments anchored into the cannula and the second segment extended and relaxed to produce locomotion. A tether connected the series of actuators to the pressure source. The ideal sequence was also identical to the sequence shown in Section 2.2, Fig. 2.3.

Theoretical System Model

The system model changed slightly from Section 2.2, Fig. 2.4 to better capture the experimental setup and manufactured components of the reduced size robot. The model is shown in Fig. 2.16, where a pump was used to maintain a pressure within a gas charged bladder accumulator and solenoid valves were used to pressurize and depressurize the actuators in the robot following a square wave input. Each passive "valve" between the actuators was modeled as a pipe resistance

which was changed due to an updated fabrication method. The fittings leading from the gas charged bladder to the tether line were also incorporated as a lumped resistance. The tether line was added to the system model as a spring-loaded hydraulic accumulator to appropriately capture any dynamics introduced by elasticity in the walls of the tether line. As with the larger-scale model, the actuators were modeled as spring-loaded accumulators.

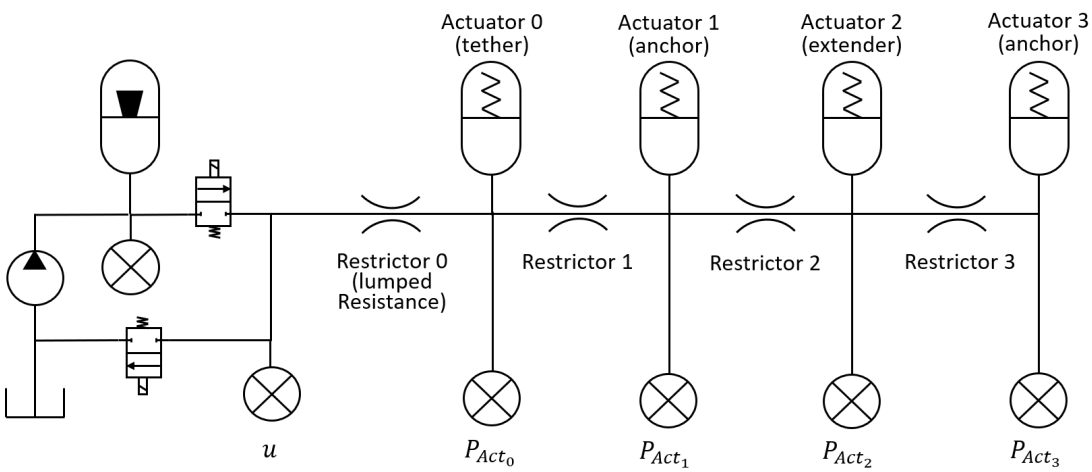

Figure 2.16: Theoretical robot modeled as a fourth order fluid system. A square wave to actuate the robot was produced using a pump, gas charged bladder accumulator, and solenoid valves. The fittings and passive valves were modeled as flow restrictors and the tether line and actuators were modeled as spring-loaded hydraulic accumulators.

The resulting volume change for each segment was described by the following system of differential equations for the flow rates:

$$\begin{aligned}
\dot{V_0} &= f_{res_0}(u, P_{Act_0}) - f_{res_1}(P_{Act_0}, P_{Act_1}) \\
\dot{V_1} &= f_{res_1}(P_{tether}, P_{Act_1}) - f_{res_2}(P_{Act_1}, P_{Act_2}) \\
\dot{V_2} &= f_{res_2}(P_{Act_1}, P_{Act_2}) - f_{res_3}(P_{Act_2}, P_{Act_3}) \\
\dot{V_3} &= f_{res_3}(P_{Act_2}, P_{Act_3})
\end{aligned} \tag{2.26}$$

where u is the pressure input, f_{res_i} describes the pipe flow through the restrictors, and P_{Act_i} is an equation to describe the behavior of the pressure in the ith accumulator based on its material properties. To avoid confusion with the larger-scale system in Section 2.2, the tether and the lumped resistance before the tether are denoted as Actuator 0 and Restrictor 0, respectively.

Model Components

Actuator (Accumulator) Model The actuator was modeled as a spring-loaded accumulator. As with Section 2.2, the volume coefficient, V, was the independent variable defined as the ratio of final actuator volume to initial actuator volume (eq. 2.27) and the internal pressure, P, was the dependent variable.

$$V = \frac{V_f}{V_i} \tag{2.27}$$

A linear function (eq. 2.28) modeled the spring-loaded accumulator where the coefficients, a_i and b_i, were determined from pressure-volume data for each actuator.

$$P_{Act_i} = a_i V + b_i \tag{2.28}$$

Restrictor (Pipe Flow) Model The flow restrictors were modeled using the Darcy-Weisbach equation to describe the volumetric fluid flow through the restrictor, f_{res_i}, (pipe flow) using eq. 2.29.

$$f_{res_i} = K_i \Delta P_i \tag{2.29}$$

where i represents the restrictor index and K_i is the restrictor coefficient, defined as

$$K_i = \frac{\pi D_i^4}{128 \mu L_i} \tag{2.30}$$

where D_i is the hydraulic diameter of the restrictor, L_i is the length of the restrictor, and μ is the dynamic viscosity of the fluid used for actuation. For this section, water was used as the actuation fluid ($\mu = 1.0005$ mPa·s at 20 °C). However, the model allows for easy transition to other actuation fluids, such as oil, to change robot dynamics. For the purposes of this model, incompressible, laminar, and steady-state flow was assumed to hold true throughout actuation of the robot.

Physical Realization and Targeted Task

Task The specified task for the robot design was to locomote through a cannula ($D = 9.53$ mm) using a combination of segments that occluded the cannula by less than 50% and experienced pressures under 280 kPa (40.6 psi) to prevent actuator failure. The timing of the actuation needed to follow Fig. 2.3 (Section 2.2). This meant that *Act 1* must anchor before extension of *Act 2* contributed to locomotion. Additionally, *Act 2* must be near its final volume before *Act 3* anchored. This prevented *Act 2* from buckling or "wasting" usable extension.

Actuator Design To achieve the task, the inner radii of the actuators were chosen as r=0.79 mm with a wall thickness of $t = 0.86$ mm, resulting in an area occlusion of 12%. This slightly differs from the area occlusion of 37% in Section 2.2 based on the availability of acrylic tube geometries and fabrication capabilities of the soft robot.

The process described in Section 2.2 was used to determine the wrap angles of the FREE actuators as dictated by the specified task of traversing a $D = 9.53$ mm diameter tube. However, given the slight change in robot and cannula geometries from Section 2.2, a target volume coefficient of $V = 4.5$ was used. This volume coefficient was driven by empirical evidence for $N = 3$ anchoring actuators, where $V = 4.5$ was the average volume coefficient required to initially anchor the actuator within an acrylic tube of $D = 9.53$ mm.

Using the methods for the larger-scale robot in [1], the α, β, γ values that minimized cost were taken to be the optimal fiber wrap angles and are shown in Table 2.5. The value for r was dictated by the fabrication process to manufacture an actuator with uniform wall thickness that could withstand pressures up to 280 kPa as specified in the task.

Table 2.5: Task-Specific Design Parameters for $D = 9.53$ mm

r	L	$\hat{R}$	$\hat{\lambda_x}$	$\hat{\delta}$
0.79 mm	130 mm	$D/2$	1.0	0.0

The second actuator was an extending McKibben actuator that was specified to consist of equal but opposite fiber wrappings greater than 54.7°. The goal of the second actuator was to maximize extension, so the wrap angles were maximized based on fabrication capabilities.

To identify the parameters in eq. 2.28 for the kinematic actuator model using a pressure input, a different experimental setup than the hydraulic test bench in Fig. 2.6 needed to be

utilized. This is because the small-scale actuators are actuated using much smaller volumetric displacements than can be achieved reliably using the setup in Fig. 2.6. The relationships between P_{Act_i} and V were found experimentally using the setup shown in Fig. 2.17. The actuator under test was pressurized using a syringe while volumetric displacement was recorded at 60 fps using video (Canon Rebel t7i) and pressure data were recorded at 100 Hz using a pressure transducer (MLH050PGP06A, Honeywell International Inc.) connected to a Teensy 3.5 microcontroller. Volumetric displacement data were determined in post-processing using measurement tools in the video recording, which was synced to the pressure data using an LED that signaled the start of the pressure recording. To determine the pressure-volume relationship of actuators using water as an actuation medium, the water was dyed with red food coloring to aid in visibility. Eq. 2.28 was then applied to determine the pressure-volume relationship from the data.

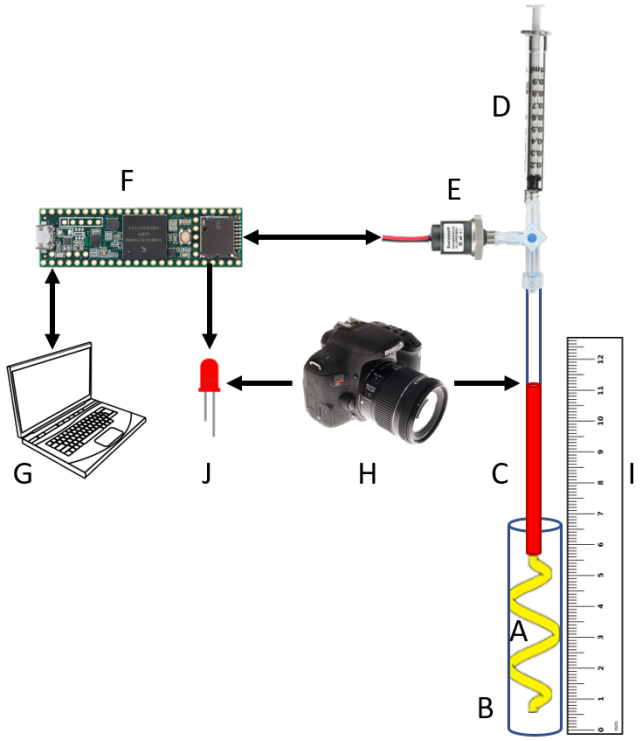

Figure 2.17: Illustrative experimental setup used to determine the volume-pressure relationship for small-scale actuators. The actuator (A) is placed inside of an acrylic tube (B), which is connected to a rigid, transparent tube containing the actuation fluid (C) with a known initial level. The actuator is pressurized using a syringe (D), which is connected to a pressure transducer (E). A Teensy 3.5 microcontroller (F) is used to read the pressure transducer values and a laptop (G) is used to communicate with the microcontroller and store pressure data. A camera (H) is used to record video of the change in the actuation fluid level, which is used in calculating the volumetric displacement and measured with a ruler (I). The volumetric displacement and pressure data are coordinated using an LED (J) captured by the camera.

Custom Actuator Mold A custom mold was created to provide more flexibility in fabricating actuators of desired small-scale geometries and selectable materials. Another major reason for the shift from off-the-shelf latex tubing used in Section 2.2 aside from the geometries was the poor bonding properties and durability of latex. The latex base tube and outer dip layer used previously did not bond well to each other, leading to the actuator falling apart after short periods of time. The actuators used in this section were made from a two-part, liquid polyurethane RTV (Poly 74-20 Liquid Rubber, Polytek) because polyurethane bonds well to itself and has elastic properties desirable for generating deformation in the desired pressure

range.

The mold design utilized a stainless steel rod that dictated the inner diameter of the soft actuator and a glass rod that dictated the outer diameter, as shown in 2.18. The rod was tensioned using hex nuts as rod tensioners to keep the rod straight and concentric within the glass tube. The glass tube was held concentric with the rod using an O-ring to help with centering. Uncured elastomer was injected into the space between the glass tube and stainless steel rod using a barbed fitting and air bubbles were minimized by using a second barbed fitting as a vent port. Prior to injection, the two-part polyurethane was mixed thoroughly and degassed in a vacuum chamber. Once cured, the elastomer and rod can be removed from the glass tube, cleaned using ethyl alcohol, then wrapped with desired fibers using the custom CNC lathe.

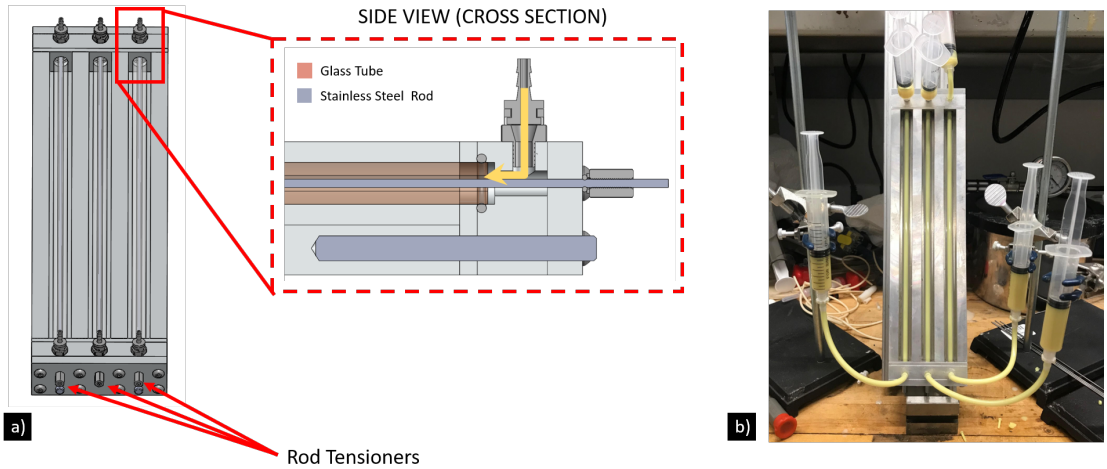

Figure 2.18: Custom mold design to make the base tubes of soft actuators. a) Render of custom mold for making soft robot base tubes. The cross section shows the path the uncured elastomer takes when injected from the barbed fitting into the space between the glass tube and steel rod. b) Custom mold after injection.

Custom CNC Lathe Update The custom CNC lathe shown in Fig. 2.7 was updated to provide increased accuracy of the fiber wrap angle. The chuck and linear stage control was updated to be controlled with Maxon DC motors and a zero backlash MXL belt drive system. A 22-bit absolute inductive encoder (NC-3-150-221001-SPI1-RFC4-5-AN Zettlex Systems, Inc) and a 3000 counts per inch linear encoder (EM2, US Digital) were implemented to provide precise rotational and linear position feedback. Further details on the lathe upgrade are provided in Appendix A.

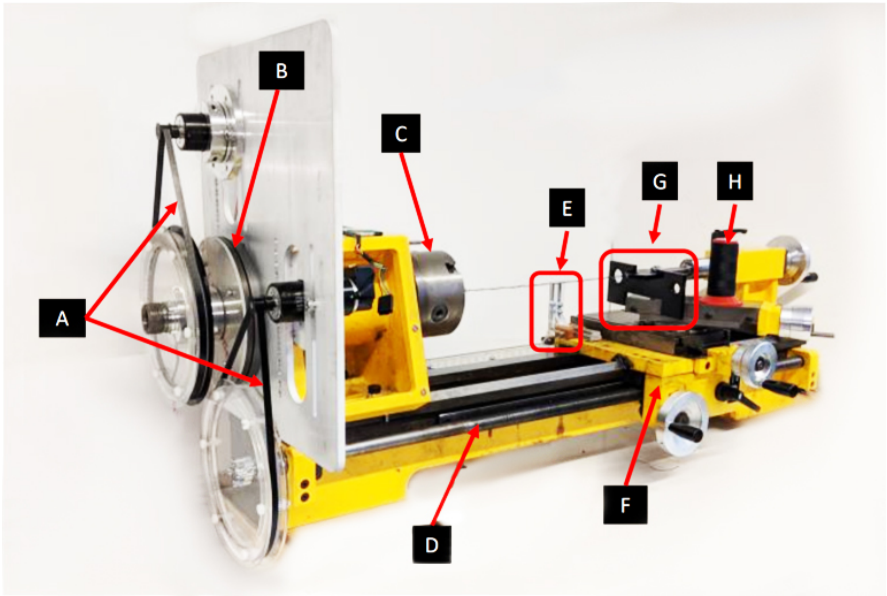

Figure 2.19: Custom CNC lathe used to manufacture soft robotic actuators. A. zero backlash MXL belt drive, B. 22-bit absolute rotary encoder, C. rotation stage (chuck), D. linear stage (worm gear), E. linear encoder, F. linear stage, G. fiber guide, H. fiber spool.

The FREE actuators were constructed by using the CNC lathe to turn 30 wt. cotton thread (Coats) onto the tubes fabricated using the custom mold. Once wrapped, each actuator was dipped into uncured, two-part polyurethane mix to secure the wrapped fibers in place. Although the outer dip layer was not guaranteed to be perfectly uniform, the actuator was rotated and flipped while curing to achieve as uniform of a layer as possible.

Valve Design and Construction A model describing the volumetric change in each actuator as a function of the valve design and pressures within the robot was created in a similar manner to Section 2.2. Substituting eqs. 2.29 and 2.30 into eq. 2.26 produces the dynamic equations shown in 2.34.

$$\dot{V}_0 = \frac{\pi}{128\mu}\left(\frac{D_0^4}{L_0}(u - P_0) - \frac{D_1^4}{L_1}(P_0 - P_1)\right) \tag{2.31}$$

$$\dot{V}_1 = \frac{\pi}{128\mu}\left(\frac{D_1^4}{L_1}(P_0 - P_1) - \frac{D_2^4}{L_2}(P_1 - P_2)\right) \tag{2.32}$$

$$\dot{V}_2 = \frac{\pi}{128\mu}\left(\frac{D_2^4}{L_2}(P_1 - P_2) - \frac{D_3^4}{L_3}(P_2 - P_3)\right) \tag{2.33}$$

$$\dot{V}_3 = \frac{\pi}{128\mu}\left(\frac{D_3^4}{L_3}(P_2 - P_3)\right) \tag{2.34}$$

Optimization of the model shown in 2.34 was performed using the same methodology as Section 2.2, but with the design parameters being the restrictor diameters, D_i. The objective function utilized the same structure as the function for the larger-scale robot, but is rewritten in eqs. 2.35 - 2.37 for clarity.

$$V_{fwd} = V_{Act_2}(t_B) - V_{Act_2}(t_C) \tag{2.35}$$

$$V_{rev} = V_{Act_2}(t_E) - V_{Act_2}(t_F) \tag{2.36}$$

$$\begin{aligned} \underset{K_2,K_3}{\text{maximize}} \quad & J_{vol} = [V_{fwd}^2 \;\; V_{rev}^2][c_1 \;\; c_2]^T - c_3|V_{fwd} - V_{rev}|^2 \\ \text{subject to} \quad & D_2, D_3 = [0.221, D_1] \end{aligned} \tag{2.37}$$

where $c_i = 1$ for $i = 1, 2, 3$. D_1, D_2, and D_3 represent the restrictor diameters where D_1 is the largest manufacturable diameter (1.397 mm) to allow Actuator 1 to reach its target volume quickly while D_2 and D_3 are limited to values between the smallest and largest manufacturable restrictor diameters (0.221 mm and 1.191 mm), respectively.

MATLAB and Simulink were again utilized to simulate the robot response to the chosen input pressure signal. A square wave with an amplitude of 275.79 kPag (40 psig), frequency 0.5 Hz, and pulse width of 50% was used as the input. The pressure was based on the materials and geometry of the actuator with the goal of generating enough deformation to sufficiently anchor and extend within the cannula. The frequency was chosen to stay consistent with the larger-scale robot and because it allowed the largest range of solutions for forward locomotion for frequencies between 0.5 and 1 Hz. The contact and anchoring volume coefficients were defined as 2.0 and 4.5, respectively, as dictated by the actuator design and initial empirical evidence using $N = 3$ anchoring actuators.

The diameter of the restrictor for the tether line, D_0, was dictated by the off-the-shelf Tygon tubing used with a diameter of 1.68 mm. The restrictor diameter for the valve leading into Actuator 1 was set to its maximum value ($D_1 = 1.191$ mm) dictated by the restrictor geometry to maximize flow through the valve and pressurize Actuator 1 as quickly as possible. A grid search was performed over D_2 and D_3 for values between the smallest and largest manufacturable restrictor diameters (0.221 mm and 1.191 mm), respectively. Eq. 2.37 was evaluated and the combination of D_2 and D_3 that maximized J_{vol} was implemented into the experimental robot.

The restrictors were machined from brass into barbed fittings, shown in Fig. 2.20. The critical dimension that dictated flow through the valve was D_i, which was created by drilling a hole through the solid center of the barbed fitting. The limiting factor on the restrictor diameters was based on the smallest drill size capable of drilling a fluid pathway of sufficient length, which was a #90 drill bit (0.221 mm diameter). The restrictor diameters were also discrete, ranging from a #90 drill bit (0.221 mm diameter) to a #54 drill bit (1.191 mm diameter) in increments of one drill bit size.

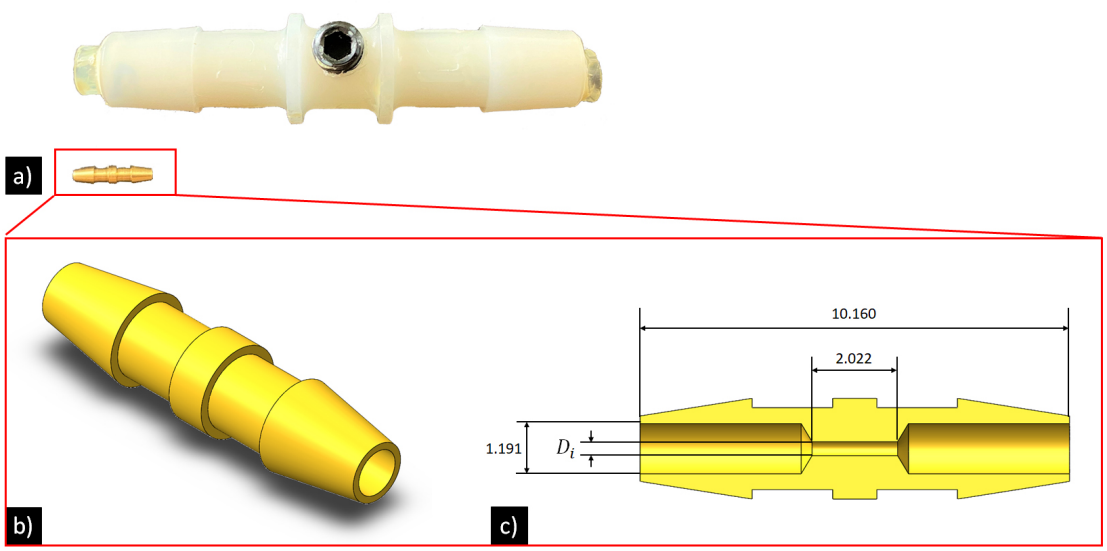

Figure 2.20: a) Size comparison of the two passive valves used in experimentation, as built, for the larger prototype (top) and scaled down prototype (bottom). b) Isometric view of the passive valve (restrictor) used for the scaled down robot. The valve is manufactured from brass and a fluid pathway is drilled through the center of the barbed valve to dictate the diameter of the restrictor. c) Cross-sectional view showing relevant dimensions. All dimensions shown in millimeters.

Experimental Setup

With the valves and actuators fabricated, each segment of the robot was assembled and combined to form the scaled down robot. The setup in Fig. 2.16 was built and connected to the robot. The 0.5 Hz square wave input with an amplitude of 275.79 kPag (40 psig) and 50% pulse width was implemented using a Teensy 3.5 microcontroller connected to solenoid valves. The robot was then placed in an acrylic cannula of $D = 9.53$ mm and the segments were inflated and deflated to actuate the robot.

2.3.3 Results

Actuator (Accumulator) Models and Design Outputs

The actuator lengths (L) and wrap angles (α, β, γ) that optimized cost objectives specified by the design tasks and extender empirical study are shown in Table 2.6. The lengths were chosen to match the length-to-diameter scaling of the larger scale robot in Section 2.2.

Table 2.6: Actuator length (L) and wrap angles (α, β, γ) that best met objectives

	L (mm)	α	β	γ
Helix	130	73°	−73°	6°
Extender	80	80°	−80°	–*

*wrap angle not used.

Fig. 2.21 shows the experimental results from the pressure-volume experiment for a spring-loaded accumulator (helical actuator, $L = 130$ mm). The same protocol was repeated for the other two actuators and the resulting coefficients are listed in Table 2.7. However, the pressure volume relationship for each actuator followed similar curves and values.

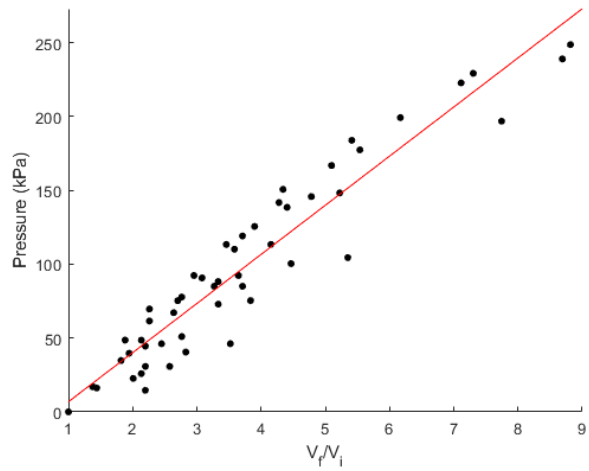

Figure 2.21: Spring-loaded accumulator relationship shown with a linear fit for Actuator 1. Fit parameters are listed in Table 2.7.

Table 2.7: Pressure Volume Relationship found with eq. 2.28.

	Fit Parameter	
	Slope (kPa)	Offset (kPa)
	a	b
P_{Act_0}	10488	-10452
P_{Act_1}	33.275	-26.407
P_{Act_2}	38.706	-38.504
P_{Act_3}	35.160	-34.957

Valve Results

The simulation produced a contour plot showing the output of the objective function, J_{vol}, (eq. 2.37) for each combination of D_2 and D_3 in the grid search. The contour plot shown in Fig. 2.22 highlights the sensitivity of a positive objective output (i.e. successful locomotion) to small changes in D_2 and D_3, with only 152 of 1369 physically-realizable combinations resulting in a positive J_{vol}.

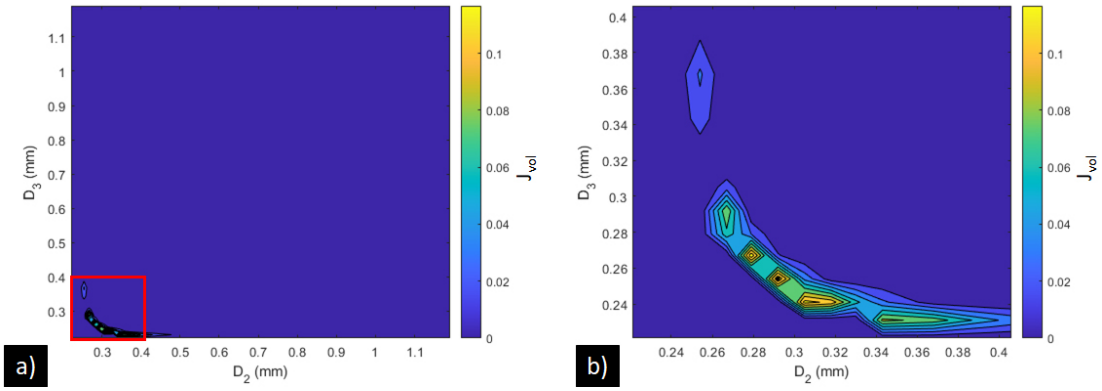

Figure 2.22: a) The objective function grid search was performed over the full range of D_2 and D_3 values. b) Zoomed-in region of the red box to show the sensitivity of the objective function to small changes in D_2 and D_3, where the black dot represents the maximum of eq. 2.37.

The values of D_2 and D_3 that maximized the objective function were 0.292 mm and 0.254 mm, respectively. The values were then entered into the simulation to produce the optimized volumetric response (Fig. 2.23) where V_{fwd} and V_{rev} took 19.6 ms and 55.4 ms, respectively. The resulting change in volume coefficients, V_{fwd} and V_{rev}, were 0.496 and 0.256, respectively. Due to the different polynomial constants describing each accumulator, the peak volume coefficients vary.

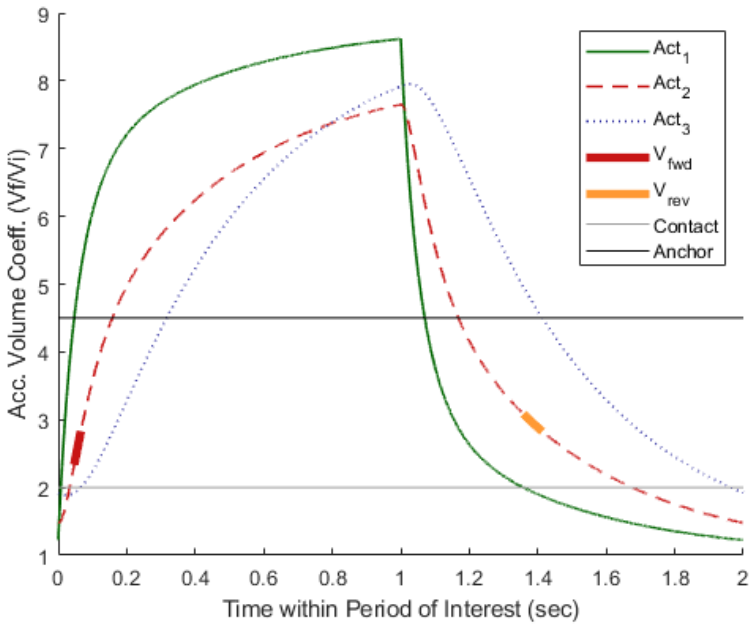

Figure 2.23: Optimized volumetric response for one actuation period. States corresponding to Fig. 2.3 (a,b) are shown, with the extender volume objective (eq. 2.37) highlighted in bold for *Act 2*. ($V_i = 1.00$, $V_c = 2.00$, $V_a = 4.50$); (Event timings: $t_A = 0.00s$, $t_B = 0.04s$, $t_C = 0.07s$, $t_D = 0.30s$, $t_E = 1.28s$, $t_F = 1.40s$, $t_G = 2.00s$). The expected time and volume change of the extender (Act_2) are in bold line segments to indicate the "unwasted" motion of the extender expected to contribute to locomotion.

It should be noted that the lengths of all three actuators for the results above were chosen to resemble the length-to-diameter ratio of the larger scale robot. A search was performed to examine combinations of different helical (Acts. 1 and 3) and extending (Act. 1) actuator lengths to determine how the combinations performed compared to the lengths used for the experimental robot, shown in Fig. 2.24. These results suggest that a longer length of the extender (Act. 2) compared to the anchoring actuators (Acts. 1 and 3) may provide better performance.

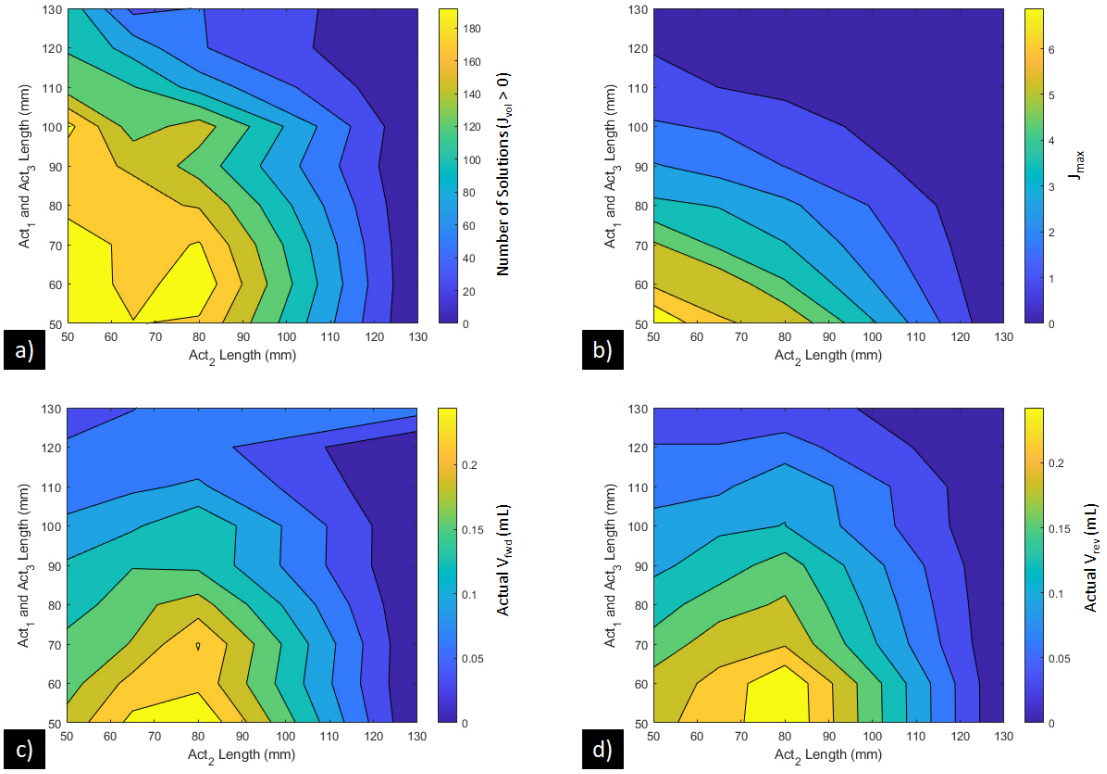

Figure 2.24: Objective function grid searches performed over helical and extending actuator lengths, showing: a) The total number of physically-realizable combinations resulting in a positive J_{vol}, b) The maximum value of J_{vol} for a given combination of actuator lengths and restrictor diameters, c) The actual forward volume change for the combinations in the plot from b, d) The actual reverse volume change for the combinations in the plot from b. Actual lengths used in the experiment were $Act_1 = 130$ mm, $Act_2 = 80$ mm, $Act_3 = 130$ mm to facilitate comparison with [1].

Soft Robot Modeling

The locomotion of the scaled down robot is shown in two environments, unlubricated and lubricated, in Figs. 2.25 and 2.26, respectively. The unlubricated environment did not have a lubricating layer of oil between the outer surface of the robot and the acrylic cannula. The robot moved backwards, in the opposite direction than intended, at an average of 6.84 mm (2.01% body length) per cycle, likely caused by the friction between the polyurethane outer coating and the acrylic cannula.

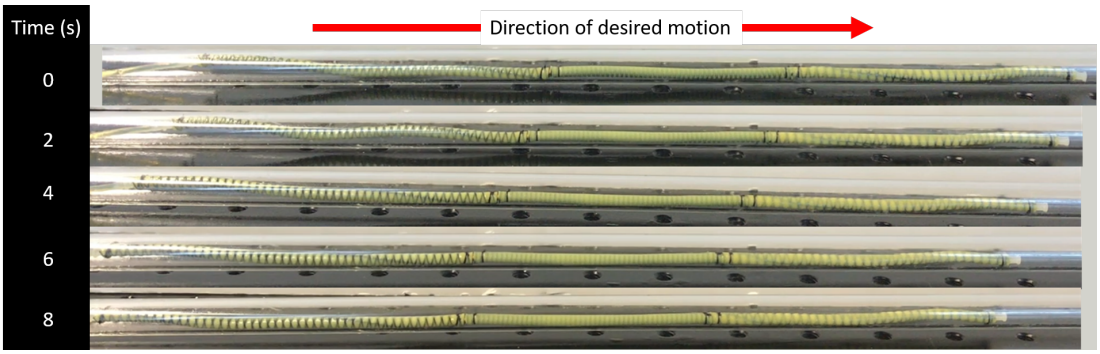

Figure 2.25: Soft robot locomotion in acrylic cannula (D = 9.53 mm) over several cycles (T = 2 s). Instead of generating forward motion, the robot moved backwards at an average of 6.84 mm (2.01% body length) per cycle. The substantial friction between the polyurethane outer coating (even when unactuated) and the acrylic cannula was suspected as a dominant contributor to this phenomenon.

The lubricated environment contained oil (Mobil 1 SAE 0w20 [127]) on the inside of the cannula to reduce the friction. As can be seen in Fig. 2.26, the robot forward an average of 5.66 mm (1.67% body length) per cycle.

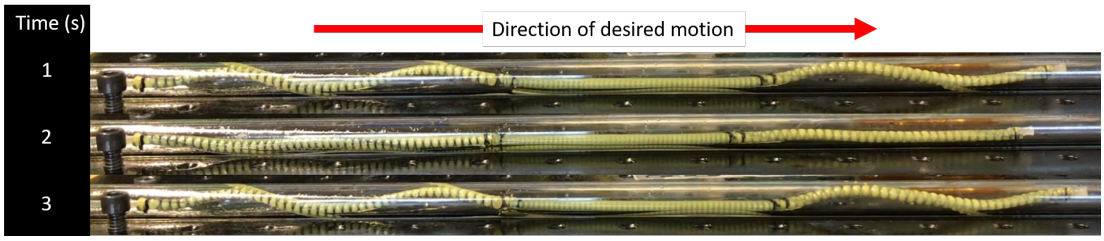

Figure 2.26: Soft robot locomotion in acrylic cannula (D = 9.53 mm) over one cycle (T = 2 s). The cannula was lubricated with Mobil 1 SAE 0w20 motor oil [127]. The robot moved forward an average of 5.66 mm (1.67% body length) per cycle. As can be seen between t = 1 s and t = 2 s, the lubrication caused a significant amount of "slip" at the tip of the robot with each stroke.

2.3.4 Discussion

The results show that several factors not included in the model play a larger role at smaller scales compared to larger scales, particularly when compared to [1]. For example, the larger-scale robot in Section 2.2 was able to locomote successfully without the need to model factors like friction between the robot and the cannula nor the interaction forces required to create a successful anchor. Scaling down the size of the robot underscored the need to better understand

the interaction between soft robots and their environments, which become no longer negligible at small scales, particularly as their interaction relates to anchoring force and friction.

Additionally, the scaled down robot was limited due to fabrication capabilities. The restrictors were manufactured using discrete drill numbers, which limited their diameters and thus the search space. More generally, the size limitations of the robot drastically limit the complexity that can be implemented within the valve to aid in control. Another major factor to be considered is the ratio of the actuator wall thickness to the outer diameter. The FREE model assumes negligible wall thickness in each of the formulas used to inform the design of the helical actuators [70, 71, 72, 73]. At the larger scale, thin-walled, off-the-shelf tubing was purchased where the ratio of wall thickness to outer diameter was 6.9%. However, at small scales and especially when using custom in-lab fabrication methods, it is difficult to manufacture thin-walled tubing of uniform wall thickness. Additionally, the walls must be thick enough to withstand operating pressures while comprising material that is compliant enough to deform into desired shapes. As a result, the ratio of wall thickness to outer diameter in the scaled down robot was 25.9%. The lack of wall thickness consideration in the FREE model emphasizes the need for a model that can better predict the deformation of uniquely shaped, thick-walled actuators and how the deformation relates to anchoring force.

In addition to an improved anchoring actuator behavior, the overall locomotion ability of the robot could be improved with a more detailed model of the extender. This chapter section only focused on an experimental robot prototype with one helix of a specific length and one extender of a specific length. However, the length of the extender plays a large role in locomotion because of its affect on buckling resistance and strain (i.e. extension) achieved with each stroke. Further investigation into the relationships between wrap angle, length, strain, and critical buckling load could be used to improve the robot model and performance.

The differences in locomotion between the unlubricated and lubricated cannulas (Figs. 2.25 and 2.26) show the importance of modeling friction between the robot and its environment. The results showed that too much friction resulted in movement in the direction opposite of desired motion, but too little friction reduced the anchoring force of the first and third actuators. Because of this, the robot in the lubricated cannula “slipped” with each cycle. Since the frictional, or anchoring, force depends on both the coefficient(s) of friction and the normal force, a stronger model of the forces between the robot and its environment would benefit locomotion.

Finally, Fig. 2.22 showed the high sensitivity of the objective function, meaning small errors in manufacturing or the experimental setup could lead to failed locomotion. Furthermore, this suggests such sensitivities will become prohibitive and impractical when scaling down further. As can be seen in Fig. 2.24, the number of solutions resulting in $J_{vol} > 0$ and the largest values for J_{max} occur when the actuator lengths are smallest (i.e. near 50 mm for the lengths searched). However, shorter actuator lengths lead to trade offs. Shorter helical actuators may not be able to generate a helical shape and anchor within the cannula if their overall length is too short. Shorter extending actuators are less prone to buckling, but may not be able to generate enough axial displacement to move the robot forward. Interestingly, Fig. 2.24c,d show that the greatest volumetric displacement occurs not at 50 mm, but instead near 80 mm which may merit further examination into the volumetric displacement needed to achieve sufficient axial strain.

Overall, gaining a stronger understanding of the variables that were not included in the models used for both the large and small-scale robots could help make the model more robust and generate successful locomotion regardless of scale.

2.3.5 Conclusion

This chapter section focused on scaling down the locomoting soft robot from Section 2.2 to examine how the behavior of the robot changes with a reduction in its size – both in diameter and length. As a part of scaling down, a novel method for creating soft robot base tubes with custom geometries and material properties was presented in addition to an updated CNC lathe used to create FREEs and a passive valve design that does not require manual tuning via a set screw. A robot was fabricated based on objective functions used in the larger-scale robot in Section 2.2 and the robot was tested experimentally in an acrylic cannula of ID = 9.53 mm. The results showed that directly scaling down a successfully locomoting robot of 11.6 mm in diameter does not directly result in a successfully locomoting robot of 3.3 mm in diameter. Overall, the results underscore the need for an improved understanding of the behavior of each of the robot components, specifically how the anchoring actuators interact with constraining environments and how the small-scale extender performance is affected by its geometry and design.

2.4 Anchoring Capabilities of Soft Actuators within Tube-Like Environments

2.4.1 Introduction

The locomotion behavior of the scaled down soft robot in Section 2.3 underscored the importance of better understanding the anchoring capabilities of the helical actuators as well as how closely the experimental actuator deformation matched the theoretical deformation produced using optimal FREE parameters. Existing models for helical FREE actuators make the critical assumption that wall thickness is negligible, but the scaled down actuators in Section 2.3 use a wall thickness to outer diameter percentage of 25.9%, which is far from negligible [70, 71]. One of the main reasons close alignment between the theoretical and actual shapes for the unconstrained (i.e. not within a tube) helical actuators is critical is because the unconstrained shape informs the constrained shape and anchoring behavior. Beyond properly capturing the unconstrained deformation of helical FREE actuators, no groups have modeled the interaction forces and anchoring forces achieved by helical actuators within tube-like environments.

This concept is illustrated in Fig. 2.27 and shows that when an unconstrained helical actuator is pressurized, the shape of the actuator expands radially and contracts axially (Fig. 2.27b). However, when the same actuator is pressurized to the same pressure within a constraining environment (Fig. 2.27c), radial expansion is limited by the environment while the wrapped fibers promote extension when $\alpha, \beta > 54.7°$. Thus, the base-to-tip distance of the actuator is even greater than the unpressurized distance (Fig. 2.27a). This interaction-driven behavior is critical to predicting locomotion of the robot and has not been modeled in soft robotics literature to date.

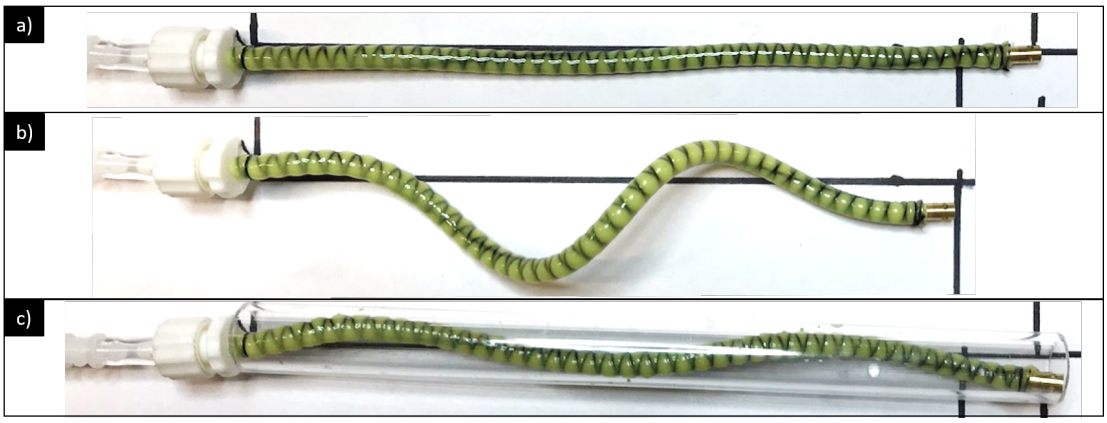

Figure 2.27: a) Unpressurized helical actuator with initial length, L = 130 mm, outer diameter, D = 3.3 mm, inner diameter, d = 1.59 mm, and wrap angles α, β, γ = 73°, -73°, 6°. b) Same helical actuator pressurized to 137.90 kPa (20 psi). Note the radial expansion of the helix and corresponding contraction in base-to-tip distance. c) Same helical actuator pressurized to 137.90 kPa (20 psi) within acrylic tube of ID = 9.53 mm. Note that because the acrylic tube prevents the actuator from expanding radially, the base-to-tip distance of the actuator increases.

However, helical FREE actuators are difficult to model because of the shortcomings of the FREE model to account for the effect of wall thickness on overall deformation. Even if wall thickness was accounted for, the shape of helical actuators is extremely sensitive to the γ wrap angle and relies heavily on accurate and precise fabrication. The uncertainty in unconstrained actuator deformation makes modeling the interaction between helical actuators and constraining environments particularly difficult, especially when the deformation is in three dimensions.

Perez-Guagnelli et al. presented an axially and radially expandable helical soft actuator that achieved radial forces of 1 N at 19 kPa, but the actuator was over 40 mm in diameter and did not utilize FREE methodology [128]. Instead, the robot deformed using radial and axial polyester constraints to control the location of inflation in the silicone base layer. The group did not derive a model for radial force nor did it test the anchoring capabilities of the device Galloway et al. proposed an underwater gripper that utilized FREE methodology to transform the gripper from a straight to helical structure [129]. The group characterized the load bearing capabilities of the gripper with both horizontal and vertical loads placed within the helical actuator, but did not examine using the helix as an anchoring mechanism. Blumenschein et al. adapted the idea of using inextensible fibers to generate helical motions in vine robots [130]. However, their work primarily focused on the achievable helical patterns of the actuator and only considered

measuring axial and grasping forces, similar to the gripper by Galloway et al.

In this chapter section, the unconstrained deformation and anchoring capabilities of soft robot actuators is empirically characterized. First, theoretical and actual helical shapes are compared using a 3D scanning process. Next, new anchoring actuator designs are proposed that can be fabricated more reliably. Finally, the anchoring capability of each actuator design is tested in both an acrylic tube and a mock artery. The findings will be used to inform future soft robot designs (e.g. locomoting robot) to improve modeling, control, and performance.

2.4.2 Methods: Helical Actuator

Determining Efficacy Using 3D Scans To determine how closely the experimental helical actuator shapes matched the theoretical shapes over a range of volume coefficients (or pressures), three helical FREE actuators were fabricated using the geometry and wrap angles from Section 2.3 (L = 130 mm, D = 3.3 mm, d = 1.59 mm, α, β, γ = 73°, -73°, 6°). Each experimental actuator was scanned using a handheld 3D scanner (Artec Spider, Artec3D) and a syringe and luer lock valve were used to fill the actuator to specified volume coefficients for each scan.

The scan software produced 3D point cloud data of the actuator surface, which was then imported into a 3D visualization and post-processing application (VMTKLab, Orobix). The post-processing application produced a visualization of the point cloud and computed the centerline of the actuator shape. The process is shown in Fig. 2.28 where the FREE optimization informed the actuator design, the actuator was fabricated and scanned, then the centerline of the actuator shape was extracted. Iterative closest point (ICP) was performed to compare the theoretical and experimental centerlines and provide a visual metric for how closely the two aligned.

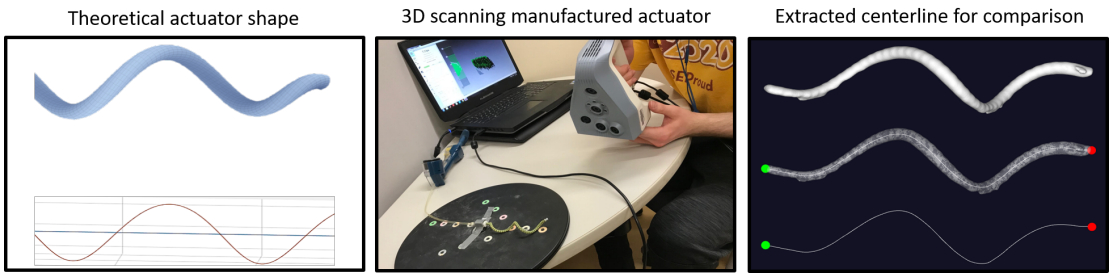

Figure 2.28: Process for comparing theoretical helical actuator shapes to the actual manufactured shapes. The Artec Spider 3D scanner was used to collect 3D point cloud data of the experimental actuator and VMTKLab was used to determine the centerline from the point cloud data.

2.4.3 Results: Helical Actuator

The experimental centerlines resulting from the 3D scan process were compared to the theoretical centerlines for volume coefficients ($\frac{V_f}{V_i}$) of 1.2, 1.3, and 1.4. All actuators were pressurized without mechanical constraints (e.g. not in clear tubes) and measured at rest on a flat surface, as shown in Fig. 2.29.

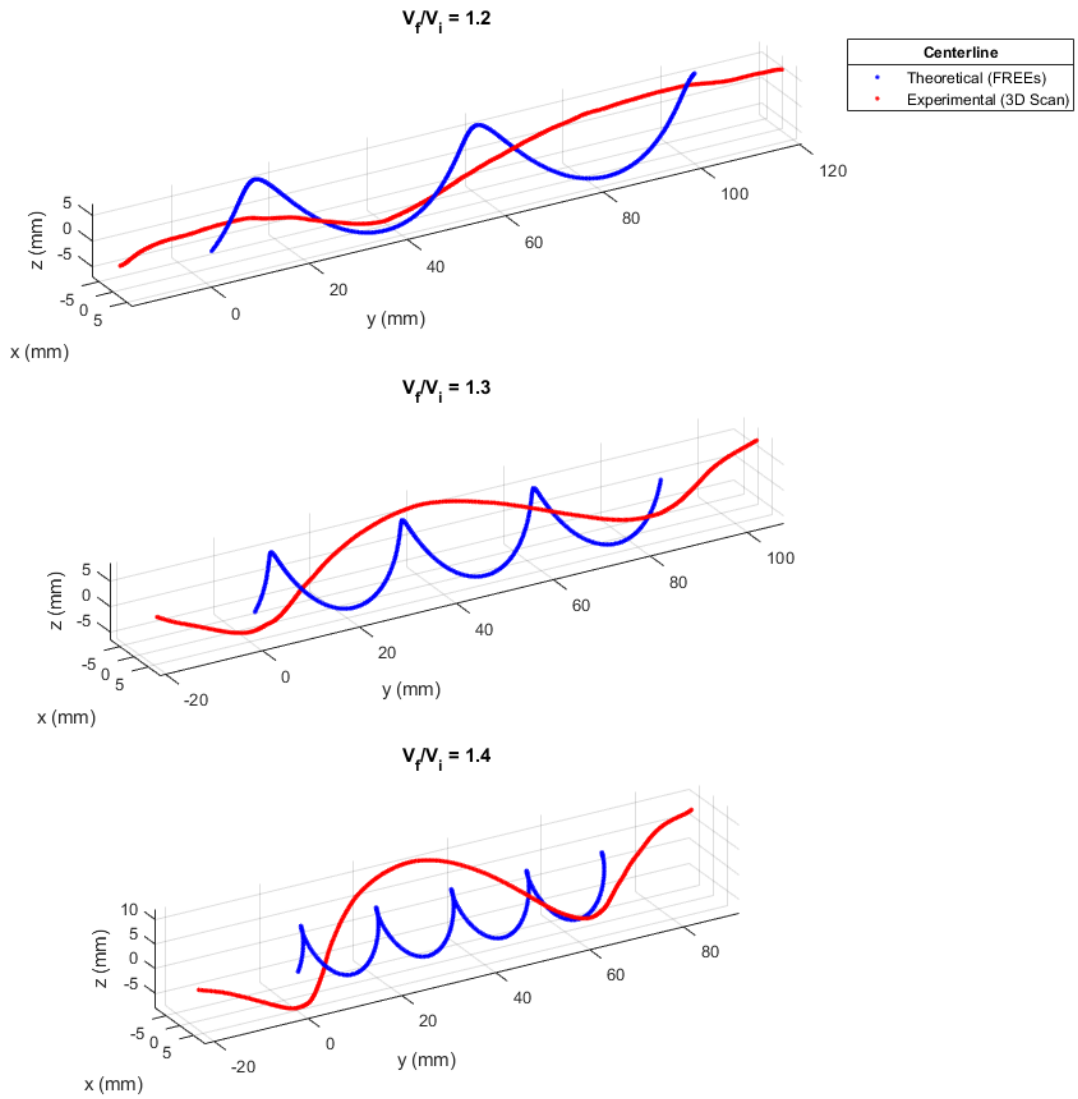

Figure 2.29: Iterative closest point (ICP) comparison between theoretical and experimental centerlines of helical actuators determined by FREE math and 3D scans, respectively. The helix examined in this case was of length $L = 130$ mm, outer diameter $D = 3$ mm, and utilized wrap angles of $\alpha, \beta, \gamma = 73°$, -73°, 6°. The experimental actuator had an inner diameter of $d = 1.59$ mm, whereas the theoretical FREE actuator assumes $d \approx D$.

2.4.4 Discussion: Helical Actuator

As can be seen in Fig. 2.29, the experimental, helical actuator centerlines did not align with the theoretical centerlines found using FREE methodology. The number of turns in the experimental actuators is consistently less than the theoretical centerlines (approximately 50 to 67% decrease in number of turns) which corresponds to the experimental actuators having a greater axial length from base-to-tip (approximately 33 to 64% more length). These are not negligible lengths when considering the total extender motion is of a similar magnitude. The misalignment between the two centerlines is likely caused by a combination of the FREE model not accounting for wall thickness as well as the sensitivity of the experimental actuator shapes to the accuracy and precision of the wrap angles.

Although the custom lathe in Fig. 2.19 is unique to the soft robotics field and utilizes high resolution encoders for control, the lathe is least accurate with wrapping low angles, like the $\gamma = 6°$ angle used in the experimental helices (Appendix A). The major contributing factor to this is the fabrication process and the amount of slip that occurs between the fiber and the actuator base tube when a small number of turns of the fiber around the base tube are present. Additionally, the fibers are hand-tied on either end of the actuator before and after the automated lathe wrapping, which introduces error by potentially shifting the fiber after the wrapping is complete. In cases of low wrap angles where the fiber is not wound tightly numerous times around the base tube, a small change in fiber placement when hand-tying the end knots leads to error in the wrap angle along the length of the actuator. Unfortunately, the γ angle is the most critical angle in dictating the actuator shape because it controls the helical pitch and radius. An error in γ of $\pm 5°$ relates to errors of one helical turn and greater in the final, pressurized shape, and the effects of this sensitivity can be seen in Fig. 2.29.

2.4.5 Methods: Alternative Anchoring Actuator

Alternative Anchoring Actuator Design

To avoid the inaccuracy of helical FREE actuators and their modeling complexity, non-helical designs were explored to anchor within tube-like environments while simplifying modeling and making fabrication more repeatable. Galloway et al. and the group that created the Soft Robotics Toolkit introduced the idea of adding a sheet of inextensible material to a fiber-wrapped

bladder to generate bending when pressurized [131, 132]. The bend radius was controlled by the length of the inextensible material and the actuation pressure, which can be seen in Fig. 2.30. The focus within the soft robotics community has been to fabricate individual actuators and combine them to create more complex motions (Fig. 2.30c).

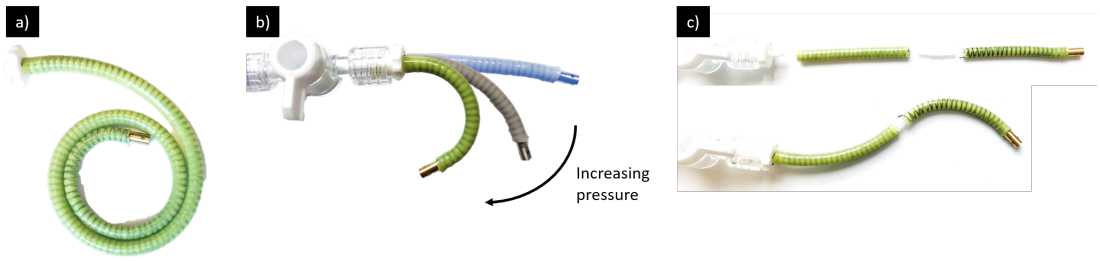

Figure 2.30: Concept for anchoring actuator made from a series of benders. a) A McKibben actuator that has wrap angles of -73°, 73° and a strain limiting layer along its length on one side has a tendency to bend. When the actuator is long enough, it will curl upon itself. b) The same design but with a smaller length creates a bending actuator, where the severity of the bend is controllable with pressure. c) Combining multiple bending actuators in series creates a planar, "S"-like actuator.

However, combining individual actuators to generate desired motion is cumbersome, often requires the incorporation of rigid components (e.g. valves, fittings), and increases the likelihood of failure near the connection points. To resolve this issue, this work integrated strain-limiting layers (3M Durapore Surgical Tape) smoothly over the length of a single actuator base tube, as shown in Fig. 2.31, to generate streamlined, predictable deformation.

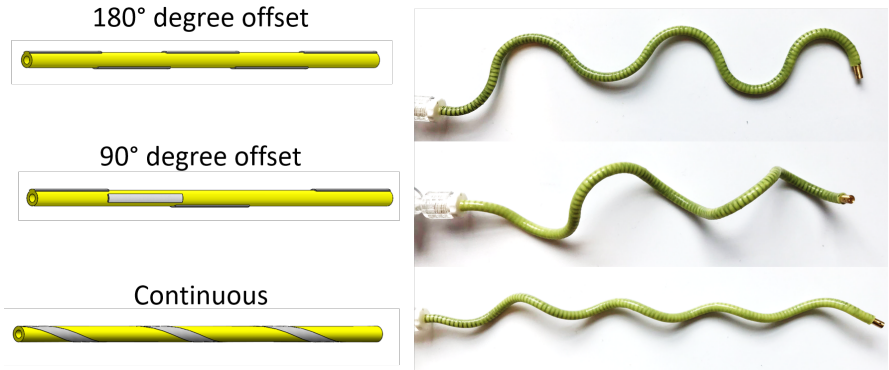

Figure 2.31: Experimental anchoring actuators with varying strain limiting layer patterns. **Left:** Strain limiting patterns. **Right:** The resulting experimental actuators after being wrapped with fibers at angles of -73°, 73°. **Top:** A planar, "S"-like actuator made from a series of strain limiting layers offset by 180° along the length of the actuator. **Middle:** A helix-like actuator created from a series of strain limiting layers offset by 90° along the length of the actuator. The outer radius and pitch of the helix is dictated by the length of each strain limiting strip. **Bottom:** A helical actuator made from a strain limiting layer wrapped at a constant angle along the length of the actuator. This is comparable to using a third, inextensible fiber to create a helical actuator where the wrap angle dictates the outer radius and pitch.

The location of the strain-limiting layers on the surface of the actuator dictated the shape of the deformation, where a continuous strain-limiting layer recreated helical deformation. The effect of strain-limiting layer (bender) length on bending deformation can be seen in Fig. 2.32, where longer layers generated taller bend heights when all layers were placed in an alternating fashion offset by 180° along the length of the actuator.

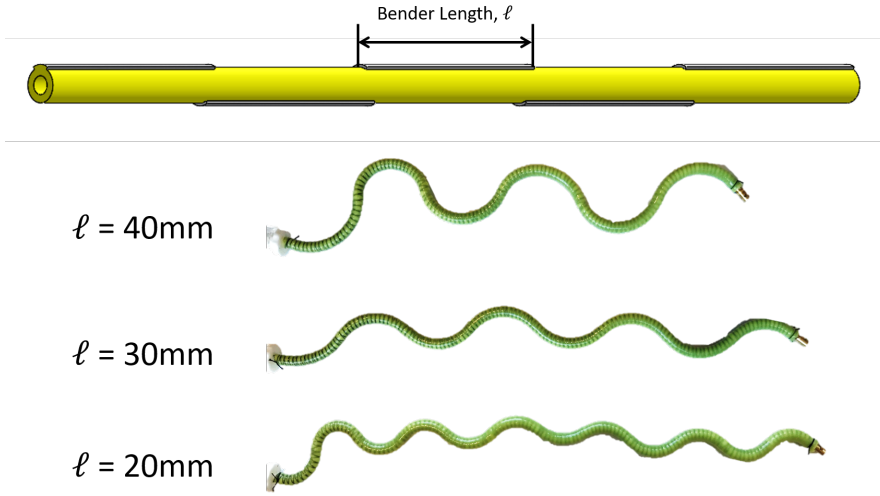

Figure 2.32: Experimental anchoring actuators made from a series of strain limiting layers (benders) with varying lengths offset by 180° along the length of the actuator. The bender length dictates the height of the planar bend when the actuator is pressurized. The larger the height of the planar bend, the more axial contraction from base-to-tip. Note: The actuator lengths shown are for illustration purposes only. The lengths of the actuators tested are shorter (120 mm) than the actuators pictured.

The actuators tested are listed in Table 2.8.

Table 2.8: Anchoring actuators tested.

Test Type	Qty. Tested	Overall Length, L (mm)	Bender Length, ℓ (mm)	Cannula Tested (ID = 9.53 mm)
Tape Pattern	3 per pattern	120	30	Acrylic
Bender Length	3 per length	120	30	Acrylic
Cannula	3 per cannula	90	30	Acrylic & Mock Artery

Experimental Setup

The anchoring ability of each actuator design was tested using the setup shown in Fig. 2.33. Each actuator was placed inside of a cannula (ID = 9.53 mm), either acrylic tube or silicone mock artery with realistic frictional properties (BDC Laboratories). The actuators were connected to a pressure source (syringe) via a luer lock valve. The cannula was rigidly connected to a load cell (500 g, straight bar, TAL221, SparkFun), which was mounted on the carriage of a linear

stage (ET-250-22, Newmark Systems, Inc.). A motor and encoder attached to the linear stage were used to control the movement of the carriage and pull the acrylic tube off of the actuator at a constant speed (1 mm/sec). While the stage was moving, force data were collected at 10 Hz using a load cell amplifier (HX711, SparkFun) connected to a microcontroller (Teensy 3.5, PJRC).

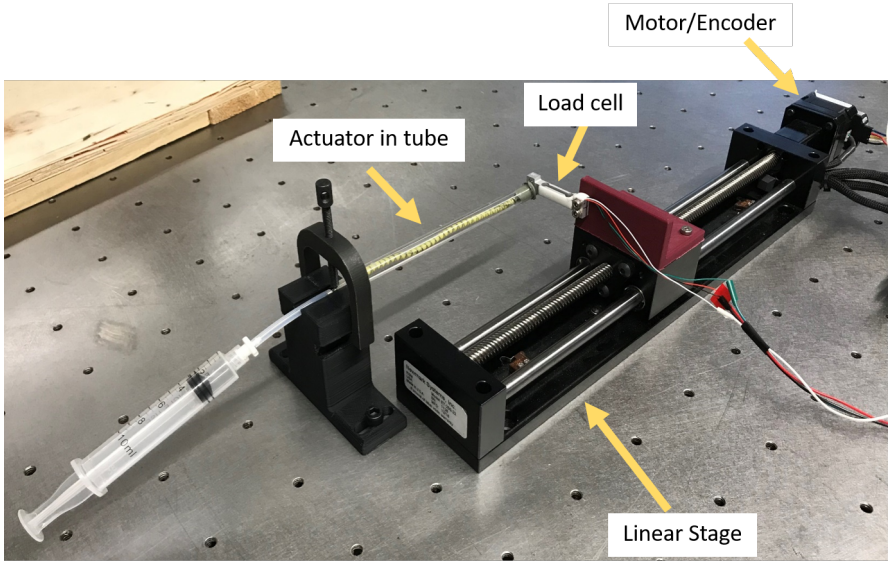

Figure 2.33: Experimental setup for determining the anchoring (traction) force of anchoring actuators. Not pictured: The pressure within the actuator was set using a pressure transducer and a three-way locking valve between the pressure source and the actuator.

The maximum force recorded throughout the test was considered to be the maximum anchoring force, shown in Fig. 2.34.

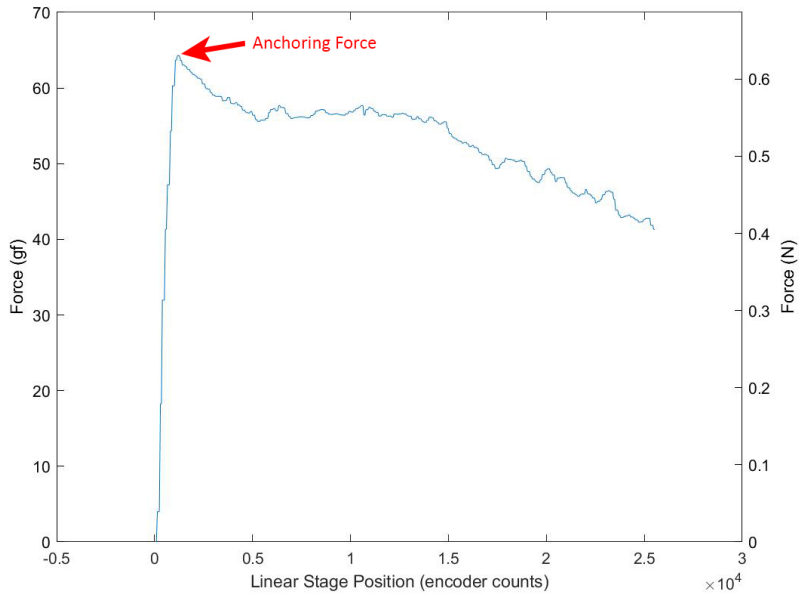

Figure 2.34: The maximum anchoring force of each actuator was determined by plotting the force read from the load cell against the position of the linear stage and extracting the peak force value.

2.4.6 Results: Alternative Anchoring Actuator

The results for the 120 mm long actuators with varying strain limiting layer patterns (Fig. 2.31) are shown in Fig. 2.35.

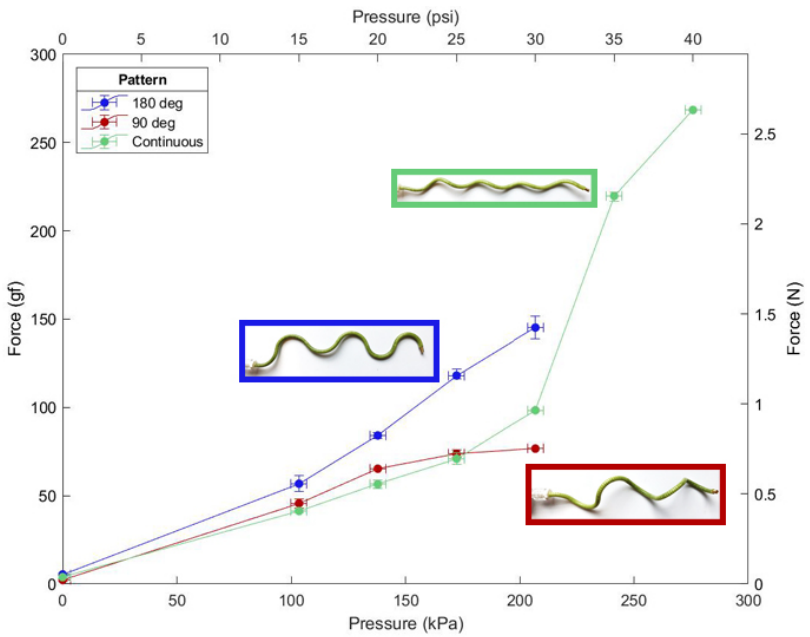

Figure 2.35: The maximum anchoring (pull-out) force of the three anchoring actuators with varying strain limiting patterns inside of a 9.53 mm ID acrylic tube. The maximum anchoring force achieved as a function of input pressure appeared to be greatest for the 180° offset strain limiting layer pattern for the pressure range tested. Actuators for 180° and 90° pattern burst before pressures above 206.84 kPa (30 psi) could be measured. N = 2 or N = 3 for each data point, dependent on actuator bursting. Vertical error bars represent range in force values. Horizontal error bars represent pressure fluctuations from readings throughout one test cycle.

The results for the actuators with 120 mm long actuators with varying bender lengths (Fig. 2.32) placed in the 180° offset pattern are shown in Fig. 2.36.

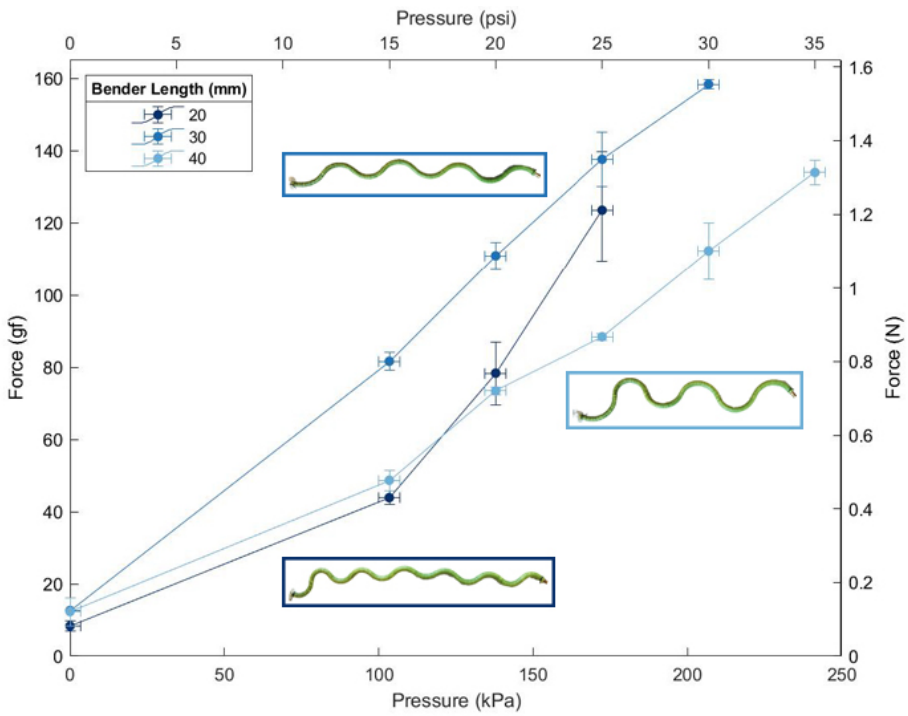

Figure 2.36: The maximum anchoring (pull-out) force achieved inside of a 9.53 mm ID acrylic tube as a function of input pressure for 120 mm long actuators with varying bender lengths placed in a 180° offset pattern. The 20 mm bender length actuators burst before pressures above 172.37 kPa (25 psi) could be measured. The 30 mm bender length actuators burst before pressures above 206.84 kPa (30 psi) could be measured. N = 2 or N = 3 for each data point, dependent on actuator bursting. Vertical error bars represent range in force values. Horizontal error bars represent pressure fluctuations from readings throughout one test cycle.

The results for the 90 mm long actuators anchored into either an acrylic tube or mock artery are shown in Fig. 2.36.

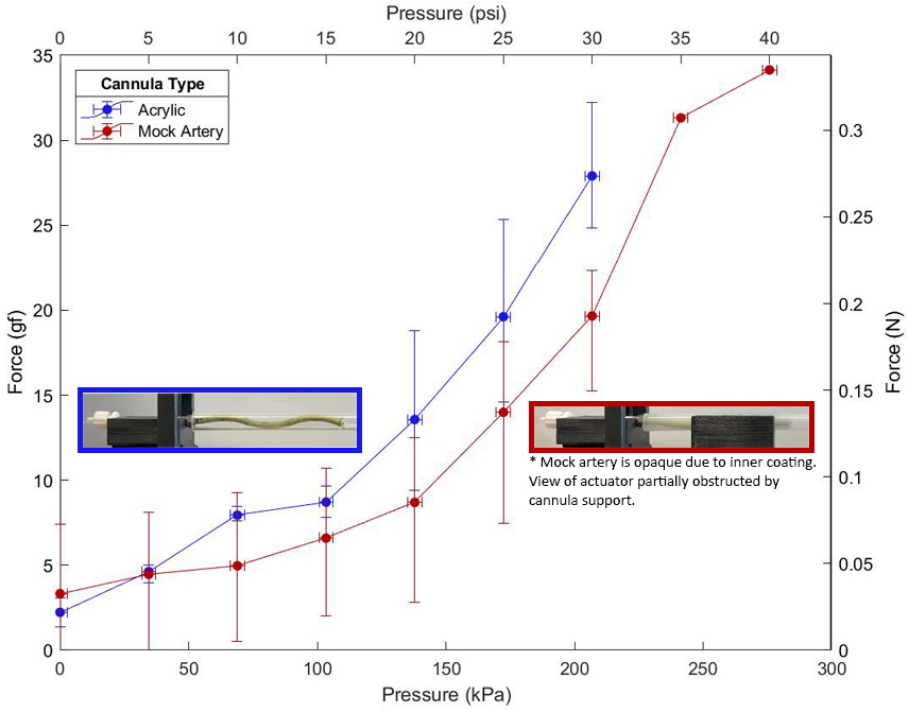

Figure 2.37: The maximum anchoring (pull-out) force achieved inside of a 9.53 mm ID acrylic tube or mock artery as a function of input pressure. The maximum anchoring force appeared to be greater for tests done within the acrylic tube. However, the force data follow similar shapes with response to pressure. N = 3 for each data point. Vertical error bars represent range in force values. Horizontal error bars represent the range of pressure fluctuations from readings throughout one test cycle.

2.4.7 Discussion: Alternative Anchoring Actuator

The results from Fig. 2.35 show that the strain limiting layer pattern of 180° offset achieved the greatest anchoring force for pressures from 0-206.84 kPa (0-30 psi). At 206.84 kPa, the anchoring forces achieved by the 90°, 180°, and continuous strain limiting layer patterns were 145.23 gf, 76.68 gf, and 98.40 gf, respectively. However, due to actuator burst failure, pressures greater than 206.84 kPa were only tested using the continuous pattern which generated a helical shape. The continuous pattern actuator showed a significant increase in anchoring force at pressures greater than 206.84 kPa, jumping from 98.40 gf at 206.84 kPa to 219.80 gf and 268.50 gf at 241.32 kPa and 275.79 kPa, respectively. Further testing would need to be conducted to determine if the 180° pattern would outperform the other patterns in anchoring force at pressures above 200

kPa.

Because the 180° strain limiting pattern achieved greater anchoring forces than the other two patterns from 0-200 kPa, the pattern was further examined to determine how bender length affects anchoring performance. The results from Fig. 2.36 show that the actuator with 30 mm bender lengths outperformed the actuators fabricated with 20 mm and 40 mm bender lengths for testing within an acrylic cannula with ID = 9.53 mm. For pressures of 172 kPa (25 psi), the 20 mm, 30 mm, and 40 mm designs achieved anchoring forces of 123.5 gf, 137.6 gf, and 88.45 gf, respectively.

One potential reason for the difference in anchoring force between bender lengths could be because the actuators with the 20 mm bender lengths did not deform enough to provide sufficient forces to anchor within the cannula. The shorter bender lengths created shorter bend heights as can be seen in Fig. 2.32. Upon examination of the actuators within the cannula while the test was being conducted, the shorter bend heights appeared to result in the actuators being "stiffer" when pulled axially, meaning they were able to maintain their "S"-like shape. On the contrary, the 40 mm bender length actuators appeared to be less "stiff", meaning the actuator was prone to straightening out when pulled axially. This may have been a contributing factor to the lower anchoring forces achieved in comparison to the 30 mm bender length actuators.

Since the 30 mm bender length, 180° strain limiting pattern achieved the greatest anchoring forces in the previous tests, the design was used to evaluate the anchoring performance of the actuator within an acrylic cannula and mock silicone artery. The results in Fig. 2.37 show that the anchoring force was consistently greater within the acrylic cannula compared to the mock artery, with the exception of pressures below 50 kPa where the actuator was not yet in contact with the cannula. These results were expected because the mock artery was manufactured with frictional properties that closely match the slick surface of arteries using BDC Laboratories proprietary SLIC friction reduction coating [133]. The maximum force achieved was 27.90 gf at 206.84 kPa (30 psi) and 34.14 gf at 275.79 kPa (40 psi) within the acrylic cannula and mock artery, respectively. These forces were lower than what was observed in the previous tests, which is likely attributed to the shorter overall length of the actuators (90 mm instead of 120 mm) and potential differences in the coefficient of friction between the actuator and the cannula because the actuators for this test were manufactured at a different time than the actuators used in the other tests. It is also worth noting that the compliance of the mock artery was greater than the

acrylic tube, meaning the pressurization of the actuator caused slight deformation of the mock artery walls as opposed to the acrylic tube, which maintained its cylindrical geometry.

Although each set of actuators (i.e. varying pattern, bender length, and cannula) were fabricated and tested in groups to reduce variation in the material properties with time, the frictional properties and fabrication variations cannot be ruled out as being a contributing factor to the differences observed in the results.

2.4.8 Conclusion

This chapter section focused on characterizing the unconstrained deformation of helical FREE actuators as well as the anchoring capabilities of non-helical actuator designs. Using a 3D scanning process and iterative closest point, it was shown that the deformation of the helical actuators tested in this section (L = 130 mm, D = 3.3 mm, d = 1.59 mm, α, β, γ = 73°, -73°, 6°) did not match the deformation modeled by FREE methodology. This is likely because of the effect of wall thickness on deformation and the current best fabrication capabilities for accurate fiber-wrapping.

Because the helical actuators do not behave as expected for unconstrained deformation, it can be assumed that modeling their behavior when constrained by a cannula would be difficult. As such, new anchoring actuator designs were proposed and their anchoring capabilities were empirically evaluated. The design that achieved the greatest anchoring force was a design with 30 mm long strain limiting layers offset by 180° along the length of the actuator, resulting in a planar "S"-like deformation. Actuators of 120 mm lengths using the design achieved anchoring forces of 150-160 gf at 206.84 kPa (30 psi) in an acrylic cannula, and actuators of 90 mm lengths achieved anchoring forces of approximately 27.90 gf at 206.84 kPa (30 psi).

Overall, this chapter section provided insight into the performance of helical FREE actuators and provided a new anchoring actuator design. The proposed "S"-like anchoring actuator produces deformation that is more straightforward to predict compared to helical actuators. The interaction between the proposed actuator and a constraining environment will be explored in the next chapter. Future work could include an exploration of the optimal actuator length for anchoring, as well as the role friction and material properties (e.g. friction coefficients) play in anchoring performance.

An additional anchoring study was performed with the larger-scale actuators (D = 11.6 mm)

from Section 2.2 and is shown in Appendix C.

2.5 Soft Passive Conical Valves for Serial Actuation [2]

2.5.1 Introduction

As discussed throughout Chapter 1 and throughout this chapter in relation to locomotion, the combination and control of multiple soft actuators can create soft robots capable of performing unique tasks. However, soft robots' capabilities are dictated and often significantly limited by the ability or inability to control each individual actuator that comprises the robot. In the case of pneumatic and hydraulic robots, control typically requires multiple input lines or precisely-controlled or timed valves (e.g. solenoid or check valves). However, in applications where space is limited and soft robots must fit within environments that are on the order of millimeters in diameter (e.g. within the human body), space for control mechanisms is limited — both inside and outside of the robot. This limitation means that multiple input lines may not be possible and valves with complex or bulky structures cannot be used to control the pressurization of each actuator.

Although much research has been performed in soft robotics, less attention has been paid to the hydraulic valves used. Napp et al. have developed a passive band pass valve that consists of two moving diaphragms [117]. However, the valve is bulky (D = 14.5 mm) and requires precise fabrication and control of the component thicknesses. As mentioned previously, Ikuta et al. have also utilized multiple diaphragms to create a band pass valve within their pressure pulse drive system [85]. The group successfully scaled the size of the valve to approximately 3 mm in diameter, but the fabrication process is complex and actuation of the soft actuators connected to the valve is slow. Unlike previous works, the valve discussed in this chapter section consists of a single diaphragm and simple structure. The valve acts like a two-way check valve. Low pressure differentials are blocked out while pressures above the cracking pressure are able to flow through the valve wall, allowing each segment to fill up to a desired pressure.

As was shown in Section 2.2, it is possible to create a locomoting robot using all passive elements and only one pressure input. However, a more sophisticated valve design would allow for better flow control and potentially overall improved capabilities (e.g. locomotion efficiency). New valves that comprise of scalable elements must be created to allow for better control over

the sequential actuation of the locomotion segments with a single pressure line, as shown in Fig. 2.38. This chapter section contributes a design of asymmetrical cracking pressure valves with an empirical design table in an aim to achieve the cannular locomotion proposed in Figure 2.38. The design is scalable for both large- and small-scale applications, allows for tunable and asymmetric cracking pressures (i.e. pressure required to allow flow) in the forward and reverse directions, and is MRI compatible.

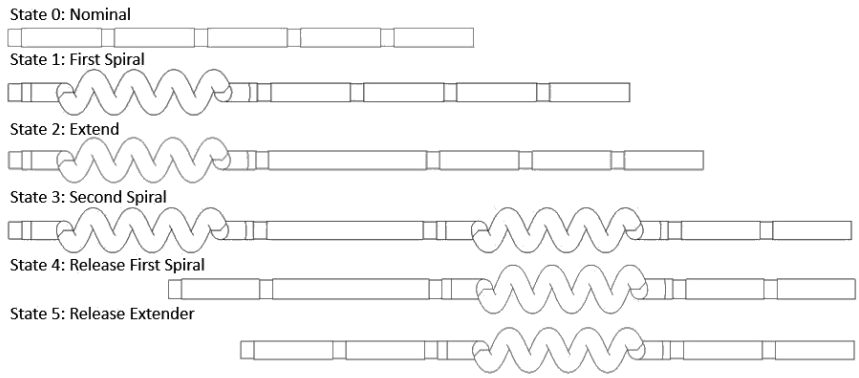

Figure 2.38: Actuation states of catheter robot segments.

2.5.2 Methods

The design draws inspiration from the mitral valve which consists of three flaps that form a cone. However, unlike the mitral valve, the cone valve design allows for the flaps of the cone to invert on themselves, allowing for bi-directional flow. The valves created in Figure 2.39 show the design and flow path for the forward and reverse flow directions. The inversion of the cone created asymmetric cracking pressures which was a desired design parameter. The cracking pressure was defined as the pressure that first generated noticeable flow through the valve. This was determined manually by measuring the pressure when water first cracked through the valve.

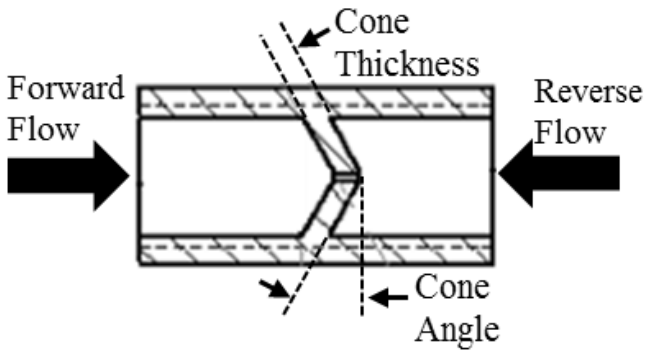

Figure 2.39: Valve diagram showing the thickness and angle of the flaps that form the cone. The ability of the flaps that form the cone to invert allows flow in both the forward and reverse directions. The flaps are molded out of silicone within a plastic bushing.

The valves were fabricated using a silicone molding process. A two part mold was 3D printed (Objet260 Connex, Stratasys Inc.), which contained six varying cone angles from $0° - 50°$ as shown in Figure 2.40. A 3/8" diameter bushing with a 3/8-16 UNC hole was placed into the mold and served as the outer casing for the silicone valve. To mold the valve within the casing, 8A durometer silicone (TAP Platinum Silicone, TAP Plastics) was injected into each bushing and the mold was degassed to remove bubbles. The top half of the mold was placed and a set of adjustable parallels was used to precisely set the thickness of the valves.

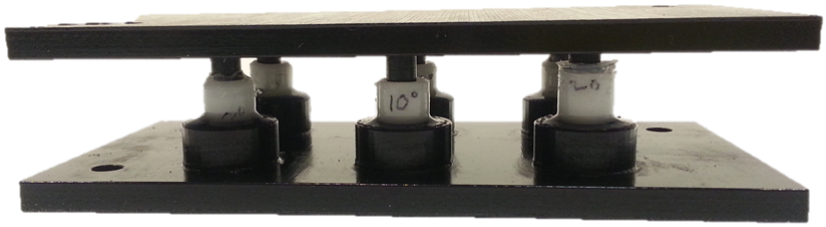

Figure 2.40: Two-piece mold with six varying cone angles and a variable height.

An empirical study was performed, using water as the working fluid, to test the bidirectional cracking pressure of the soft valves in both the forward and reverse directions. The cone thickness and cone angle ranged from $0.025" - 0.100"$ and $0° - 50°$, respectively. To test the cracking pressure of each valve, the pressure of the hydraulic source was gradually increased from 0 kPa (0 psi). The pressure that first cracked the valve, resulting in flow, was recorded based on the

reading from a pressure transducer (MLH100PGL06A, Honeywell International Inc.). The test setup, shown in Figure 2.41, consisted of a pressure source connected to a needle valve to control the input pressure, as well as a pressure transducer used to measure the pressure applied to the soft valve using a microcontroller (Arduino Nano, Arduino LLC) sampling at 500 Hz.

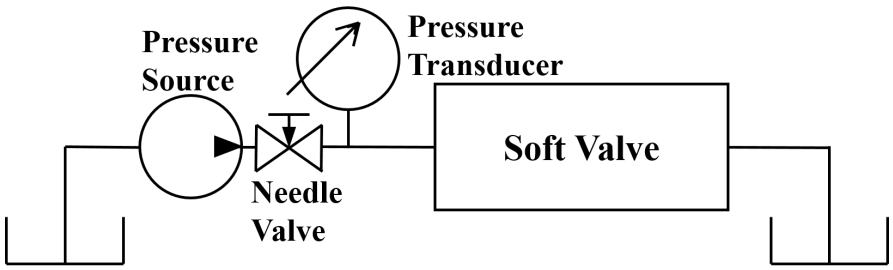

Figure 2.41: Hydraulic pump setup.

2.5.3 Results

The results of the bidirectional cracking pressure analysis are shown in Table 2.9. P_{fwd} represents the cracking pressure in the forward direction and P_{rev} is the cracking pressure in the reverse direction both reported in PSI. Figure 2.42 shows the normalized cracking ratio which was found by $\frac{P_{rev}}{P_{fwd}} - 1$.

2.5.4 Discussion

Table 2.9 shows that varying the cone angle and valve thickness substantially changes the bidirectional cracking pressure. Thicker valves resulted in higher cracking pressures. Steeper cone angles resulted in a lower forward cracking pressure and a higher reverse cracking pressure. The normalized cracking ratio in Figure 2.42 shows a saddle where the cracking pressure ratio varies from 3.5 (35°, 0.075") to less than 0.5 (0°, 0.1"). The valve design created through this process has the potential to achieve the locomotion in Figure 2.38 through the utilization of asymmetric cracking pressures.

Table 2.9: Results of valve experiment (pressures in psi).

	Valve Thickness							
	0.050”		0.075”		0.100”		0.110”	
Angle	P_{fwd}	P_{rev}	P_{fwd}	P_{rev}	P_{fwd}	P_{rev}	P_{fwd}	P_{rev}
0°	3.0	3.0	7.3	7.3	12.6	12.6	15.0	15.0
10°	3.0	5.8	5.2	9.8	10.6	15.5	12.3	15.6
20°	3.1	5.3	7.6	12.1	8.6	16.5	11.5	17.5
30°	2.7	5.6	2.4	11.3	7.1	17.8	9.3	19.8
40°	2.4	5.3	2.6	12.8	4.1	17.8	7.0	20.1
50°	2.8	4.9	2.5	6.8	4.0	17.9	6.4	20.8

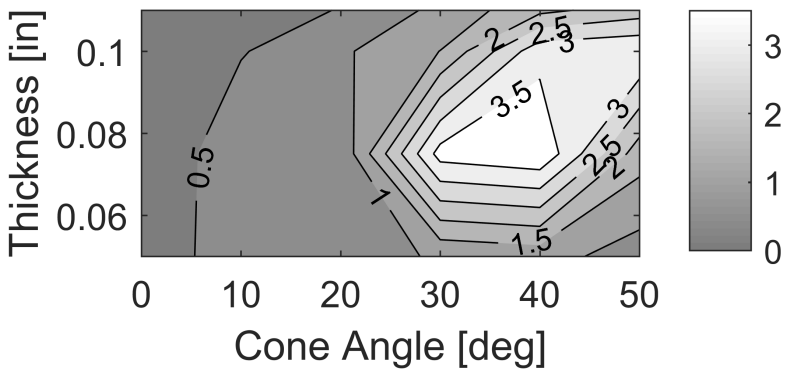

Figure 2.42: Contour of the cracking pressure ratios $\left(\frac{P_{rev}}{P_{fwd}} - 1\right)$ for varying thicknesses and cone angles.

The tests were subject to several sources of error, mainly in the recording of the cracking pressure since a manual detection of initial flow through the valve was used. Additionally, various valves cracked with varying flow rates, which made it difficult to obtain a true and definite cracking pressure. The normalized cracking ratio was developed to reduce the error in the cracking pressure method by examining the relationship between the forward and reverse cracking pressures for each valve. The results provide a promising design approach that could be scalable for soft actuator valves to help improve controllability within serially actuated systems.

2.5.5 Specific Contributions

This research was performed with Mark Gilbertson. My contributions to section 2.5 were the design of the conical valves and creating the mold in Figure 3.19. Mark Gilbertson was responsible for the hydraulic pump setup. Running the experiments and developing the results were performed by both myself and Mark Gilbertson.

2.6 Chapter Summary

This chapter focused on the effect that scaling down the size of catheter-like soft robots has on overall locomotion performance with a specific on a novel design for a hydraulic soft robot capable of locomoting within a cannula while requiring only one input line (i.e. serially actuated). Throughout the chapter, several design and modeling strategies were introduced to predict the behavior of both individual actuators and multiple actuators combined with passive valves. The results of the locomotion studies suggest the need for a modeling strategy to describe the interaction between anchoring actuators and their environments, as well as a stronger understanding of the trade off between buckling resistance and achievable strain in extending actuators. These findings are explored further in the rest of this work.

Empirical studies were conducted to determine how closely theoretical FREE helical actuator deformation aligns with the actual deformation of experimental actuators with the same design parameters and non-negligible wall thickness. To inform the design of new anchoring actuator designs that are more reliable to fabricate and straightforward to model, several studies were conducted to determine the anchoring force capabilities of proposed designs. Ultimately, an "S"-like anchoring actuator with planar deformation was both straightforward to manufacture and achieved the greatest anchoring force of the designs explored. This design will be the focus of the next chapter.

Finally, several valve and restrictor designs were discussed to examine controllability of serially actuated soft robots. It was shown that passive valves (flow restrictors) were sufficient to achieve serial locomotion in a cannula. To explore methods of bi-directional flow control, a novel, conical valve design was introduced and characterized. Overall, designing and fabricating valves capable of more complex flow control at < 3 mm diameters would require sophisticated equipment and manufacturing techniques. However, particularly in light of the major challenges

and increasing obstacles (e.g. friction and interaction dominance, sensitivity of design variables, impracticality of thin walls) made evident at and likely below such 3 mm diameter scales, such design or fabrication is not warranted.

Chapter 3

Actuator-Environment Interaction Model

This chapter includes work from a submitted International Journal of Robotics Research manuscript titled, "Contact modeling for high aspect ratio soft robots using Hencky bar-chain and linear complementarity techniques" [134] and an Institute for Engineering in Medicine (IEM) Conference (2019) poster presentation titled, "Medical Soft Robots: Overcoming Scaling Challenges" [135].

3.1 Introduction

3.1.1 Motivation and Contributions

The soft and compliant nature of soft robots promises safe interactions with various environments, which is one of soft robots' greatest benefits. This compliance is advantageous in a wide-range of fields, from medical interventions to pick-and-place mechanisms used to sort delicate fruit. However, the benefits of having an inherently safe, variable stiffness robot come with trade-offs. The pliancy of soft robots makes modeling contact (i.e. shape change and interaction forces) with other objects non-trivial. Yet, such information remains critically important in situations where such knowledge is vital to safety.

One example of where the knowledge of these two aspects, force and shape, are imperative is in minimally invasive surgery. Surgeons must navigate their robotic tools while interacting

with delicate anatomy. To ensure patient safety, the contact forces between the robot and its environment must remain below a safety threshold while also being high enough to perform effectively in situations like clearing plaque, anchoring within arteries, or manipulating tissue. In many cases involving small anatomy, such as neurosurgery, researchers seek to reduce the size of their robot to millimeter scale as shown by Weisenberg et al. [136]. The reduction in size drastically reduces torque and force transmission along the length of the robot. To overcome these challenges, a contact model that accurately predicts the constrained shape and reaction forces generated over the contact area between a soft robot and its environment is necessary.

The core contribution of this chapter is a theoretical contact model and experimental validation of the shapes and forces generated by soft actuators when constrained by a rigid environment. The model applies Hencky bar-chain and linear complementarity methods to soft robots to model both self-deformation and contact modeling. Although these methods have been used for other applications outside of robotics, such as the work presented by Wang et al., Challamel et al. [104, 137], and others, the combination of these methods has yet to be applied to soft actuators that deform due to eigenstrains; that is, deformation caused not from external forces but from internal actuation forces and the structure of the actuator. Moreover, modeling using the contributions of this chapter can be completed using only static images, thus eliminating the need for embedded sensors, real-time measurements, and detailed knowledge of the actuator's material properties. Ultimately, the contributions of this chapter benefit the soft robotics community by introducing a contact model that is generalizable to any class of soft actuators that deform due to eigenstrains and the model does so using computationally tractable algorithms that can be computed in soft real-time.

Other contributions of this chapter include a simple method to estimate bending stiffness of composite actuators using a free-fold test approach, a comparison between the linear complementarity approach and nonlinear gradient descent, as well as a computer vision algorithm to determine the centerline of soft actuators, both unconstrained and constrained, as a function of input pressure.

3.1.2 Related Work

Hencky Bar-Chain

The Hencky bar-chain approach was first introduced in 1920 by Professor Heinrich Hencky and discretizes structures into a series of rigid bars and torsion springs to predict buckling behavior. Since 1920, many researchers, particularly in the fields of Civil and Structural Engineering, have expanded on Hencky's work, which is summarized comprehensively by Wang et al. [104].

Some examples of Hencky bar-chain applied to engineering problems include the buckling of columns and frames subject to external axial loads as shown by Pan et al. and others [138]. Other examples include the bending, buckling, and vibration response of elastica shown by Challamel et al. [137], the dynamics of uniformly loaded elastica as proposed by Baroudi et al. [139], and Zhang et al. who examined buckling and vibration in Euler beams with various end conditions [140]. Liakou and Detournay specifically looked at the dynamic response of a beam colliding with rigid obstacles using the Hencky bar-chain. However, the listed examples focus on the deformation of beams and elastica under external loads rather than self-deformation as discussed in this paper [141]. Additionally, none of the groups combined their Hencky bar-chain work with a linear complementarity approach.

Linear Complementarity Method

The linear complementarity method was first proposed in 1966 by Richard Cottle as a mathematical optimization problem [106]. Given a matrix $\mathbf{K}$ and a vector $\mathbf{z}$, the solution of the problem seeks vectors $\mathbf{R}$ and $\mathbf{g}$ that satisfy the following constraints

$$\begin{cases} \mathbf{R} = \mathbf{K}\mathbf{g} + \mathbf{z} \\ \mathbf{R} \geq 0 \\ \mathbf{g} \geq 0 \\ \mathbf{g}^\top \mathbf{R} = 0 \end{cases} \tag{3.1}$$

This method is used in modeling the contact and spacing between an object and a constraint given a complete description of the system.

Specific to soft robotics, Al-Fahed et al., Ciocarlie et al., and Zhang et al. formulated their problems as Linear Complementarity Problems (LCPs) [142, 143, 144]. Al-Fahed et al. focused

on exploring the difference between two finger grippers, "hard" and "soft", and found that soft grippers have the added advantage of constraining the rotation of objects. Ciocarlie et al. used known expressions for contact between elastic bodies to solve an LCP to model soft fingers. Zhang et al. modeled the motion of a cable-driven continuum robot contacting simulated anatomy. Again, none of these applications utilized the Hencky bar-chain as a discretization technique and assumed known, external force applied to the soft bodies.

Katz and Givli also examined minimally invasive surgical techniques specific to guidewires [145]. Their work focuses on the post-buckling behavior of a beam constrained by springy walls to model how guidewires deform when inserted into an occluded artery. However, the work differs in that the deformation of the beam is dictated by an external, axial force and utilizes energy methods to find a solution.

Many have modeled the contact mechanics for soft fingers [146, 147, 148, 149]. However, these models also require an external, axial force to describe contact and do not use the same approach as shown in this chapter.

Other groups have utilized the deformation of soft robots to locomote in both flat and tube-like environments [1, 150, 151]. These groups and others, including Haibin et al. [152], have utilized soft robotics' pressure-controlled curvature and flexural rigidity to explore how those variables affect behavior and performance.

Haibin et al., Coevoet et al., Berselli et al., and others use FEM-based methods to produce results for contact forces for grasping and biomimetic applications [152, 153, 154]. Zhang et al. focused on the modeling of a flexible catheter during insertion and used FEM to model the catheter [144]. While FEM methods may provide rigorous modeling, the drawbacks of FEM approaches include the large computational cost and requirement for detailed material properties for each actuator component.

3.2 Unconstrained Actuator Description

3.2.1 Problem Description

To accurately describe the contact forces and shape of a soft actuator when constrained by its environment, the unconstrained shape of the actuator and its relation to input pressure, P, must first be described. The actuator used throughout this chapter is representative of a popular

design used in soft robotics, as shown by Galloway et al. [132], and is comprised of three key components, shown in Fig. 3.1a: i. base tube made from elastic rubber, ii. strain-limiting layer, iii. inextensible fibers. The angle at which the fibers are wrapped generates extension when the actuator is pressurized, which makes the actuator a Fiber Reinforced Elastomeric Enclosure (FREE), as described by Bishop-Moser and Kota [60]. Conversely, the strain-limiting layer prevents extension along the side of the actuator on which the layer is placed. This causes each strain-limited section of the actuator to bend, similar to the concept shown by Galloway et al. [132]. This tendency for self-deformation can be modeled as an eigenstrain ("eigen" in German means "inherent" or "self"), meaning the deformation is not caused by external mechanical stresses.

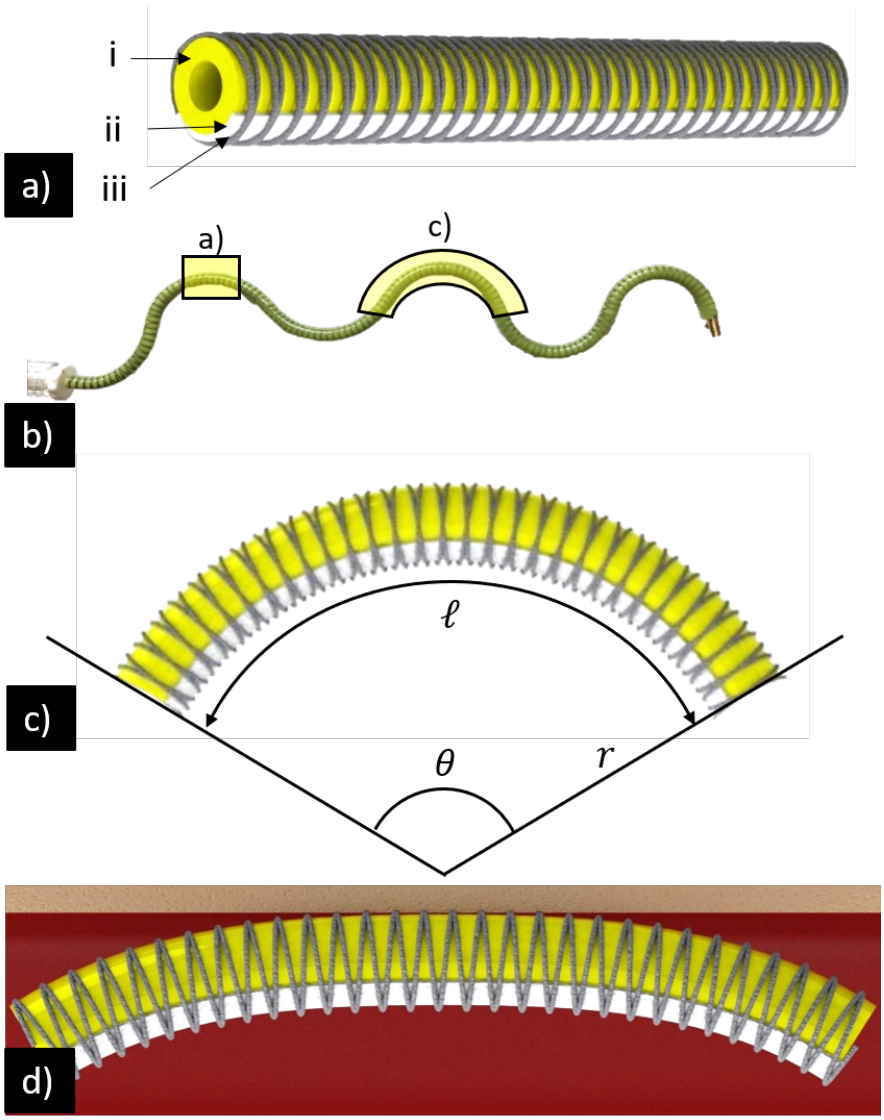

Figure 3.1: a) Section of a soft robotic actuator showing the construction used to generate bending, including: i. a pressurizable, elastomeric base tube, ii. an inextensible, strain-limiting layer, and iii. inextensible fibers with known wrap angles. b) Example of soft actuator comprised of multiple bending sections, which are used to anchor in constraining environments when the actuator is pressurized. c) Bending section defined by bend angle, θ, bend radius, r, and section length, ℓ. d) Bending section constrained by an environment (e.g. arterial wall), which causes deformation.

Multiple strain-limiting layers placed in an alternating pattern along the length of a base tube form a planar, anchoring actuator as shown in Fig. 3.1b, which can be used to anchor

within or locomote through tube-like structures reminiscent of the work in Section 2.2 [1]. Each segment section within the anchoring actuator can be described by its overall length, which is the same length as the strain-limiting layer, as well as its bend angle, θ, and bend radius, r, shown in Fig. 3.1. The bend angle, θ, in each section of length ℓ can be expressed as

$$r = \frac{\ell}{\theta} \tag{3.2}$$

where θ increases with input pressure, P (Fig. 3.1c). The model in this chapter will rely solely on bend angle, θ and an experimental relationship between θ and P that will change based on material properties of the actuator is shown later in this chapter.

When the actuator is constrained by its environment (e.g. anchored into an artery or pipe), the actuator assumes a new shape and reaction forces are generated along the contact area. Both of which are dictated by actuation pressure and the height of the environment, shown in Fig. 3.1d.

3.2.2 Notation for Unconstrained Actuator

Throughout this chapter, scalars are represented using lowercase letters not in bold typeface (e.g. d, μ, b_1). Vectors are lowercase, bold typeface letters (e.g. $\boldsymbol{\alpha}$, $\bar{\boldsymbol{\tau}}$, $\mathbf{c_1}$). Matrices are uppercase, bold typeface letters (e.g. $\mathbf{A}$, $\mathbf{B}$, $\mathbf{L}$). The exception to this is the reaction force vector, $\bar{\mathbf{R}}$, which is one of the variables for which we are solving. A bar above the variable (e.g. $\bar{\boldsymbol{\phi}}$, $\bar{\mathbf{u}}$) represents that the vector has been truncated to only consider the variables within the vector definition (e.g. $[u_2, \cdots, u_N]$) instead of variables 1 through N.

The following notation is used to describe an unconstrained actuator: $\boldsymbol{\alpha}^*$ is a $N \times 1$ vector describing the ordinary angles between each link and the horizontal, $\bar{\boldsymbol{\phi}}^*$ is a $(N-1) \times 1$ vector describing the angles between each pair of links (joint angles), $\bar{\mathbf{u}}^*$ is a $(N-1)\times 1$ vector describing the vertical displacement of each node, and $\bar{\boldsymbol{\tau}}^*$ is a $(N-1) \times 1$ vector containing all zeros for the unconstrained actuator. This is because there is no unconstrained torque due to the "eigen" curvature of the actuator, where the unconstrained curvature is induced by fluid pressure and not external forces. Each variable is shown in Fig. 3.2 and the star* notation denotes the unconstrained, "eigenstrain" configuration.

The unconstrained actuator description is based on an N-link discretization of the actuator bending section described by Fig. 3.2 based on the Hencky bar-chain method. Each of the $N+1$

nodes can be thought of as an elastic rotational spring capable of generating torque when the rigid links are displaced. It is assumed that in the initial, unconstrained configuration shown in Fig. 3.2b, no torques have been developed (i.e. $\bar{\boldsymbol{\tau}} = \mathbf{0}$).

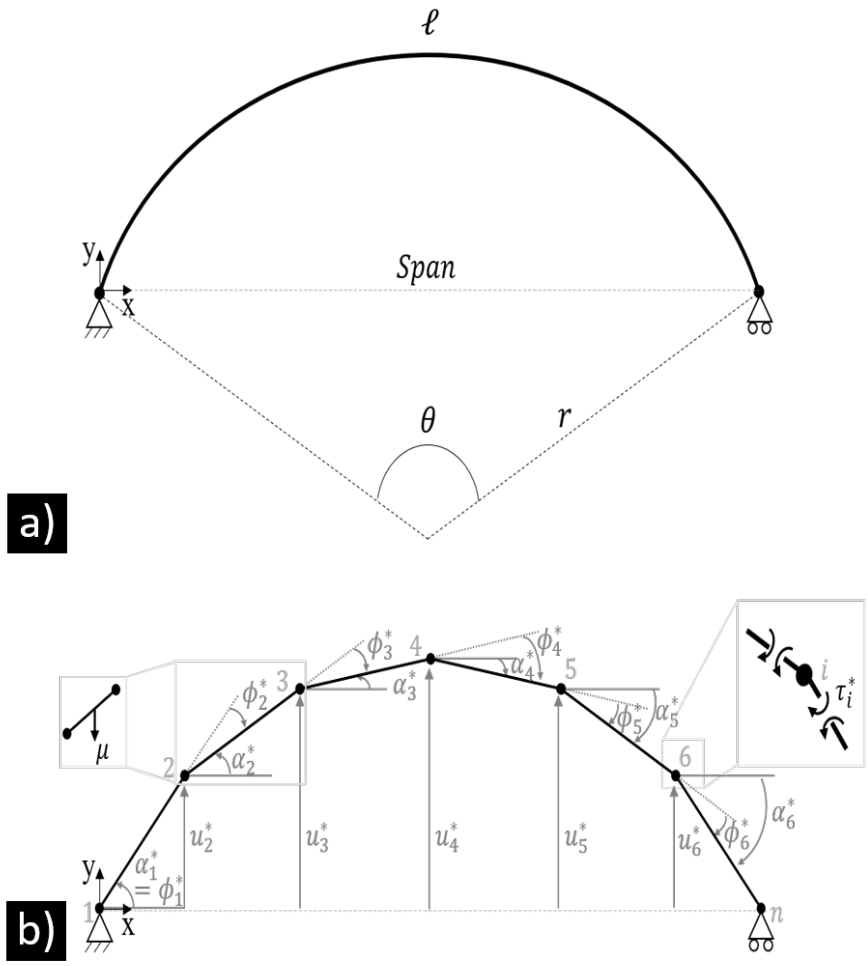

Figure 3.2: a) Simplified description of the soft actuator bending section shown in Fig. 3.1c. b) Discretized description of soft actuator of N links and $N+1$ nodes, where $N = 6$ in this example. Each link is subject to self-weight, μ. The orientation of each link relative to the positive x-axis is defined as α, ϕ describes the orientation of each link relative to the previous link, and u describes the displacement of each node in the y-direction. When each node undergoes an angular displacement a torque, τ_i, is developed.

This unconstrained description is used in two ways. The first is to create a baseline, eigenstrain configuration on which the environmental constraint is imposed. This is further outlined

in the next section. The second is to later derive a relationship between actuation pressure and the resulting bend angle.

3.3 Constrained Actuator Description

3.3.1 Problem Definition

As described previously, the major contribution of this chapter is a description of the actuator shape and the forces developed along the contact area when the actuator is constrained by its environment. This is achieved by discretizing the actuator using the Hencky bar-chain approximation and formulating the constraint problem as a LCP. More specifically, a final, nonlinear solution is reached by linearizing the equations describing the actuator and solving a sequence of linear problems corresponding to a changing configuration of the actuator. The process is shown below in Fig. 3.3 and the notation is outlined in Section 3.3.2.

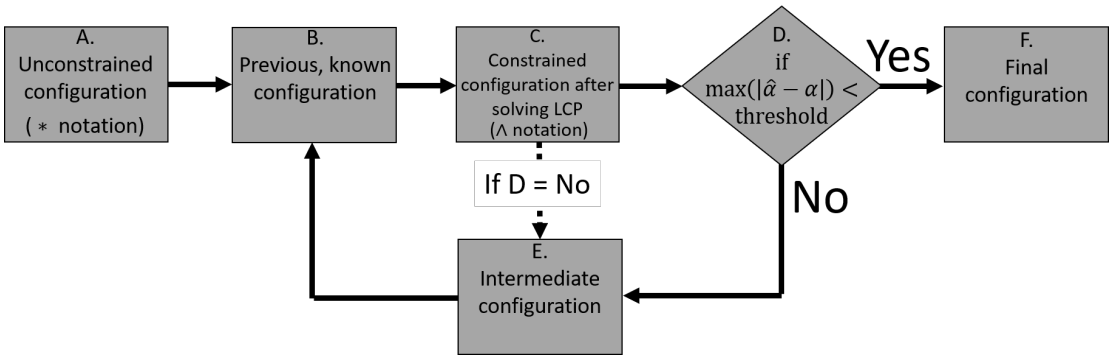

Figure 3.3: Iterative process for determining the final solution for reaction forces and actuator configuration. A. Refers to the unconstrained configuration ($*$ notation) found using the Hencky bar-chain method, B. Represents the previous, known configuration used as a "trial" value in the iterative process, C. Represents the constrained configuration after solving each subsequent iteration of the LCP ($\wedge$ notation), D. Represents a conditional statement used to determine whether the maximum change in link orientation ($\max(|\hat{\boldsymbol{\alpha}} - \boldsymbol{\alpha}|)$) is less than a threshold, E. Refers to the intermediate configuration, F. Is the final configuration.

3.3.2 Notation for Constrained Actuator

Throughout this chapter, the hat notation is used to communicate when a variable represents the unknown configuration of the constrained actuator (e.g. $\hat{\boldsymbol{\alpha}}$, $\bar{\hat{\boldsymbol{\phi}}}$, $\bar{\hat{\mathbf{u}}}$) and a non-hat to represent

the previous, known configuration of the actuator (e.g. $\boldsymbol{\alpha}$, $\bar{\boldsymbol{\phi}}$, $\bar{\mathbf{u}}$). In addition to the hat and bar notation, as well as the variables introduced in Section 3.2.2, we use the following variables to describe an actuator constrained by its environment: $\bar{\mathbf{g}}$ is a $(N-1)\times 1$ vector describing the vertical gap between each node and the environment, $\bar{\mathbf{h}}$ is a $(N-1)\times 1$ vector representing the height of the environment, and $\bar{\mathbf{R}}$ is a $(N-1)\times 1$ vector describing the reaction force at each node. These variables, shown in Fig. 3.4, are used in the LCP formulation to solve for the reaction forces, $\bar{\mathbf{R}}$, and the constrained configuration using the gap between each node and the environment, $\bar{\mathbf{g}}$.

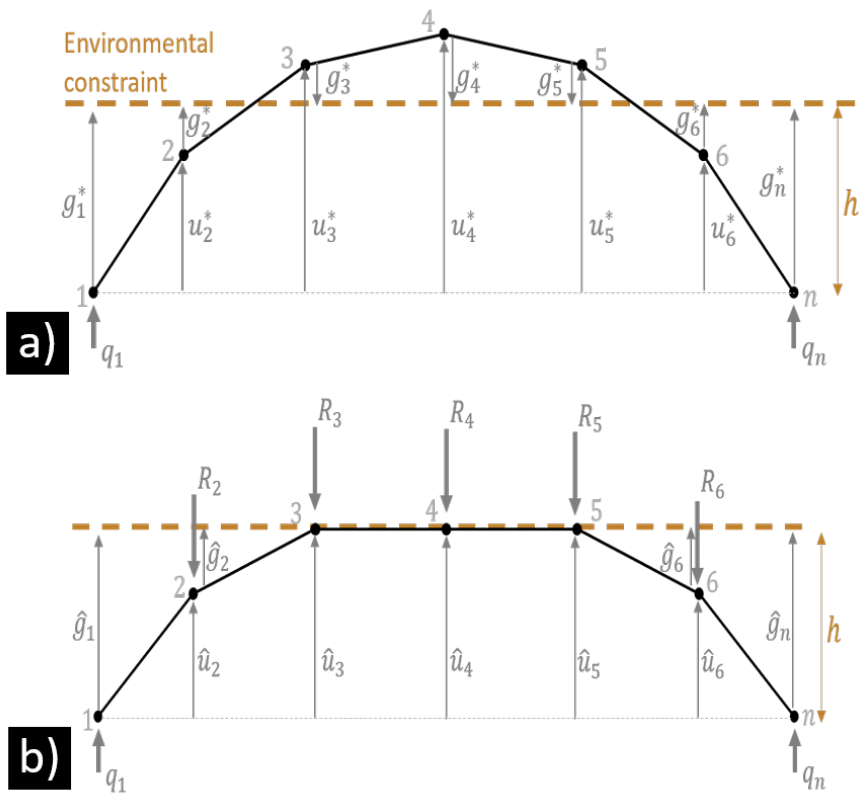

Figure 3.4: a) Unconstrained, discretized description of soft actuator relative to the environmental constraint of height, h, where u^* represents the y-direction displacement of each node and g^* represents the y-distance between each node and the constraint. b) Constrained, discretized description of soft actuator, where the $\hat{hat}$ notation specifies the constrained orientation.

3.3.3 Linear Complementarity Problem Formulation

Formulating the constrained actuator problem as an LCP allows us to not only determine the reaction forces developed along the length of the actuator created through contact with the environment, but also to understand the constrained configuration (e.g. position of each node and angle of each link). Understanding both of these variables is critical in delicate environments and situations where the relationship between change in actuator shape and interaction forces must be known to ensure adequate contact between the robot and its environment (e.g. traction for anchoring, locomotion, and tissue manipulation) without exceeding force limitations.

First, expressions for the support reactions q_1 and q_n as functions of the external reaction forces, $\bar{\mathbf{R}}$, must be determined. Summing the moments about node n generated from external forces, we get

$$q_1 = \frac{1}{d}(\mu b_1 + \mathbf{c_1}^\top \bar{\mathbf{R}}) \tag{3.3}$$

where d is defined as

$$d = \sum_{i=1}^{N} \cos \alpha_i \tag{3.4}$$

The weight of each link, μ, acts at the center of mass and is defined as

$$\mu = \frac{w\ell}{N} \tag{3.5}$$

b_1 is expressed as

$$b_1 = \frac{d}{2} + \sum_{i=1}^{N-1} i \cos \alpha_{i+1} \tag{3.6}$$

$\mathbf{c_1}$ can be defined as an $(N-1) \times 1$ vector

$$\begin{aligned} \mathbf{c_1} &= [c_{1_1}, \cdots, c_{1_{N-1}}]^\top \\ \text{where } \mathbf{c_1}(i) &= \sum_{j=i+1}^{N} \cos \alpha_j \end{aligned} \tag{3.7}$$

Following a similar process, the reaction force at node n is obtained by summing the moments about node 1 generated by external forces. The following relationship is obtained

$$q_n = \frac{1}{d}(\mu b_n + \mathbf{c_n}^\top \bar{\mathbf{R}}) \tag{3.8}$$

The expression for b_n is

$$b_n = \frac{d}{2} + \sum_{i=1}^{N-1} (N-i)\cos\alpha_i \tag{3.9}$$

and $\mathbf{c_n}$ is a $(N-1)\times 1$ vector defined as

$$\begin{aligned} \mathbf{c_n} &= [c_{n_1}, \cdots, c_{n_{N-1}}]^\top \\ \text{where } \mathbf{c_n}(i) &= \sum_{j=1}^{i} \cos\alpha_j \end{aligned} \tag{3.10}$$

The torque acting on each node can be calculated by summing all of the moments generated by external forces, resulting in

$$\bar{\boldsymbol{\tau}} = \frac{a}{2}(\boldsymbol{\gamma} + \mathbf{A}\bar{\mathbf{R}}) \tag{3.11}$$

where a represents the length of each link, defined as

$$a = \frac{\ell}{N} \tag{3.12}$$

and $\boldsymbol{\gamma}$ is a $(N-1)\times 1$ vector defined as

$$\boldsymbol{\gamma} = \frac{a}{2}\left(m\left(\mathbf{s} - \frac{1}{d}(b_1\mathbf{c_n} + b_n\mathbf{c_1})\right)\right) \tag{3.13}$$

$\mathbf{s}$ is a $(N-1)\times 1$ vector defined as

$$\begin{aligned} \mathbf{s} &= [s_1, \cdots, s_{N-1}]^\top \\ \text{where } \mathbf{s}(i) &= \frac{d}{2} + \sum_{j=1}^{N-2} \zeta_j \cos\alpha_{j+1} \\ \text{and } \zeta_j &= \begin{cases} j & \text{if}(i > j); \\ N-j-1 & \text{otherwise;} \end{cases} \end{aligned} \tag{3.14}$$

$\mathbf{A}$ is a $(N-1)\times(N-1)$ matrix defined as

$$\mathbf{A} = \mathbf{B} - \frac{1}{d}(\mathbf{c_n}\mathbf{c_1}^\top + \mathbf{c_1}\mathbf{c_n}^\top) \tag{3.15}$$

where $\mathbf{B}$ is a $(N-1)\times(N-1)$ matrix defined as

$$\mathbf{B} = \begin{bmatrix} 0 & \sum_{i=2}^{2} \cos\alpha_i & \sum_{i=2}^{3} \cos\alpha_i & \dots & \sum_{i=2}^{N-1} \cos\alpha_i \\ \sum_{i=2}^{2} \cos\alpha_i & 0 & \sum_{i=3}^{3} \cos\alpha_i & \dots & \sum_{i=3}^{N-1} \cos\alpha_i \\ \sum_{i=2}^{3} \cos\alpha_i & \sum_{i=3}^{3} \cos\alpha_i & 0 & \dots & \sum_{i=4}^{N-1} \cos\alpha_i \\ \vdots & \ddots & \ddots & \ddots & \vdots \\ \sum_{i=2}^{N-1} \cos\alpha_i & \sum_{i=3}^{N-1} \cos\alpha_i & \sum_{i=4}^{N-1} \cos\alpha_i & \dots & 0 \end{bmatrix} \tag{3.16}$$

A second expression for torque can be defined by relating torque and the change in joint angle from the unconstrained configuration, $\bar{\boldsymbol{\phi}}^*$, using the constitutive equation for a torsion spring.

$$\bar{\boldsymbol{\tau}} = -\frac{EI}{a}\left(\bar{\hat{\boldsymbol{\phi}}} - \bar{\boldsymbol{\phi}}^*\right) \tag{3.17}$$

where EI represents the bending stiffness of the actuator.

Utilizing kinematics, the relationship between $\bar{\hat{\boldsymbol{\phi}}}$ and $\hat{\boldsymbol{\alpha}}$ can be expressed as

$$\bar{\hat{\boldsymbol{\phi}}} = \mathbf{L}\hat{\boldsymbol{\alpha}} \tag{3.18}$$

where $\mathbf{L}$ is a $(N-1) \times N$ matrix

$$\mathbf{L} = \begin{bmatrix} -1 & 1 & 0 & \dots & 0 \\ 0 & -1 & 1 & \dots & 0 \\ \vdots & \vdots & \ddots & \ddots & \vdots \\ 0 & 0 & \dots & -1 & 1 \end{bmatrix} \tag{3.19}$$

To relate small y-direction displacements of each node, $\hat{\mathbf{u}}$, to the angular deflections of each link, $\hat{\boldsymbol{\alpha}}$, a linearization about the previous value for $\boldsymbol{\alpha}$ must be performed using

$$\sin\hat{\alpha}_i \approx \sin\alpha_i + \cos\alpha_i\left(\hat{\alpha}_i - \alpha_i\right) \tag{3.20}$$

The linearization results in the following expression for $\hat{\boldsymbol{\alpha}}$

$$\hat{\boldsymbol{\alpha}} = \frac{1}{a}\mathbf{M}\bar{\hat{\mathbf{u}}} - \mathbf{v} \tag{3.21}$$

where $\mathbf{M}$ is a $N \times (N-1)$ matrix

$$\mathbf{M} = \begin{bmatrix} \frac{1}{\cos\alpha_1} & 0 & 0 & \dots & 0 \\ -\frac{1}{\cos\alpha_2} & \frac{1}{\cos\alpha_2} & 0 & \dots & 0 \\ 0 & -\frac{1}{\cos\alpha_3} & \frac{1}{\cos\alpha_3} & \dots & 0 \\ \vdots & \ddots & \ddots & \ddots & \vdots \\ 0 & 0 & 0 & \dots & -\frac{1}{\cos\alpha_N} \end{bmatrix} \tag{3.22}$$

and the displacement of each node is a $(N-1) \times 1$ vector

$$\bar{\hat{\mathbf{u}}} = [\hat{u}_2, \cdots, \hat{u}_N]^\top \tag{3.23}$$

and $\mathbf{v}$ is a $N \times 1$ vector

$$\begin{gathered} \mathbf{v} = [v_1, \cdots, v_N]^\top, \\ \text{where } \mathbf{v}(i) = \tan\alpha_i - \alpha_i \end{gathered} \tag{3.24}$$

Solving for $\bar{\mathbf{R}}$, eqs. 3.18 and 3.21 must first be combined to get an expression for $\bar{\hat{\phi}}$.

$$\bar{\hat{\phi}} = \frac{1}{a}\mathbf{L}(\mathbf{M}\bar{\hat{\mathbf{u}}} - \mathbf{v}) \tag{3.25}$$

Combining eqs. 3.17 and 3.25, the torque at each node can be expressed as a function of the y-direction displacement of each node.

$$\bar{\boldsymbol{\tau}} = -\frac{EI}{a}\left(\frac{1}{a}\mathbf{L}\left(\mathbf{M}\bar{\hat{\mathbf{u}}} - \mathbf{v}\right) - \bar{\boldsymbol{\phi}}^*\right) \tag{3.26}$$

Comparing eqs. 3.11 and 3.26, a solution for $\bar{\mathbf{R}}$ is found.

$$\bar{\mathbf{R}} = -\frac{2EI}{a^2}\mathbf{A}^{-1}\left(\frac{1}{a}\mathbf{L}\left(\mathbf{M}\bar{\hat{\mathbf{u}}} - \mathbf{v}\right) - \bar{\boldsymbol{\phi}}^*\right) - \mathbf{A}^{-1}\boldsymbol{\gamma} \tag{3.27}$$

The relationship between the y-direction displacement of each node and the y-direction gap between each node and the environmental constraint can be expressed as (Fig. 3.4)

$$\bar{\hat{\mathbf{u}}} = \bar{\mathbf{h}} - \bar{\mathbf{g}} \tag{3.28}$$

Combining eqs. 3.27 and 3.28 and solving for the reaction forces at each node, $\bar{\mathbf{R}}$, produces

$$\bar{\mathbf{R}} = \mathbf{K}\bar{\mathbf{g}} + \mathbf{z} \tag{3.29}$$

where $\mathbf{K}$ represents the system's stiffness matrix, expressed as

$$\mathbf{K} = \frac{2EI}{a^3}\mathbf{A}^{-1}\mathbf{L}\mathbf{M} \tag{3.30}$$

and

$$\mathbf{z} = -\mathbf{K}\bar{\mathbf{h}} + \frac{2EI}{a^2}\mathbf{A}^{-1}\left(\mathbf{L}\mathbf{v} + \bar{\boldsymbol{\phi}}^*\right) - \mathbf{A}^{-1}\boldsymbol{\gamma} \tag{3.31}$$

The expressions for $\mathbf{K}$ and $\mathbf{z}$ can then be used to solve the LCP (e.g. *LCPSolve* in MATLAB, [155]). To find a nonlinear solution to the contact problem, the LCP is solved iteratively until

$$\max(|\hat{\boldsymbol{\alpha}} - \boldsymbol{\alpha}|) < 0.001 \text{ rad} \tag{3.32}$$

The threshold of 0.001 radians was chosen to ensure the LCP has converged to a solution with minimal change in link orientation.

The solution of the LCP provides the reaction forces at each node, $\bar{\mathbf{R}}$, as well as the gap in the y-direction, $\bar{\mathbf{g}}$, between each node and the environment constraint. The expression for $\bar{\mathbf{g}}$ can be used to deduce the actuator's constrained shape.

With the proposed problem formulation established, we now discuss how the formulation was implemented to perform analysis on the relationships between the bend angle, length, and material properties of an actuator and the shapes the actuator obtains and the reaction forces developed when constrained by a rigid environment.

3.3.4 Determination of Discretization Resolution

The number of links used for discretizing the soft actuator was determined using a thresholding method. The LCP was solved to find the total reaction force produced for actuators with unconstrained bend angles of 10° through 180°, constraint height of 2 mm through 7 mm, and a constant bending stiffness and actuator length of $EI = 32.01$ Nmm^2 and $\ell = 30$ mm. For each combination of bend angles and constraint heights, the number of links in the discretization were increased by 10. A sufficient number of links was determined when the percent change in total reaction force was below a 0.01% threshold. The percent change was calculated by

$$\%\ change = \frac{R_{total} - R_{prev}}{R_{prev}} \times 100 \tag{3.33}$$

where

$$R_{total} = \sum_{i=1}^{N-1} \bar{R}_i \tag{3.34}$$

and R_{prev} represents the total reaction force for the previous discretization of $N - 10$ links.

A conservative estimate was used when determining the necessary number of links, meaning the largest number of links that resulted in every percent change in reaction force throughout the entire space was below the threshold was used. These results are shown for $h = 3$ mm in Fig. 3.5.

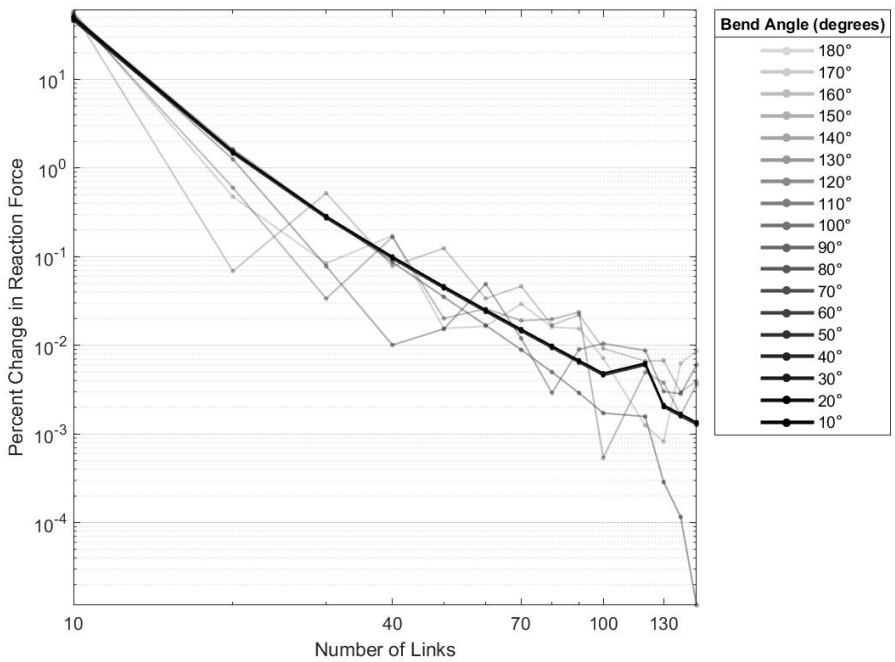

Figure 3.5: The percent change in the total reaction force appears to trend toward zero with a convergence rate of about three as the number of links is increased. This example is shown for an actuator of length $\ell = 30$ mm, bending stiffness EI = 32.01 Nmm^2, and constraint height h = 3 mm.

Further analyses throughout this chapter utilize discretizations of 140 links because 140 links proved to be a sufficient discretization for all bend angles listed above.

3.3.5 Theoretical Shape of a Constrained Actuator

The relationship between the constrained shape of the actuator and its unconstrained bend angle, θ (e.g. due to an increase in actuation pressure) can be seen in Fig. 3.6. As the bend angle increased, the actuator came into contact with the environmental constraint, which generated

a reaction force. As the bend angle continued to increase, the actuator's shape flattened and the contact area increased. Evident in Fig. 3.6a, the actuator's span changed in length as its bend angle increased, where span is defined as the x-direction distance between the ends of the actuator. The total change in actuator span was dependent on both the bend angle and the height of the constraint.

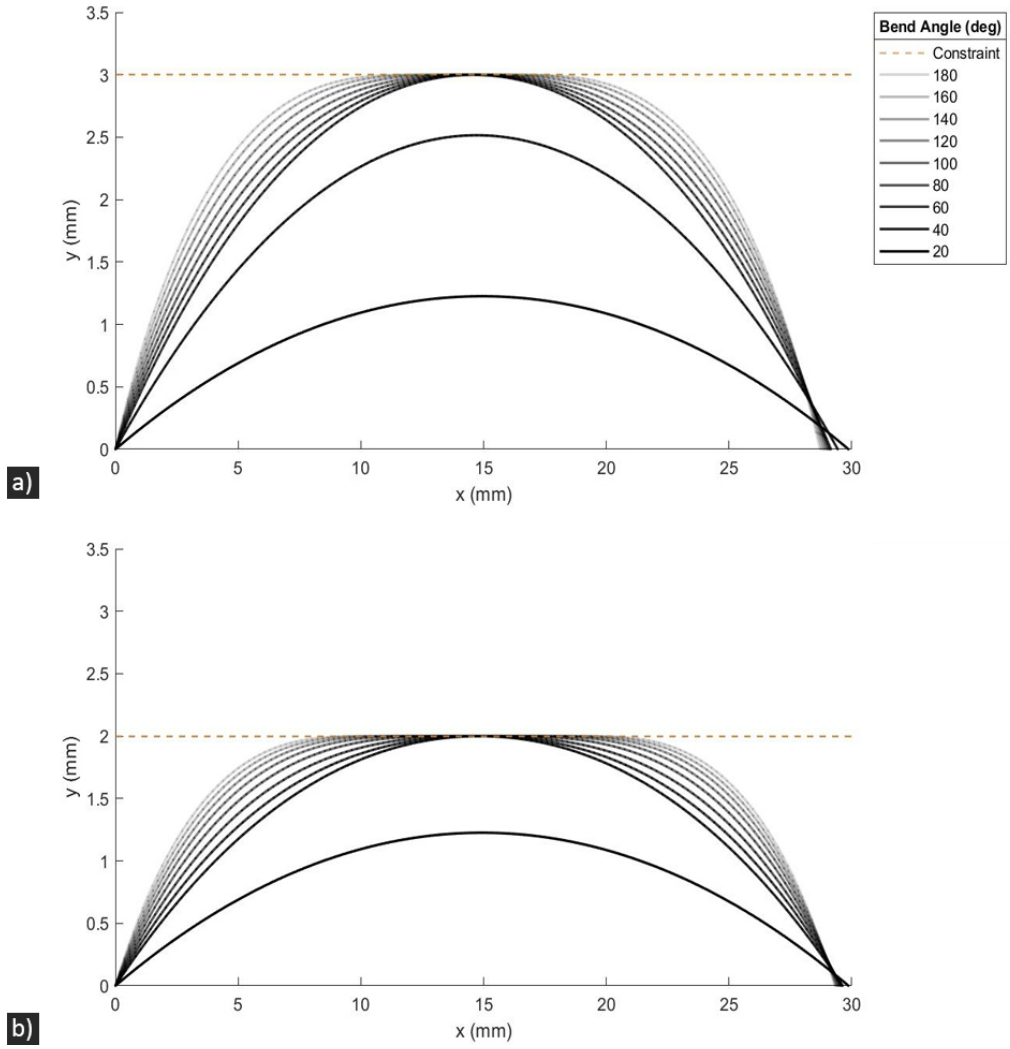

Figure 3.6: Theoretical, constrained actuator shape for constraint heights of: a) h = 3 mm and b) h = 2 mm. This example is shown for actuator length $\ell = 30$ mm, and bending stiffness EI = 32.01 Nmm^2. The theoretical actuator shape flattened as the bend angle was increased and the actuator came into contact with the constraint. The actuator flattened more as bend angle increased and constraint height decreased, corresponding to a larger contact area.

Fig. 3.7 shows the relationship between the actuator's shape and the height of the environmental constraint. To effectively explore this relationship, the bend angle was kept constant. Again it can be observed that the constrained actuator's span was related to the constraint height.

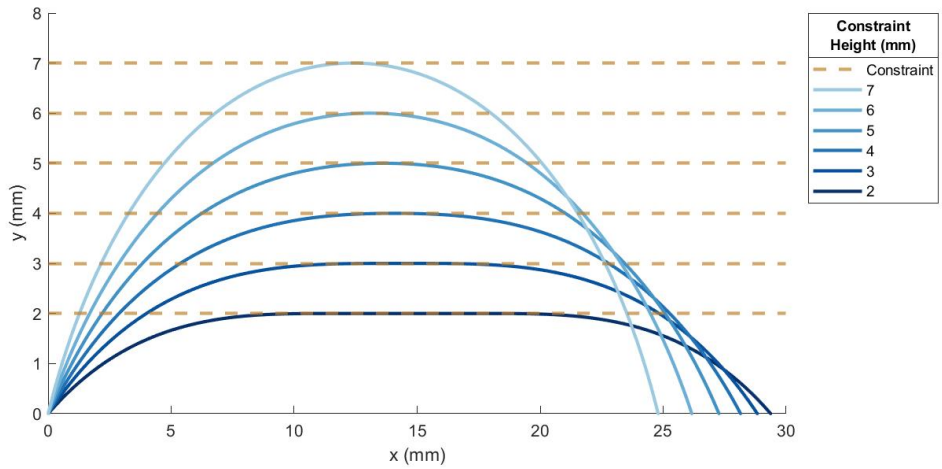

Figure 3.7: The flattening of the theoretical actuator shape increased as constraint heights decreased. This example is shown for actuator length $\ell = 30$ mm, bending stiffness EI $= 32.01$ Nmm^2, and bend angle $\theta = 150°$.

Observations: Theoretical Shape of a Constrained Actuator

The results show that the actuator has a tendency to flatten when in contact with a rigid constraint. The amount of flattening, or the amount of actuator in contact with the constraint, increased both with a decrease in constraint height as well as an increase in bend angle. The results also showed that the constrained actuator span increased in comparison to the unconstrained actuator span, where a decrease in constraint height corresponded to a larger the increase in span. This was because the overall actuator length stayed constant, but vertical deflection was limited by the constraint.

The model provides a better understanding of the relationships between actuator shape, bend angle, bending stiffness, and constraint height to use as both a design tool and predictive model of actuator contact behavior. This understanding of actuator shape could be used to predict surface traction and contact, estimate locomotion performance by understanding how the actuator's span changes as it is pressurized, and avoid critical structures by understanding the actuator's configuration.

3.3.6 Theoretical Reaction Force of a Constrained Actuator

The relationship between reaction force and bend angle was determined by keeping constant the actuator length (ℓ = 30 mm), number of links (N = 140), and bending stiffness (EI = 32.01 Nmm^2) while increasing the bend angle from 0° to 180°. The results are shown in Fig. 3.8. The regions where the total reaction force was equal to 0 mN represent the bend angles for which the actuator was not in contact with the environment.

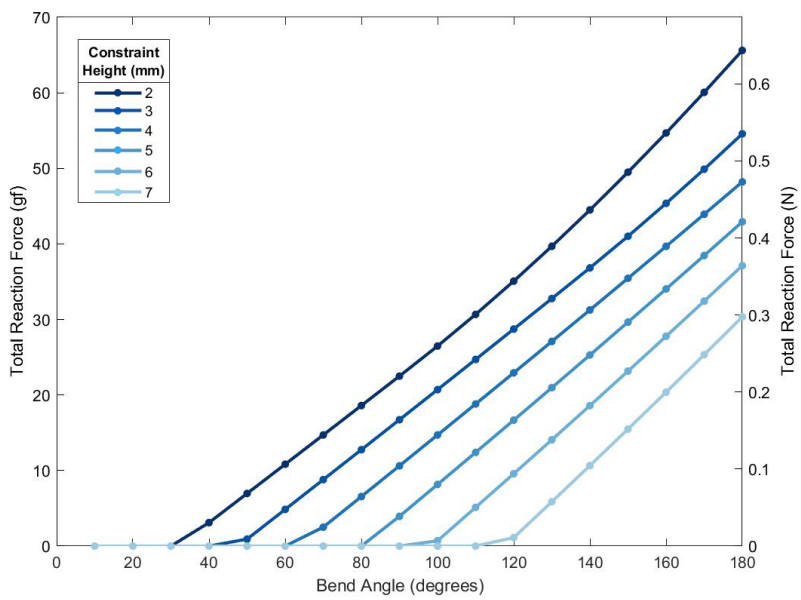

Figure 3.8: The total theoretical reaction force displayed a consistent increase as the bend angle is increased. The total reaction force consistently increased as the constraint height was decreased for the same bend angle. This example is shown for actuator length $\ell = 30$ mm and bending stiffness $EI = 32.01$ Nmm^2.

The interaction between reaction force and bending stiffness, EI, was explored by keeping the actuator length (ℓ = 30 mm), number of links (N = 140), and bend angle (θ = 150°) constant while increasing the bending stiffness from 10 Nmm to 100 Nmm. This was repeated for the a range of constraint heights (2 mm to 7 mm). The results are shown in Fig. 3.9.

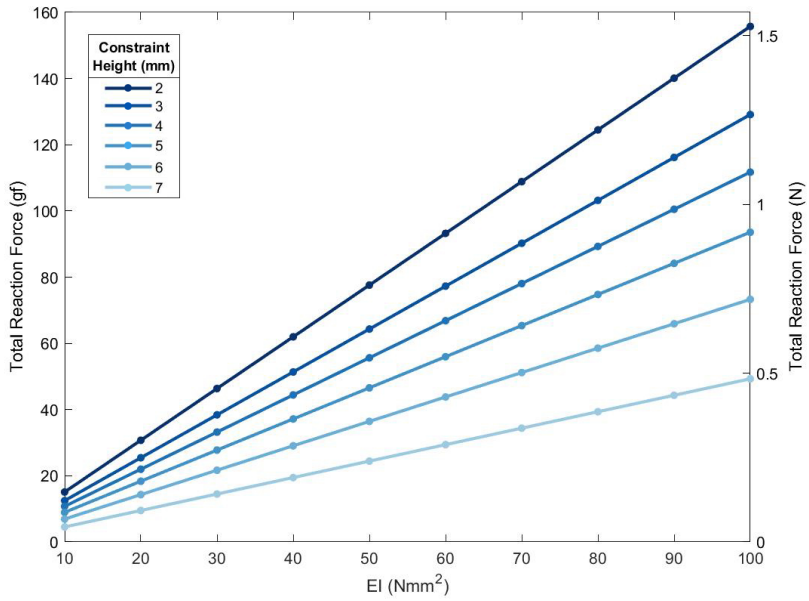

Figure 3.9: The total reaction force displayed a consistent, linear-like increase as the bending stiffness, EI, increased. This example is shown for an actuator length $\ell = 30$ mm and a bend angle $\theta = 150°$.

Similar trends were seen after examining how the reaction force vs. bending stiffness relationship changes as the constraint height stays constant but the bend angle varies. This was determined by keeping constant the actuator length ($\ell = 30$ mm), number of links ($N = 140$), and constraint height ($h = 3$ mm) while increasing the bending stiffness from 10 Nmm to 100 Nmm. This was repeated for the full range of bend angles (10° to 180°) to ensure contact between the theoretical soft actuator and the environment. The results are shown in Fig. 3.10.

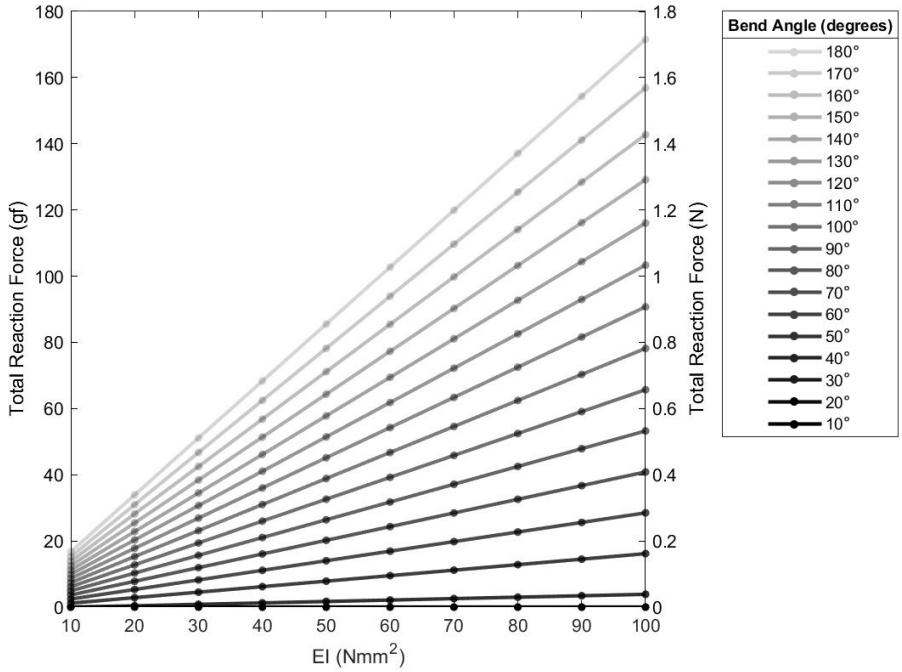

Figure 3.10: The total reaction force displayed a consistent, linear like increase as bending stiffness, EI, increased. This example is shown for actuator length $\ell = 30$ mm and constraint height $h = 3$ mm.

Observations: Theoretical Reaction Force of a Constrained Actuator

The results showed that the largest reaction forces consistently occurred for the smallest constraint heights. This implies that the more deformation required to reach the constraint, the more force is lost to deformation. The results also showed a consistent increase in the total reaction force as both the bend angle and bending stiffness were increased. This implies that stiffer actuators may exert more force when in contact with a constraint. However, increasing the stiffness of actuators comes with a potential trade-off of reduced deflection (i.e. bend angle). Thus, the proposed model could be used as a design tool to determine the ideal combination of stiffness and deflection for a given application.

Overall, the model provides a better understanding of the relationships between reaction forces, bend angle, constraint height, and bending stiffness, which could be valuable while actuating in delicate environments where forces must be predicted and controlled. Knowledge of actuator forces could also be used to model robot performance in manipulation or locomotion

where interaction with other objects or constraints is critical.

3.3.7 Validation of Linear Complementarity Approach

Cantilever Beam

A cantilever beam was used to validate the LCP approach and explore the accuracy of the approach outlined in Sections 3.3.1 and 3.3.3. The cantilever beam was subject to a uniformly distributed load, with the beam a distance h away from an environmental constraint, as shown in Fig. 3.11. For simplicity, the weight of the beam was ignored.

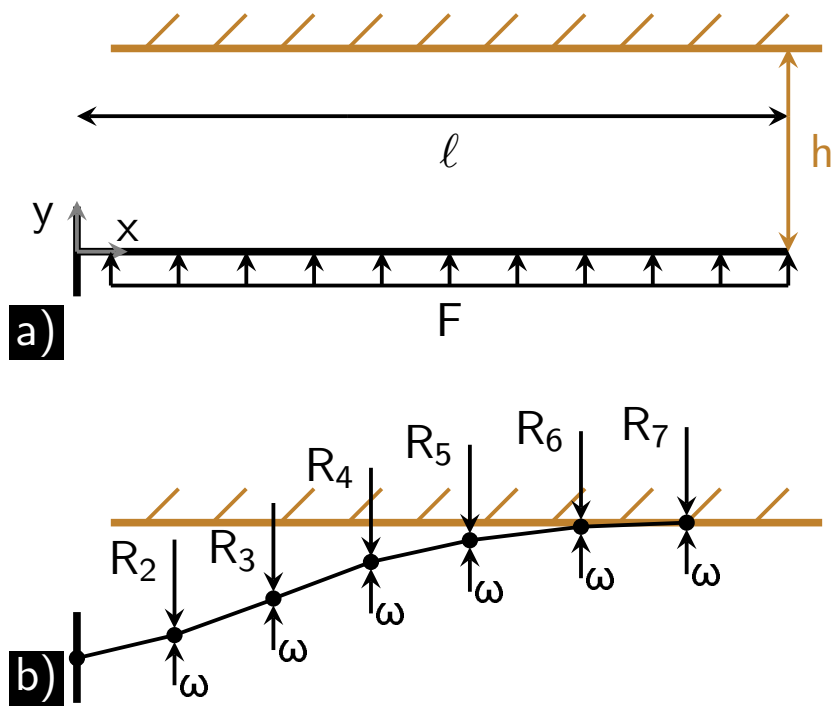

Figure 3.11: a) Continuous cantilever beam of length ℓ separated from a constraining environment by distance h and subject to a uniformly distributed load of F. b) Discretized cantilever beam subject to uniformly distributed load, where the reaction force between the beam and its environment at each node is denoted by R_i and the discretized load is $\omega = \frac{F\ell}{N}$.

A similar process to that described in Section 3.3.3 was followed and the resulting deflection

was compared to the theoretical beam deflection equation expressed as

$$\Delta y = -\frac{Fx^2}{24EI}\left(6\ell^2 - 4\ell x + x^2\right) \tag{3.35}$$

The results are shown for a cantilever beam of length $\ell = 30$ mm, $EI = 32.01$ Nmm^2, and $F = 0.001$ N that was unconstrained (Fig. 3.12a as well as constrained by its environment (Fig. 3.12b and discretized into $N = 140$ links. The reaction force determined using LCP was found to be 7.9 mN and the theoretical reaction force found using beam deflection equations was 7.7 mN, resulting in a 2.60% percent difference.

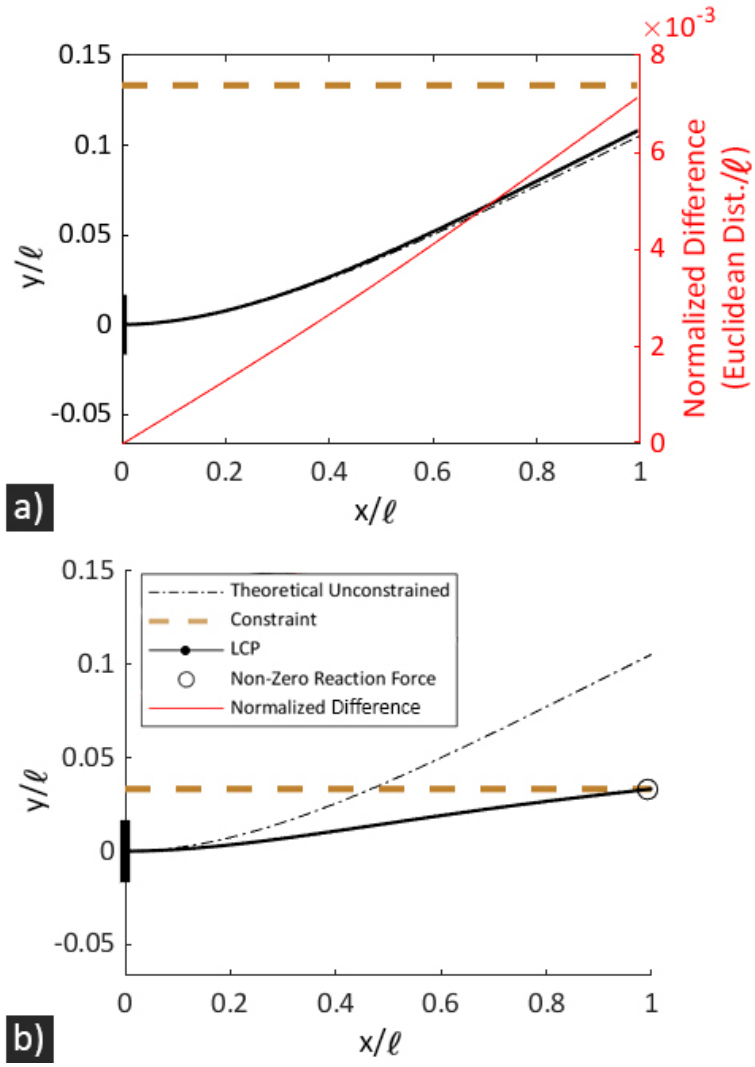

Figure 3.12: a) Comparison between theoretical beam deflection and deflection found using LCP for an unconstrained cantilever beam under a uniformly distributed load. The reported difference is the Euclidean distance between each node in the LCP beam and an equivalent node in the theoretical beam divided by the overall length of the beam. b) Comparison between theoretical beam deflection and LCP deflection for a constrained cantilever beam under uniformly distributed load. The deflection comparison demonstrates that the LCP method maintains the expected environmental constraint.

Simply Supported Beam

Validation of the LCP approach was also performed using a simply supported beam using a similar process outlined in Section 3.3.7 as shown in Fig. 3.13. The process described in Section 3.3.3 was followed and the resulting deflection was compared to the theoretical beam deflection equation expressed as

$$\Delta y = -\frac{Fx^2}{24EI}\left(\ell^3 - 2\ell x^2 + x^3\right) \tag{3.36}$$

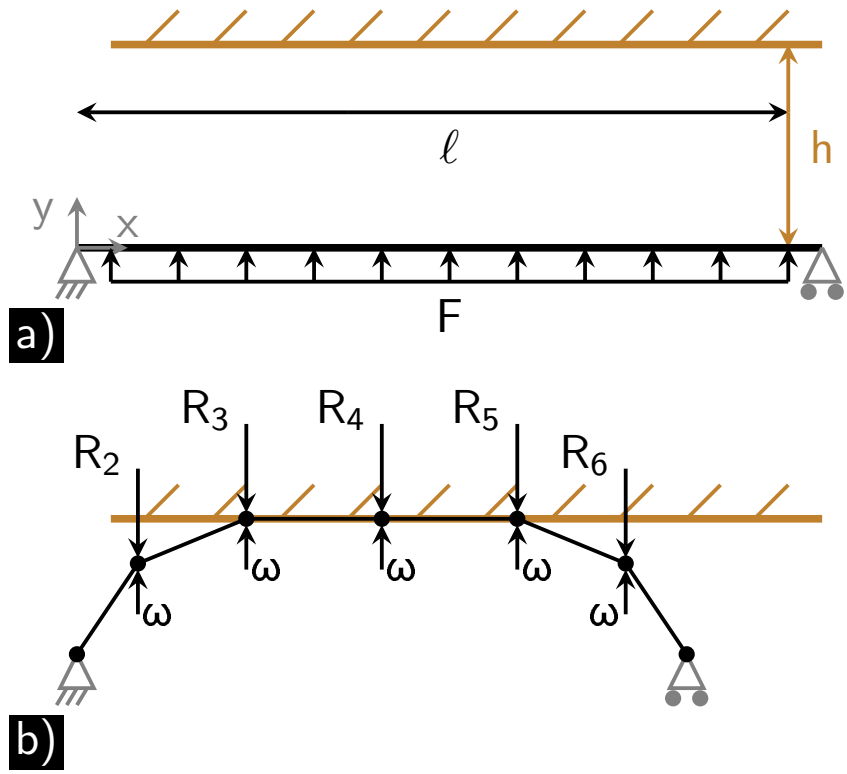

Figure 3.13: a) Continuous simply supported beam of length ℓ separated from a constraining environment by distance h and subject to a uniformly distributed load of F. b) Discretized simply supported beam subject to uniformly distributed load, where the reaction force between the beam and its environment at each node is denoted by R_i and the discretized load is $\omega = \frac{F\ell}{N-1}$.

The results are shown for a simply supported beam of length $\ell = 30$ mm, $EI = 32.01$ Nmm^2, and $F = 0.005$ N that was unconstrained (Fig. 3.14a as well as constrained by its environment (Fig. 3.14b and discretized into $N = 140$ links. The reaction force determined using LCP was

found to be 33.7 mN and the theoretical reaction force found using beam deflection equations was 33.4 mN, resulting in a 0.90% percent difference.

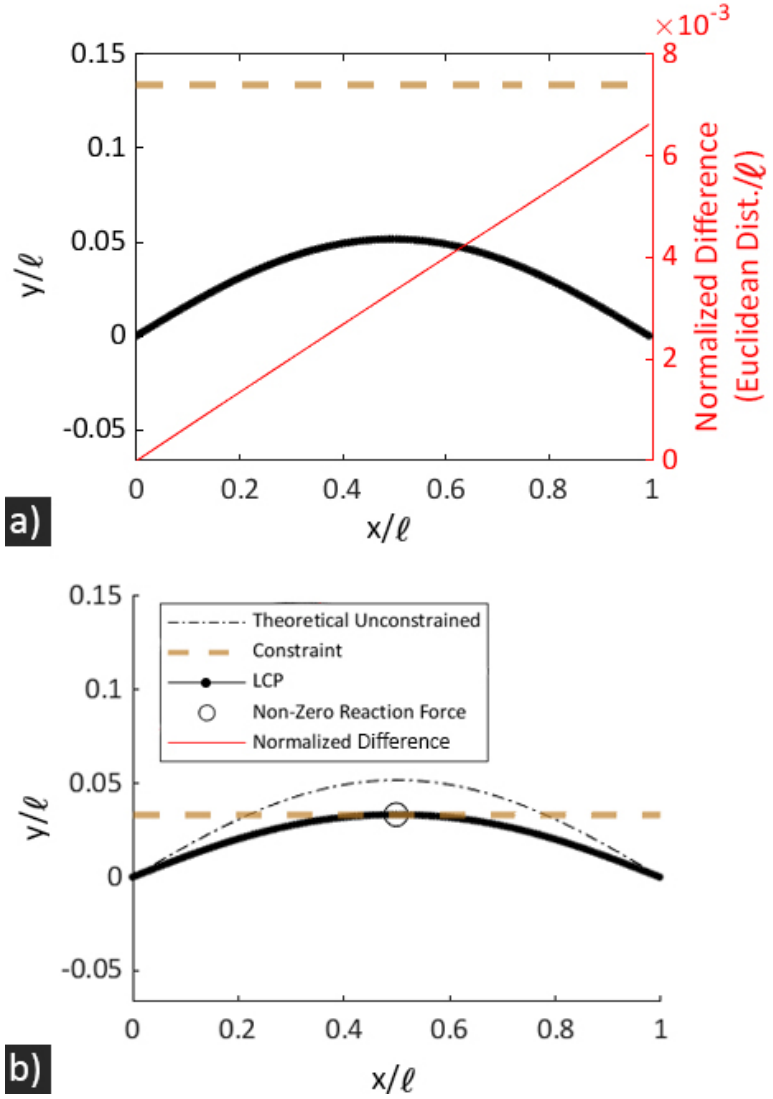

Figure 3.14: a) Comparison between theoretical beam deflection and deflection found through LCP for an unconstrained simply supported beam under a uniformly distributed load. The reported difference is the Euclidean distance between each node in the LCP beam and an equivalent node in the theoretical beam divided by the overall length of the beam. b) Comparison between theoretical beam deflection and LCP deflection for a constrained simply supported beam under uniformly distributed load. The deflection comparison demonstrates that the LCP method maintains the expected environmental constraint.

Observations: Validation of Linear Complementarity Approach

The comparison between the proposed LCP formulation and the classic beam deflection equations showed that the LCP model was able to predict interaction forces with less than 3% difference to the linear beam theory solution and a normalized difference in deflection of less than 8×10^{-3}. The results showed that the normalized difference in deflection (i.e. Euclidean distance between the LCP and theoretical models scaled by beam length) increased linearly over the length of the beam. A portion of this difference could be attributed to the limitations of the theoretical beam deflections as being valid only for deflections of less than 10% of the overall beam length. Another possible explanation is that small differences in the orientation of the links relative to one another build up over the length of the beam.

The results also demonstrated that the LCP model maintains the expected constraint. That is, the constrained beam deflection in the y-direction never exceeds the limitation imposed by the constraint. Overall, the cantilever and simply supported beam comparison between commonly used theoretical equations and the proposed LCP formulation sufficiently confirmed that the LCP model behaves as expected.

3.3.8 Comparison of Two Contact Model Approaches

With the confirmation of the LCP formulation, an alternative approach to modeling the contact between an actuator and a rigid constraint is briefly discussed, acknowledging that an iterative LCP approach is not the only method to solve a nonlinear contact problem. The constrained contact problem was formulated as a system of nonlinear equations to compare to the LCP approach. The nonlinear system of equations was solved using a gradient descent optimization approach, which solves a problem specified by $F(\mathbf{x}) = \mathbf{0}$ for the vector $\mathbf{x}$.

Single-Point Approximation with Nonlinear System of Equations

The gradient descent optimization of a nonlinear system of equations approach was closely aligned with the LCP formulation developed in Section 3.3.3, but had one fundamental difference. Instead of solving for a vector of reaction forces as in the LCP formulation, only the reaction force at the actuator's mid-span was found to minimize computational complexity. This is analogous to using a single "haptic interaction point" to model more complex haptic interactions, as shown by [156]. It was specified that the deflection of the mid-span node in

the y-direction must be equal to the environmental constraint (Fig. 3.15). If the actuator was discretized into an odd number of links, reaction forces developed at the two nodes on either side of the actuator's mid-span and their sum was the total reaction force.

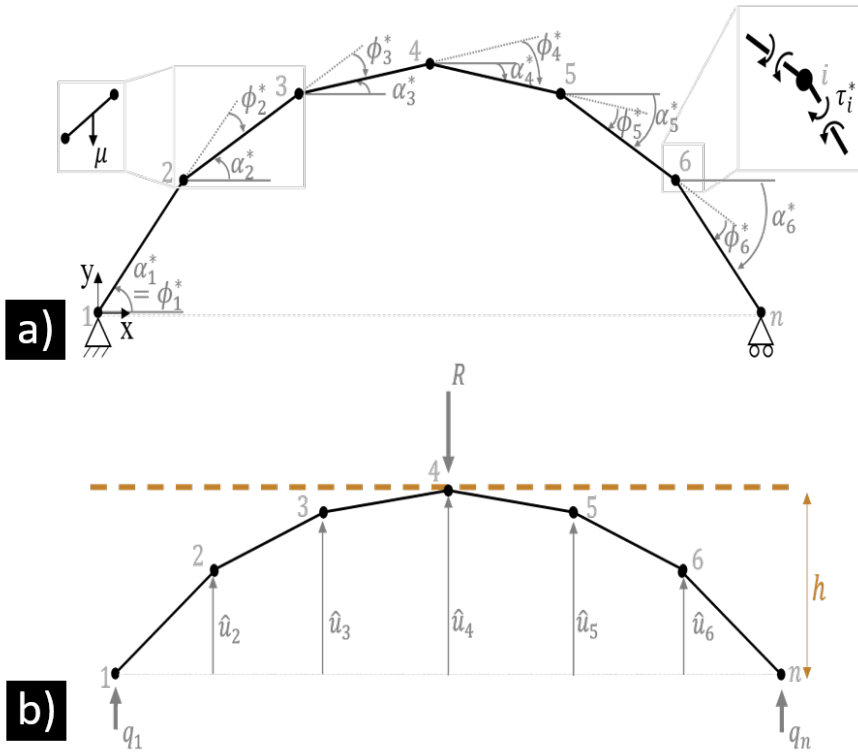

Figure 3.15: a) Unconstrained actuator. b) Constrained actuator used for nonlinear gradient descent approach, where a reaction force is only modeled at the mid-span node.

This requirement was enforced with the addition of two constraining equations. The first of which was an equation specifying that the sum of all joint angles, $\phi_{1:N}$, must be zero. This forced both end nodes to lie along $y = 0$.

$$a \sum_{i=1}^{N} \sin\left(\sum_{j=1}^{i} \hat{\phi}_j\right) = 0 \tag{3.37}$$

The second constraining equation specified that the deflection of the mid-span node must be equal to the constraint height.

$$a \sum_{i=1}^{\text{floor}(\frac{N}{2})} \sin\left(\sum_{j=1}^{i} \hat{\phi}_j\right) - h = 0 \tag{3.38}$$

Description	Number of Equations	
	Nonlinear	LCP (Relevant Eqs.)
Support reaction forces (q_1, q_n)	2	2 (4.33 & 3.8)
Torques (summing external moments)	N-1	1 (4.41)
Torques (constitutive)	N-1	1 (4.53)
Relation between $\hat{\phi}$ and $\hat{\alpha}$	N	1 (4.54)
Constraining equations	2	N/A
Total	**3N+2**	**5**

Table 3.1: Relationship between nonlinear gradient descent and LCP formulations.

Actual Computation Time Normalized to 24.7 ms	Bend Angle (degrees)							
	40	60	80	100	120	140	160	180
Nonlinear	1796.96	1723.37	2007.18	2014.69	11506.69	15527.64	19608.82	22847.96
LCP	1	1.52	1.63	1.60	2.13	2.14	2.07	3.31

Table 3.2: Comparison of the normalized, actual computation time for the nonlinear system and LCP approaches for $N = 140$ links and a constraint height of $h = 1$ mm. The computation was normalized against the shortest computation time of 24.7 ms (LCP, bend angle $\theta = 40°$) running on an Intel Core i7-9700K processor. Only bend angles from 40° to 180° were evaluated because bend angles less than 40° were not in contact with the constraint.

In total, the solution required solving $3N + 2$ equation simultaneously (Table 3.1). The computation times required for both the nonlinear gradient descent and LCP approaches were compared in Table 3.2.

A comparison of the percent difference in total reaction force vs. bend angle for the LCP and nonlinear system of equations approach is shown in Fig. 3.16.

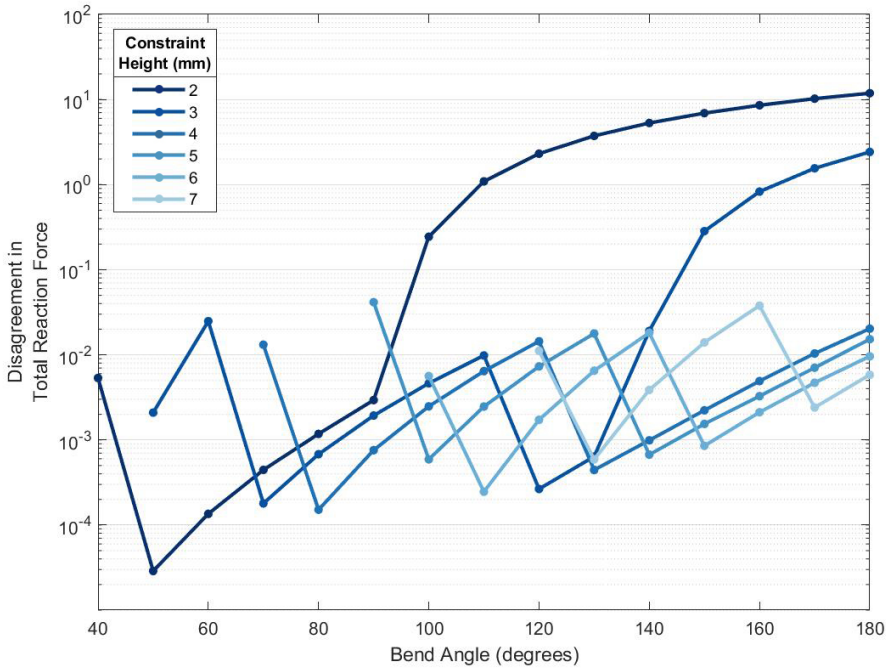

Figure 3.16: Disagreement in the total reaction force for LCP (R_{LCP}) and nonlinear gradient descent (R_{NL}) for $\ell = 30$ mm, $EI = 32.01$ Nmm^2, and $N = 140$ links. The disagreement was determined by $\frac{|R_{LCP} - R_{NL}|}{\frac{R_{LCP} + R_{NL}}{2}} \times 100$.

A comparison of the actuator shapes generated for the two approaches is shown in Fig. 3.17.

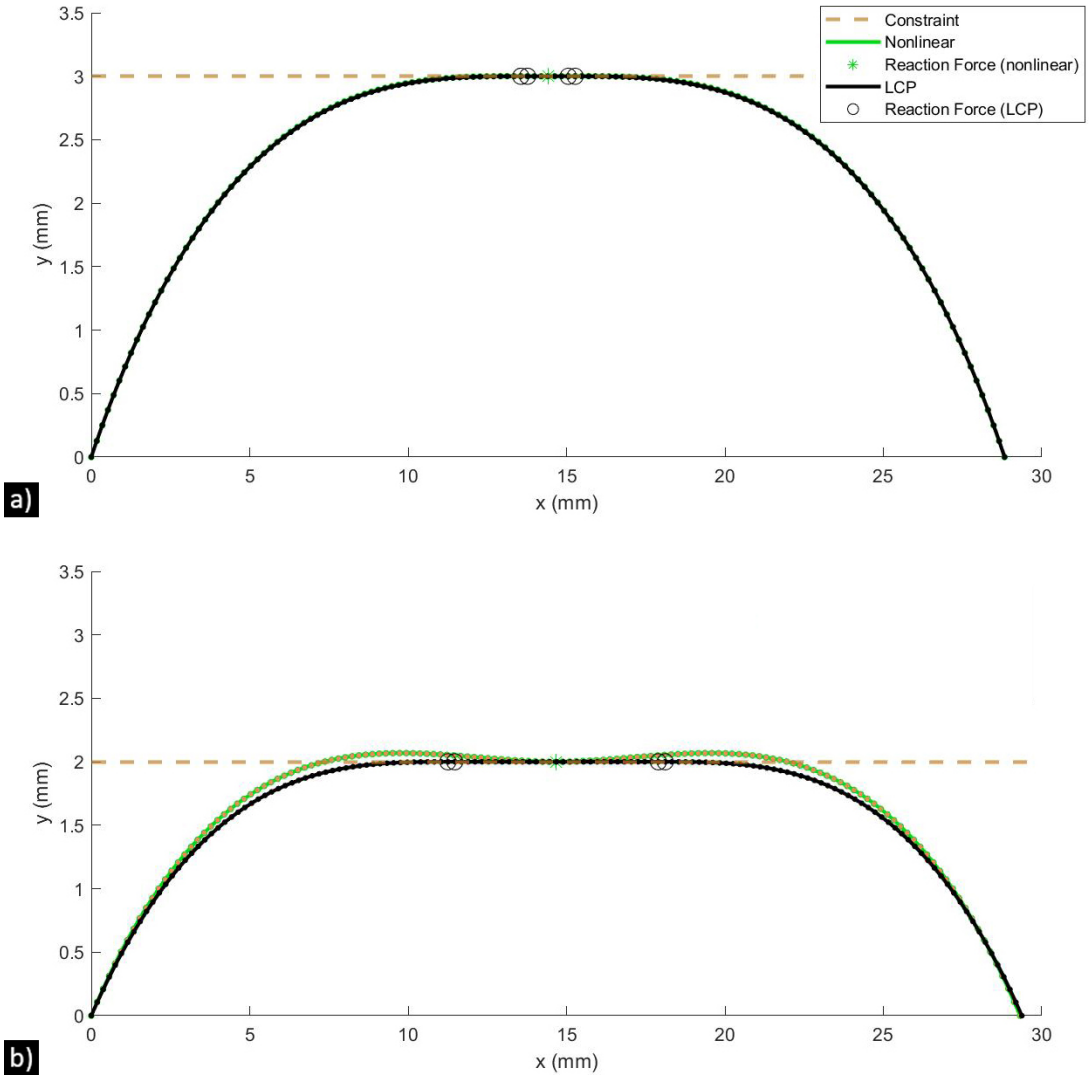

Figure 3.17: a) Comparison of the constrained shape for linear (LCP) and nonlinear gradient descent for an actuator length $\ell = 30$ mm, bending stiffness $EI = 32.01$ Nmm^2, $N = 140$ links, and a bend angle $\theta = 150°$ where: a) $h = 3$ mm, b) $h = 1$ mm.

Observations: Comparison of Two Contact Model Approaches

With regard to computation time, Tables 3.1 and 3.2 show that the large number of equations being optimized in the nonlinear gradient descent approach caused an increase in computation time greater than three orders of magnitude. The benefit of the LCP approach was that a

nonlinear problem was solved using an iterative, linear formulation which played a significant role in decreasing the computation time of the contact model.

The results also showed that the shapes and reaction forces found using the two models are closely aligned, with the disagreement in total reaction force consistently below 0.1% for constraint heights of 4 mm and above. The largest percent differences in reaction force appeared when the constraint height was 3 mm and below. This difference was likely attributed to the noticeable difference in the constrained actuator shape for small constraint heights, as shown in Figure 3.17.

Similar to the force comparison, the two methods were closely aligned with regard to actuator shape for constraint heights above 3 mm (Fig. 3.17a). However, the performance of the nonlinear gradient descent approach broke down when the constraint height was below 3 mm. Fig. 3.17b shows that the actuator shape was not fully constrained within the environment and bowed out on either side of the mid-span node. Conversely, the LCP approach was fully constrained and develops reaction forces in regions on either end of the contact area.

The comparison showed that LCP appears superior in terms of both accuracy and computation time, particularly in situations where the height of the constrained shape is much larger than the height of the environmental constraint (i.e. large bend angle, low constraint height). The LCP successfully modeled actuators constrained to low constraint heights of less than 10% of the actuator length, provided more information about the distribution of reaction forces, and was significantly more computationally efficient because it solves a linear problem iteratively to find a nonlinear solution rather than optimizing $3N + 2$ equations.

3.4 Experiments

3.4.1 Actuator Construction

The actuators used for experimentation in this chapter were Fiber Reinforced Elastomeric Enclosures (FREEs) manufactured using the steps shown in Fig. 3.18.

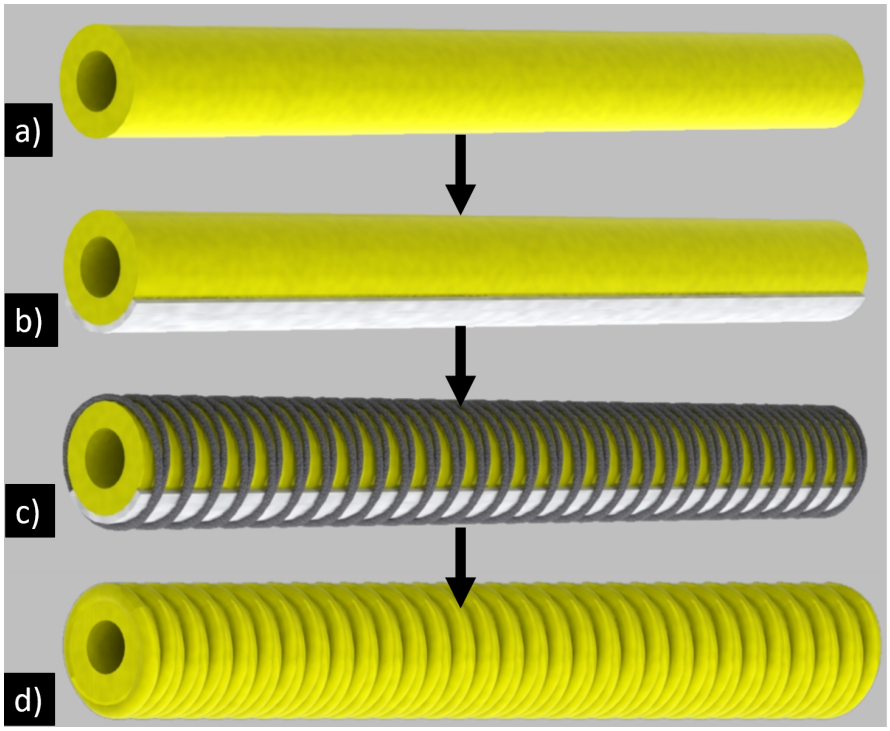

Figure 3.18: Actuator state throughout the manufacturing process used for experimentation. a) Polyurethane base tube (ID = 1.59 mm, OD = 2.80 mm) created from custom mold. b) Base tube with the strain-limiting layer (3M Durapore Tape) placed along the bottom to create mechanically-programmable bending generating an eigenstrain. c) Actuator wrapped with inextensible fibers (30 wt. cotton thread) using a custom CNC lathe. d) Actuator dipped with a final, thin coat of polyurethane to secure the fibers in place.

The base tube shown in Fig. 3.18a was created by injecting liquid, two-part polyurethane (Polytek 74-20) into the custom fixture and mold shown in Fig. 3.19. The outer diameter of the base tube was dictated by the inner diameter of the borosilicate glass tube placed in the mold. The inner diameter of the base tube was determined by the diameter of the tensioned, stainless steel rod running through the center of the glass tube. The custom fixture and mold enabled the manufacturing of base tubes with selectable material properties and geometries.

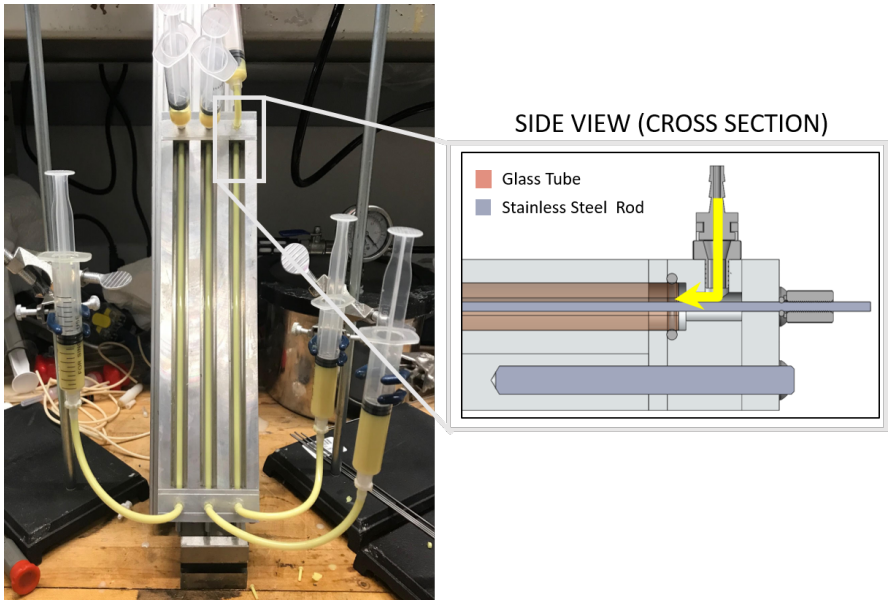

Figure 3.19: Custom fixture and mold used to create polyurethane base tubes with tunable material properties. The liquid polyurethane was injected into the space between a tensioned, stainless steel rod and the inner diameter of a borosilicate glass tube.

Once the base tubes (ID = 1.59 mm, OD = 2.80 mm) were removed from the mold, a strain-limiting layer (3M Durapore tape) was placed in the pattern necessary to generate the desired actuator behavior. The desired behavior to relate the experimental actuator to the theoretical model was a bending actuator, so the strain-limiting layer was placed on one side of the actuator and kept in place using adhesive backing.

The tube and strain-limiting layer were then inserted into a custom CNC lathe (Fig. 2.19) that wrapped an inextensible fiber (30 wt. cotton thread) at known angle along the length of the actuator [1]. To create the bend, a second fiber is wrapped along the actuator at the opposite angle as the first ($\pm 78°$ relative to the longitudinal axis).

The wrapped actuators were then dip-coated in a final, thin layer of polyurethane to prevent the fibers from slipping and make the actuator walls more robust.

3.4.2 Free-Fold Bending Stiffness Estimate

Due to the composite nature of the hydraulic actuators, obtaining an accurate prediction of the elastic modulus, E, of the overall structure is difficult. To avoid this, the elastic modulus

and area moment of inertia were lumped together into a single bending stiffness term, EI. The bending stiffness was found experimentally using a free-fold test approach, first introduced by [157] to determine the bending rigidity and bending length for fabric sheets. The approach was later explored by others, including [158]-[159].

Using the free-fold test, the bending stiffness was estimated by folding a long elastica, in this case the actuator, back on itself and letting it fall into a loop. The bending stiffness was calculated using the height of the folded loop, where

$$EI = 1.342\omega h_{loop}^3 \tag{3.39}$$

where ω denotes the uniform weight per length and h denotes the height of the fold as shown by [159]. It was necessary to use an actuator longer than $4.683\sqrt[3]{\frac{EI}{\omega}}$ as outlined by [160] and [159].

The elastica used for the free-fold test were four high-aspect ratio actuators of lengths 635 mm, 643 mm, 587 mm, and 600 mm and diameters 5.0 mm, 5.5 mm, 5.1 mm, 4.9 mm, respectively. They were manufactured using a process similar to that described in 3.4.1. Each actuator was filled with actuation fluid (water) and measured for weight. The actuators were placed on a flat surface, suspended into an initial pre-release shape, and released to freely form a loop (Fig. 3.20). To prevent out-of-plane deflection of the actuator, the loop was supported on either side by acrylic plates and lightly coated with vegetable oil to minimize friction.

Two of the four actuators were pressurized in increments of 17.24 kPa (2.5 psi) and their weights and lengths measured at each increment until they reached a maximum bursting pressure. This was done to accurately account for any changes in bending stiffness caused by pressurizing the actuator. Each free-fold test was repeated three times at each pressure increment.

Using equation 3.39, an average experimental bending stiffness of $EI = 32.01$ Nmm^2 and weight per unit length of $\omega = 2.45 \times 10^{-4}$ N/mm was found for the soft actuators.

Figure 3.20: Experimental free-fold test used to estimate the bending stiffness of the actuator.

Observations: Free-Fold Bending Stiffness Estimate

The free-fold test provided a simple and efficient method for predicting the bending stiffness of composite actuators that has not yet been utilized in soft robotics. The variation in measured loop height, and thus bending stiffness, demonstrated that manufacturing variability plays a role in material properties of soft actuators. Because of the thick-walled nature of the actuators proposed in this work (ID = 1.59 mm, OD = 2.80 mm and OD $\simeq$ 5 mm before and after outer dip layer, respectively), pressurizing the actuators and incorporating a strain-limiting layer did not produce a noticeable effect on bending stiffness. Overall, using the free-fold test to estimate bending stiffness proved an effective and simple alternative to using precisely measured material parameters to model composite actuators using complex equations or a finite element model.

3.4.3 Experimental Setup

Custom Test Fixture

The reaction forces and constricted shape of the soft actuator were tested using a custom test fixture shown in Fig. 3.21. The fixture consisted of a soft actuator (Fig. 3.21b D) attached to barbed fitting (Fig. 3.21a inset) and a barbed cap (Fig. 3.21b G) on either end. The barbed fitting allowed a pressure source to be connected to the actuator. The barbed fittings were pronged to allow them to be press fit into flanged ball bearings (McMaster, 57155K201) within the bearing holders (Fig. 3.21b F).

The bearing holders were attached to carriages on a low-friction, low-profile linear rail (Fig. 3.21b D, PBC Linear, LPM17-0200-1). The carriage near the input end was fixed in place (Fig. 3.21b B) while the carriage near the cap was allowed to slide freely along the rail (Fig. 3.21b E) to properly simulate the simply supported boundary conditions in the model. This also enabled the change in span of the actuator as it was pressurized and constricted. The linear rail could be moved vertically along slots to change the height of the environmental constraint (Fig. 3.21b H) while the position of the bearing holder was adjusted accordingly to ensure the bearing lied along the midline between the linear guide rail and the load cell attachment (Fig. 3.21b A).

A straight bar load cell (Fig. 3.21b J, SparkFun, TAL221, 500 g) was rigidly attached to the load cell attachment using spacers (Fig. 3.21b I), which allowed any force generated from the soft actuator to be captured. Out-of-plane deflection was prevented using two guidance plates

made from anti-glare acrylic (Fig. 3.21c K).

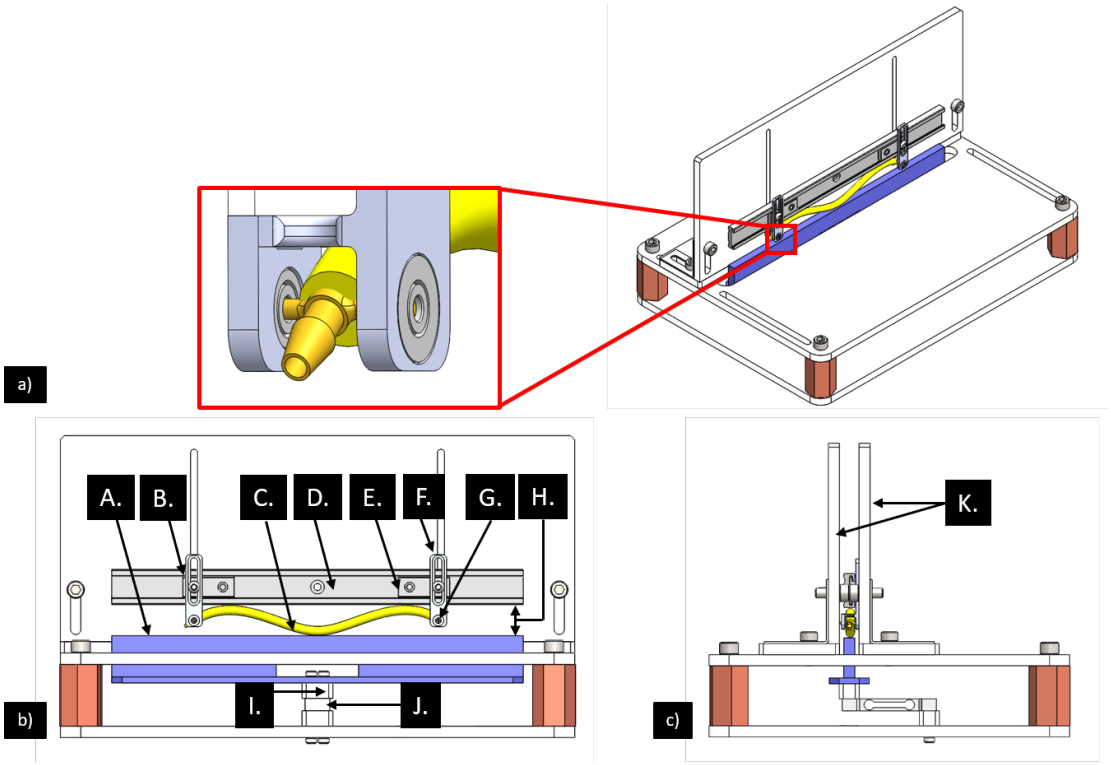

Figure 3.21: a) Experimental setup for testing the reaction forces and centerline shapes generated when a pressurized soft actuator was constrained by its environment. Inset: close-up of pin joint used to enforce pinned-pinned end conditions. A barbed fitting was inserted into the actuator to allow pressurization, while two prongs on the fitting were press fit in low-friction bearings to allow the fitting to rotate freely. b) Front view of setup where: A. load cell attachment that served as the bottom half of the constraining environment, B. carriage that was fixed in place to prevent linear translation of the left pin joint, C. soft actuator, D. linear guide rail that served as the top half of the constraining environment, E. low-friction carriage that was able to translate linearly to allow axial change in length when the actuator was constrained, F. bearing holder with adjustable height to ensure the pin joint sat halfway between the environment walls, G. capped barbed fitting with prongs press fit into the rotational bearing, H. separation between the two plates was set to be equal to double environment height ($2h$), I. load cell spacer, J. load cell c) Side view of experimental setup where: K. guidance plates to prevent out-of-plane deflection.

It is important to note that an experimental actuator comprised of three identical bending sections was used, but the only section of interest for this chapter was the middle bending section that was in contact with the load cell attachment. The reason for using an actuator comprised

of three bending sections rather than one was to minimize the effects that the barbed fittings and input pressure line had on the behavior of the actuator as it was pressurized. The two end bending sections created a symmetric environment for the middle bending section that matched the simply-supported end conditions of the model.

Data Collection

Data were collected on three actuators. Each actuator was connected to the setup shown in Fig. 3.21 and pressurized using a syringe connected to the setup via a pressure line. Each actuator was pressurized from 0 to 172.37 kPa (25 psi) in 17.24 kPa (2.5 psi) increments in four configurations: unconstrained and constraint heights of 4.5 mm, 5.5 mm and 6.5 mm. An image of the actuator was captured at each pressure increment. The pressurization sequence was repeated three times for each actuator for each of the four configurations. Pressurization was done slowly so as to minimize the dynamic phenomena of the actuators.

For the constrained actuators, the constraint heights were determined by changing the separation between the upper and lower constraints shown in Fig. 3.21b H, where the separation was equal to twice the constraint height (e.g. separation was 11 mm for a constraint height of 5.5 mm). Force data were collected at each pressure increment using a calibrated and tared load cell.

Data were collected at 10 Hz using a microcontroller (Teensy 3.5) connected to a pressure transducer (Honeywell TBPDANS030PGUCV) and the load cell, each connected to load cell amplifiers (SparkFun, HX711). The camera used for capturing the images was placed at a fixed distance from the test setup and at the same height as the actuator.

3.4.4 Computer Vision

Once experimental data collection was complete, computer vision was used to determine variables such as the relationship between input pressure and the resulting bend angle of the actuator, length of the bending section, and a quantitative comparison of the similarity between experimental and theoretical centerlines for a given input pressure. Determining the relationship between actuation pressure and bend angle, θ, for each actuator was a critical step to compare the experimental force and centerline shape with the theoretical model. This was because the unconstrained bend angle was used as an input to the constrained actuator model, as described

in Section 3.2.1. Similarly, determining the length of the experimental bending section was a critical input to the model and allowed us to create a better baseline for comparison.

The desired variables were determined using an interactive program (implemented in Python 3.7.8) to analyze the images captured during experimentation. The analysis was broken down into several stages:

Pre-Processing

Image rectification was performed on all images before quantitative analysis to properly account for warping caused by the camera lens (using OpenCV's *undistort*() function) or unlevel images. The image was leveled by comparing the bearing centers on either side of the test stand. The bearing centers were determined using the circle Hough Transform technique as shown in Fig. 3.22. The difference in the coordinates of each of the bearing centers determined the rotation angle to level the image.

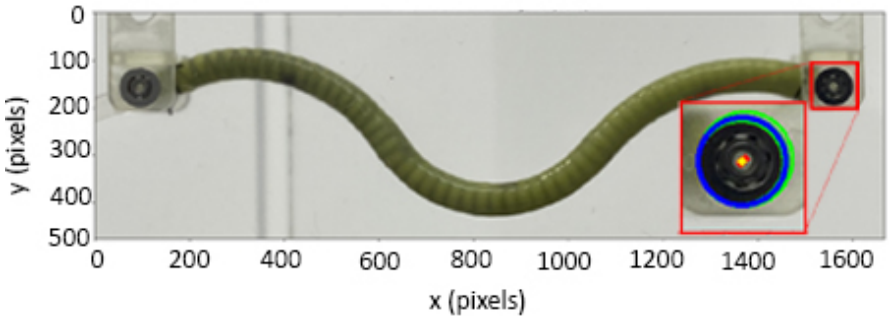

Figure 3.22: Cropped and leveled actuator image. Inset image shows the bearing center detection using Hough Circles.

Coordinate System Setup

Once the image was leveled, a coordinate system was created using the center of the left bearing as the origin. The pixel-to-mm conversion ratio was calculated using an Augmented Reality University of Cordoba (ArUco) tag of known dimensions (25 mm×25 mm) fixed to the test stand ([161], [162]).

Segmentation

Segmentation of the image was performed using HSV color ranging. A preview of the segmentation was displayed to the user and updated as the user manipulated sliders controlling the HSV values. Once a satisfactory segmentation of the image was achieved, the segmented portion of the image was converted to RGB and the background pixels were set to pure black. The segmentation can be seen in Fig. 3.23.

Centerline Detection

Using the segmented image, the actuator centerline was detected using an edge-finding technique. Starting in the upper left pixel in the image, the detection was conducted using the following pseudocode:

```
for column in image do
    for row in column do
        if pixel_current != black and pixel_previous == black then
            TOP EDGE
        else if pixel_current == black and pixel_previous != black then
            BOTTOM EDGE
        else
            CONTINUE SEARCH
        end
    end
end
```

where each previous pixel refers to the pixel above the current pixel.

The actuator's centerline coordinates were determined by calculating the average of the rows of the top and bottom edge pixels for each column in the image. These coordinates were then converted to length units using the pixel-to-mm conversion. Thus, only y-pixel height was used to determine robot edges corresponding to each position or centerline. The detected edges and resulting centerline are shown in Fig. 3.23.

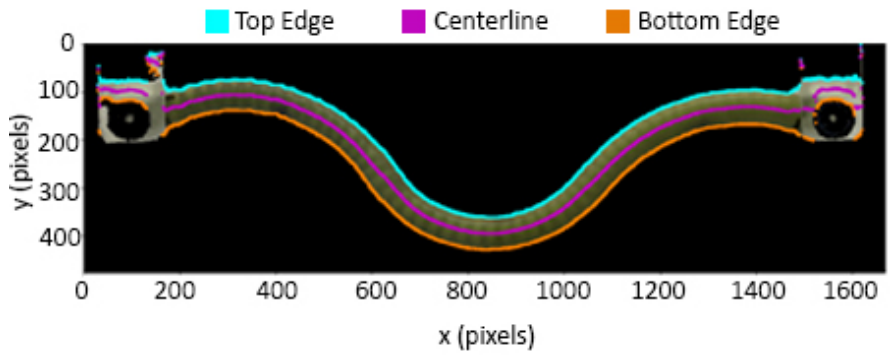

Figure 3.23: Detected centerline after finding the top and bottom edges of the actuator using segmentation and an edge-finding technique.

Critical and Inflection Point Detection

Using the extracted centerline, the start and end of the middle bending section of the experimental actuator were determined by finding the critical points along the entire centerline. The critical points were defined to be the inflection points (where each bending section starts and stops), as well as the minima and maxima of each bending section. To find the critical points, quadratic and linear functions were fit to two windows of points, lengths 200 pixels and 50 pixels, respectively. Changes in the sign of the concavity of the quadratic function identified inflection points while changes in the sign of slope of the linear function identified local minima and maxima. The widths of these windows could be adjusted to appropriately handle any noise in the data caused by "unsmooth" segmentation, thus avoiding erroneous changes in sign of the concavity or slope values.

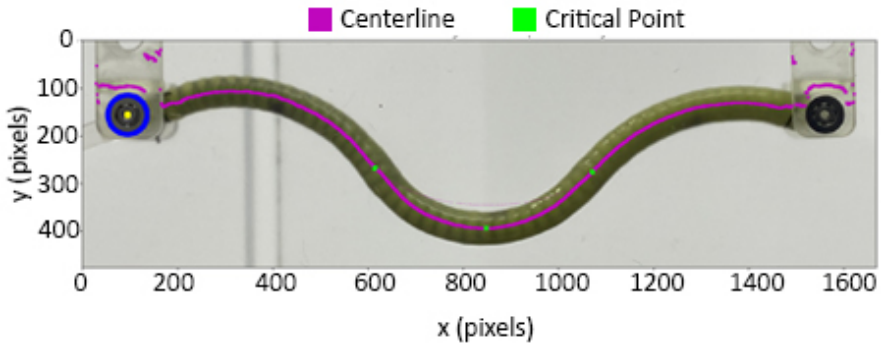

Figure 3.24: Detected centerline, inflection points, and minima for the middle bending section overlaid on the actuator.

Circle Fit

Because the middle bending section of the actuator was the section of interest for comparing the experimental results to the proposed model, the relationship between pressure and the bend angle of the middle section was determined using a least-squares circle fit. The circle fit was performed on the centerline points between the two inflection points and returned the fit circle's center coordinates and radius. Given the respective x- and y-coordinates of the middle section centerline, the algorithm sought a circle with center $(x_c,\ y_c)$ and its radius, r_c, which minimize the residual function (using the method implemented by [163]):

$$\min \sum (r_i - r_c)^2 \tag{3.40}$$

where

$$r_i = \sqrt{(x - x_c)^2 + (y - y_c)^2}$$

Fig. 3.25 shows the resulting circle fit for a illustrative sample centerline.

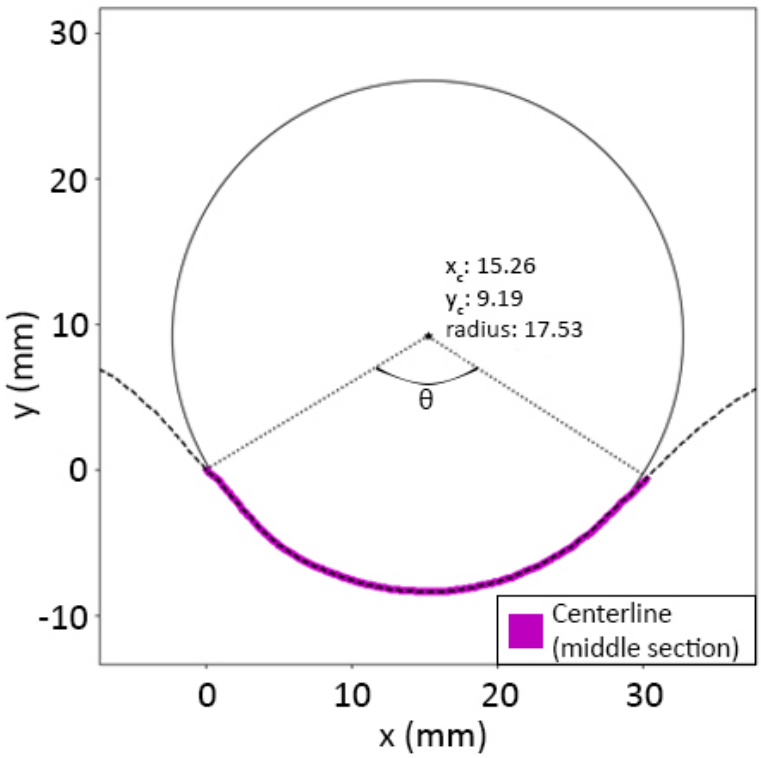

Figure 3.25: A circle fit was performed on the middle bending section of an unconstrained actuator, where the bold, purple points represent the points of the middle bending section determined by the inflection points. The key output of this step is θ which corresponds to the model (Eq. 3.2).

Bend Angle and Arc Length

The bend angle, θ, of the middle section of the actuator was calculated using the center of the circle fit (x_c, y_c), as well as the inflection points, (x_1, y_1) and (x_2, y_2), where:

$$\theta = \arctan \left| \frac{x_{1c} y_{2c} - x_{2c} y_{1c}}{x_{1c} x_{2c} + y_{1c} y_{2c}} \right| \tag{3.41}$$

where

$$x_{1c} = x_1 - x_c$$

$$y_{1c} = y_1 - y_c$$

$$x_{2c} = x_2 - x_c$$

$$y_{2c} = y_2 - y_c$$

The radius of the circle fit, r_c, and the bend angle, θ, were then used to calculate the arc length of the centerline points between the inflection points with

$$\ell = r_c\theta \tag{3.42}$$

Centerline Coordinate Comparison

Quantitative comparison between the constrained experimental and theoretical centerlines was performed using an Iterative Closest Point (ICP) algorithm, as implemented by [164]. The 2-D point clouds used to perform ICP were the constrained experimental centerline found using the computer vision analysis and the corresponding constrained theoretical centerline found using the LCP analysis outlined earlier in the chapter. The constrained theoretical centerline was determined using an input bend angle and length found from the unconstrained circle fit analysis for the experimental actuator. The theoretical centerline was offset by the outer radius of the experimental actuator (1.5 mm) to properly account for actuator thickness.

To facilitate pairwise comparison correspondence, random points were removed from the experimental point cloud until it contained an equal number of points (200) as the theoretical point cloud.

The ICP algorithm then calculated Euclidean distances to the nearest neighbor in the experimental point cloud for every point in the theoretical point cloud. Next, a least-squares best fit transformation was applied to align the experimental point cloud with the modeled point cloud.

The best-fit homogeneous transformation matrix $\mathbf{T}$ comprised of an optimal rotation matrix, $\mathbf{R}$, found using singular value decomposition (SVD), as well as the translation between the

experimental and theoretical point cloud centroids, $\mathbf{t}$, given as:

$$\mathbf{T} = \begin{bmatrix} R_{11} & R_{12} & t_1 \\ R_{21} & R_{22} & t_2 \\ 0 & 0 & 1 \end{bmatrix} \tag{3.43}$$

The transformation matrix was then applied to the experimental point cloud. The process of calculating Euclidean distances and best-fit transformations was repeated until the change between iterations in average distance between neighbors fell below a threshold of 1×10^{-7} or a maximum of 2000 iterations was reached.

3.5 Results

3.5.1 Baseline Computer Vision Measurement Error

The performance of the computer vision program was characterized using ground truth shapes. Ground truth actuators with known bending section arc lengths (30 mm), bend angles (10°-180°), and critical points were 3D printed (Formlabs Form 3). Each print was attached to the experimental setup and the images were analyzed using the computer vision program. The results are shown in Fig. 3.26.

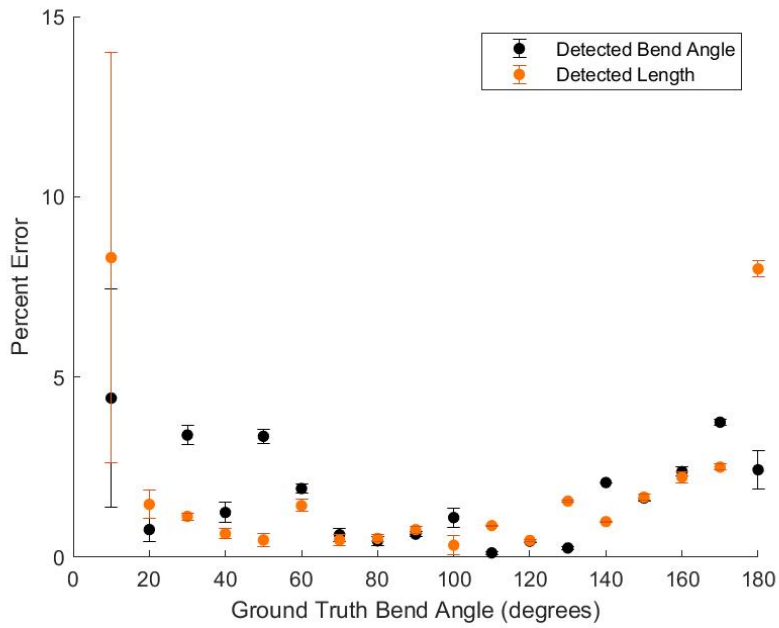

Figure 3.26: Average percent error in the detected bend angle and arc length of the middle bending section of each of the ground truth 3D prints. The percent error was calculated by: $\% \, error = \frac{|truth - detected|}{truth} \times 100$. N = 3 samples for each data point. The error bars indicate the standard deviation of the measurements for each data point.

Observations: Baseline Computer Vision Measurement Error

The results show that the computer vision algorithm measured actuators with an average baseline measurement error of 1.72% and 1.88% for bend angle and bending section length, respectively. The baseline measurement error was relatively constant for both bend angle and length, although performance appeared best when detecting bend angles near the middle of the range. For the proposed application, the baseline measurement error corresponds to fractions of a degree and sub-millimeter accuracy for bend angle and length, respectively.

3.5.2 How Unconstrained Bend Angle Changes with Pressure

The relationship between unconstrained bend angle vs. pressure was critical to compare experimental and theoretical centerlines and interaction forces because unconstrained bend angle was used as an input to the model. The average experimental relationship between the unconstrained

bend angle and input pressure for each of the three actuators is shown in Fig. 3.27. A simple linear model was adopted to approximate the empirical relationship between each unconstrained bend angle, θ (degrees), and pressure, P (kPa), for each actuator, described by:

$$\theta_1 = 0.81P + 9.78 \tag{3.44}$$

$$\theta_2 = 0.52P + 7.84 \tag{3.45}$$

$$\theta_3 = 0.65P + 12.1 \tag{3.46}$$

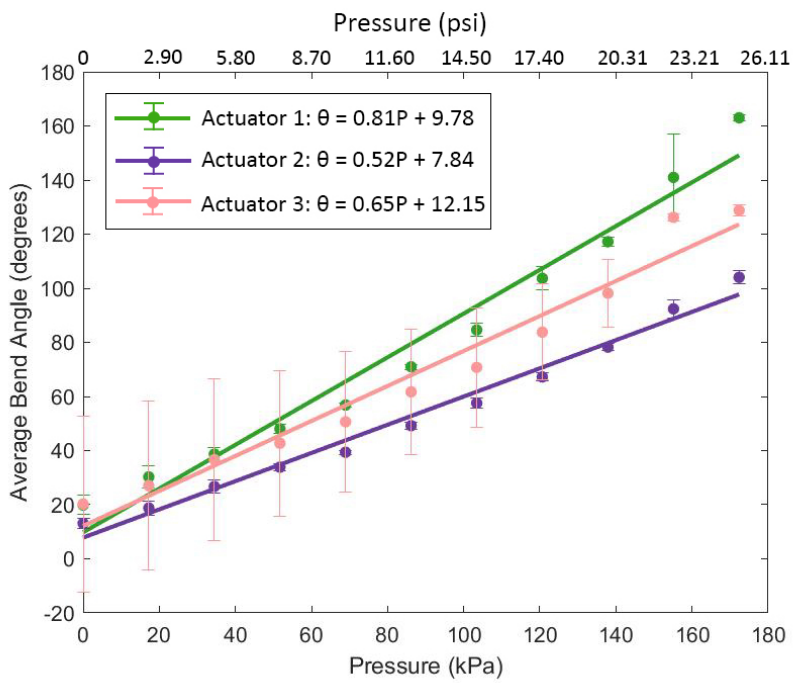

Figure 3.27: The average detected bend angle appears to increase linearly with pressure for the three experimental actuators. N = 3 samples for each data point. The error bars indicate the standard deviation of the measurements for each data point.

Observations: How Unconstrained Bend Angle Changes with Pressure

The relationship between the bend angle of the actuator and pressure appeared to be approximately linear. The difference in slope and y-intercept for each of these actuators was likely caused by variations introduced during the manufacturing process described in Section 3.4.1.

As such, the experimental results were evaluated based on the actuator-specific bend angle to pressure relationship outlined in Figure 3.27.

3.5.3 Determination of Pressure Range for Comparison

To ensure the middle bending section of the experimental actuator matched the conditions of the model (i.e. symmetry in inflection points created from the first and third bending sections) and that the actuator was in contact with the environmental constraint, only a select range of pressures for each constraint height was analyzed.

The pressure range was determined by plotting the average force vs. pressure for each constraint height and identifying the knee point in the force behavior (Fig. 3.28). An angle-based knee detection for discrete data was used as introduced by [165] and [166]. The approach searched each consecutive triple of points in the data set $((x_1, y_1),\ (x_2, y_2), \text{and}\ (x_3, y_3))$ and found the local minima of successive differences:

$$y_1 + y_3 - 2y_2 > threshold \tag{3.47}$$

A threshold of 1.0 was used to identify the knee point in each data set. The knee points indicated pressure ranges of 68.95-172.37 kPa (10-25 psi), 103.42-172.37 kPa (15-25 psi), and 120.66-172.37 kPa (17.5-25 psi) for constraint 4.5 mm, 5.5 mm, and 6.5 mm, respectively.

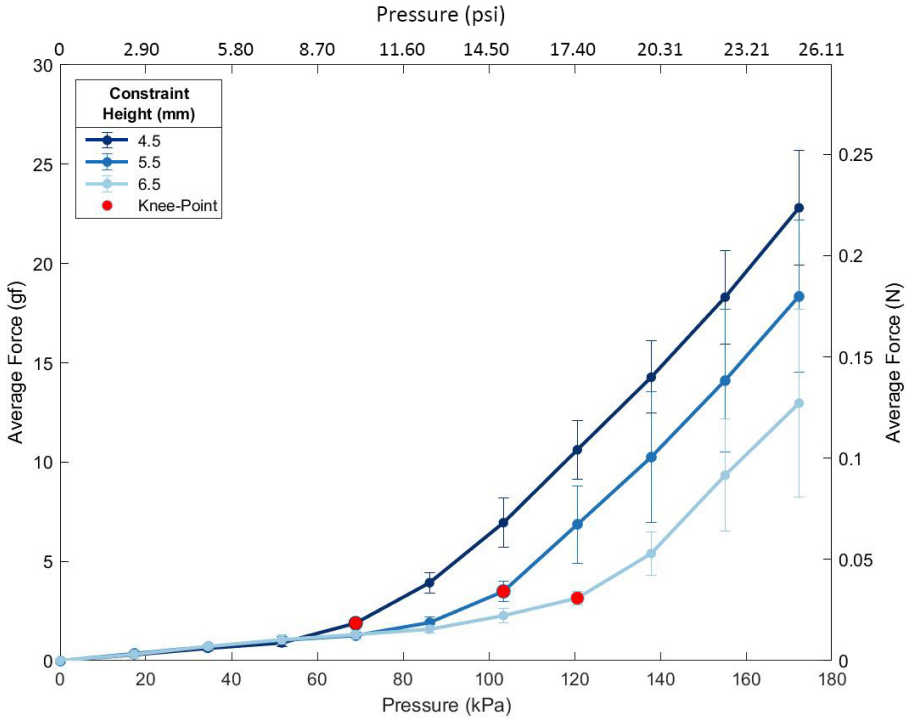

Figure 3.28: The average force behavior displays a knee point at a specific pressure that is different for each actuator, followed by a steeper increase in force as pressure is increased. The knee points were identified using angle-based knee detection. N = 9 samples for each data point. The error bars indicate the standard deviation of the measurements for each data point.

Observations: Determination of Pressure Range for Comparison

The appearance of knee points in the data was most likely attributed to all three bending segments of the actuator not being fully in contact with the environmental constraints. This would explain why the knee points appear at increasing values of pressure as the constraint height is increased.

As was observed in the theoretical shape analysis as a function of bend angle, the detection of forces at low pressures (i.e. below the knee point) was not anticipated. The non-zero forces recorded for pressures below the knee point were likely caused by manufacturing imperfections or gravity causing the actuator to contact the load cell. Although gravity was modeled in the formulation of the problem, only the middle bending section of the overall experimental actuator comprised of three sections was modeled. Because of this, the start and end points of the middle

segment may have deviated from the conditions of the model. As such, the experimental results were only evaluated for pressures above the knee point for each constraint height to compare conditions that most closely aligned with the conditions presented in the LCP model.

3.5.4 Comparison of Constrained Centerline Shapes

ICP analysis was performed on each image for the pressure ranges determined in Section 3.5.3. An illustrative sample for the constrained actuators is shown in Fig. 3.29. The illustrative sample was chosen to be the median of all data points (all constraint heights and corresponding pressure ranges) for Actuator 1, with a 5.5 mm constraint height and pressure of 137.9 kPa (20 psi). The results of the ICP analysis are shown in Fig. 3.30 for both the illustrative sample and all 144 samples.

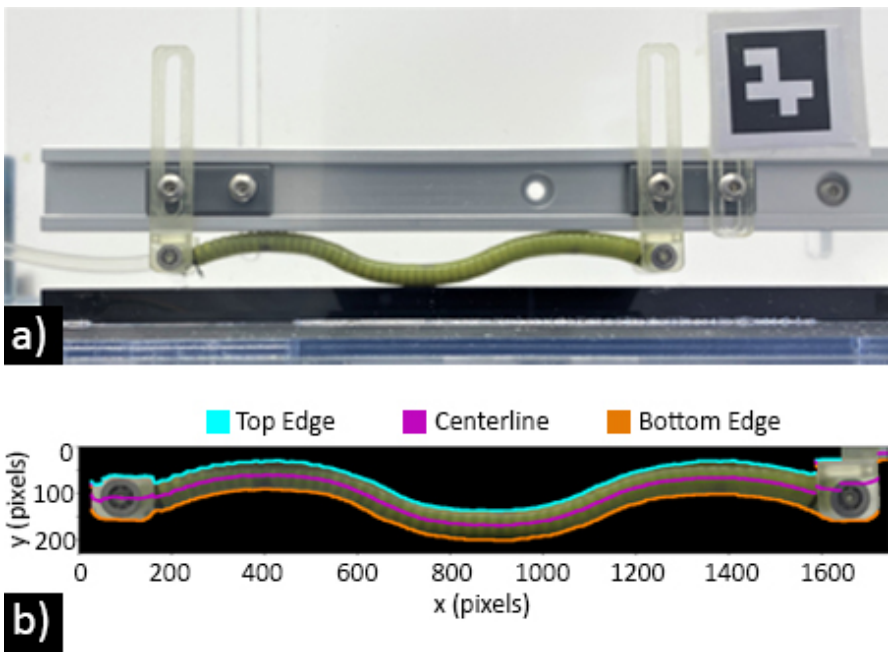

Figure 3.29: a) Illustrative sample of an unsegmented, constrained actuator (Actuator 1, 5.5 mm constraint height, 137.9 kPa (20 psi) pressure. b) Detected centerline after finding the top and bottom edges of the actuator using segmentation and an edge-finding technique.

The percent difference for the ICP point pair distances was determined by

$$\% \text{ diff} = \left(\frac{\text{Point pair distance}}{\text{Actuator span in } x\text{-direction}} \right) \times 100 \tag{3.48}$$

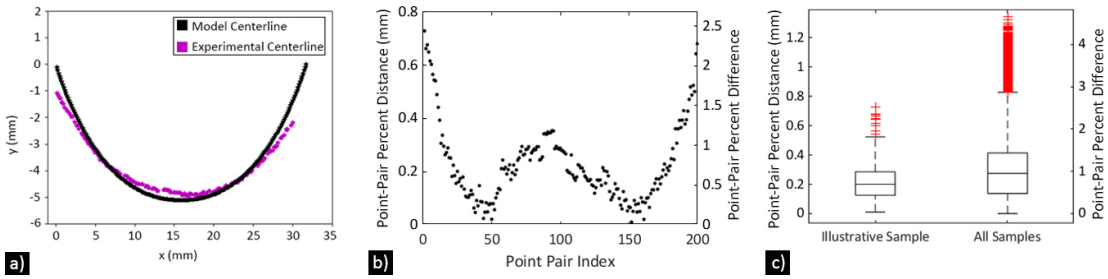

Figure 3.30: a) Illustrative sample showing the centerline comparison between model and experiment after alignment from ICP. b) Point pair distances and percent difference for the illustrative sample. The point pair index represents the index of the point in the point cloud, where zero corresponds to the left-most point in each centerline and 200 corresponds to the right-most point. c) Point pair distance and point pair percent difference statistics for both the illustrative sample (N = 1 sample) and all samples collected (N = 144 samples).

Observations: Comparison of Constrained Centerline Shapes

The results show that after ICP, the comparison between the theoretical and experimental centerline produced a mean point pair distance and percent difference in point pair distance between the model and experiment for all 144 samples of 0.31 mm and 1.06%, respectively. The outliers appeared to be caused by the difference in length between the model and experimental centerlines, where the model centerline was consistently longer than the detected experimental centerline. This can be seen in Figure 3.30b, where the point-pair percent difference was largest for point pair indices corresponding to the ends of the actuator.

3.5.5 Comparison of Interaction Forces

The interaction force for each experimental data sample was compared to the theoretical interaction force from the model. The model used the average experimental bending stiffness of $EI = 32.01$ Nmm^2 and weight per unit length of $\omega = 2.45 \times 10^{-4}$ N/mm found from the free-fold tests. To properly show the force range created by variations in material properties during the manufacturing process, the model was also analyzed using both the overall minimum and maximum bending stiffness and weight per unit length values found from the free-fold tests. The minimum values were of $EI = 15.18$ Nmm^2 and $\omega = 2.37 \times 10^{-4}$ N/mm, respectively, and the maximum values were $EI = 41.80$ Nmm^2 and $\omega = 2.47 \times 10^{-4}$ N/mm, respectively.

The model also used the average bending section length, ℓ, and the average relationship

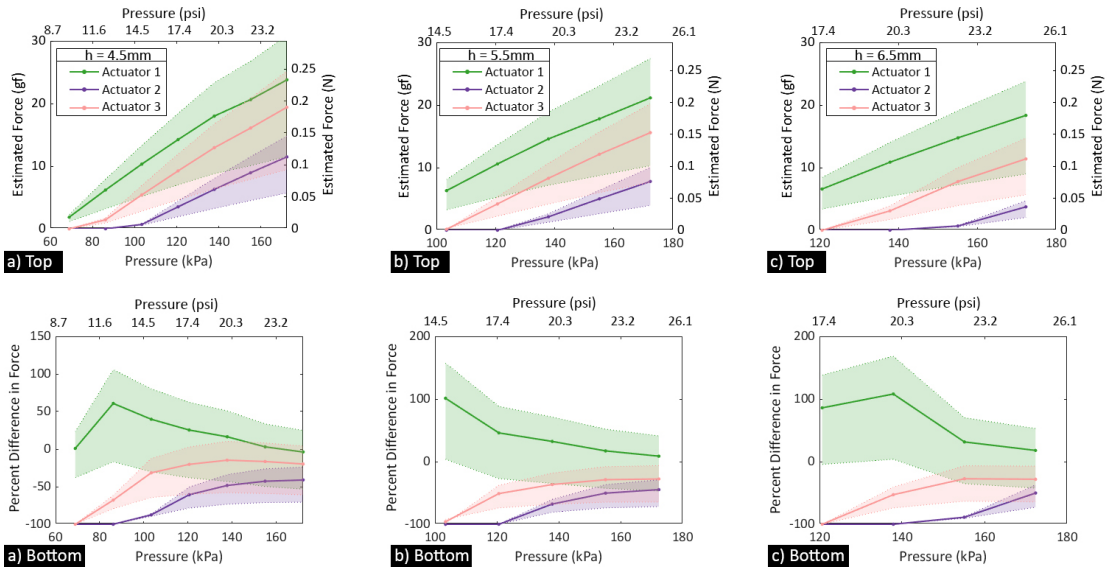

Figure 3.31: Data for three different constraint heights of: a) 4.5 mm, b) 5.5 mm, and c) 6.5 mm. **Top:** The estimated force found from the model for each of the three actuators displayed a consistent increase as pressure increased. **Bottom:** Percent difference in force between the experiment and theoretical model was calculated over a range of pressures for the three constraint heights. The percent difference was calculated by: $\% \, diff = \frac{theoretical - experimental}{theoretical} \times 100$. The shaded region displays the range of possible values bounded by the minimum/maximum bending stiffness, EI, and weight per unit length, ω, that were determined experimentally. The line within each region represents the results using the average experimental bending stiffness of $EI = 32.01$ Nmm^2 and weight per unit length of $\omega = 2.45 \times 10^{-4}$ N/mm. The dots represent where data were collected at each point.

between unconstrained bend angle, θ, and input pressure found from the computer vision algorithm to ensure an accurate comparison between experiment and theoretical models. The results are shown in Fig. 3.31.

Observations: Comparison of Interaction Forces

The results show that the difference in force between the experimental and theoretical actuators trended toward zero as pressure was increased, where the average magnitude of the difference was 45.34% and 20.98% for pressures at the low and high ends of the tested range, respectively. One possible reason for this is that the interaction forces between the actuator and its environment were minimal at low pressures (i.e. on the order of 1 gf), as shown in the top plots of Fig. 3.31, so the percent difference was large at low pressures. Another potential cause of the trend is that

the experimental actuators were not perfectly manufactured, nor perfectly symmetric, so each of the three bending sections in the experimental actuator were not all in contact for low pressures. This asymmetry may have cause the experimental "support conditions" to stray from the simply supported conditions of the model and prevented the end points from lying perfectly along the midline between the environmental constraints. As pressure increased and each bending section made contact with the environmental constraint, the experimental actuator became more symmetric and better aligned with the model assumptions for the support conditions.

These results also highlight the non-trivial effect of small changes in material properties on actuator behavior. Although manufactured using the same process and materials, the three actuators varied slightly from each other in structure. This caused differing relationships between both bend angle and force as functions of pressure. Finally, since the theoretical model is highly dependent on the bending stiffness, an accurate estimate of the actuator bending stiffness is also critical to reduce the percent difference in force between the model and the experiment. As is shown by eq. 3.39, the bending stiffness estimate depends on accurate measurements for weight per unit length and is particularly sensitive to errors in the loop height using the free-fold test. Thus, to reduce any potential difference between the model and the experiments, emphasis should be placed on measurements taken during the free-fold test.

3.6 Conclusions and Future Work

In this chapter, a model for soft actuator behavior in constrained, rigid environments that requires no embedded sensor integration and can be done using only static images was presented.

A model for soft actuators that deform due to eigenstrains was developed and the results showed that linear complementarity and Hencky bar-chain methods can be applied to soft robots to provide an elegant and fast solution to modeling soft actuators. This is a valuable contribution to the soft robotics community because it allows for contact modeling without the need for computationally-expensive analysis, such as FEA. In addition, a free-fold test traditionally used in textile research was adapted as a method for estimating the bending stiffness of soft actuators. This approach eliminates the need for detailed modeling of composite structures, like the soft actuator presented in this work, and helps account for variations introduced throughout the manufacturing process.

This chapter presented a custom experimental setup and computer vision program used to

validate the model for both shape and force. This contribution allowed for efficient experimental analysis of a large number of static images. The setup was used to analyze over 297 images (54 ground truth, 99 unconstrained, 144 constrained images). Additionally, it was shown that the approaches analyzed images with a percent difference below 2% for the critical measurement characteristics. The analysis produced a mean percent difference in shape between the model and experiment of 1.06% using ICP analysis. The results also indicated the percent difference in interaction forces between the model and experiment decreased as pressure increased, where the average magnitude of the percent difference was 45.34% and 20.98% for pressures at the low and high ends of the tested range, respectively. The results showed the percent difference in force to be nearly two orders of magnitude larger than the shape percent difference, though in practice this is likely because the measured forces were less than 20 gram-force (0.2 N).

Although the experiments of this chapter focus on hydraulically-actuated soft robots, the impact of this chapter is not limited to the fluid-powered subset of soft actuators. The presented model can be used for any high aspect ratio ($\ell >> \emptyset$) soft actuator that undergoes deformation caused by eigenstrains, independent of actuation technique (e.g. pneumatic, thermal, electrohydraulic, etc.). Overall, the work in this chapter can be used to efficiently search the design space of soft actuators to determine how actuator shapes and forces are affected by design changes (e.g. material properties, geometries, etc.).

Future work could include expanding this model to account for elastic environments like tissue, as well as an incorporation of a friction model to better capture the environments in which soft robots are often used.

Chapter 4

Pressure-Dependent Bending Stiffness for Soft Robotic Actuators

This chapter includes work from a submitted IEEE Robotics and Automation Letters paper titled, "Modeling and Measurement of Pressure-Dependent Bending Stiffness for Soft Robotic Actuators via a Simple Free-Fold Test" (Section 4.2) [167].

4.1 Chapter Overview

This chapter contains two core sections that explore the effect that internal pressure has on the bending stiffness of soft robotic actuators. First, Section 4.2 presents several models to describe how the bending stiffness of both unreinforced and fiber-reinforced actuators is affected by pressure, and more specifically, the contribution of each actuator design variable to the overall bending stiffness. Empirical studies are conducted and utilize a free-fold test, which has been primarily used in textile research, to determine the bending stiffness of soft elastica — both composite and homogeneous. Second, Section 4.3 applies methods introduced in Chapter 3 to provide a more detailed description of the free-fold test to use for further analysis and comparison to empirical free-fold test results.

4.2 Empirically-Based Models for Pressure-Dependent Bending Stiffness

4.2.1 Introduction

When modeling the behavior of soft robots, knowledge of the bending stiffness plays a critical role in everything from predicting the critical buckling force of an actuator to modeling the contact between a compliant, soft actuator and objects with which it comes into contact. Many soft robotic actuators are composed of multiple materials that help dictate their behavior upon actuation. Due to such composite nature, obtaining an accurate prediction of the bending stiffness, EI, of the overall structure is challenging and often requires both computationally expensive modeling (e.g. finite element) and in-depth knowledge of the material properties of the actuator. Additionally, describing the bending stiffness becomes even more difficult for fluid-powered soft robots because of the effect that internal actuation pressure has on robot behavior.

In 1930, Peirce introduced the concept of a free-fold test approach to determine the bending rigidity and bending length for fabric sheets [157]. The free-fold test describes how a long sheet of material can be folded back on itself and, when released, the sheet forms a loop. The bending stiffness of the sheet can be deduced from the height of the loop and the weight per unit length of the sheet. The approach was later explored by others, including Stuart and Baird [158, 168], Lloyd et al. [169], Wang [160], Mahadevan and Keller [170], Zhou and Gosh [171], Cassidy et al. [172], and Plaut [159], but has remained utilized primarily by the textile research community.

Although various groups have studied how the stiffness of soft robots can be controlled, none have explicitly provided a method for determining the bending stiffness of fluid-powered soft robots as a function of pressure despite bending stiffness playing a critical role in many aspects of soft robot modeling. Blanc et al. provide a comprehensive literature review of flexible medical devices with controllable stiffness, including fluid-based solutions in soft robotic joints, but do not discuss bending stiffness models [173]. One article cited by Blanc et al. compares artificial actuators to muscle and emphasizes the importance of stiffening as a mechanical characteristic, but does not provide a stiffening model [174].

Specific to fiber-reinforced McKibben actuators, Tondu, Chou and Hannaford, and Thomalla and Van de Ven provided in-depth analyses for the strain and force behavior of McKibben

acctuators as functions of pressure [66, 95, 96]. Additionally, Van den Horn and Kuipers modeled the stresses and strains that develop in steel-braided flexible tubes as a result of internal pressure [175]. However, each of the models require knowledge of the material properties like Poisson's ratio and are not generalized to describe the bending stiffness of flexible tubes with multiple composite layers.

Outside of soft robotics, others have explored the effect of internal pressure on pipes and tubes using finite element methods. Catinaccio explored the behavior of straight, both uniform and composite laminate pipes subject to internal pressure and in-plane bending [176]. Teng et al. examine the deformation behavior of thin-walled tubes under internal pressure and combined bending, showing that pressure enhances bending stiffneses by preventing ovalization [177]. Although these works provide insight as to how pressure combats bending for uniform pipes and tubes, they both required finite element modeling and did not derive an explicit relationship between bending stiffness and pressure.

This chapter section provides two core contributions:

1. The introduction of the free-fold test to soft robotics to provide an empirical estimate of actuator bending stiffness, regardless of whether the actuator is uniform or composite, using straightforward experimentation.

2. A determination of the factors controlling the underlying dependence of soft actuator bending stiffness on actuation pressure, presented using three models.

When combined, the contributions of this chapter section provide a comprehensive design tool for the soft robotics community that can be used to determine how actuator stiffness is affected by actuation pressure, when the magnitude of this effect is negligible, and how each actuator design variable plays a role in the bending stiffness behavior.

4.2.2 Methods

Bending Stiffness as a Function of Pressure

Existing Textile Model The free-fold test method discussed in the Introduction and utilized by the textile research community states that bending stiffness, EI, can be determined using

the height of the folded loop, where

$$EI = 1.342\omega h^3 \tag{4.1}$$

where ω denotes the uniform weight per length, h denotes the height of the fold, and bending stiffness is a product of the elastic modulus, E, and area moment of inertia, I, as shown by Plaut [159]. The length of the sheet must be

$$\ell > 4.683\sqrt[3]{\frac{EI}{\omega}} \tag{4.2}$$

as outlined by [160] and [159].

Underlying Dependence of Bending Stiffness on Actuation Pressure

One of the major contributions of this chapter is a determination of the variables that control the underlying dependence of bending stiffness on actuation pressure. To discover the driving variables, consider a tube-like, fluidic actuator comprised of incompressible elastomeric material, an internal pressure, p, a pressure-dependent inner radius, r_p, and a pressure-dependent outer radius, R_p. Each pressure-dependent variable is denoted by a subscript p for notation simplicity. The models discussed throughout this chapter assume that the elastic modulus, E, is known and constant across the pressure range of interest.

To determine the dependence of bending stiffness on actuation pressure, it is assumed here that the actuator length does not change with pressure, which is equivalent to a plane strain assumption. This assumption was motivated by experimental results for the fluidic actuators not reinforced by fibers discussed in later sections. The area moment of inertia, I_p, of the actuator can be described as

$$I_p = \frac{\pi}{4}\left(R_p^4 - r_p^4\right) = \frac{\pi}{4}\left(R_p^2 - r_p^2\right)\left(R_p^2 + r_p^2\right) \tag{4.3}$$

Since the elastomer is assumed to be incompressible,

$$\pi\left(R_p^2 - r_p^2\right) = S \tag{4.4}$$

where S is a constant. The pressure-dependent radial displacement at the inner radius is expressed as

$$u_p = \frac{A}{2\pi r_0} \tag{4.5}$$

where A denotes the increase area of the inner cross-section of the tube. Similarly, the radial displacement at the outer radius can be described as

$$U_p = \frac{A}{2\pi R_0} \tag{4.6}$$

where A is the same in eqs. 4.5 and 4.6 on account of the incompressibility of the elastomer. The variation of moment of inertia can be expressed as

$$\Delta I_p = I_p - I_0 = \frac{S}{4}\left(R_p^2 + r_p^2 - R_0^2 - r_0^2\right) \tag{4.7}$$

Since the radial displacement $u_p = r_p - r_0$ and $U_p = R_p - R_0$, eq. 4.7 can be rewritten as

$$\Delta I_p \simeq \frac{S}{4}\left(2u_p r_0 + 2U_p R_0\right) \simeq \frac{AS}{2\pi} \tag{4.8}$$

Let Δw_p denote the increase in weight per unit length of the actuator with pressurization. Then

$$A\rho = \Delta\omega_p \tag{4.9}$$

on account of the assumed incompressibility of the actuation fluid. Hence,

$$\Delta I_p \simeq \frac{\Delta w_p S}{2\pi\rho} \tag{4.10}$$

From eq. 4.10, it can be concluded

$$\Delta I_p \sim \Delta\omega_p \tag{4.11}$$

The elastic modulus, E, is assumed constant throughout pressurization, meaning the change in bending stiffness with pressure, ΔEI_p, is fully dependent on the change in moment of inertia, ΔI_p, described by eq. 4.11.

Theoretical Model for Pressure-Dependent Bending Stiffness

The resulting equations from Section 4.2.2 show that the change in actuator bending stiffness as pressure increases, ΔEI_p, is controlled by the measurable quantity Δw_p that corresponds to the pressure-dependent change in weight per unit length of the actuator, but a theoretical baseline for comparison is desirable.

Since the actuation fluid is assumed to be incompressible, the pressure increase is due to the compliance of the elastomeric actuator. The actuator can be treated as a thick-walled cylinder

with open ends, internal pressure, p, pressure-dependent inner radius, r_p, and outer radius, R_p. The radial stress, σ_{r_p}, can be expressed as

$$\sigma_{r_p} = \left(\frac{r_p^2 p}{R_p^2 - r_p^2}\right) - \left(\frac{r_p^2 R_p^2 p}{R_p^2 - r_p^2}\right)\frac{1}{b_p^2} \tag{4.12}$$

where b_p represents the radius to a point of interest on the cylinder. The tangential stress, σ_{t_p}, can be expressed as

$$\sigma_{t_p} = \left(\frac{r_p^2 p}{R_p^2 - r_p^2}\right) + \left(\frac{r_p^2 R_p^2 p}{R_p^2 - r_p^2}\right)\frac{1}{b_p^2} \tag{4.13}$$

Assuming now that the axial stress, σ_{a_p}, is zero, the tangential strain, ε_{t_p}, in terms of radial and tangential stresses using Hooke's law is

$$\varepsilon_{t_p} = \frac{\left(\sigma_{t_p} - \nu\sigma_{r_p}\right) b_p}{E} \tag{4.14}$$

where Poisson's ratio, ν, is 0.5 due to the assumed incompressibility of the elastomer [178]. The radial displacement of the cylinder is expressed as

$$u_{b_p} = \varepsilon_{t_p} b_p \tag{4.15}$$

where the radial and tangential stresses are calculated at radius, b_p. The change in radius can be expressed in terms of internal pressure as

$$u_{b_p} = \left(\frac{1-\nu}{E}\right)\left(\frac{r_p^2 p}{R_p^2 - r_p^2}\right) b_p + \left(\frac{1+\nu}{E}\right)\left(\frac{r_p^2 R_p^2 p}{R_p^2 - r_p^2}\right)\frac{1}{b_p} \tag{4.16}$$

The inner and outer radii, r_p and R_p, respectively, can be calculated by substituting $b_p = r_p$ and $b_p = R_p$ into the eq. 4.16, where

$$r_p = r_0 + u_p \tag{4.17}$$

$$R_p = R_0 + U_p \tag{4.18}$$

I_p can be determined by substituting eqs. 4.17 and 4.18 into eq. 4.3. Finally, the theoretical bending stiffness can be expressed as

$$(EI)_p = EI_p \tag{4.19}$$

Empirical Models for Pressure-Dependent Bending Stiffness

This chapter section presents three empirical models (Weight-Dependent, Elastomer Volume, and McKibben) to estimate bending stiffness using measurable quantities (e.g. length, weight, strain, and outer diameter) as pressure changes.

The following variables are used throughout each of the models:

- ω_0 — initial overall actuator weight per unit length
- ω_p — overall actuator weight per unit length
- ω_e — weight per unit length of the elastomer and non-fluid materials
- ℓ_0 — initial actuator length
- ℓ_p — pressurized actuator length
- ρ — density of the actuation fluid
- R_0 — initial outer radius
- R_p — outer radius
- E — elastic modulus
- θ_0 — initial, positive fiber wrap angle for McKibbens

Weight-Dependent Model The result from eq. 4.11 shows that the pressure-dependent relationship relies on variables that can be empirically measured in a simple manner, specifically $\Delta\omega_p$. Since the pressure-dependent bending stiffness, EI_p, must be determined but the inner radius, r_p, is not empirically measurable using simple methods, eq. 4.10 can be verified by deducing expressions for r_p and R_p from eqs. 4.5, 4.6, and 4.9 to get

$$r_p = \frac{\Delta\omega_p}{2\pi\rho r_0} + r_0 \tag{4.20}$$

$$R_p = \frac{\Delta\omega_p}{2\pi\rho R_0} + R_0 \tag{4.21}$$

The "Weight-Dependent" bending stiffness can be determined by substituting eqs. 4.20 and 4.21 into eq. 4.3, then plugging the result into eq. 4.19.

Elastomer Volume Model The Elastomer Volume model determines bending stiffness based on the initial volume of the elastomeric material in the actuator and other material properties. The model assumes the following variables are known or measurable: ω_0, ω_e, ℓ_0, ℓ_p, ρ, R_0, R_p, and E.

First, the initial inner radius, r_0, is determined by

$$r_0 = \sqrt{\frac{\omega_0 - \omega_e}{\pi\rho}} \tag{4.22}$$

The volume of the elastomer and non-fluid materials can be expressed as

$$V_e = \pi\ell_0 \left(R_0^2 - r_0^2\right) \tag{4.23}$$

Since ℓ_0, ℓ_p, R_0, R_p, r_0 are known and elastomer volume is conserved throughout actuation, the pressure-dependent inner radius, r_p, is determined by

$$r_p = \sqrt{{R_p}^2 - \frac{\ell_0}{\ell_p}\left(R_0^2 - r_0^2\right)} \tag{4.24}$$

Finally, the moment of inertia and bending stiffness can be found from eqs. 4.3 and 4.19.

McKibben Model The McKibben model is specific to fiber-wrapped actuators and estimates the bending stiffness as a function of pressure assuming the following variables are known: ω_0, ω_e, ℓ_0, ℓ_p, ρ, R_0, E, and θ_0.

First, known equations are adapted from [66] to describe how the outer radius changes as a function of pressure using the known variables, where

$$R_p = \frac{R_0\sqrt{1 - (1+\varepsilon_p)^2\cos^2\theta_0}}{\sin\theta_0} \tag{4.25}$$

where the axial strain, ε_p, is

$$\varepsilon_p = \frac{\ell_p - \ell_0}{\ell_0} \tag{4.26}$$

The wall thickness as a function of pressure, t_p, can be described by

$$t_p = R_p - \sqrt{{R_p}^2 - \frac{t_0(2R_0 - t_0)}{1+\varepsilon_p}} \tag{4.27}$$

where the initial wall thickness, t_0, is found by

$$t_0 = R_0 - r_0 \tag{4.28}$$

and the initial inner radius is expressed as

$$r_0 = \sqrt{\frac{\omega_0 - \omega_e}{\pi \rho}} \tag{4.29}$$

The inner radius can be determined as a function of pressure using

$$r_p = R_p - t_p \tag{4.30}$$

Finally, the moment of inertia and "Elastomer Volume Model" bending stiffness can be found from eqs. 4.3 and 4.19.

Experiments

The goal of the experiments was three-fold. The first goal was to confirm that the fold test could be used as a simple, effective method for determining the bending stiffness of soft actuators regardless of whether they were constructed of uniform or composite materials. The second goal was to validate eq. 4.11 to approximately predict the change in bending stiffness with the change in weight per unit length. The third goal was to determine how both geometry and fiber-reinforcement affect the bending stiffness-pressure relationship.

The experiments were conducted using four actuator types describe in Table 4.1. A visual comparison of each actuator is shown in Fig. 4.1. The elastic modulus, E, for the natural rubber tube (Kent Elastomer natural rubber latex tubing) was 1.31 MPa (190 psi) based on the data sheet provided by the supplier (latex-tubing.com) [179]. The Poisson's ratio for the natural rubber tube was assumed to be 0.50 ± 0.01 [178].

Table 4.1: Actuators tested using free-fold test

Reference Name	Description	OD (mm)	ID (mm)
Baseline	Solid elastic rod; polyurethane	3.23	N/A
Small, Unwrapped	Natural rubber tube; no fiber-reinforcement	3.18	1.59
Large, Unwrapped	Natural rubber tube; no fiber-reinforcement	4.76	3.18
Small, Wrapped	Natural rubber tube; fiber-reinforced; dipped in polyurethane	3.99	1.59

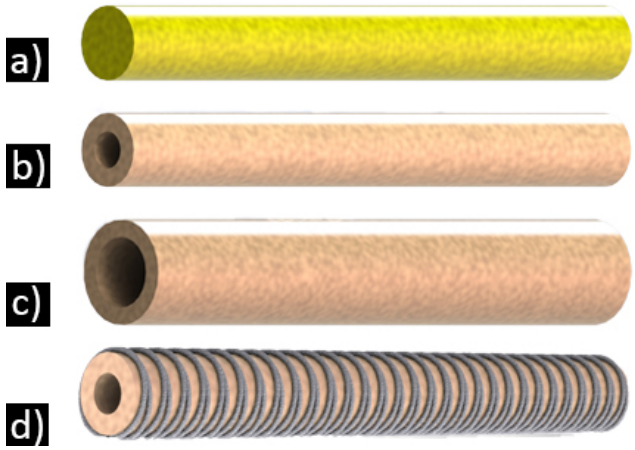

Figure 4.1: Actuators tested experimentally using free-fold test: a) Baseline actuator; a solid cross-section, elastic rod of polyurethane (Polytek 74-20). b) Small, unwrapped actuator made from natural rubber tubing with OD of 3.18 mm and ID of 1.59 mm. c) Large, unwrapped actuator made from natural rubber tubing with OD of 4.76 mm and ID of 3.18 mm. d) Small, wrapped actuator made from natural rubber tubing, wrapped with 100%, 30 wt. cotton fibers, and dipped in polyurethane to secure the fibers in place (polyurethane dip layer not pictured), with OD of 3.99 mm and ID of 1.59 mm.

Free-Fold Test Process Each free-fold test was conducted by tying five strands of thread (30 wt. 100% cotton, Coats) to the actuator so that the actuator could be suspended into a pre-release configuration (Fig. 4.2a). The actuator was placed between two panes of transparent

acrylic to prevent out-of-plane deflection and the actuators were coated with talc free powder (Up&Up Talc Free Powder) to reduce friction developed between the actuator and acrylic. For all experiments aside from the baseline experiment, each actuator was pressurized to the appropriate pressure before being suspended into the pre-release configuration. Pressure data were collected at 10 Hz using a micro-controller (Teensy 3.5) connected to a pressure transducer (Honeywell TBPDANS030PGUCV) and load cell amplifier (SparkFun, HX711). With the actuator suspended into the pre-release configuration, all strands of thread were released at the same time and the actuator formed a post-release, free-fold loop (Fig. 4.2b). After the actuator was released, a static image was taken using a camera placed at a fixed distance from the test setup and at the same height as the actuator. This process was repeated five times for each actuator tested.

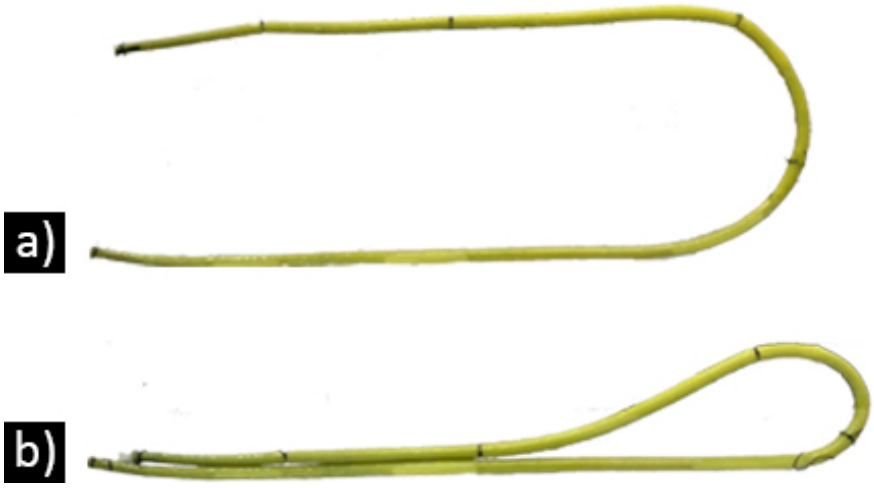

Figure 4.2: a) Example pre-release configuration with strands of thread used to suspend one half of the actuator. b) Example post-release configuration with gravity forcing the actuator to form a free-fold loop.

The full setup is shown in Fig. 4.3. The pixel-to-mm conversion ratio was calculated using an Augmented Reality University of Cordoba (ArUco) tag of known dimensions (25 mm$\times$25 mm) fixed to the test stand [161], [162].

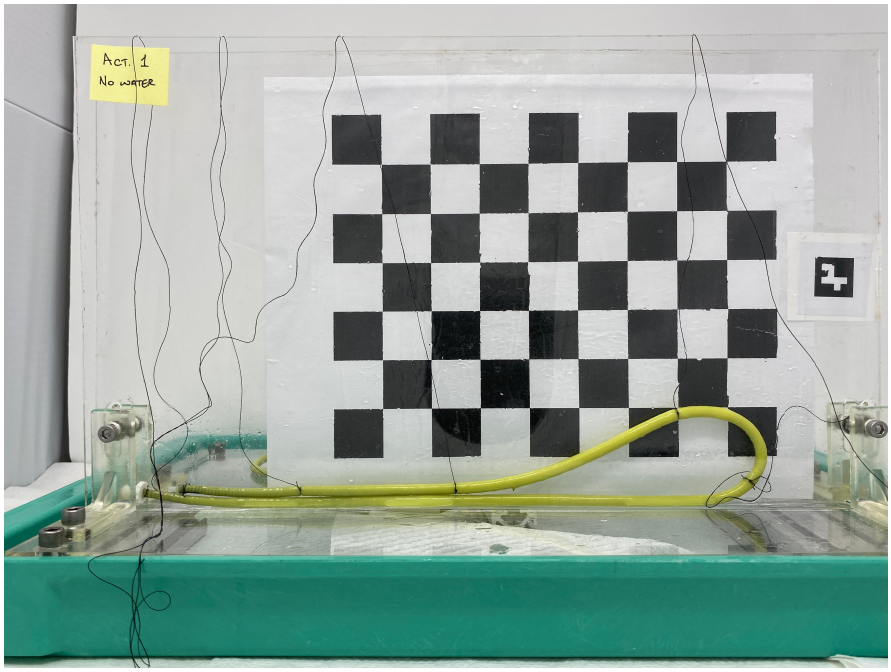

Figure 4.3: Experimental test stand used for all free-fold tests. Actuators were placed between two panes of acrylic, suspended into the pre-release configuration using thread, and released to form the free-fold loop shown. Note: to adequately capture the details of the test stand, the camera angle used in this figure is not the same as was used to capture images of each free-fold test.

Before each free-fold test was conducted, each actuator was measured for initial length, initial weight of the actuator without fluid, and the weight of the actuator over the pressure range of 0 to 172.37 kPa (0-25 psi) in 34.47 kPa (5 psi) increments. The weight measurements properly accounted for the weight of the powder, thread, and barbed caps and fittings. Additionally, the relationship between actuator length and pressure, as well as outer radius and pressure, were determined using static images where the actuator was placed on a flat surface and pressurized over the pressure range in 34.47 kPa (5 psi) increments. A static image was taken at each pressure increment and the actuator length and outer diameter were measured in post-processing using a pixel-to-mm conversion.

Baseline A baseline experiment was conducted using solid-bodied actuators, shown in Fig. 4.1a, to confirm that the free-fold test can be used to characterize the bending stiffness of soft actuators despite being originally used to characterize textile strips. Four solid-bodied

polyurethane (Polytek 74-20) actuators were fabricated using a custom mold and injection process with dimensions shown in Table 4.2. The actuators were tested using the process outlined in Section 4.2.2.

Table 4.2: Actuator dimensions for baseline free-fold test

Actuator	OD (mm)	Length (mm)
1	3.25	614
2	3.20	462
3	3.24	612
4	3.23	612
Avg	3.23 ± 0.02	575

Pressurized Actuators Two of each type of actuator listed in Table 4.1, excluding the baseline actuators, were tested using the process outlined in Section 4.2.2. Data were recorded for the initial length and weight of each actuator, as well as strain and outer radius as functions of pressure. It should be noted that the large, unwrapped actuator (Table 4.1) was tested over a smaller pressure range of 0 to 137.90 kPa (0 to 20 psi) to ensure the actuator did not burst or bulge.

4.2.3 Results

Experimental Results

Baseline The average loop height of the four baseline actuators was 29.97 mm and the average weight per unit length was 7.77×10^{-5} N/mm. This resulted in an average bending stiffness of 2.51 Nmm^2. Extracting the elastic modulus from the bending stiffness using the known geometry from Table 4.2 resulted in an average extracted modulus of 0.49 ± 0.11 N/mm^2. This value was compared to the elastic modulus for the same polyurethane (Polytek 74-20) found using tensile tests conducted on dog bone samples (2 mm thick, 5 mm wide, 40 mm long) using an Instron machine, where the average tensile test modulus (N = 3 samples) was 0.46 ± 0.03 N/mm^2. Thus, the percent difference between the elastic modulus extracted from the free-fold test and the elastic modulus determined from tensile tests was 6.86%.

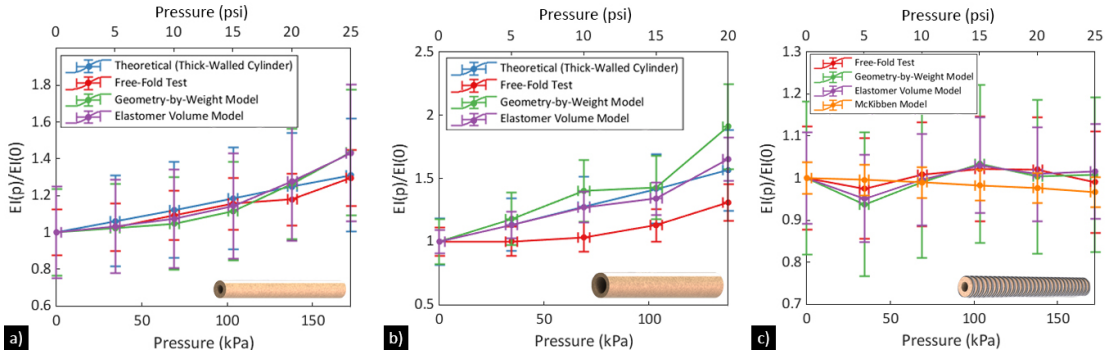

Figure 4.4: The ratio of pressure-dependent to initial bending stiffness for: a) Small, Unwrapped Actuator, b) Large, Unwrapped Actuator, and c) Small, Fiber-Wrapped Actuator. The pressure shown is gauge pressure. The x-error bars were determined by the overall variation ($\pm$ 2.76 kPa) in pressure observed throughout the free-fold tests. The y-error bars were determined using error propagation based on the measurement error of each of the known quantities described in Section 4.2.2.

Pressurized Actuators The relationship between the experimental and modeled bending stiffness as a function of pressure, from Section 4.2.2, is shown in Fig. 4.4 for each of the pressurized actuator types. The contribution of each experimental variable to the percent change in the experimental bending stiffness is shown in Fig. 4.5 for each of the pressurized actuator types.

4.2.4 Discussion

Baseline

The baseline experiment conducted using a solid-cross section elastic rod confirmed that despite being originally formulated for ribbon-like textiles, the free-fold test is an adequate approach to estimate the material properties of the soft actuators discussed throughout this paper given that the percent difference between the elastic modulus found from tensile tests and the free-fold test was 6.86%. This is on the order of the smallest percent difference between the elastic moduli of the three dog bone samples of the Polytek 74-20 polyurethane (6.73%) found using the Instron machine (Appendix F) — with the largest percent difference between the three samples being 13.46%. The free-fold test resulted in a larger variation in measurement as compared to the tensile tests, although this was expected because the tensile tests were conducted on dog bone samples using an industrial Instron machine specifically designed for the purpose.

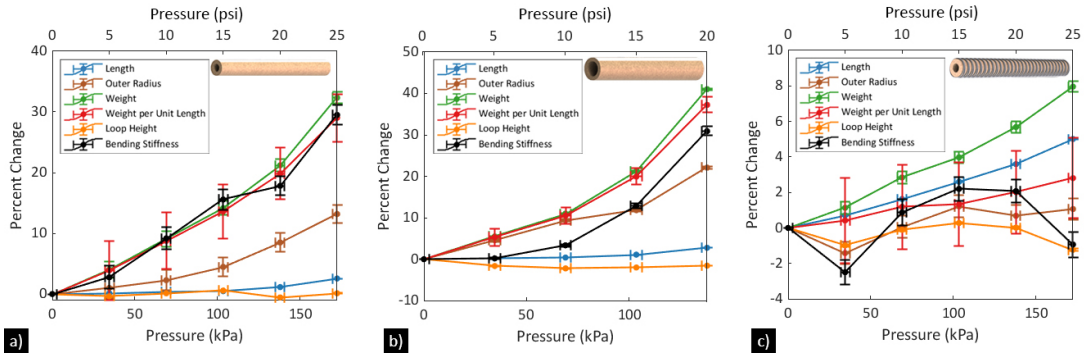

Figure 4.5: The percent change in experimental variables with increasing pressure is shown for the: a) Small, Unwrapped Actuator, b) Large, Unwrapped Actuator, c) Small, Fiber-Wrapped Actuator. Pressure shown is gauge pressure. The x-error bars were determined by the overall variation ($\pm$ 2.76 kPa) in pressure observed throughout the free-fold tests. The y-error bars were determined using error propagation based on the measurement error of each known quantity described in Section 4.2.2.

It is also critical to emphasize that one of the greatest benefits of the free-fold test, aside from its simplicity, is to characterize the bending stiffness of composite soft actuators as well as fluid-filled actuators. With this in mind, the purpose of the baseline experiment was to confirm that the free-fold test is valid for elastica beyond ribbon-like textiles rather than prove the accuracy of the free-fold test in extracting the elastic modulus of a homogeneous material.

Pressurized Actuators

Pressure-Dependent Bending Stiffness The experimental results for the pressurized actuators provided insight on how bending stiffness changes with pressure, as well as how the change is dictated by the cross-sectional geometry of the actuators and whether the actuator is fiber-reinforced. As can be seen from Figs. 4.4a and 4.4b, bending stiffness increased with pressure for actuators that were not fiber-reinforced. The results showed that the proposed models were in agreement with the experiment for the small, unwrapped actuator.

A greater difference was observed between the experimental bending stiffness and the models for the large, unwrapped actuator. One possible explanation for this is measurement error and the high sensitivity of the experimental bending stiffness value to the measured loop height (i.e. h^3 term). A second possible explanation is that when the ratio between inner radius and outer radius is large enough, the actuator cross section has a tendency to ovalize due to gravity

when resting on a flat surface (Fig. 4.6). This ovalization would result in a slightly smaller loop height measurement, which would greatly affect the bending stiffness value, EI, due to its sensitivity to h. This ovalization would also cause a reduction in the area moment of inertia, I, which is directly related to bending stiffness. Interestingly, the actuator geometry with a larger inner radius to outer radius ratio (i.e. the large, unwrapped actuator) appeared to display an exponential relationship between bending stiffness and pressure.

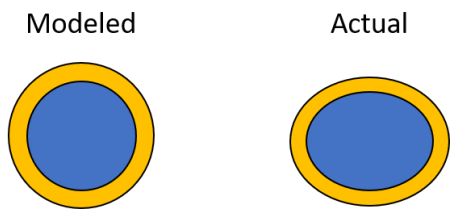

Figure 4.6: One potential explanation for the discrepancy between experimental and modeled behavior for the large, unwrapped actuator is ovalization of the cross-section.

Finally, a comparison between the actuators of similar geometry but differing fiber-reinforcement (e.g. small, unwrapped vs. small, wrapped) as shown in Figs. 4.4a and 4.4c, showed that the presence of fibers significantly affects the bending stiffness and pressure relationship. Fig. 4.4c showed that the bending stiffness does not increase with pressure when the actuator is reinforced with fibers. This is likely caused by the fibers restricting the amount of radial expansion and instead translating pressure to axial extension. With radial expansion restricted, the change in moment of inertia is less significant with pressure. It is important to note that this relationship may change for McKibben actuators with fiber angles that promote contraction as opposed to extension. In the case of contracting McKibben actuators, the actuator displays significant radial expansion. Contracting McKibben actuators are not a focus of this work, but similar methodology could be applied to explore the pressure-dependency. Finally, although the McKibben model predicted a negative correlation between bending stiffness and pressure, the free-fold test and elastomer volume model results did not display any correlation.

Effect of Actuator Parameters on Bending Stiffness The results helped provide a stronger understanding of why bending stiffness changes — or does not change — with pressure by investigating the variable change with pressure, as shown in Fig. 4.5. The results showed that the percent change in bending stiffness to pressure relationship followed most closely to the

pressure-dependent relationships for outer radius, weight, and weight per unit length. Although the percent change in loop height as pressure increased followed a similar trend to bending stiffness, the percent change in loop height was smaller than that of bending stiffness. Again, the high sensitivity of the experimental bending stiffness value to the measured loop height (i.e. h^3 term) could be an explanation for this, meaning that although the loop height has a smaller percent change over the range of pressures, a small change in h leads to a larger change in EI. The variable breakdown for the small, wrapped (McKibben) actuator showed that the fiber-reinforcement restricted the outer radius from increasing while promoting axial strain. The restriction of the outer radius impacted the moment of inertia for the actuator and thus, the bending stiffness.

4.2.5 Conclusion

Throughout this chapter section, a model was presented to determine the bending stiffness of soft actuators, composite or homogeneous, using the free-fold test. Additionally, it was shown that the change in weight per unit length controls the underlying dependence of bending stiffness on actuation pressure, which is easily measurable in soft robotics. Finally, three models were provided that predict the relationship between actuator bending stiffness and pressure for fluid-filled soft actuators, which is not incorporated into existing work such as [159].

The presented models and experiments also shed light on the roles that cross-sectional actuator geometry and fiber-reinforcement play in the bending stiffness-pressure relationship. An analysis was provided for the specific contributions of each variable to the overall bending stiffness behavior, which elucidated the measurements and design variables that were most impactful to bending stiffness.

Overall, this chapter section contributed a design tool and insight to the soft robotics community as to how fluid-powered soft robot bending stiffness is affected by pressure. Furthermore, it outlined straightforward and manageable experiments that can be conducted without the need for computationally expensive finite element modeling and detailed knowledge of the structure and materials within composite actuators. Although this chapter section touched briefly on modeling radial strains as a function of pressure without the need for empirical measurements (Thick-Walled Cylinder Model, Section 4.2.2), the benefit of the proposed models is that they do not require in-depth knowledge of the actuator's material properties to provide a bending

stiffness estimate.

The presented work could be extended to actuators that contain composite components beyond fibers (e.g. strain limiting layers, rigid elements, etc.). Finally, a comparison between the free-fold test and other tests, such as a cantilever elastica under its own weight or a four-point flexural test, could be used to further explore the pressure-dependent bending stiffness of elastica [180, 181, 182].

4.3 Applying Hencky Bar-Chain and Linear Complementarity Methods to the Fold Test

4.3.1 Introduction

To allow for more in-depth analysis of the free-fold test, the Hencky bar-chain and linear complementarity methods introduced in Chapter 3 can be applied to soft robotic actuators as a simple and computationally efficient method for modeling how loop shape and height of the free-fold test change with actuator bending stiffness, EI, and weight per unit length, ω.

4.3.2 Methods

Problem Description

The contribution of this section is a description of the actuator shape during the free-fold test, which was shown earlier in this chapter to be an effective tool to determine the bending stiffness of soft actuators. This can be achieved by discretizing the free-fold actuator using the Hencky bar-chain approximation and formulating the constraint problem as a LCP, then solving the LCP iteratively to find a final, nonlinear solution. Although the approach presented in this chapter section is similar to the Hencky bar-chain and LCP methods shown in Chapter 3, the formulation differs slightly.

The concept is shown in Fig. 4.7, where the actuator starts in the undeformed configuration (Fig. 4.7a). The actuator is of scaled length ℓ and is discretized into N links and $N+1$ nodes based on the Hencky bar-chain method. Each of the $N+1$ nodes can be thought of as an elastic rotational spring capable of generating torque when the rigid links are displaced. Each link has a scaled weight, μ, and a scaled link length, a.

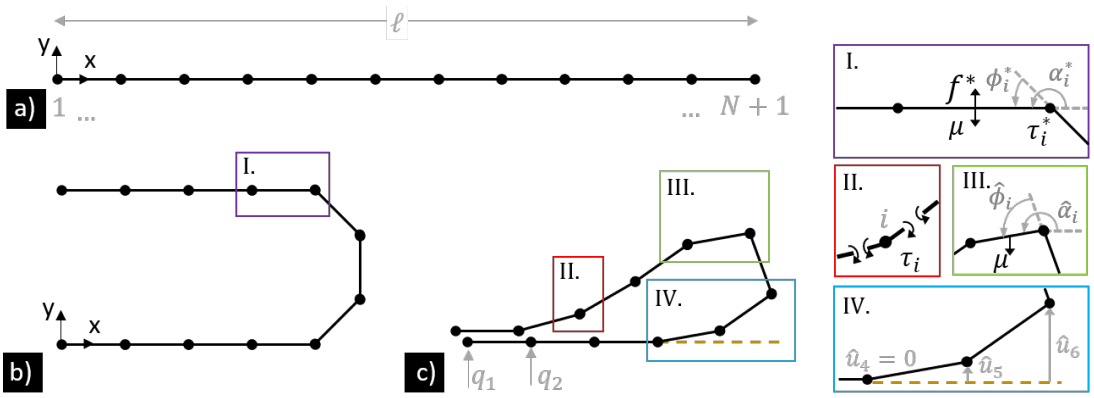

Figure 4.7: a) Initial, undeformed configuration of the actuator discretized into N links and $N+1$ nodes. b) Pre-release configuration generated by applying initial forces and torques to offset the weight of each link and force the actuator into the desired "⊃" shape. c) Post-release configuration showing the shape of the free-fold loop. Inset: I) Expanded view of one link in the pre-release shape, showing that each link has a self-weight, μ, acting at its center. The orientation of each link relative to horizontal is denoted by α_i and the orientation of each link relative to the previous link is denoted by ϕ_i. An initial forces, f^*, and torque, τ_i^*, act on each link and node in the pre-release configuration. II) Each node is modeled as a rotational spring such that a torque is developed when the links are deformed from their initial configurations. III) The link orientations in the post-release shape are denoted using hat notation. IV) The displacement of each node relative to the ground ($y = 0$) is denoted by u_i.

The actuator is forced into a pre-release configuration (Fig. 4.7b) by applying a scaled initial force, f^*, at the center of each link to offset the weight of each link, μ. The curvature of the pre-release configuration is determined by applying an initial torque, $\tau_i{}^*$, at each node, where the value of $\tau_i{}^*$ is determined based on the desired, user-specified initial configuration. The initial configuration does not affect the result of the fold test, so long as the actuator is folded back onto itself, resembling a "⊃" shape. To resemble a release of the actuator from the pre-release configuration, the initial forces and torques holding the holding the "⊃" shape (f^* and $\tau_i{}^*$, respectively) are reduced with each iteration of the LCP until their magnitudes are equal to zero. The resulting post-release configuration resembles the free-fold loop, as shown in Fig. 4.7c.

The process is shown in Fig. 4.8 and the notation is outlined below in the Notation section.

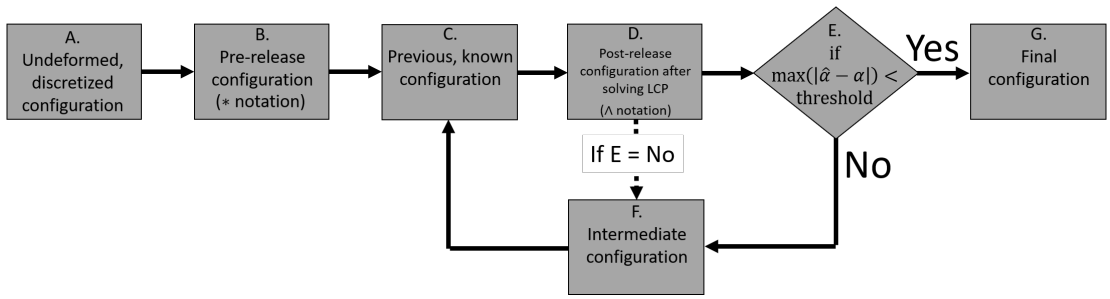

Figure 4.8: Iterative process for determining the final actuator configuration. A. Denotes the undeformed, discretized configuration before any forces are applied, B. Refers to the pre-release configuration ($*$ notation) after initial forces and torques are applied to hold the "$\supset$" shape, C. Represents the previous, known configuration, D. Represents the post-release configuration after solving the LCP ($\wedge$ notation), E. Represents a conditional statement used to determine whether the maximum change in link orientation between C and D ($\max(|\hat{\boldsymbol{\alpha}} - \boldsymbol{\alpha}|)$) is less than a threshold, F. Refers to the intermediate configuration where the holding forces and torques in B are iteratively reduced until no holding forces or torques act on the actuator, G. Is the final configuration.

Notation

Throughout this chapter section, scalars are represented using lowercase letters not in bold typeface (e.g. d, μ, b_1). Vectors are lowercase, bold typeface letters (e.g. $\boldsymbol{\alpha}$, $\bar{\boldsymbol{\tau}}$, $\mathbf{c_1}$). Matrices are uppercase, bold typeface letters (e.g. $\mathbf{A}$, $\mathbf{B}$, $\mathbf{G}$). The exception to this is the reaction force vector, $\bar{\mathbf{R}}$, which is one of the variables for which the problem is solving. A bar above the variable (e.g. $\bar{\boldsymbol{\phi}}$, $\bar{\mathbf{u}}$) represents that the vector has been truncated to only consider the variables within the vector definition (e.g. $[u_2, \cdots, u_N]$) instead of variables 1 through N.

The following notation is used to describe the actuator

- $\boldsymbol{\alpha} = [\alpha_1, \cdots, \alpha_N]^\top$
- $\bar{\boldsymbol{\phi}} = [\phi_2, \cdots, \phi_N]^\top$
- $\bar{\boldsymbol{\tau}} = [\tau_2, \cdots, \tau_N]^\top$
- $\bar{\mathbf{u}} = [u_2, \cdots, u_N]^\top$
- $\bar{\mathbf{g}} = [g_3, \cdots, g_{N+1}]^\top$
- $\bar{\mathbf{R}} = [R_3, \cdots, R_{N+1}]^\top$

where each variable is shown in Fig. 4.7. The star* notation (e.g. $\boldsymbol{\alpha}^*$, $\bar{\boldsymbol{\phi}}^*$, $\bar{\mathbf{u}}^*$) denotes the pre-release configuration (Fig. 4.7b). The $\hat{\text{hat}}$ notation represents the post-release configuration

(Fig. 4.7c). These variables are used in the LCP formulation to solve for the reaction forces, $\bar{\mathbf{R}}$, and the constrained configuration using the gap between each node and the ground, $\bar{\mathbf{g}}$.

Scaling

Before describing the problem formulation, the scaling for the fold test problem must be defined. Scaling the governing equations for length, force, and moment result in the following, respectively

$$\breve{\ell} = \sqrt[3]{\frac{EI}{\omega}}, \quad \breve{f} = \sqrt[3]{\omega^2 EI}, \quad \breve{\tau} = \sqrt[3]{\omega(EI^2)} \tag{4.31}$$

where the scaled quantities are determined by

$$\ell = \frac{L}{\breve{\ell}}, \quad f = \frac{F}{\breve{f}}, \quad \tau = \frac{T}{\breve{\tau}} \tag{4.32}$$

where L, F, and T represent the unscaled length, force, and moment, respectively.

Problem Formulation

First, expressions for the support reactions, q_1 and q_n, as functions of the external reaction forces, $\bar{\mathbf{R}}$, must be defined. Summing the moments about node 2 generated from external forces provides

$$q_1 = \frac{1}{\cos(\alpha_1)} \left((\mu - f^*) b_1 + \mathbf{c_1}^\top \bar{\mathbf{R}} \right) \tag{4.33}$$

where d is

$$d = \sum_{i=1}^{N} \cos(\alpha_i) \tag{4.34}$$

The scaled weight of each link, μ, acting at the center of mass is defined as

$$\mu = \frac{\omega L}{N \breve{f}} \tag{4.35}$$

where ω and L are the unscaled weight per unit length and unscaled overall actuator length, respectively. The expression for b_1 in eq. 4.33 is

$$b_1 = \cos(\alpha_1) - \frac{d}{2} + \sum_{i=1}^{N-2} -(N - (i+1)) \cos(\alpha_{i+1}) \tag{4.36}$$

$\mathbf{c_1}$ is an $(N-1) \times 1$ vector

$$\begin{aligned} \mathbf{c_1} &= [c_{1_1}, \cdots, c_{1_{N-1}}]^\top, \\ \text{where } \mathbf{c_1}(i) &= \sum_{j=2}^{i+1} \cos(\alpha_j) \end{aligned} \tag{4.37}$$

Following a similar process, the reaction force at node 2 can be obtained by summing the moments about node 1 generated by external forces, resulting in

$$q_2 = \frac{1}{\cos(\alpha_1)} \left((\mu - f^*) b_2 - \mathbf{c_2}^\top \bar{\mathbf{R}} \right) \tag{4.38}$$

The expression for b_2 is

$$b_2 = \frac{d}{2} + \sum_{i=1}^{N-1} (N - i) \cos(\alpha_i) \tag{4.39}$$

and $\mathbf{c_2}$ is a $(N-1) \times 1$ vector defined as

$$\begin{aligned} \mathbf{c_2} &= [c_{2_1}, \cdots, c_{2_{N-1}}]^\top, \\ \text{where } \mathbf{c_2}(i) &= \sum_{j=1}^{i+1} \cos(\alpha_j) \end{aligned} \tag{4.40}$$

The torque acting on each node is calculated by summing all of the moments generated by external forces, resulting in

$$\bar{\boldsymbol{\tau}} = \frac{a}{2} \left(\boldsymbol{\gamma} - \mathbf{A}\bar{\mathbf{R}} \right) - \mathrm{I}_{N-1} \bar{\boldsymbol{\tau}}^* \tag{4.41}$$

where a represents the scaled length of each link

$$a = \frac{\ell}{N} \tag{4.42}$$

and $\boldsymbol{\gamma}$ is a $(N-1) \times 1$ vector

$$\boldsymbol{\gamma} = (\mu - f^*) \left(\mathbf{s} - \frac{1}{\cos(\alpha_1)} \left(b_1 \mathbf{t_1} + b_2 \mathbf{t_2} \right) \right) \tag{4.43}$$

$\mathbf{s}$ is a $(N-1) \times 1$ vector defined as

$$\mathbf{s} = [s_1, \cdots, s_{N-1}]^\top \tag{4.44}$$

where

$$\mathbf{s}(i) = \frac{d}{2} + \sum_{1}^{N-2} \zeta_j \tag{4.45}$$

and

$$\zeta_j = \begin{cases} \cos(\alpha_{j+1}) & \text{if } (j = 1) \text{ or} \\ & (j = N-2) \\ (N - 1 - j) \cos(\alpha_{j+1}) & \text{if } (j \geq i); \\ j \cos(\alpha_{j+1}) & \text{otherwise;} \end{cases} \tag{4.46}$$

The $(N-1)\times 1$ vectors $\mathbf{t_1}$ and $\mathbf{t_2}$ are expressed as

$$\mathbf{t_1} = [t_{1_1}, \cdots, t_{1_{N-1}}]^\top \tag{4.47}$$

where

$$\mathbf{t_1}(i) = \sum_{j=1}^{i} \cos(\alpha_j) \tag{4.48}$$

and

$$\mathbf{t_2} = [t_{2_1}, \cdots, t_{2_{N-1}}]^\top \tag{4.49}$$

where

$$\mathbf{t_2}(i) = \begin{cases} 0 & \text{if } (i=1); \\ \sum_{j=2}^{i} \cos(\alpha_j) & \text{otherwise;} \end{cases} \tag{4.50}$$

In eq. 4.41, $\mathbf{A}$ is a $(N-1)\times(N-1)$ matrix

$$\mathbf{A} = \mathbf{B} + \frac{1}{\cos(\alpha_1)}\left(\mathbf{t_1}\mathbf{c_1}^\top + \mathbf{t_2}\mathbf{c_2}^\top\right) \tag{4.51}$$

where $\mathbf{B}$ is a $(N-1)\times(N-1)$ matrix defined as

$$\mathbf{B} = \begin{bmatrix} \sum_{i=2}^{2}\cos(\alpha_i) & \sum_{i=2}^{3}\cos(\alpha_i) & \sum_{i=2}^{4}\cos(\alpha_i) & \dots & \sum_{i=2}^{N}\cos(\alpha_i) \\ 0 & \sum_{i=3}^{3}\cos(\alpha_i) & \sum_{i=3}^{4}\cos(\alpha_i) & \dots & \sum_{i=3}^{N}\cos(\alpha_i) \\ \sum_{i=3}^{3}\cos(\alpha_i) & 0 & \sum_{i=4}^{4}\cos(\alpha_i) & \dots & \sum_{i=4}^{N}\cos(\alpha_i) \\ \vdots & \ddots & \ddots & \ddots & \vdots \\ \sum_{i=3}^{N-1}\cos(\alpha_i) & \sum_{i=4}^{N-1}\cos(\alpha_i) & \sum_{i=5}^{N-1}\cos(\alpha_i) & \dots & \sum_{i=N}^{N}\cos(\alpha_i) \end{bmatrix} \tag{4.52}$$

A second expression for torque can be determined by relating the scaled torque and the change in joint angle from the unconstrained configuration, $\bar{\boldsymbol{\phi}}^*$, using the constitutive equation for a torsion spring.

$$\bar{\boldsymbol{\tau}} = -\frac{1}{a}\left(\bar{\hat{\boldsymbol{\phi}}} - \bar{\boldsymbol{\phi}}^*\right) \tag{4.53}$$

Utilizing kinematics, the relationship between $\bar{\hat{\boldsymbol{\phi}}}$ and $\hat{\boldsymbol{\alpha}}$ is

$$\bar{\hat{\boldsymbol{\phi}}} = \mathbf{G}\hat{\boldsymbol{\alpha}} \tag{4.54}$$

where $\mathbf{G}$ is a $(N-1) \times N$ matrix

$$\mathbf{G} = \begin{bmatrix} -1 & 1 & 0 & \dots & 0 \\ 0 & -1 & 1 & \dots & 0 \\ \vdots & \vdots & \ddots & \ddots & \vdots \\ 0 & 0 & \dots & -1 & 1 \end{bmatrix} \tag{4.55}$$

To relate small y-direction displacements of each node, $\hat{\mathbf{u}}$, to the angular deflections of each link, $\hat{\boldsymbol{\alpha}}$, linearization about the previous value for $\boldsymbol{\alpha}$ is performed using

$$\sin(\hat{\alpha}_i) \approx \sin(\alpha_i) + \cos(\alpha_i)\,(\hat{\alpha}_i - \alpha_i) \tag{4.56}$$

The linearization results in the following expression

$$\hat{\boldsymbol{\alpha}} = \frac{1}{a}\mathbf{M}\bar{\hat{\mathbf{u}}} - \mathbf{v} \tag{4.57}$$

where $\mathbf{M}$ is a $N \times (N-1)$ matrix

$$\mathbf{M} = \begin{bmatrix} \frac{1}{\cos(\alpha_1)} & 0 & 0 & \dots & 0 \\ -\frac{1}{\cos(\alpha_2)} & \frac{1}{\cos(\alpha_2)} & 0 & \dots & 0 \\ 0 & -\frac{1}{\cos(\alpha_3)} & \frac{1}{\cos(\alpha_3)} & \dots & 0 \\ \vdots & \ddots & \ddots & \ddots & \vdots \\ 0 & 0 & 0 & \dots & -\frac{1}{\cos(\alpha_N)} \end{bmatrix} \tag{4.58}$$

and the displacement of each node is a $(N-1) \times 1$ vector

$$\bar{\hat{\mathbf{u}}} = [\hat{u}_3, \cdots, \hat{u}_{N+1}]^\top \tag{4.59}$$

and $\mathbf{v}$ is a $N \times 1$ vector

$$\mathbf{v} = [v_1, \cdots, v_N]^\top, \text{ where } \mathbf{v}(i) = \tan(\alpha_i) - \alpha_i \tag{4.60}$$

Solving for $\bar{\mathbf{R}}$, eqs. 4.54 and 4.57 can be combined to obtain an expression for $\bar{\hat{\phi}}$.

$$\bar{\hat{\phi}} = \frac{1}{a}\mathbf{G}(\mathbf{M}\bar{\hat{\mathbf{u}}} - \mathbf{v}) \tag{4.61}$$

Combining eqs. 4.53 and 4.61, the torque at each node is expressed as a function of the y-direction displacement of each node.

$$\bar{\boldsymbol{\tau}} = -\frac{1}{a}\left(\frac{1}{a}\mathbf{G}\left(\mathbf{M}\bar{\hat{\mathbf{u}}} - \mathbf{v}\right) - \bar{\boldsymbol{\phi}}^*\right) \tag{4.62}$$

The relationship between the y-direction displacement of each node and the y-direction gap between each node and the ground ($y = 0$, Fig. 4.7) is

$$\bar{\hat{\mathbf{u}}} = \bar{\mathbf{g}} \tag{4.63}$$

where the first link is assumed to stay flat, so $\mathbf{u}_{1,2} = \mathbf{g}_{1,2} = 0$.

Combining eqs. 4.62 and 4.63 and solving for the reaction forces at each node, $\bar{\mathbf{R}}$, results in

$$\bar{\mathbf{R}} = \mathbf{K}\bar{\mathbf{g}} + \mathbf{z} \tag{4.64}$$

where $\mathbf{K}$ represents the system's stiffness matrix, expressed as

$$\mathbf{K} = \frac{2}{a^3}\mathbf{A}^{-1}\mathbf{G}\mathbf{M} \tag{4.65}$$

and

$$\mathbf{z} = -\frac{2}{a^2}\mathbf{A}^{-1}\left(\mathbf{G}\mathbf{v} + \bar{\phi}^*\right) + \mathbf{A}^{-1}\boldsymbol{\gamma} - \frac{2}{a}\mathbf{A}^{-1}\mathbf{I}_{N-1}\bar{\boldsymbol{\tau}}^* \tag{4.66}$$

The x- and y- coordinates can be deduced from the solution of the LCP and the scaled height of the folded loop is considered to be the maximum y-coordinate

$$h = \max(\mathbf{y}) \tag{4.67}$$

4.3.3 Results

The results of the Hencky bar-chain model and linear complementarity method confirmed that the method can model the free-fold test. An example of the modeled actuator is shown in Fig. 4.9.

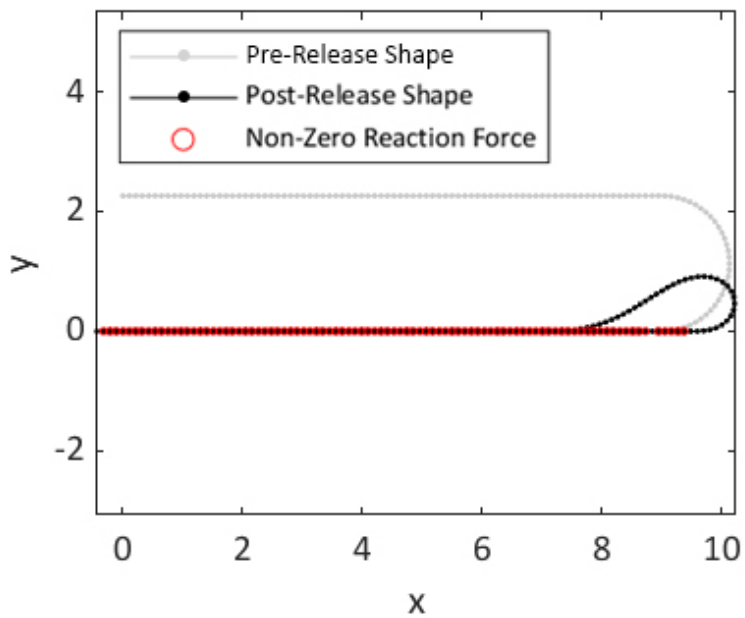

Figure 4.9: Example of the simulated free-fold test using Hencky bar-chain and linear complementarity methods. The results show that the modeled actuator forms a folded shape when released from the forced initial shape.

Scaling eq. 4.1 using eqs. 4.31 and 4.32 resulted in a theoretical scaled loop height of 0.907. A search was conducted over a range of bending stiffness values (10 to 150 Nmm^2) using a length of 1000 mm, weight per unit length of 5×10^{-4} N/mm, and a discretization of 200 links. The scaled loop heights, h_{LCP}, were then compared to the theoretical scaled loop height, h_{theor}, using

$$\% \text{ difference} = \left(\frac{h_{LCP} - h_{theor}}{h_{theor}} \right) \times 100 \tag{4.68}$$

The resulting percent difference across the range of of bending stiffness values is shown in Fig. 4.10.

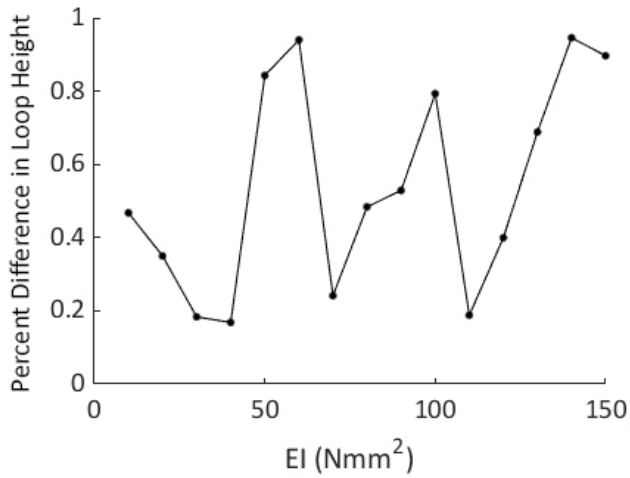

Figure 4.10: The percent difference in scaled loop height between the theoretical model and the proposed linear complementarity method with Hencky bar-chain model.

4.3.4 Conclusion

The results showed that the combined Hencky bar-chain and linear complementarity methods could be used to successfully describe the shape of a free-fold test loop. Existing models are able to correlate loop height to the overall bending stiffness of sheet-like materials, but do not provide further detail about the shape of the folded loop. However, knowing the theoretical shape of the loop is a useful tool to use as a baseline for experimentation or in evaluating additional properties like the curvature over of the loop over the length of the elastica. Understanding properties like the curvature over the loop allow us to predict whether the cross-sectional geometry has changed, which has a known relationship to bending stiffness. Although the loop shape could be calculated using a number of methods because it is a similarity solution, the use of the Hencky bar-chain and linear complementarity methods provide a simple and efficient method for describing the loop shape, in addition to coordinating with the prediction of soft robot interaction forces as described in Chapter 3.

4.4 Chapter Summary

In this chapter, a fold test approach primarily used in textile research was translated to soft robotics to describe the effect that internal pressure has on the bending stiffness of soft elastica — both composite and homogeneous. Three models were presented to describe the relationship between bending stiffness and not only pressure, but also cross-sectional geometry and fiber-reinforcement. Interestingly, it was shown that the change in weight per unit length controls the underlying dependence of bending stiffness on actuation pressure, which is easily measurable in soft robotics. Additionally, the results showed that pressure has more of an effect on bending stiffness for unwrapped elastica compared to fiber-reinforced elastica (FREEs). This is is likely because wrapping elastica with fibers — specifically wrap angles above 54.7° — limits the expansion of the outer diameter of the elastica. Because this chapter showed that bending stiffness is related to cross-sectional geometry, fiber-reinforcement changes the effect that pressure has on bending stiffness.

The results of this chapter also showed that the Hencky bar-chain and linear complementarity methods introduced in Chapter 3 can be applied to the fold test to allow for further analysis of the fold test shape (e.g. curvature) than existing models. Overall, bending stiffness plays a major role in the behavior of soft actuators (e.g. critical buckling load, deformation models, and interaction forces) and the results of this chapter can be used to inform the design and modeling of fluid-powered soft robots as a function of pressure.

Chapter 5

Characterization of Extending Actuators for Soft Robots

5.1 Introduction

McKibben actuators, or pneumatic muscles, have been around since the 1950s when they were first introduced by physician Joseph L. McKibben for use in orthotics and patented by Richard H. Gaylord [58, 183]. The concept of a McKibben actuator is to utilize inextensible fibers wrapped around an elastic tube to generate contraction when pressure is applied to the tube, thus converting fluid power into a pulling force. The advantages of the design include a high force-to-weight ratio, simple construction containing no mechanical parts, and simple operation requiring control of one variable (i.e. pressure). The design is also scalable; McKibben actuators have been used in orthotics, industrial grippers, aerospace designs, and surgical instruments [58, 184, 185, 186].

McKibben actuators are a subset of fiber reinforced elastomeric enclosures (FREEs) and comprise two fibers wrapped at equal and opposite angles from one another over the length of the actuator, as shown in Fig. 1.5. Although McKibbens were designed with the intention of generating contraction, they can also generate extension with a small change in the fiber angle. A fiber angle of 54.7°, commonly referred to as the "magic angle" or the angle of "kinematic lock", is the angle that exactly balances the 2:1 hoop to longitudinal stress induced by internal

pressure [187]. The angle of kinematic lock represents the threshold at which no change in axial length is generated regardless of the input pressure. Wrap angles below and above 54.7° cause the actuator to contract and extend, respectively, with increasing applied pressure. As pressure increases and the actuator changes in length, the angles of the fibers also change until they reach kinematic lock, at which point no more axial change occurs.

Several groups have modeled the strains and forces generated by McKibben actuators. Chou and Hannaford derived a static physical model of McKibbens widely used throughout the soft robotics community, which is based on energy conservation and the geometry of the actuator [95]. The Chou-Hannaford model assumes the actuator is cylindrical, fibers are inextensible and always in contact with the elastomer, friction forces are negligible, and the elastomer forces are negligible. Tondu and Lopez derived a similar model that also incorporated a friction model to better account for hysteresis behavior as a result of thread-on-thread friction within the actuator [188]. Tondu also provided a comprehensive review of McKibben actuators, identifying the lack of a model that addresses effects from the elastomer [96]. Thomalla and Van de Ven addressed this shortcoming by deriving a model to account for the force generated by the elastomer upon contraction and/or extension while also adapting the Chou-Hannaford model to solve for force generated by fibers using only initial geometry [66].

These groups focused on contracting McKibben actuators with large outer diameters (i.e. >10 mm) that generated large contraction forces (i.e. >500 N) [66]. However, very few groups have focused on characterizing actuators below 5 mm in outer diameter, particularly with extending capabilities. De Volder et al. presented a miniature McKibben actuator of 1.5 mm in diameter and 22 mm in length that was able to achieve contraction forces of 6 N and strains up to 15% at 1 MPa [186]. Despite its remarkable force-to-size capabilities, the miniature McKibben did not provide insight into the performance of extending actuators at comparable scales. Other groups, such as Connolly et al. and Bishop-Moser, have explored both extension and compression capabilities of FREE actuators but either assume the elastomeric effects are negligible or require computationally-expensive finite element methods [60, 69].

This chapter applies existing models for contracting McKibben actuators, applies them to extending actuators like the actuator used in the robot in Chapter 2, and characterizes small-scale actuators with outer diameters below 5 mm using empirical methods. Ultimately, this

chapter provides design insight on the tradeoffs between strain and force capabilities for small-scale extending actuators.

5.2 Methods

5.2.1 Applying Contraction Models to Extenders

The Chou-Hannaford models predicts the contraction force by assuming an ideal actuator within a lossless system without energy storage. The "virtual work" argument provides [95]

$$dW_{out} = dW_{in} \tag{5.1}$$

The output work is done when the actuator changes length based on some volume change and the input work is done when fluid – water in this case – pushes against the inner actuator surface. Thus, for an extender that experiences positive axial displacement, dL, for a given input pressure, P, and volume change, dV, eq. 5.1 becomes

$$F_{fibers} dL = P dV \tag{5.2}$$

An adaptation of Thomalla and Van de Ven's model to account for extending actuators provides an expression for F_{fibers} using initial actuator geometries shown in Fig. 5.1 [66]

$$F_{fibers} = P\left(\pi C_1^2 + \pi C_1\left(\frac{t_k(t_k - D_i)}{C_1(\varepsilon - 1)} + D_i(1 - C_2)\left(\frac{t_k}{C_1 C_2(\varepsilon - 1)} - \frac{1}{\sin(\theta_0)\sqrt{C_2}}\right)\right)\right) \tag{5.3}$$

Where C_1 and C_2 are lumped parameter coefficients defined as

$$C_1 = \sqrt{\frac{D_i^2 C_2}{4\sin^2(\theta_0)} - \frac{1}{\sin(\theta_0)\sqrt{C_2}}} \tag{5.4}$$

$$C_2 = 1 - \cos^2\theta_0(\varepsilon - 1)^2 \tag{5.5}$$

and P represents the input pressure, t_k is the initial wall thickness, D_i is the initial outer diameter, θ_0 is the absolute value of the initial fiber wrap angles, and ε is the contraction ratio where the contraction ratio is defined as [66]

$$\varepsilon = \frac{L_0 - L}{L_0} \tag{5.6}$$

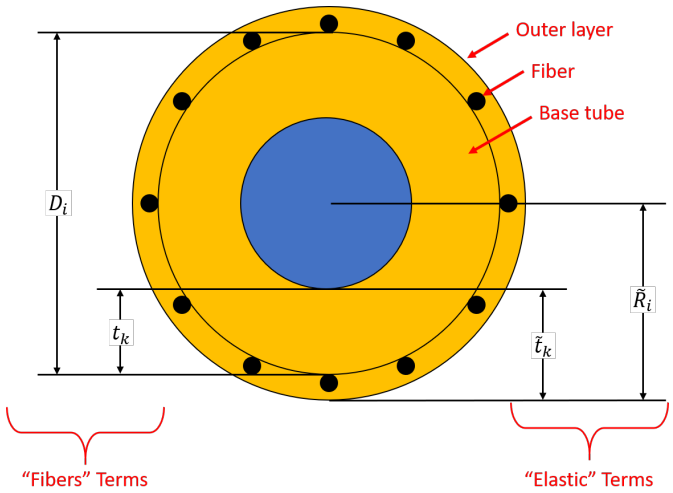

Figure 5.1: Cross-section of extending actuator showing the geometries used calculate the force contributions from both the fibers and elastomer. The actuator contains an inner, elastomeric base tube that is wrapped in inextensible fibers, then dipped in an the same elastomeric material to secure the fibers in place.

However, F_{fibers} represents the force exerted by the ideal actuator and the total force exerted must account for the elastic force within the system [66, 96]. For an extender, the elastic force works against the force generated by fibers as the elastomer is stretched, providing

$$F = F_{fibers} - F_{elastic} \tag{5.7}$$

Thomalla and Van de Ven developed an elastic force model based on the model developed by Kothera et al. [66, 189]. Adapting the model for extending actuators provides

$$F_{elastic} = \pi E \left(\left(\tilde{R}_i^2 - (\tilde{R}_i - \tilde{t}_k)^2 \right) \frac{\varepsilon}{\varepsilon - 1} + \frac{2\tilde{R}_i^2 (1-\varepsilon)^2}{\tilde{R}\tan^2(\theta_0)} \left(\tilde{t} - \frac{\tilde{t}_k}{1-\varepsilon} \right) \right) \tag{5.8}$$

Where the $\tilde{tilde}$ represents the geometry with the outer dip layer thickness included, E is the elastic modulus of the elastomer, and $\tilde{R}_i$ is the initial outer radius as can be seen in Fig. 5.1. $\tilde{R}$ is the current outer radius where $\tilde{R} = \frac{\tilde{D}}{2}$ and

$$\tilde{D} = \frac{\tilde{D}_i \sqrt{1 - (1-\varepsilon)^2 \cos^2(\theta_0)}}{\sin(\theta_0)} \tag{5.9}$$

The current wall thickness, $\tilde{t}$, in eq. 5.8 is expressed as

$$\tilde{t} = \frac{\tilde{D}}{2} - \sqrt{\frac{\tilde{D}^2}{4} - \frac{\tilde{t}_k(\tilde{D}_i - \tilde{t}_k)}{1-\varepsilon}} \tag{5.10}$$

The model assumes the actuator is made from an incompressible, linearly elastic material and conservation of volume throughout pressure application.

5.2.2 Pressure-Dependent Strain and Force Models

The force model from eqs. 5.3, 5.7, and 5.8 provided a better understanding of the pressure- and geometry-dependent behavior of small-scale extenders to use as a design tool for soft robots. The strain capabilities of extending actuators within the operating pressure ranges were deduced from the model, as well as the critical buckling load and blocking force.

Pressure-Dependent Strain

The actuator reached a maximum axial strain when the force generated by pressure and the fiber wrapping was offset by the opposing elastic force, meaning the actuator could not extend any further. To determine the pressure-dependent strain relationship, eq. 5.7 was set equal to 0. The equation was solved over a range of input pressures, P, and the resulting length of the actuator, L, was deduced from the contraction ratio, ε.

Pressure-Dependent Critical Load

The critical load was determined using the pressure-strain relationship above. Eqs. 5.3, 5.7, and 5.8, provided insight on the actuator length, L, outer diameter, $\tilde{D}$, and wall thickness, $\tilde{t}$, as a function of pressure. The cross-sectional dimensions were then used to solve Euler's column formula to determine the critical load [190], where

$$F_{crit} = \frac{\pi^2 EI}{(kL^2)} \tag{5.11}$$

The value of k was chosen to be 0.5 to represent the fixed-fixed end conditions used in testing. The area moment of inertia was calculated by

$$I = \frac{\pi}{64}\left(\tilde{D}^4 - \left(\tilde{D} - \tilde{t}\right)^4\right) \tag{5.12}$$

It is important to note that the critical load determined by eq. 5.11 is for Euler columns with slenderness ratios above the transition slenderness ratio, which is the point at which the Johnson formula becomes more appropriate. All actuators throughout this chapter are assumed to follow the Euler column formula.

Pressure-Dependent Blocking Force

The blocking force is the force achieved when displacement of an actuator is completely blocked, meaning the actuator is working against a load of infinite stiffness [191]. The blocking force was measured by determining the force the actuator exerted after displacing a nominal distance, δL, from its initial length, L_0, without load where

$$\delta L = L - L_0 \tag{5.13}$$

The displacement was incorporated into the contraction ratio, ε, and eqs. 5.7, 5.3, and 5.8 were used to solve for the resulting force, F.

The theoretical pressure-dependent relationships for strain, critical load, and blocking force were determined for three actuator lengths (20 mm, 40 mm, 60 mm) to match the experimental conditions with outer diameters of of 4.27 mm, 4.39 mm, and 4.36 mm, respectively. Two material types (Polytek 74-20 and 74-29) were also modeled and a wrap angle, θ, of 73° was used to match the experimental conditions. A pressure range of 0-30 psi was used for the pressure-dependent strain and critical load and a range of 0-25 psi was used for the blocked force to match the experimental operating pressure while ensuring the actuators did not suffer burst failure before all tests could be completed.

5.2.3 Experimental Setup

The experimental setup for each pressure-dependent relationship is shown below. All experimental tests were run on the same set of actuators of lengths 20 mm, 40 mm, and 60 mm, wrapped at ±73°, and manufactured using the process described in Chapter 3. The actuators were manufactured from a two-part polyurethane of two different stiffnesses (Poly 74-20 and Poly 74-29 Liquid Rubber, Polytek). The tensile test data for the elastomers are shown in Appendix F. Data were collected at 10 Hz using a microcontroller (Teensy 3.5) connected to a pressure transducer (Honeywell TBPDANS030PGUCV) and a load cell amplifier (SparkFun, HX711). Where applicable, a straight bar load cell (SparkFun, TAL221, 500g) was used to collect force data. All pressures discussed throughout this chapter refer to gauge pressure. The camera used for capturing the images (Apple, iPhone 11) was placed at a fixed distance from each test setup.

Pressure-Dependent Strain

The experimental pressure-strain relationship was determined by attaching each actuator to a pressure source (i.e. syringe) and the pressure transducer using a luer lock connection. Each actuator was placed on a sheet of vegetable oil-lubricated acrylic to reduce friction and a 2 mm×2 mm grid was placed under the acrylic for reference. A total of 18 actuators were tested (nine of each material, three at each length) by pressurizing the actuators in increments of 2.5 psi and taking a picture at each increment. The process was repeated three times for each actuator and the images were evaluated using MATLAB's Image Viewer.

Pressure-Dependent Critical Load

The pressure-critical load relationship was determined using the setup shown in Fig. 5.2.

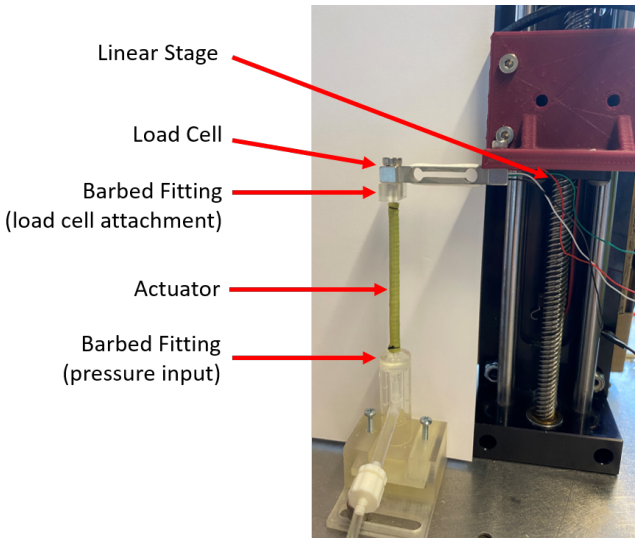

Figure 5.2: Experimental setup for determining critical buckling load of soft actuators.

Each actuator was connected to barbed fittings (manufactured using Form 3 printer, Formlabs), where the bottom barbed fitting was rigidly fixed to the table and connected to the pressure source and the top barbed fitting was rigidly connected to the load cell. The load cell was mounted to a linear stage (ET-250-22, Newmark Systems, Inc.) controlled using the microcontroller (Teensy 3.5) to compress the actuator at a constant speed (1 mm/sec) while collecting force data. The load cell was calibrated before experimentation and tared prior to

each test. Additionally, the linear stage was positioned to account for the axial displacement due to pressurization, which was held constant at each test over the range of 0-30 psi in 5 psi increments. The critical load was determined to be the knee point of the force-displacement data.

Pressure-Dependent Blocking Force

The blocking force was determined using the setup shown in Fig. 5.3.

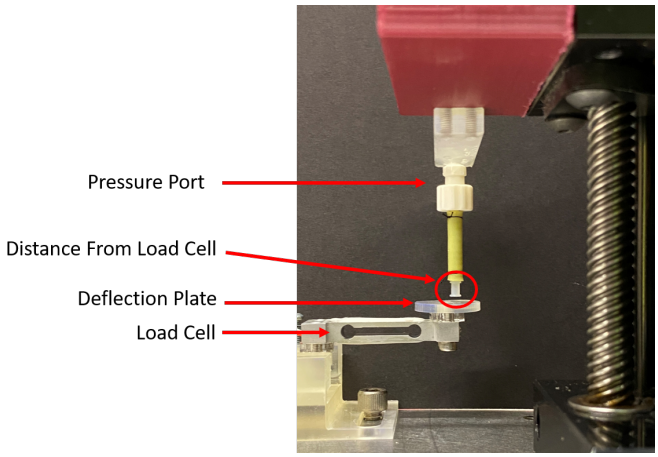

Figure 5.3: Experimental setup for determining blocking force of extending soft actuators.

Each actuator was connected to a pressure port and capped using an off-the-shelf barbed fitting. The pressure port was rigidly connected to the linear stage to allow for accurate spacing between the tip of the actuator and the deflection plate. A load cell was aligned with the actuator and rigidly mounted to the table. A deflection plate was mounted to the load cell to allow forces to still be captured despite small out-of-plane deflections caused by imperfections in the fabrication process. The blocking force capability of each actuator was tested at distances of 0 mm, 1 mm, 2 mm, 3 mm, and 4 mm between the tip of the actuator for pressures of 0-30 psi in 2.5 psi increments. The blocked force was determined as the maximum force recorded by the load cell before buckling.

5.3 Results and Discussion

5.3.1 Theoretical Results and Discussion

The theoretical results for each pressure-dependent relationship are shown below. Although theoretical data were continuous throughout the pressure range modeled, discrete data points are plotted at the pressure increments used for experimentation to allow for easier visual comparison.

Pressure-Dependent Strain

The theoretical results for the pressure-dependent strain are shown in Fig. 5.4 for the two materials examined.

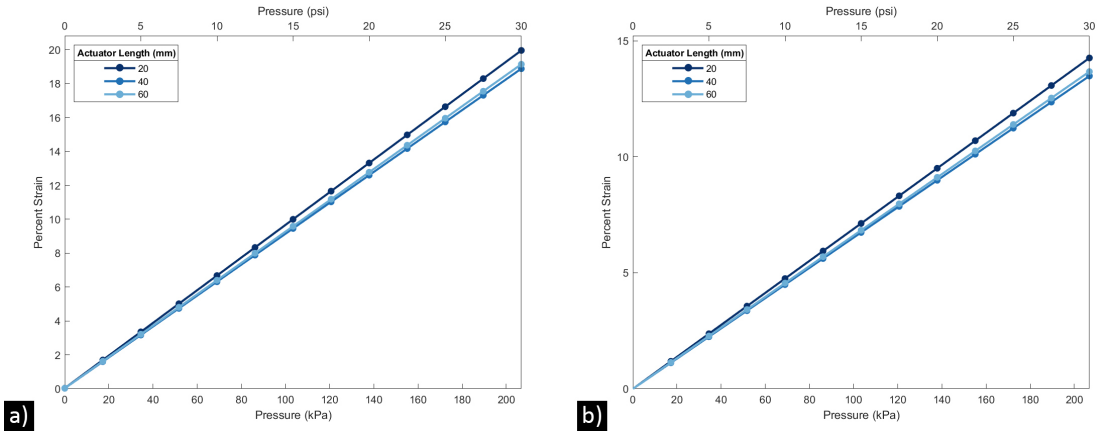

Figure 5.4: Theoretical percent strain with varying pressure for extending actuators of different initial lengths. The theoretical wrap angle of the fibers was $\pm 73°$. The elastic moduli from tensile test data were used for: a) Polytek 74-20 polyurethane, b) Polytek 74-29 polyurethane.

The results show maximum achievable strains of approximately 20% for the softer Polytek 74-20 actuators and maximum strains of approximately 15% for the stiffer Polytek 74-29 actuators. Because the elastomer is assumed to be linearly elastic over the pressure range being modeled, the theoretical strain-pressure relationship is linear as well. The only reason the theoretical strain-pressure relationship is slightly different for each actuator length is because of the slight difference in outer diameters being modeled ($\tilde{D}_i$ = 4.27 mm, 4.39 mm, and 4.36 mm for L_0 = 20 mm, 40 mm, 60 mm, respectively) to match the experimental conditions. Otherwise, the strain-pressure relationship is independent of initial actuator length.

Pressure-Dependent Critical Load

The theoretical results for the pressure-dependent critical load are shown in Fig. 5.5 for the two materials examined.

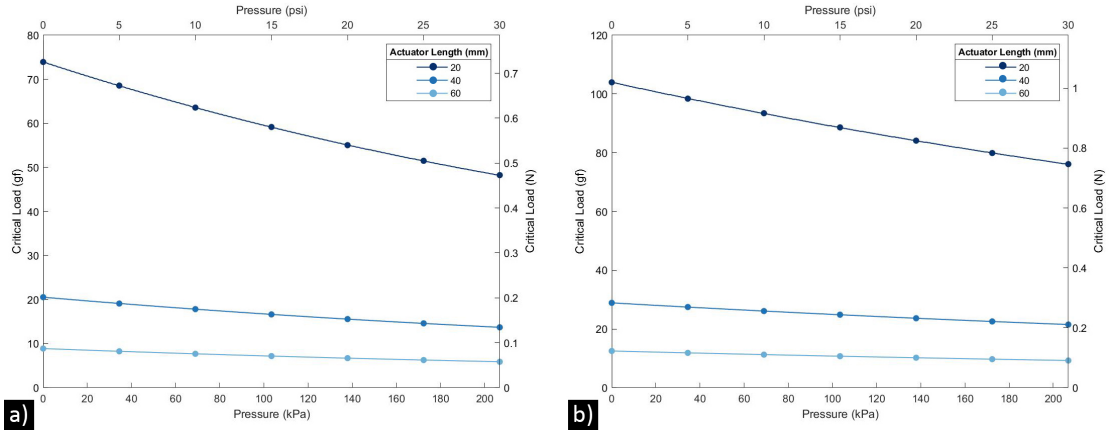

Figure 5.5: Average critical buckling load for pressurized, extending actuators of different initial lengths. The theoretical wrap angle of the fibers was $\pm 73°$. The elastic moduli from tensile test data were used for: a) Polytek 74-20 polyurethane, b) Polytek 74-29 polyurethane.

The results show that the theoretical critical load decreases with pressure, with pressure-sensitivity increasing as initial actuator length is decreased. As expected, the stiffer 74-29 actuators can withstand larger loads before buckling.

Pressure-Dependent Blocking Force

The theoretical results for the pressure-dependent blocking force are shown in Fig. 5.6 for the two materials and three actuator lengths examined.

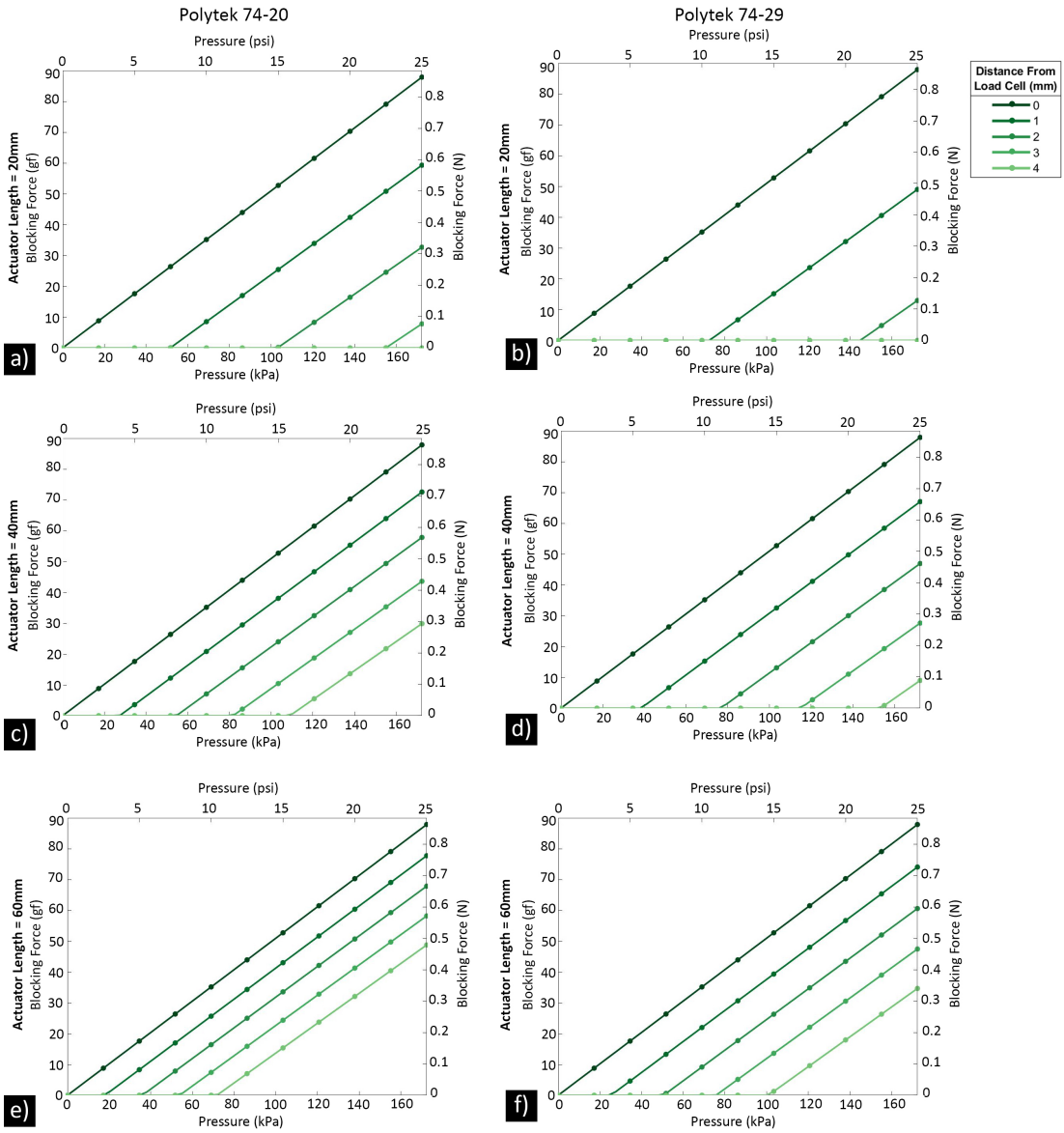

Figure 5.6: Theoretical blocking force with varying pressure and distance from blockage. The theoretical wrap angle of the fibers was $\pm 73°$. The elastic moduli from tensile test data were used for: a,c,e) Polytek 74-20 polyurethane, b,d,f) Polytek 74-29 polyurethane, with initial lengths of a-b) 20 mm, c-d) 40 mm, e-f) 60 mm.

The results show that across both materials and all initial actuator lengths, the theoretical blocking force decreases with distance from the blockage (i.e. load cell) because energy is used to axially displace the actuator. The theoretical blocking force is the same across initial actuator

lengths when the actuator is directly against the blockage (i.e. 0 mm from load cell). However, as distance is introduced between the actuator and blockage, the blocking force-pressure relationship changes because longer actuators displace greater distances per unit of pressure. It should be noted that for the theoretical, pressure-dependent blocking force, actuator failure due to buckling was not considered.

Exploring Strain and Critical Load Over Wrap Angles and Pressure

A grid search was performed to examine the maximum achievable strains and critical loads over the range of extender wrap angles (55°-90°) and operating pressures (0-206.8 kPa, 0-30 psi) for actuators made from Polytek 74-20 at lengths of 20 mm, 40 mm, and 60 mm, as shown in Fig. 5.7. Although results for Polytek 74-29 are not shown, the resulting contours are similar to those of Polytek 74-20.

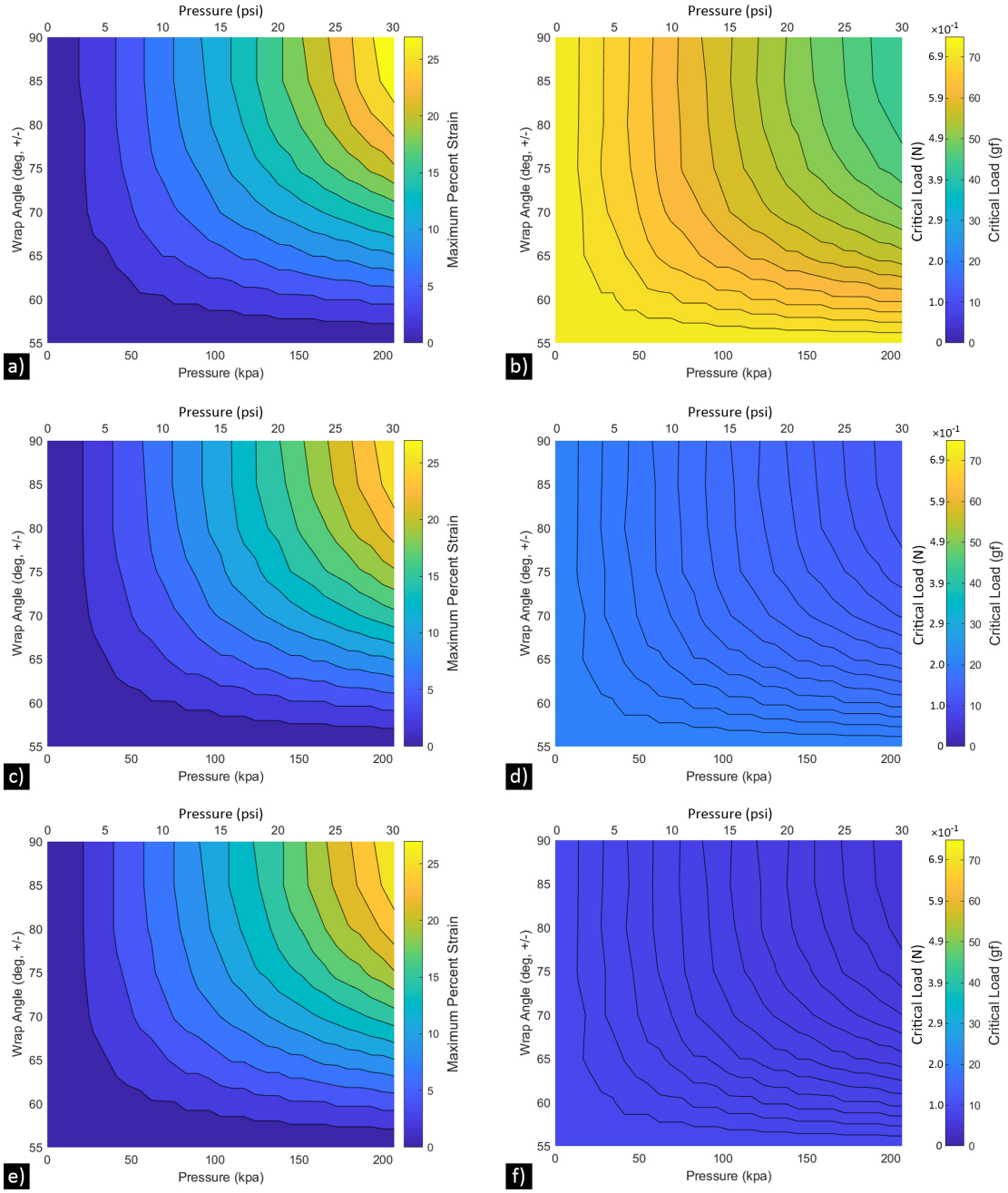

Figure 5.7: a,c,e) Contour plot showing the maximum percent strain achieved from extending actuators as an interaction of wrap angle and pressure. b,d,e) Contour plot showing the critical load of extending actuators as an interaction of wrap angle and pressure. The actuator initial lengths were: a-b) 20 mm, c-d) 40 mm, e-f) 60 mm. The elastic modulus from Polytek 74-20 tensile test data was used.

As was shown in the strain-pressure relationship for the actuators with wrap angles of $\pm 73°$, the strain is independent of initial actuator length. Strain increases with both pressure and wrap angle for $54.7° < \theta \leq 90°$. However, a significant difference can be seen in the critical load contour plots for each initial actuator length. This is because actuators with a longer initial length achieve larger axial displacements per unit of pressure and greater reduction in outer diameter, thus resulting in smaller critical loads. This trade-off is crucial when designing soft robots and must be considered when deciding the geometry and wrap angle of extending actuators. In other words, researchers should determine the maximum load that must be withstood throughout actuation of the robot and use that in combination with the expected operating pressure to prevent actuator failure due to buckling or bursting. For locomoting robots, the blocking force should also be considered to ensure that the extending actuator can not only withstand sufficient loads, but also generate large enough forces to "push" connecting actuators forward without buckling. Finally, the contour plots show the sensitivity of the strain and critical buckling behavior to wrap angle at pressures near the upper end of the operating range, which emphasizes the need for accurate and fabrication techniques to ensure actuators behave as predicted in the model.

Exploring Strain and Critical Load Over Geometry

Beyond the effect of wrap angle on strain and critical load, the effect of cross-sectional geometry can also be explored. The connection between scaling of cross-sectional geometry and size sheds substantial light on the limitations of actuator performance as robot size is reduced. To explore the connection, the cross-sectional geometry of the experimental actuators (ID and Base Tube OD) was scaled up to 3x while keeping the fiber + outer layer thickness, as well as actuator length, constant. Example geometries are shown in Fig. 5.8 and the corresponding dimensions are listed in Table 5.1.

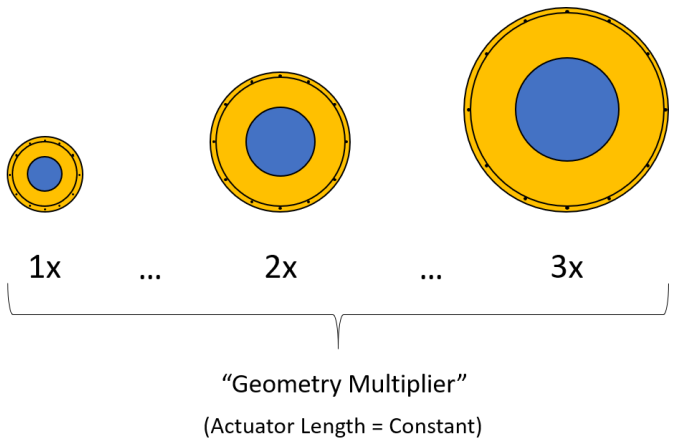

Figure 5.8: The effect of actuator size on strain and critical load capabilities can be explored by scaling the cross-sectional geometry, both inner diameter and outer diameter, of the actuator.

Table 5.1: Cross-sectional geometry dimensions after scaling by geometry multiplier.

Geometry Multiplier	**ID (mm)**	**OD: Base Tube (mm)**	**Total OD: Base Tube + Fiber + Outer Layer (mm)**	**Length (mm)**
1x	1.59	2.80	4.34	60
2x	3.18	5.60	7.14	60
3x	4.77	8.40	9.94	60

The effect of scaling actuator size was explored graphically with contour plots using the equations from Sections 5.2.1 and 5.2.2 to solve for the theoretical strain and critical load of each geometry. The search area for geometry multipliers reached a maximum of 3x to ensure that Euler's column formula was valid for over the entire search area given the constant actuator length of 60 mm in the example shown. The results are shown in Fig. 5.9.

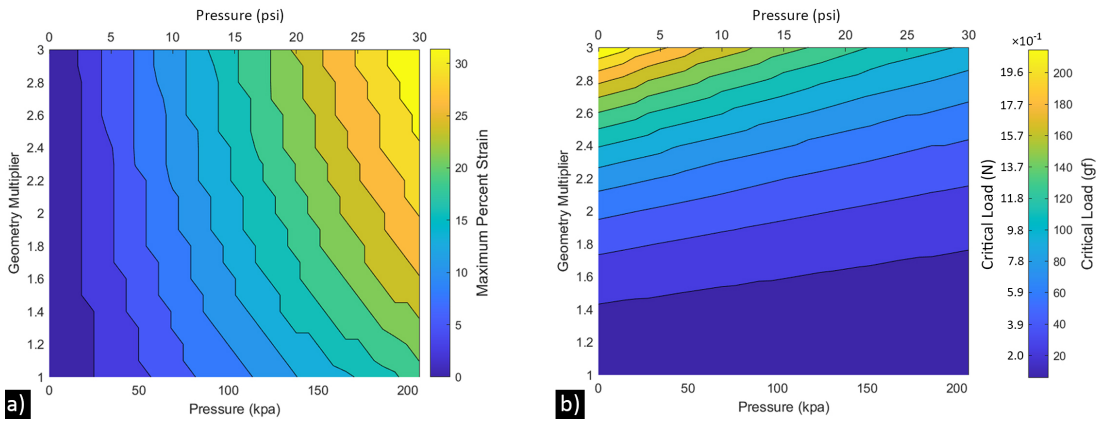

Figure 5.9: Contour plots showing: a) The maximum percent strain achieved from extending actuators as an interaction of geometry multiplier and pressure. b) The critical load of extending actuators as an interaction of geometry multiplier and pressure. The actuator initial length was 60 mm and initial wrap angle was ±73°. The elastic modulus from Polytek 74-20 tensile test data was used.

To provide a second perspective of the results in Fig. 5.9, the percent strain and critical load can be normalized to the values of the "1x" geometry multiplier, as shown in Fig. 5.10.

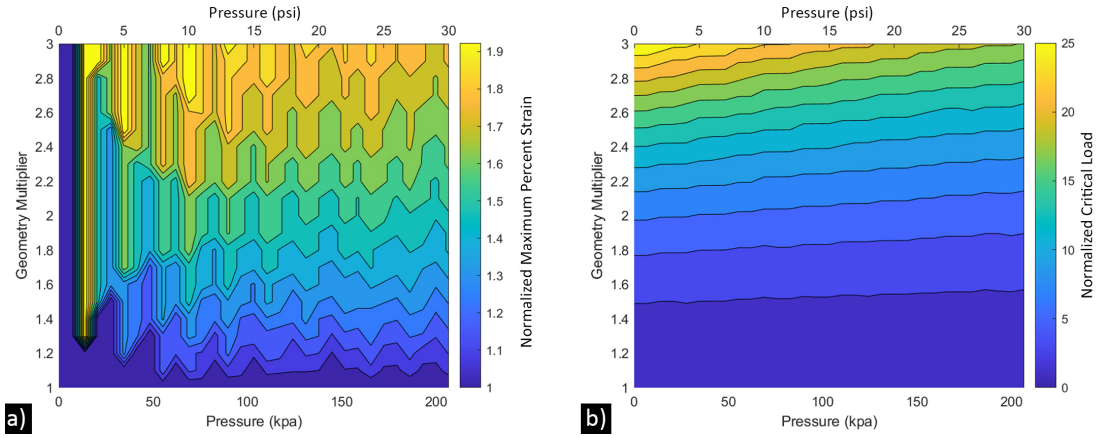

Figure 5.10: Contour plots showing: a) The normalized maximum percent strain achieved from extending actuators as an interaction of geometry multiplier and pressure. b) The normalized critical load of extending actuators as an interaction of geometry multiplier and pressure. The actuator initial length was 60 mm and initial wrap angle was ±73°. The elastic modulus from Polytek 74-20 tensile test data was used.

The results from Figs. 5.9 and 5.10 show that percent strain stays relatively constant regardless of the actuator geometry multiplier. The reason the contour lines in Fig. 5.9a) are not

perfectly vertical, showing that strain stays constant across geometry multipliers, is because it was assumed that the thickness of the fiber + outer layer would be the same for all actuator geometries based on the fabrication process. This assumption prevented the total outer diameter from being scaled linearly, which meant the fiber + outer layer thickness played a much greater role in the overall actuator diameter for geometry multipliers near 1x compared to 3x. Hence, the elastic force from eq. 5.8 is larger near 1x and limits the strain more than at 3x. This effect also appears in the pattern of Fig. 5.10a.

One of the major takeaways of the examination of how actuator size affects behavior is shown in Fig. 5.10b. It is shown that a 3x increase in actuator geometry leads to a 25x increase in the normalized critical load. Looked at another way, the plots show that small reductions in actuator size lead to nearly an order of magnitude greater reduction in resistance to buckling. This consideration is critical when designing robots at the millimeter scale.

5.3.2 Experimental Results and Discussion

The experimental results for pressure-dependent strain are shown in Fig. 5.11.

Pressure-Dependent Strain

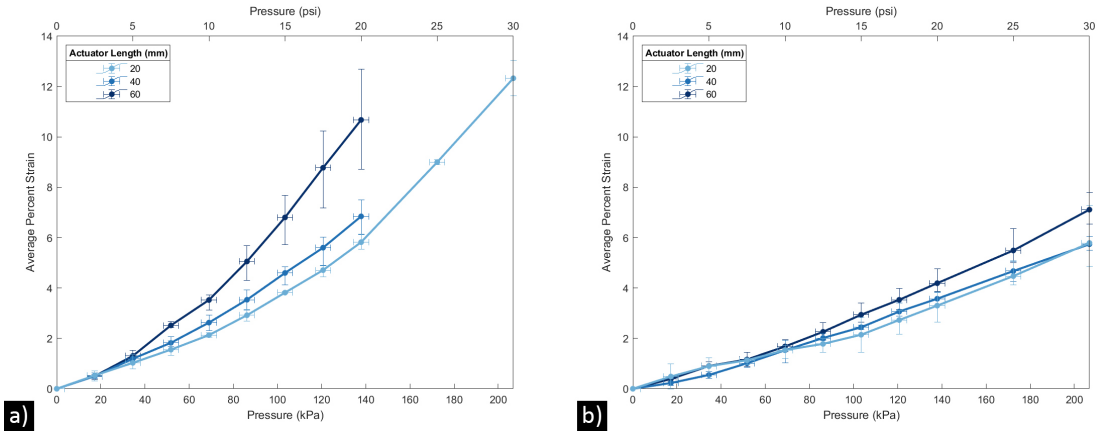

Figure 5.11: Average percent strain with varying pressure for extending actuators of different initial lengths. Each actuator was wrapped with fiber angles of ±73°. N = 9 samples for each data point. The x-error bars indicate the uncertainty in pressure calculated by the maximum fluctuations in pressure transducer output when the pressure port valve was closed. The y-error bars indicate the range of the percent strain measurements for each data point. Actuators made from: a) Polytek 74-20 polyurethane, b) Polytek 74-29 polyurethane.

The relationships for both materials show that the experimental strain-pressure relationships are lower than the theoretical relationships shown in Fig. 5.4 by more than 42% and 61% for Polytek 74-20 and 74-29, respectively. This could be caused by errors in measurement for both the inner and outer diameters as well as the wrap angle, which were both determined using static images and MATLAB's Image Viewer application. The experimental strain-pressure relationship appears nonlinear, particularly for the actuators made from Polytek 74-20, which could be because of the material properties of the elastomer and deviations from the perfect cylinder assumption due to the fabrication process. Because the fabrication process does not guarantee a uniform outer layer used to secure the fibers, slight out-of-plane deflection was observed as the actuator was pressurized, which deviates from the model which assumes all of the energy is being converted into axial displacement.

Pressure-Dependent Critical Load

A comparison between the theoretical critical load and the experimental critical load of unpressurized extending actuators is shown in Fig. 5.12 for the two elastomer materials tested. The yellow envelope displays the theoretical critical load values determined using the elastic moduli from either the tensile test ($E_{tensile}$) or the fold test discussed in Chapter 4 (E_{fold}) and either the full actuator length (L_{full}) or the adjusted length that accounts for the insertion length of the barbed fittings in the experimental setup (L_{short}), diagrammed in Fig. 5.13. It is important to note that the yellow envelopes in Fig. 5.12 represent the theoretical critical load found using Euler's column formula. However, based on the material properties shown in Appendix F and the cross-sectional geometry of the experimental actuators, a transition point from Euler to Johnson formulas occurs near 20 mm and 15 mm for the Polytek 74-20 and 74-29 actuators, respectively.

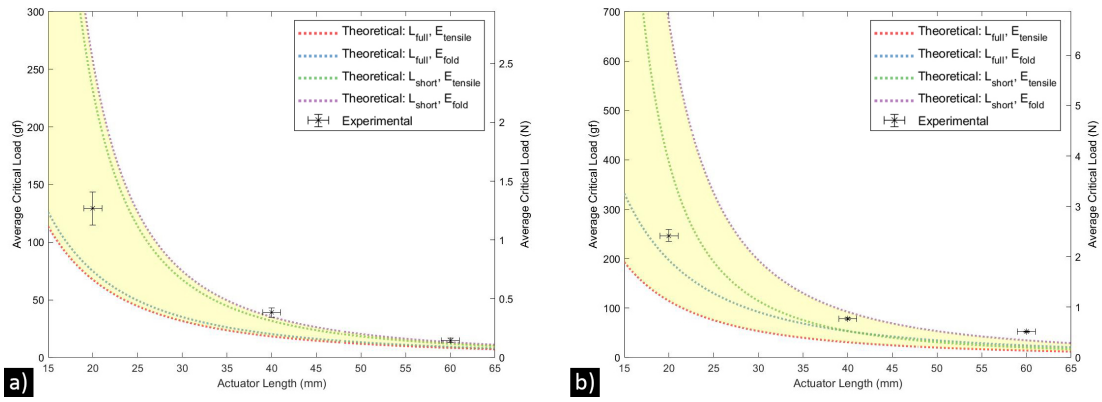

Figure 5.12: Average critical buckling load for unpressurized, extending actuators of different initial lengths fabricated from: a) Polytek 74-20 polyurethane, b) Polytek 74-29 polyurethane. Each actuator was wrapped with fiber angles of $\pm 73°$. N = 3 samples for each data point. The x-axis shown represents L_{full}. The x-error bars indicate the average uncertainty in actuator length based on how the actuators were cut prior to experimentation. The y-error bars indicate the range of the critical load measurements for each data point.

The results show the experimental critical load follows the general theoretical trend, which is that the critical load decreases exponentially as actuator length increases. Additionally, the actuators made from Polytek 74-29, which has a greater elastic modulus than Polytek 74-20, achieved larger critical loads. The unpressurized critical loads for actuator lengths 40 mm and 60 mm fall just above the theoretical envelope for actuators made from Polytek 74-20, as does the critical load for the 60 mm actuator made from Polytek 74-29. These discrepancies are likely caused by inconsistencies in the outer diameter of the experimental actuators caused by the fabrication process, or could be the result of the equipment used in the experimental setup (e.g. the load cell), given that the overall difference between the experimental critical load and the theoretical envelope is less than 10 gf. As can be seen from Fig. 5.12, the theoretical models that utilized the full actuator length (L_{full}) were conservative and consistently underestimated the critical load, with the model that used the elastic modulus from the tensile test ($E_{tensile}$) being the most conservative model. The models that utilized the shorter actuator length (L_{short}) provided less conservative estimates which lead to overestimation of the critical load in some cases, with the model that used the elastic modulus from the free-fold test (E_{fold}) being the least conservative model.

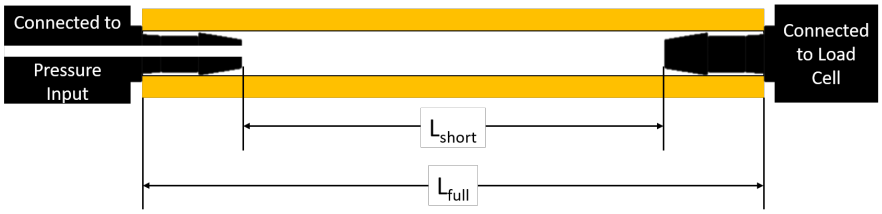

Figure 5.13: Cross-sectional diagram of the actuator and barbed fittings showing the two lengths considered for the unpressurized critical load model.

The experimental pressure-dependent critical load is shown in Fig. 5.14 for the two elastomeric materials tested.

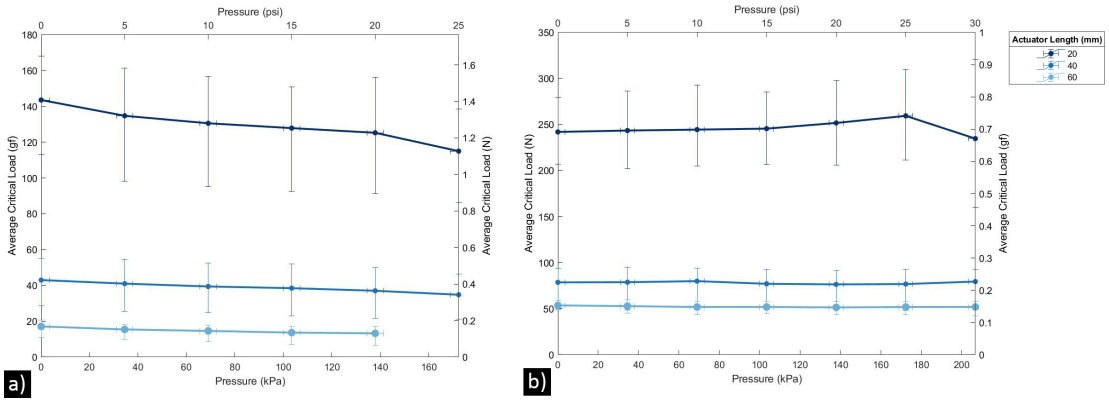

Figure 5.14: Average critical buckling load for pressurized, extending actuators of different initial lengths. Each actuator was wrapped with fiber angles of $\pm 73°$. N = 3 samples for each data point. The x-error bars indicate the uncertainty in pressure calculated by the maximum fluctuations in pressure transducer output when the pressure port valve was closed. The y-error bars indicate the range of the critical load measurements for each data point. Actuators were fabricated from: a) Polytek 74-20 polyurethane, b) Polytek 74-29 polyurethane.

The results show that the experimental critical loads are greater than the theoretical critical loads shown in Fig. 5.5, which is likely a result of slight variations in the actuators due to the fabrication process. However, the slight downward trend for the experimental actuators made from Polytek 74-20 is similar to the theoretical critical load-pressure relationship, where the critical load decreases with an increase in pressure. However, the experimental results for the actuators made from 74-29 do not show a distinguishable pressure dependency. It should be noted that the Polytek 74-20 actuators were tested in ascending order, starting at 0 psi and concluding at 25 psi. However, the Polytek 74-29 actuators were tested in descending order,

starting at 25 psi and ending at 0 psi. Although it was not ideal to induce critical buckling repeatedly for the same actuator, the setup was necessary to ensure that actuators of identical geometries were being tested for the full pressure range. It is possible that the continued buckling of the actuators contributed to lower critical loads as the test progressed.

Pressure-Dependent Blocking Force

The experimental results for the blocking force-pressure relationship are shown in Fig. 5.15.

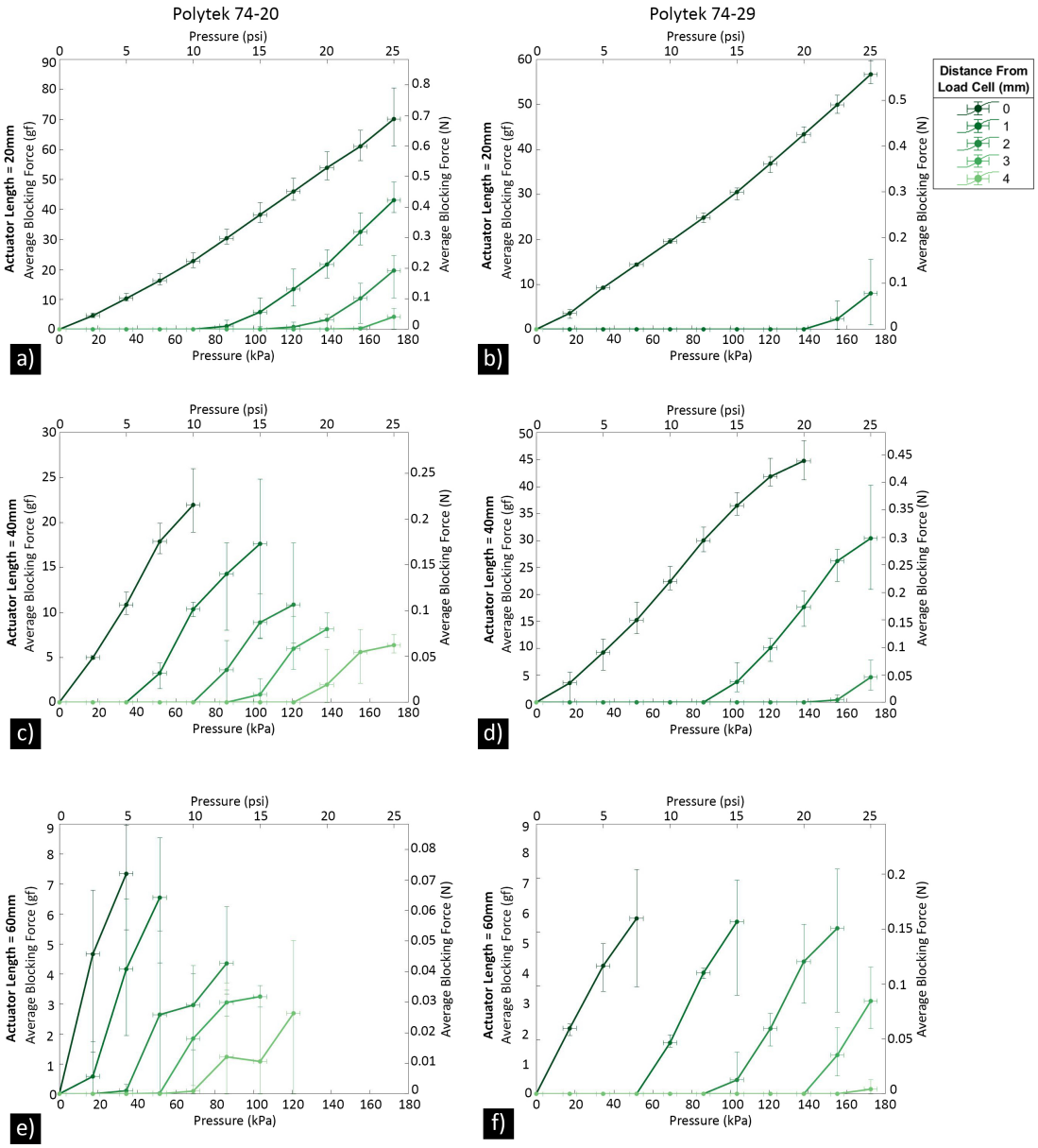

Figure 5.15: Average blocking force with varying pressure and distance from load cell. Each actuator was wrapped with fiber angles of $\pm 73°$. N = 3 samples for each data point. The x-error bars indicate the uncertainty in pressure calculated by the maximum fluctuations in pressure transducer output when the pressure port valve was closed. The y-error bars indicate the range of the blocking force measurements for each data point. Actuators were fabricated from: a,c,e) Polytek 74-20 polyurethane, b,d,f) Polytek 74-29 polyurethane, with initial lengths of a-b) 20 mm, c-d) 40 mm, e-f) 60 mm.

The experimental results are consistent with the critical load results, showing that greater blocking forces can be achieved with shorter actuators because they are more resistant to buckling. However, the benefit comes with the cost of not being able to achieve large strains, which is shown in Fig. 5.15a,b where the 20 mm initial length Polytek 74-20 actuators did not make contact with the load cell at a distance of 4 mm, and the 20 mm, Polytek 74-29 actuators did not make contact with the load cell at distances above 1 mm. In several instances, most notably the 60 mm initial length actuators, the blocking force is only shown up to the pressure at which the actuators did not buckle.

The experimental results are consistent with the theoretical blocking force in that there is clear separation in blocking force as the distance to the load cell is increased. The results also are consistent in that the longer the initial length, the lower the pressure required to generate blocking force. However, the experimental blocking force is consistently lower than the theoretical force because of buckling. The theoretical blocking force did not consider the possibility of the actuators failing due to buckling, although it could be deduced from the critical load results. Additionally, the experimental actuators may have buckled due to fabrication inconsistencies or out-of-plane deflection.

The results for the maximum achievable blocking force, shown in Fig. 5.16, display the trade-off of strain vs. blocking force capabilities. Although the McKibben models discussed throughout Sections 5.2.1 and 5.2.2 do not incorporate actuator buckling into the blocking force prediction, the maximum achievable blocking force could be predicted by overlapping the models for pressure-dependent blocking force and critical buckling load to determine whether blocking force output or critical load is the limiting factor.

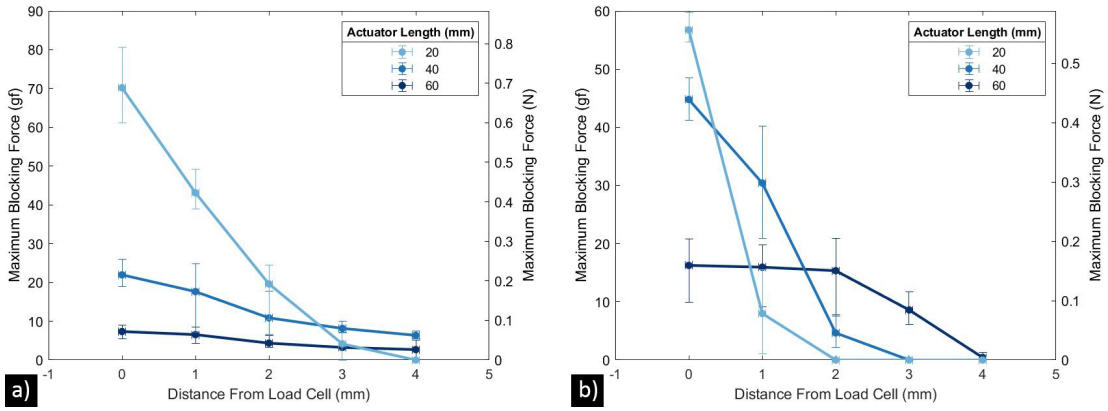

Figure 5.16: Maximum blocking force values for extending actuators of different initial lengths and varying distances from the load cell. Each actuator was wrapped with fiber angles of $\pm 73°$. The x-error bars indicate the average uncertainty in the distance between the tip of the actuator and the load cell. The y-error bars indicate the range of the blocking force at the maximum value. Actuators were fabricated from: a) Polytek 74-20 polyurethane, b) Polytek 74-29 polyurethane.

The compromise is most apparent in the actuators fabricated from Polytek 74-29 (Fig. 5.16b) where the 20 mm initial length actuator achieves the greatest blocking force at 0 mm from the load cell, but quickly declines because the strain the actuator can achieve is not great enough to generate large blocking forces at distances above 1 mm. This has significant consequences for the locomoting soft robot envisioned in earlier chapters due to this fundamental design conflict. Not only do longer actuators (i.e. larger stroke) suffer from increased buckling, but they also suffer lower force output (i.e. blocking force) along the stroke.

Translating the Results

Returning to the example of a locomoting robot, such as the design shown in Chapter 2, extending actuators must withstand sufficient critical loads and achieve sufficient blocking force to advance the most distal actuator, but also must achieve strains large enough to successfully move the robot forward despite inevitable losses due to slippage. In the case required to advance an unpressurized distal actuator that has not begun to anchor into its environment, the blocking force and critical load required by the extender can be approximated by

$$F_{required} = \mu_{s_d} \omega_d L_d \tag{5.14}$$

where μ_{s_d} is the static coefficient of friction between the distal actuator and its environment, and ω_d and L_d are the weight per unit length and overall length of the distal anchoring actuator, respectively.

Taking the example one step further, an approximation of $F_{required}$ for a small-scale, locomoting robot can be performed using information provided throughout this thesis. Let the extending actuator be of length 60 mm, wrap angle $\pm 73°$, and fabricated from Polytek 74-20. Let the environment be a dry acrylic cannula, as discussed in Chapter 2. An approximation of the static coefficient of friction between Polytek 74-20 polyurethane and acrylic is $\mu_{s_d} \approx 1$, $\omega_d = 0.025$ g/mm or 2.45×10^{-4} N/mm per Chapter 3, and $L_d = 120$ mm per Table 2.8. Thus, the minimum blocking force and critical load required by the extending actuator is approximately 3 grams-force (3×10^{-2} N).

This is a reasonable force to withstand even for actuators of millimeter-scale diameters, but two other factors must be kept in mind. The first is that the results, specifically Figs. 5.12 and 5.16 show how quickly force capabilities diminish as actuator length is increased, even at 60 mm. Yet, Fig. 5.7e underscores that for an actuator of length 60 mm and wrap angle $\pm 73°$, the maximum achievable strain in the operating pressure range is about 15%, just 9 mm, of the extender's length. In situations where locomotion efficiency is critical (e.g. surgery), this extension length is detrimental to the robot's efficacy.

The second factor that must be kept in mind is that this example also assumes that the timing of actuation is fully and perfectly controllable, meaning the extender does not "waste" any extension by being pressurized too early, nor does the distal actuator begin to anchor too early, thus creating additional frictional resistance. As Chapter 2 showed, this ideal timing is nearly impossible to achieve at the millimeter size scale because the complexity and sophistication of control mechanisms are limited by the robot's size. All of this must be taken into account when designing soft robots at the millimeter scale, even beyond robot's designed for the specific task of locomoting in the manner described by the example.

5.4 Conclusion

This chapter adapted existing models for contracting McKibben actuators and examined the pressure-dependent behavior of small-scale, extending actuators with outer diameters below 5 mm. Overall, the results highlight the importance of considering both strain and force when

designing soft actuators, particularly at the millimeter-scales examined.

This chapter confirmed existing work in the field of soft robotics — showing that greater strains are achieved with greater wrap angles and higher pressures — but at smaller size scale while also characterizing the force and load-bearing capacities of extending actuators without the need for finite element methods. The work in this chapter is the first known work of its kind in characterizing sub-five-millimeter extending actuators and further emphasizing that although the trade-off between strain and force may be less impactful at larger scales, the compromise plays a critical role at small scales, as was shown in Fig. 5.10b. As such, the extender characterization presented in this chapter can be used as a design tool for small-scale robots that incorporates wrap angle, actuator geometries, and material properties.

Future work could focus on improving the fabrication process and experimental measurements to ensure the actuators are manufactured more consistently and measurements are accurate. Measurements are pivotal for small-scale actuators because forces are on the order of grams-force, results are sensitive to sub-millimeter differences in geometry measurements, and the behavior of the actuators at higher pressures (e.g. above 150 kPa in this chapter) is greatly affected by the accuracy and precision of the fiber wrap angles. These improvements could involve adding a second molding process after the actuators are wrapped to secure the fibers in place with a consistent outer layer and using more advanced measurement tools. Although not discussed in this work, Barlow's Formula could be applied to determine the maximum allowable pressure for the actuators based on the geometries presented in this chapter and the allowable stress of the elastomer. Additionally, others could expand on this work by adapting the McKibben models to account for nonlinear elastic materials and other finer details regarding the interaction of fibers with each other and with the elastomer as they are displaced.

Chapter 6

Conclusions: Tying It All Together

This thesis presents modeling techniques and design tools for soft actuators and robots with a specific focus on small-scale, hydraulic robots with outer diameters below 5 mm. While the fundamental challenges shown to emerge and dominate at increasingly small scales are of key importance to applications like interventional vascular catheters, many of the models can be applied to larger-scale soft robotic actuators as well.

The specific contributions of this thesis are as follows:

- A fluid-powered soft robot capable of locomoting in tube-like environments using only one pressure input to serially control a robot comprised of multiple actuators (Chapter 2). The contribution of a fully passive, serial locomotion design and methodology is particularly valuable in space-limited applications (e.g. medical) where using multiple pressure input lines is not possible due to space restrictions. The simple orifice design of passive valves remains attractive for increasingly small scales but the resulting prohibitive increase in design sensitivity to performance suggests that the passive approach is not scalable unless a simple time-delay valve feature is added.

- Characterization of the anchoring forces achieved by small-scale actuators in tube-like environments (Chapter 2). The results of this work display the effects of anchoring actuator design choices on both fabrication (i.e. generating actual actuator shapes that match the

expected model) as well as anchoring ability. Utilizing simple, planar designs not only result in actuators that align with expected shape behaviors, but also simplify contact modeling.

- A computationally-practical interaction model to predict the shape and forces generated by soft robots when constrained by rigid environments (Chapter 3). The model introduces Hencky Bar-Chain and Linear Complementarity methods to soft robots to create a computationally-efficient contact model that can also be extended to soft actuators beyond hydraulic FREEs. The model can track the distributed position of soft actuators with high accuracy (1.06% difference between model and experiment) and get meaningful estimates of contact and internal body forces (21-45% difference between model and experiment) using only knowledge of end conditions and constraint location. Ultimately, the model offers a solution to soft robot contact modeling that does not require embedded sensors nor time-consuming alternatives like finite element methods.

- A model of pressure-dependent bending stiffness for both wrapped and unwrapped soft elastomeric tubes (Chapter 4). The model translates a simple and straightforward free-fold test used primarily in textile research to the field of soft robotics to determine the bending stiffness vs. pressure relationship of both composite and homogeneous actuators. The free-fold test method provides strong estimates (within 6.86% of bending stiffness estimates determined from tensile tests and cross section measurements) of actuator bending stiffness using only a single photo and without the need for pressure/force sensors or bending perturbations.

- Adaptation of existing McKibben models to small-scale extending actuators for pressure-dependent strain and force characterization (Chapter 5). The presented work offers insight into the trade-offs of designing small-scale actuators that must achieve sufficient axial displacements while also resisting buckling throughout actuation, which has not been presented for sub-five-millimeter diameter extending actuators to date. The models show that small scale soft actuators, particularly those with high aspect ratios — where the axial length is much greater than the diameter — have conflicting design implications. Increasing actuator length, or aspect ratio, results in greater extending stroke but decreased

resistance to buckling. Additionally, decreasing the cross-sectional geometry of the actuator by 3x leads to an approximately 25x decrease in critical buckling load for the actuators empirically tested in this work (ID = 1.59 mm, Total OD = 4.34 mm, L = 60 mm). These contributions provide insight to soft robot designers to strike the proper balance between actuator aspect ratio, buckling resistance, and achievable extension while highlighting the limitations placed on soft robot capabilities when reducing the diameter of the robot to fit in tight environments such as human arteries.

Each individual contribution ties into the design of small-scale soft robots, where effects that can be assumed negligible at large scales drastically affect robot behavior at small scales. The interaction model presented in Chapter 3 can be used to determine the limitations in anchoring capabilities while ensuring the force and shapes of the robot are safe within delicate environments. The work in Chapter 4 provides insight on how the interaction model and other models that require knowledge of the bending stiffness may change with pressure. Finally, the characterization of the extending actuators underscores the importance of considering the trade-off between strain and force capabilities and provides a design tool for deciding the actuator geometries and fiber wrap angles that work best for a given application. These contributions are particularly relevant to improving locomotion performance in robots similar to the robot presented in Chapter 2 where the design of each robot component must be carefully considered using the presented models. However, each chapter also contributes knowledge to the soft robotics community that can be adapted and built upon for actuators and applications beyond those discussed in this work.

The work presented in this thesis resulted in one published journal paper [1], two journal papers in submission [134, 167], one journal technical brief [2], two conference papers [110, 4], three conference workshop presentations [111, 3, 135], one filed patent [192], and one pending patent application.

6.1 Limitations and Future Work

As mentioned, the work presented in this thesis provides a foundation for straightforward modeling of soft robot components, from deformation to force generation. However, much of this work can be built upon in the future to continue adding contributions to the growing field of

soft robotics. One contribution that could improve the presented models would be the incorporation of friction between the robot and its environment, particularly within the anchoring force characterization for serial locomotion as well as the interaction model. Tribology, which includes the study and application of the principles of friction, is an entire field of study and biotribology particularly remains an underexplored but active area of research. As such, both static and kinetic friction should eventually be incorporated into contact and locomotion models. Nonetheless, the major effects of friction in soft robotic systems would benefit even from a simple, static friction model.

As was shown throughout this work, scaling the size of soft robots down while maintaining functionality (e.g. locomotion, anchoring, etc.) and force output is one of the biggest challenges facing soft robotics. Although hydraulic actuation is one of the most power-dense options for soft robot actuation, forces drastically decrease with size reduction. Another core challenge, particularly for hydraulically actuated robots, is the need for control methods at such small scales. Chapter 2 discussed the need for controllability at the millimeter scale, and an advancement in valve designs at the millimeter scale would be a major contribution to soft robotics. However, valves for advanced control often require complex fabrication techniques, extremely small components, and thus far have shown to significantly increase the time required for actuation.

Furthermore, the modeling and experimentation of soft robots will improve as fabrication and measurement techniques improve. As this work showed, models of robot behavior at small-scales are quite sensitive, with forces on the order of grams-force and geometries on the order of millimeters or less. Because of this challenge, many of the models presented in this work were supplemented by experimental evidence or based on empirical measurements. The ability to measure forces, fiber angles, and volumetric displacements quickly, accurately, and affordably would help resolve discrepancies between theoretical models and experimental behavior, though the fundamental challenges identified in scaling down suggest that such efforts may not be adequately motivated.

Although fiber reinforced actuators are among the most common in soft robotics, the shapes they can generate are quite limited based on their design. In turn, the limited set of shapes restricts the behaviors that can be achieved with soft robots. One potential improvement that others have begun to investigate is the concept of fabricating custom actuators using 3D printing or other means to generate shapes that are primarily limited by material properties and basic

physics. Despite not being discussed in the main portion of this thesis, additional exploratory work in the field of customizable soft actuators that utilize inverse design techniques is presented in Appendix E.

Each of these limitations are particularly pertinent to the medical relevance of soft robots. For procedures beyond the colon and other anatomy with larger cross-sections, the robots must be small in size (i.e. below 5 mm in diameter). In any medical scenario, safety and control is key and despite the compliance of soft robots being beneficial for safety, control and predictability are major challenges. The other critical component of medical soft robots is oftentimes their ability to incorporate a working channel into their structure, which allows surgical tools to be passed through the body of the robot to perform surgical asks. Unfortunately, a working channel consumes much of the necessary space in small-scale robots, especially in hydraulic robots where the center channel is needed for fluid. Beyond the space, adding tools to make the robot useful adds additional payload to already limited force capabilities. Finally, time is extremely valuable in any medical situation whether the procedure is urgent or routine. A robot must be able to locomote efficiently, actuate quickly, and integrate smoothly into well-established medical workflows. When such robots are scaled down, their whole-body locomotion efficiency can also be scaled down because of limited axial displacements and potentially slow control mechanisms or components.

Overall, the soft robotics community should continue to strive to overcome the above limitations by building off of the foundations laid in existing work and the work presented in this thesis to merge the benefits of compliant soft robots with the utility of small-scale instruments. Particular emphasis should be placed on overcoming fundamental challenges, such as the buckling limit and vanishing force density, particularly for high aspect ratio robots at millimeter to sub-millimeter scales.

Bibliography

[1] Mark D. Gilbertson, Gillian McDonald, Gabriel Korinek, James D. Van de Ven, and Timothy M. Kowalewski. Serially Actuated Locomotion for Soft Robots in Tube-Like Environments. *IEEE Robot. Autom. Lett.*, 2(2):1140–1147, apr 2017.

[2] Mark D. Gilbertson, Gillian McDonald, Gabriel Korinek, James D. Van de Ven, and Timothy M. Kowalewski. Soft Passive Valves for Serial Actuation in a Soft Hydraulic Robotic Catheter. *ASME Journal of Medical Devices*, 10(3):030931, 2016.

[3] Chaitanya Awasthi, Gillian McDonald, Mark D. Gilbertson, James D. Van de Ven, and Timothy M. Kowalewski. Generalized Kinematics for Deformable Patient-Specific Soft Robots. In *IEEE/RSJ Int. Conf. Robot. Intell. Sys. (IROS) [Poster Presentation]*, 2017.

[4] Mark D. Gilbertson, Gillian J. McDonald, Chaitanya Awasthi, Rumi Faizer, and Timothy M. Kowalewski. Computational Inverse Design of Anatomy-Specific Soft Robot Actuators with Physically-Realizable Material Conditions of Vascular Surgery. In *Hamlyn Symposium on Medical Robotics*, number 3, pages 3–4, 2018.

[5] N.G. Hockstein, C.G. Gourin, R.A. Faust, and D.J. Terris. A history of robots: from science fiction to surgical robotics. *J. Robot. Surg.*, 1(2):113–118, 2007.

[6] Charlotte Tsui, Rachel Klein, and Matthew Garabrant. Minimally invasive surgery: national trends in adoption and future directions for hospital strategy. *Surgical Endoscopy*, 27(7):2253–2257, 2013.

[7] Andrew J. Epstein, Peter W. Groeneveld, Michael O. Harhay, Feifei Yang, and Daniel Polsky. Impact of Minimally Invasive Surgery on Medical Spending and Employee Absenteeism. *JAMA Surgery*, 148(7):641, 2013.

[8] Anthony R Lanfranco, Andres E Castellanos, Jaydev P Desai, and William C Meyers. Robotic Surgery A Current Perspective. *Ann Surg*, 239:14–21, 2004.

[9] Research and Markets; 2020 Insights into Regulatory and Reimbursement Scenario of Robotic-Assisted Surgery. *Medical Devices & Surgical Technology Week*, page 1833, sep 2020.

[10] Jaydeep H Palep. Robotic assisted minimally invasive surgery. *Journal of minimal access surgery*, 5(1):1–7, jan 2009.

[11] Tiago Leal Ghezzi and Oly Campos Corleta. 30 Years of Robotic Surgery. *World Journal of Surgery*, 40(10):2550–2557, oct 2016.

[12] Salim S. Virani, Alvaro Alonso, Emelia J. Benjamin, Marcio S. Bittencourt, Clifton W. Callaway, April P. Carson, Alanna M. Chamberlain, Alexander R. Chang, Susan Cheng, Francesca N. Delling, Luc Djousse, Mitchell S.V. Elkind, Jane F. Ferguson, Myriam Fornage, Sadiya S. Khan, Brett M. Kissela, Kristen L. Knutson, Tak W. Kwan, Daniel T. Lackland, Tené T. Lewis, Judith H. Lichtman, Chris T. Longenecker, Matthew Shane Loop, Pamela L. Lutsey, Seth S. Martin, Kunihiro Matsushita, Andrew E. Moran, Michael E. Mussolino, Amanda Marma Perak, Wayne D. Rosamond, Gregory A. Roth, Uchechukwu K.A. Sampson, Gary M. Satou, Emily B. Schroeder, Svati H. Shah, Christina M. Shay, Nicole L. Spartano, Andrew Stokes, David L. Tirschwell, Lisa B. VanWagner, Connie W. Tsao, Sally S. Wong, and Debra G. Heard. Heart disease and stroke statistics—2020 update: A report from the American Heart Association. *Circulation*, 141:E139–E596, 2020.

[13] Aamir Hameed, Zafar Haroon, Mylotte Darren, and Sharif Faisal. Recent Trends in Clot Retrieval Devices: A Review. *Cardiol Ther*, 6:193–202, 2017.

[14] Jeffrey L. Saver, Mayank Goyal, Aad Van Der Lugt, Bijoy K. Menon, Charles B.L.M. Majoie, Diederik W. Dippel, Bruce C. Campbell, Raul G. Nogueira, Andrew M. Demchuk, Alejandro Tomasello, Pere Cardona, Thomas G. Devlin, Donald F. Frei, Richard Du Mesnil De Rochemont, Olvert A. Berkhemer, Tudor G. Jovin, Adnan H. Siddiqui, Wim H. Van Zwam, Stephen M. Davis, Carlos Castaño, Biggya L. Sapkota, Puck S. Fransen, Carlos Molina, Robert J. Van Oostenbrugge, Ángel Chamorro, Hester Lingsma, Frank L. Silver,

Geoffrey A. Donnan, Ashfaq Shuaib, Scott Brown, Bruce Stouch, Peter J. Mitchell, Antoni Davalos, Yvo B.W.E.M. Roos, and Michael D. Hill. Time to treatment with endovascular thrombectomy and outcomes from ischemic stroke: Ameta-analysis. *JAMA - Journal of the American Medical Association*, 316(12):1279–1288, 2016.

[15] MN Department of Health. Minnesota Stroke System Designated Hospitals. https://www.health.state.mn.us/diseases/cardiovascular/stroke/designationlist.html.

[16] Kori S. Zachrison, Jukka Pekka Onnela, Adrian Hernandez, Mathew J. Reeves, Carlos A. Camargo, Margueritte Cox, Roland A. Matsouaka, Joshua P. Metlay, Joshua N. Goldstein, and Lee H. Schwamm. Ischemic Stroke Transfer Patterns in the Northeast United States. *Journal of Stroke and Cerebrovascular Diseases*, 28(2):295–304, 2019.

[17] Jeffrey L. Saver. Time is brain - Quantified. *Stroke*, 37(1):263–266, 2006.

[18] Guanjun Bao, Hui Fang, Lingfeng Chen, Yuehua Wan, Fang Xu, Qinghua Yang, and Libin Zhang. Soft Robotics: Academic Insights and Perspectives Through Bibliometric Analysis. *Soft Robotics*, 5(3):229–241, 2018.

[19] Surya G. Nurzaman, Fumiya Iida, Cecilia Laschi, Akio Ishiguro, and Robert Wood. Soft Robotics [TC Spotlight]. *IEEE Robotics & Automation Magazine*, 20(3):24–95, sep 2013.

[20] Barbara Mazzolai and Virgilio Mattoli. Robotics: Generation Soft. *Nature*, 536(7617):400–401, 2016.

[21] Alin Albu-Schaffer, Oliver Eiberger, Markus Grebenstein, Sami Haddadin, Christian Ott, Thomas Wimböck, Sebastian Wolf, and Gerd Hirzinger. Soft Robotics. *IEEE Robotics and Automation Magazine*, 15(3):20–30, 2008, MRA.2008.927979.

[22] Deepak Trivedi, Christopher D Rahn, William M Kier, and Ian D Walker. Soft robotics: Biological inspiration, state of the art, and future research. *Appl. Bionics Biomech.*, 5(3):99–117, 2008.

[23] Jonathan Rossiter and Helmut Hauser. Soft robotics - The next industrial revolution? *IEEE Robotics and Automation Magazine*, 23(3):17–20, 2016.

[24] Erico Guizzo. Soft Robotics. *IEEE Robotics & Automation Magazine*, 19(1):123–128, mar 2012.

[25] Rolf Pfeifer, Max Lungarella, and Fumiya Iida. The Challenges Ahead for Bio-Inspired 'Soft' Robotics. *Communications of the ACM*, 55(11):76–87, 2012.

[26] Jungwook Paek, Inho Cho, and Jaeyoun Kim. Microrobotic tentacles with spiral bending capability based on shape-engineered elastomeric microtubes. *Scientific Reports*, 5, 2015.

[27] Daniela Rus and Michael T. Tolley. Design, fabrication and control of soft robots. *Nature*, 521:467–475, 2015.

[28] M. W. Hannan and I. D. Walker. Analysis and experiments with an elephant's trunk robot. *Advanced Robotics*, 15(8):847–858, 2001.

[29] Neurovascular Product Catalog. Technical report, Medtronic, 2020. https://brandcentral.medtronic.com/content/dam/medtronic-com/products/neurological/neurovascular-product-catalog.pdf.

[30] Catheters. In Jeffrey K. Aronson, editor, *Meyler's Side Effects of Drugs*, pages 175–179. Elsevier, 16 edition, 2016.

[31] Filip Ilievski, Aaron D. Mazzeo, Robert F. Shepherd, Xin Chen, and George M. Whitesides. Soft Robotics for Chemists. *Angewandte Chemie*, 123(8):1930–1935, 2011.

[32] Ela Sachyani Keneth, Alexander Kamyshny, Massimo Totaro, Lucia Beccai, and Shlomo Magdassi. 3D Printing Materials for Soft Robotics. *Advanced Materials*, 2020.

[33] Ali Zolfagharian, Akif Kaynak, and Abbas Kouzani. Closed-loop 4D-printed soft robots. *Materials and Design*, 188:108411, 2020.

[34] Benjamin Shih, Caleb Christianson, Kyle Gillespie, Sebastian Lee, Jason Mayeda, Zhaoyuan Huo, and Michael T. Tolley. Design considerations for 3D printed, soft, multi-material resistive sensors for soft robotics. *Frontiers Robotics AI*, 6:1–12, 2019.

[35] T. J. Wallin, J. Pikul, and R. F. Shepherd. 3D printing of soft robotic systems. *Nature Reviews Materials*, 3(6):84–100, 2018.

[36] François Schmitt, Olivier Piccin, Laurent Barbé, and Bernard Bayle. Soft robots manufacturing: A review. *Frontiers Robotics AI*, 5, 2018.

[37] Kirstin H. Petersen and Robert F. Shepherd. *Fluid-driven intrinsically soft robots*. Elsevier Ltd., 2019.

[38] Sangbae Kim, Cecilia Laschi, and Barry Trimmer. Soft robotics: a bioinspired evolution in robotics. *Trends in Biotechnology*, 31:287–294, 2013.

[39] Adam W Feinberg. Biological Soft Robotics. *Annu. Rev. Biomed. Eng*, 17:243–65, 2015.

[40] Cecilia Laschi, Matteo Cianchetti, Barbara Mazzolai, Laura Margheri, Maurizio Follador, and Paolo Dario. Soft Robot Arm Inspired by the Octopus. *Advanced Robotics*, 26(7):709–727, 2012.

[41] Marcello Calisti, Michele Giorelli, Guy Levy, Barbara Mazzolai, B Hochner, Cecilia Laschi, and Paolo Dario. An octopus-bioinspired solution to movement and manipulation for soft robots. *Bioinspir. Biomim.*, 6(3):036002, 2011.

[42] Ming Luo, Weijia Tao, Fuchen Chen, Tri K. Khuu, Selim Ozel, and Cagdas D. Onal. Design improvements and dynamic characterization on fluidic elastomer actuators for a soft robotic snake. *IEEE Conference on Technologies for Practical Robot Applications, TePRA*, pages 1–6, 2014.

[43] Yunteng Cao, Yilun Liu, Youlong Chen, Liangliang Zhu, Yuan Yan, and Xi Chen. A novel slithering locomotion mechanism for a snake-like soft robot. *J. Mech. Phys. Solids*, 99:304–320, 2017.

[44] Wei Wang, Jang-Yeob Lee, Hugo Rodrigue, Sung-Hyuk Song, Won-Shik Chu, and Sung-Hoon Ahn. Locomotion of inchworm-inspired robot made of smart soft composite (SSC). *Bioinsp. Biomim.*, 9(4), 2014.

[45] Paolo Dario, Pasquale Ciarletta, Arianna Menciassi, and Byungkyu Kim. Modeling and Experimental Validation of the Locomotion of Endoscopic Robots in the Colon. *The International Journal of Robotics Research*, 23(5):549–556, 2004.

[46] Andrew T. Conn, Andrew D. Hinitt, and Pengchuan Wang. Soft segmented inchworm robot with dielectric elastomer muscles. In *Proceedings of SPIE - Electroactive Polymer Actuators and Devices (EAPAD)*, volume 9056, 2014.

[47] S. Seok, C. D. Onal, K. J. Cho, R. J. Wood, D. Rus, and S. Kim. Meshworm: A peristaltic soft robot with antagonistic nickel titanium coil actuators. *IEEE/ASME Trans. Mechatronics*, 18(5):1485–1497, Oct 2013.

[48] Jinhua Zhang, Jiaqing Tang, Jun Hong, Tongqing Lu, and Hao Wang. The Design and Analysis of Pneumatic Rubber Actuator of Soft Robotic Fish. In *ICIRA Int. Robot. Appl.*, pages 320–327. Springer, dec 2014.

[49] Constantina Lekakou, Yahya Elsayed, Tao Geng, and Chakravarthini M. Saaj. Skins and Sleeves for Soft Robotics: Inspiration from Nature and Architecture. *Advanced Engineering Materials*, 17(8):1180–1188, 2015.

[50] Oded Salomon and Alon Wolf. Inclined Links Hyper-Redundant Elephant Trunk-Like Robot. *Journal of Mechanisms and Robotics*, 4(4):045001, 2012.

[51] Bao Guanjun, Yao Pengfei, Xu Zonggui, Li Kun, Wang Zhiheng, Zhang Libin, Yang Qinghua, Bao G J, Yao P F, Xu Z G, Wang Z H, and Zhang L B. Pneumatic bio-soft robot module: Structure, elongation and experiment. *Int. J. Agric. & Biol. Eng.*, 10(102):114–122, 2017.

[52] Elliot W Hawkes, Laura H Blumenschein, Joseph D Greer, and Allison M Okamura. A soft robot that navigates its environment through growth. *Sci. Robot*, 2:1–7, 2017.

[53] Joseph D. Greer, Tania K. Morimoto, Allison M. Okamura, and Elliot W. Hawkes. A Soft, Steerable Continuum Robot That Grows via Tip Extension. *Soft Robotics*, 6(1):95–108, 2019.

[54] Seref Kemal Talas, Bora Alp Baydere, Timur Altinsoy, Cem Tutcu, and Evren Samur. Design and Development of a Growing Pneumatic Soft Robot. *Soft Robotics*, 7(4):521–533, 2020.

[55] Nazek El-Atab, Rishabh B. Mishra, Fhad Al-Modaf, Lana Joharji, Aljohara A. Alsharif, Haneen Alamoudi, Marlon Diaz, Nadeem Qaiser, and Muhammad Mustafa Hussain. Soft Actuators for Soft Robotic Applications: A Review. *Advanced Intelligent Systems*, 2(10):2000128, 2020.

[56] Aline De Greef, Pierre Lambert, and Alain Delchambre. Towards flexible medical instruments: Review of flexible fluidic actuators. *Precis. Eng.*, 33(4):311–321, 2009.

[57] Koichi Suzumori, Takafumi Matsumaru, and Shoichi Iikura. Elastically Deformable Fluid Actuator, U.S. Patent 4976191, 1989.

[58] Georgios Andrikopoulos, Georgios Nikolakopoulos, and Stamatis Manesis. A survey on applications of pneumatic artificial muscles. In *Med. Conf. Cont. Autom.*, pages 1439–1446. IEEE, 2011.

[59] Soft Robotics Toolkit. PneuNets Bending Actuators. https://softroboticstoolkit.com/book/pneunets-bending-actuator.

[60] J. Bishop-Moser and S. Kota. Design and modeling of generalized fiber-reinforced pneumatic soft actuators. *IEEE Trans. Robot.*, 31(3):536–545, Jun 2015.

[61] Panagiotis et al. Polygerinos. Modeling of soft fiber-reinforced bending actuators. *IEEE Trans. Robot.*, 31(3):778–789, 2015.

[62] Larry D Peel. *Fabrication and mechanics of fiber-reinforced elastomers.* PhD thesis, Brigham Young University, 1998.

[63] Ching-Ping Chou and Blake Hannaford. Measurement and modeling of mckibben pneumatic artificial muscles. *IEEE Trans. Robot. Autom.*, 12(1):90–102, 1996.

[64] Joshua Bishop-Moser, Girish Krishnan, Charles Kim, and Sridhar Kota. Design of soft robotic actuators using fluid-filled fiber-reinforced elastomeric enclosures in parallel combinations. In *IEEE/RSJ Int. Conf. Intell. Robot. Sys.*, pages 4264–4269. IEEE, 2012.

[65] Omotayo F Ewumi. *Experimentally characterized embedded McKibben muscles as a nastic material for biomedical applications.* PhD thesis, Texas A&M University, 2007.

[66] Steven D. Thomalla and James D. Van De Ven. Modeling and Implementation of the McKibben Actuator in Hydraulic Systems. *IEEE Transactions on Robotics*, 34(6):1593–1602, 2018.

[67] Ili Najaa Aimi Mohd Nordin, AAM Faudzi, MRM Razif, E Natarajan, S Wakimoto, and K Suzumori. Simulations of two patterns fiber weaves reinforced in rubber actuator. *Jurnal Teknologi*, 69(3), 2014.

[68] Ahmad Athif M Faudzi, M Rusydi M Razif, Ili Najaa Aimi M Nordin, K Suzumori, S Wakimoto, and D Hirooka. Development of bending soft actuator with different braided angles. In *IEEE/ASME Int. Conf. Adv. Intell. Mech.*, pages 1093–1098. IEEE, 2012.

[69] Fionnuala Connolly, Panagiotis Polygerinos, Conor J Walsh, and Katia Bertoldi. Mechanical programming of soft actuators by varying fiber angle. *Soft Robotics*, 2(1):26–32, 2015.

[70] Joshua L Bishop-Moser. *Design of Generalized Fiber-reinforced Elasto-fluidic Systems*. PhD thesis, University of Michigan, 2014.

[71] Joshua Bishop-Moser and Sridhar Kota. Towards snake-like soft robots: Design of fluidic fiber-reinforced elastomeric helical manipulators. In *IEEE/RSJ Int. Conf. Intell. Robot. Sys.*, pages 5021–5026. IEEE, 2013.

[72] Girish Krishnan. Kinematics of a new class of smart actuators for soft robots based on generalized pneumatic artificial muscles. In *IEEE/RSJ Int. Conf. Intell. Robot. Sys.*, pages 587–592. IEEE, 2014.

[73] Girish Krishnan, Joshua Bishop-Moser, Charles Kim, and Sridhar Kota. Evaluating mobility behavior of fluid filled fiber-reinforced elastomeric enclosures. In *ASME 2012 International Design Engineering Technical Conferences and Computers and Information in Engineering Conference*, pages 1089–1099. American Society of Mechanical Engineers, 2012.

[74] M. Calisti, G. Picardi, and C. Laschi. Fundamentals of soft robot locomotion. *Journal of the Royal Society Interface*, 14(130):0–2, 2017.

[75] Shoue Chen, Yunteng Cao, Morteza Sarparast, Hongyan Yuan, Lixin Dong, Xiaobo Tan, Changyong Cao, S Chen, Y Cao, M Sarparast, C Cao, H Yuan, X Tan, and L Dong. Soft Crawling Robots: Design, Actuation, and Locomotion. *Advanced Materials Technologies*, 5:1–20, 2020.

[76] Chiwon Lee, Myungjoon Kim, Yoon Jae Kim, Nhayoung Hong, Seungwan Ryu, H. Jin Kim, and Sungwan Kim. Soft Robot Review. *Internation Journal of Control, Automation and Systems*, 15(1):3–15, 2017.

[77] Bradley J Nelson, Ioannis K Kaliakatsos, and Jake J Abbott. Microrobots for Minimally Invasive Medicine. *Annu. Rev. Biomed. Eng*, 12:55–85, 2010.

[78] Mark Runciman, Ara Darzi, and George P Mylonas. Soft Robotics in Minimally Invasive Surgery. *Soft Robotics*, 6(4):423–443, 2019.

[79] Ignacio Galiana, Frank L. Hammond, Robert D. Howe, and Marko B. Popovic. Wearable soft robotic device for post-stroke shoulder rehabilitation: Identifying misalignments. In *IEEE Int. Conf. Intell. Robot. Sys.*, pages 317–322, 2012.

[80] Panagiotis Polygerinos, Kevin C. Galloway, Emily Savage, Maxwell Herman, Kathleen O'Donnell, and Conor J. Walsh. Soft robotic glove for hand rehabilitation and task specific training. In *Proceedings - IEEE International Conference on Robotics and Automation*, number June, pages 2913–2919, 2015.

[81] Yong-Lae Park, Bor-rong Chen, Néstor O Pérez-Arancibia, Diana Young, Leia Stirling, Robert J Wood, Eugene C Goldfield, and Radhika Nagpal. Design and control of a bio-inspired soft wearable robotic device for ankle–foot rehabilitation. *Bioinspiration & Biomimetics*, 9(1):016007, 2014.

[82] Ellen T Roche, Robert Wohlfarth, Johannes TB Overvelde, Nikolay V Vasilyev, Frank A Pigula, David J Mooney, Katia Bertoldi, and Conor J Walsh. A bioinspired soft actuated material. *Adv. Mater.*, 26(8):1200–1206, 2014.

[83] K. Ikuta, H. Ichikawa, K. Suzuki, and D. Yajima. Multi-degree of freedom hydraulic pressure driven safety active catheter. In *IEEE Int. Conf. Robot. Autom. (ICRA)*, pages 4161–4166, May 2006.

[84] K. Ikuta, M. Matsuda, D. Yajima, and Y. Ota. Precise bending angle control of hydraulic active catheter by pressure pulse drive. In *IEEE Int. Conf. Robot. Autom. (ICRA)*, pages 5588–5593, May 2010.

[85] K. Ikuta, Y. Matsuda, D. Yajima, and Y. Ota. Pressure pulse drive: A control method for the precise bending of hydraulic active catheters. *IEEE/ASME Trans. Mechatronics*, 17(5):876–883, Oct 2012.

[86] Gang Chen, Minh Tu Pham, and Tanneguy Redarce. Development and kinematic analysis of a silicone-rubber bending tip for colonoscopy. In *IEEE/RSJ Int. Conf. Intell. Robot. Sys.*, pages 168–173, 2006.

[87] K. Suzumori, T. Hama, and T. Kanda. New pneumatic rubber actuators to assist colonoscope insertion. In *IEEE Int. Conf. Robot. Autom. (ICRA)*, pages 1824–1829, 2006.

[88] Carmen C.Y. Poon, Billy Leung, Cecilia K.W. Chan, James Y.W. Lau, and Philip W.Y. Chiu. Design of wormlike automated robotic endoscope: dynamic interaction between endoscopic balloon and surrounding tissues. *Surgical Endoscopy and Other Interventional Techniques*, 30(2):772–778, 2016.

[89] Irwan Kassim, Louis Phee, Wan S. Ng, Feng Gong, Paolo Dario, and Charles A. Mosse. Locomotion techniques for robotic colonoscopy. *IEEE Engineering in Medicine and Biology Magazine*, 25(3):49–56, 2006.

[90] M. Wildan Gifari, Hamid Naghibi, Stefano Stramigioli, and Momen Abayazid. A review on recent advances in soft surgical robots for endoscopic applications. *The International Journal of Medical Robotics and Computer Assisted Surgery*, 15(5), oct 2019.

[91] Hirozumi Takeshima and Toshio Takayama. Geometric Estimation of the Deformation and the Design Method for Developing Helical Bundled-Tube Locomotive Devices. *IEEE/ASME Transactions on Mechatronics*, 23(1):223–232, 2018.

[92] Luigi Manfredi, Elisabetta Capoccia, Gastone Ciuti, and Alfred Cuschieri. A Soft Pneumatic Inchworm Double balloon (SPID) for colonoscopy. *Scientific Reports*, 9(1):1–9, 2019.

[93] Shuichi Wakimoto, Keiko Ogura, Koichi Suzumori, and Yasutaka Nishioka. Miniature soft hand with curling rubber pneumatic actuators. *Proceedings - IEEE International Conference on Robotics and Automation*, pages 556–561, 2009.

[94] Yoonho Kim, German A. Parada, Shengduo Liu, and Xuanhe Zhao. Ferromagnetic soft continuum robots. *Science Robotics*, 4(33), 2019.

[95] Ching Ping Chou and Blake Hannaford. Measurement and modeling of McKibben pneumatic artificial muscles. *IEEE Transactions on Robotics and Automation*, 12(1):90–102, 1996.

[96] Bertrand Tondu. Modelling of the McKibben artificial muscle: A review. *Journal of Intelligent Material Systems and Structures*, 23(3):225–253, 2012.

[97] Matheus S. Xavier, Andrew J. Fleming, and Yuen K. Yong. Finite Element Modeling of Soft Fluidic Actuators: Overview and Recent Developments. *Advanced Intelligent Systems*, page 2000187, oct 2020.

[98] Eulalie Coevoet, Adrien Escande, and Christian Duriez. Soft robots locomotion and manipulation control using FEM simulation and quadratic programming. In *RoboSoft 2019 - IEEE International Conference on Soft Robotics*, Seoul, 2019.

[99] G Alici, T Canty, R Mutlu, W Hu, and V Sencadas. Modeling and Experimental Evaluation of Bending Behavior of Soft Pneumatic Actuators Made of Discrete Actuation Chambers. *Soft Robotics*, 5(1):24–35, 2018.

[100] Khaled Elgeneidy, Niels Lohse, and Michael Jackson. Bending angle prediction and control of soft pneumatic actuators with embedded flex sensors – A data-driven approach. *Mechatronics*, 50:234–247, apr 2018.

[101] Alaa Al-Ibadi, Samia Nefti-Meziani, and Steve Davis. The design, kinematics and torque analysis of the self-bending soft contraction actuator. *Actuators*, 9(2), 2020.

[102] Mohammad Fatahillah, Namsoo Oh, and Hugo Rodrigue. A Novel Soft Bending Actuator Using Combined Positive and Negative Pressures. *Frontiers in Bioengineering and Biotechnology*, 8:472, may 2020.

[103] Eulalie Coevoet, Adrien Escande, and Christian Duriez. Optimization-Based Inverse Model of Soft Robots with Contact Handling. *IEEE Robotics and Automation Letters*, 2(3):1413–1419, 2017.

[104] C M Wang, H Zhang, N Challamel, and W H Pan. *Hencky Bar-Chain/Net for Structural Analysis*. World Scientific (Europe), may 2020.

[105] D. Caleb Rucker, Bryan A. Jones, and Robert J. Webster. A geometrically exact model for externally loaded concentric-tube continuum robots. *IEEE Transactions on Robotics*, 26(5):769–780, 2010.

[106] Richard W Cottle. Nonlinear Programs with Positively Bounded Jacobians. *J. SIAM Appl. Math.*, 14(1):147–158, 1966.

[107] Richard W. Cottle and George B. Dantzig. Complementary pivot theory of mathematical programming. *Linear Algebra and Its Applications*, 1(1):103–125, 1968.

[108] Katta G Murty and Feng-Tien Yu. *Linear Complementarity, Linear and Nonlinear Programming*. Ann Arbor, 1997.

[109] A. M. Al-Fahed, G. E. Stavroulakis, and P. D. Panagiotopoulos. Hard and Soft Fingered Robot Grippers. The Linear Complementarity Approach. *ZAMM - Journal of Applied Mathematics and Mechanics / Zeitschrift für Angewandte Mathematik und Mechanik*, 71(7-8):257–265, 1991.

[110] Ben Hamlen, Gillian McDonald, Daniel Ng, and Timothy Kowalewski. Automated Manufacturing of Fiber-Reinforced Elastomeric Enclosures for Patient Specific Catheter Robots. In *Proceedings of the 2019 Design of Medical Devices Conference*, 2019.

[111] Gillian McDonald, Amer Safdari, and Timothy M. Kowalewski. Traction of Helical Soft Continuum Actuators for Endoluminal Robots. In *IEEE/RSJ Int. Conf. Robot. Intell. Sys. (IROS) [Poster Presentation]*, 2017.

[112] Joan Ortega Alcaide, Levi Pearson, and Mark E. Rentschler. Design, modeling and control of a SMA-actuated biomimetic robot with novel functional skin. *Proceedings - IEEE International Conference on Robotics and Automation*, pages 4338–4345, 2017.

[113] Jan Fras, Yohan Noh, Mateusz Macias, Helge Wurdemann, and Kaspar Althoefer. Bio-Inspired Octopus Robot Based on Novel Soft Fluidic Actuator. *Proceedings - IEEE International Conference on Robotics and Automation*, pages 1583–1588, 2018.

[114] Megan Scudellari. Soft robot hugs your heart to keep it pumping, jan 2017. https://spectrum.ieee.org/the-human-os/biomedical/devices/soft-robot-hugs-your-heart-to-keep-it-pumping.

[115] Ellen T. Roche, Markus A. Horvath, Isaac Wamala, Ali Alazmani, Sang Eun Song, William Whyte, Zurab Machaidze, Christopher J. Payne, James C. Weaver, Gregory Fishbein, Joseph Kuebler, Nikolay V. Vasilyev, David J. Mooney, Frank A. Pigula, and Conor J. Walsh. Soft robotic sleeve supports heart function. *Science Translational Medicine*, 9(373):1–12, 2017.

[116] Robert F. Shepherd, Filip Ilievski, Wonjae Choi, Stephen A. Morin, Adam A. Stokes, Aaron D. Mazzeo, Xin Chen, Michael Wang, and George M. Whitesides. Multigait soft robot. *Proceedings of the National Academy of Sciences of the United States of America*, 108(51):20400–20403, 2011.

[117] Nils Napp, Brandon Araki, Michael T Tolley, Radhika Nagpal, and Robert J Wood. Simple passive valves for addressable pneumatic actuation. In *IEEE Int. Conf. Robot. Autom. (ICRA)*, pages 1440–1445. IEEE, 2014.

[118] Ellad B Tadmor, Ronald E Miller, and Ryan S Elliott. *Continuum mechanics and thermodynamics: from fundamental concepts to governing equations*. Cambridge University Press, 2012.

[119] John S Cundiff. *Fluid power circuits and controls: fundamentals and applications*. CRC Press, 2001.

[120] Pavel Holoborodko. Smooth noise robust differentiators, 2008. http://www.holoborodko.com/pavel/numerical-methods/numerical-derivative/smooth-low-noise-differentiators/.

[121] Jungwook Paek, Inho Cho, and Jaeyoun Kim. Microrobotic tentacles with spiral bending capability based on shape-engineered elastomeric microtubes. *Scientific Reports*, 5(June):1–11, 2015.

[122] Lindsey Hines, Kirstin Petersen, Guo Zhan Lum, and Metin Sitti. Soft Actuators for Small-Scale Robotics. *Advanced Materials*, 29(13), 2017.

[123] Benjamin Gorissen, Dominiek Reynaerts, Satoshi Konishi, Kazuhiro Yoshida, Joon Wan Kim, and Michael De Volder. Elastic Inflatable Actuators for Soft Robotic Applications. *Advanced Materials*, 29(43), 2017.

[124] Benjamin Gorissen, Michaël De Volder, and Dominiek Reynaerts. Pneumatically-actuated artificial cilia array for biomimetic fluid propulsion. *Lab on a Chip*, 15(22):4348–4355, 2015.

[125] Wook Choi, Minoo Akbarian, Vladimir Rubtsov, and Chang Jin Kim. Microhand with internal visual system. *IEEE Transactions on Industrial Electronics*, 56(4):1005–1011, 2009.

[126] Yoshinori Inoue and Koji Ikuta. Hydraulic driven active catheters with optical bending sensor. In *Proceedings of the IEEE International Conference on Micro Electro Mechanical Systems (MEMS)*, pages 383–386. IEEE, 2016.

[127] Exxon Mobil. Mobil 1™ 0W-20. https://www.exxonmobil.com/en/apps/pds/mobil/passenger-vehicle-lube/2019/09/29/15/48/iocamobil-1-0w20.

[128] Eduardo R. Perez-Guagnelli, Sarunas Nejus, Jian Yu, Shuhei Miyashita, Yanqiang Liu, and Dana D. Damian. Axially and Radially Expandable Modular Helical Soft Actuator for Robotic Implantables. *Proceedings - IEEE International Conference on Robotics and Automation*, (January):4297–4304, 2018.

[129] Kevin C. Galloway, Kaitlyn P. Becker, Brennan Phillips, Jordan Kirby, Stephen Licht, Dan Tchernov, Robert J. Wood, and David F. Gruber. Soft Robotic Grippers for Biological Sampling on Deep Reefs. *Soft Robotics*, 3(1):23–33, 2016.

[130] Laura H. Blumenschein, Nathan S. Usevitch, Brian H. Do, Elliot W. Hawkes, and Allison M. Okamura. Helical actuation on a soft inflated robot body. *2018 IEEE International Conference on Soft Robotics, RoboSoft 2018*, pages 245–252, 2018.

[131] Soft Robotics Toolkit. Fiber-Reinforced Actuators. https://softroboticstoolkit.com/book/fiber-reinforced-bending-actuators.

[132] Kevin C. Galloway, Panagiotis Polygerinos, Conor J. Walsh, and Robert J. Wood. Mechanically programmable bend radius for fiber-reinforced soft actuators. In *2013 16th International Conference on Advanced Robotics, ICAR 2013*. IEEE Computer Society, 2013.

[133] BDC Laboratories. Mock Vessel Friction Reduction Coating, 2014. http://www.bdclabs.com/silicone-mock-vessels/slic-friction-reduction-coating/.

[134] Gillian J. McDonald, Benjamin Hamlen, Emmanuel Detournay, and Timothy M. Kowalewski. [Submitted, in review] Contact modeling for high aspect ratio soft robots using Hencky bar-chain and linear complementarity techniques. *The International Journal of Robotics Research*, 2021.

[135] Gillian J. McDonald, Khoi H.T. Nguyen, Andrew W. Grande, and Timothy M. Kowalewski. Medical Soft Robots : Overcoming Scaling Challenges. In *Institute for Engineering in Medicine (IEM) Annual Conference*, page 1, 2019.

[136] Sofy H Weisenberg, Stephanie C Termaath, Chad E Seaver, and James A Killeffer. Ventricular catheter development: past, present, and future. *Journal of Neurosurgery*, 125(December):1504–1512, 2016.

[137] N Challamel, C M Wang, and I Elishakoff. Discrete systems behave as nonlocal structural elements: Bending, buckling and vibration analysis. *European Journal of Mechanics A/Solids*, 44:125–135, oct 2013.

[138] W. H. Pan, C. M. Wang, and H. Zhang. Matrix Method for Buckling Analysis of Frames Based on Hencky Bar-Chain Model. *International Journal of Structural Stability and Dynamics*, 19(8):1–28, 2019.

[139] Djebar Baroudi, Ivan Giorgio, Antonio Battista, Emilio Turco, and Leonid A. Igumnov. Nonlinear dynamics of uniformly loaded Elastica: Experimental and numerical evidence of motion around curled stable equilibrium configurations. *ZAMM Zeitschrift fur Angewandte Mathematik und Mechanik*, 99(7), 2019.

[140] Hong Zhang, C.M. Wang, and Noël Challamel. Buckling and vibration of Hencky bar-chain with internal elastic springs. *International Journal of Mechanical Sciences*, 119:383–395, 2016.

[141] Anna Liakou, Vincent Denoël, Aff M Asce, Emmanuel Detournay, and A M Asce. Fast In-Plane Dynamics of a Beam with Unilateral Constraints. *J. Eng. Mech.*, 143(2), 2017.

[142] A. M. Al-Fahed, G. E. Stavroulakis, and P. D. Panagiotopoulos. Hard and Soft Fingered Robot Grippers. The Linear Complementarity Approach. *ZAMM - Journal of Applied Mathematics and Mechanics / Zeitschrift für Angewandte Mathematik und Mechanik*, 71(7-8):257–265, 1991.

[143] Matei Ciocarlie, Claire Lackner, and Peter Allen. Soft finger model with adaptive contact geometry for grasping and manipulation tasks. In *Proceedings - Second Joint EuroHaptics Conference and Symposium on Haptic Interfaces for Virtual Environment and Teleoperator Systems, World Haptics 2007*, pages 219–224, 2007.

[144] Zhongkai Zhang, Jeremie Dequidt, Junghwan Back, Hongbin Liu, and Christian Duriez. Motion Control of Cable-Driven Continuum Catheter Robot through Contacts. *IEEE Robotics and Automation Letters*, 4(2):1852–1859, 2019.

[145] Shmuel Katz and Sefi Givli. The post-buckling behavior of a beam constrained by springy walls. *Journal of the Mechanics and Physics of Solids*, 78:443–466, 2015.

[146] Nicholas Xydas and Imin Kao. Modeling of Contact Mechanics and Friction Limit Surfaces for Soft Fingers in Robotics, with Experimental Results. *The International Journal of Robotics Research*, 18(9):941–950, 1999.

[147] Imin Kao and Fuqian Yang. Stiffness and contact mechanics for soft fingers in grasping and manipulation. *IEEE Transactions on Robotics and Automation*, 20(1):132–135, feb 2004.

[148] Sadeq H Bakhy, Shaker S Hassan, Somer M Nacy, K Dermitzakis, and Alejandro Hernandez Arieta. Contact mechanics for soft robotic fingers: modeling and experimentation. *Robotica*, 31:599–609, 2013.

[149] Sadeq Hussein Bakhy. Modeling of contact pressure distribution and friction limit surfaces for soft fingers in robotic grasping. *Robotica*, 32:1005–1015, 2014.

[150] Carmel Majidi, Robert F Shepherd, Rebecca K Kramer, George M Whitesides, and Robert J Wood. Influence of surface traction on soft robot undulation. *Int. J. Rob. Res.*, 32(13):1577–1584, 2013.

[151] Nathaniel N Goldberg, Xiaonan Huang, Carmel Majidi, Alyssa Novelia, Oliver M O'reilly, Derek A Paley, and William L Scott. On Planar Discrete Elastic Rod Models for the Locomotion of Soft Robots. *Soft Robotics*, 6(5):595–610, 2019.

[152] Yin Haibin, Kong Cheng, Li Junfeng, and Yang Guilin. Modeling of grasping force for a soft robotic gripper with variable stiffness. *Mechanism and Machine Theory*, 128:254–274, 2018.

[153] Eulalie Coevoet, Adrien Escande, and Christian Duriez. Optimization-Based Inverse Model of Soft Robots with Contact Handling. *IEEE Robotics and Automation Letters*, 2(3):1413–1419, 2017.

[154] Giovanni Berselli, Marco Piccinini, Gianluca Palli, and Gabriele Vassura. Engineering design of fluid-filled soft covers for robotic contact interfaces: Guidelines, nonlinear modeling, and experimental validation. *IEEE Transactions on Robotics*, 27(3):436–449, jun 2011.

[155] Andreas Almqvist. A pivoting algorithm solving linear complementarity problems, 2020. https://www.mathworks.com/matlabcentral/fileexchange/41485-a-pivoting-algorithm-solving-linear-complementarity-problems.

[156] Lei Wei, Alexei Sourin, Zoran Najdovski, and Saeid Nahavandi. Function-Based Single and Dual Point Haptic Interaction in Cyberworlds. In Marina L. Gavrilova and C. J. Kenneth Tan, editors, *Transactions on Computational Science XVI*, pages 1–16. Springer-Verlag Berlin Heidelberg, 2012.

[157] F. T. Peirce. The "handle" of cloth as a measurable quantity. *Journal of the Textile Institute Transactions*, 21(9):T377–T416, jan 1930.

[158] I.M. Stuart. A loop test for bending length and rigidity. *J. Appl. Phys.*, 17:1215–1220, 1966.

[159] Raymond H. Plaut. Formulas to determine fabric bending rigidity from simple tests. *Textile Research Journal*, 85(8):884–894, 2015.

[160] C. Y. Wang. Post-Buckling of Horizontal Heavy Elastic Sheet. *Journal of Engineering Mechanics*, 110(6):871–878, jun 1984.

[161] Francisco J. Romero-Ramirez, Rafael Muñoz-Salinas, and Rafael Medina-Carnicer. Speeded up detection of squared fiducial markers. *Image and Vision Computing*, 76(June):38–47, 2018.

[162] S. Garrido-Jurado, R. Muñoz-Salinas, F. J. Madrid-Cuevas, and R. Medina-Carnicer. Generation of fiducial marker dictionaries using Mixed Integer Linear Programming. *Pattern Recognition*, 51(March):481–491, 2016.

[163] Randy Bullock. Least-Squares Circle Fit, 2017. https://www.dtcenter.org/sites/default/files/community-code/met/docs/write-ups/circle_fit.pdf.

[164] Clay Flannigan, Maxim Bazik, and Joe Dinius. icp, 2017. https://github.com/ClayFlannigan/icp/blob/master/icp.py.

[165] Qinpei Zhao, Ville Hautamaki, and Pasi Fränti. Knee point detection in BIC for detecting the number of clusters. In *Advanced Concepts for Intelligent Vision Systems. ACIVS 2008.*, volume 5259 LNCS, pages 664–673. Springer Verlag, 2008.

[166] Ville Satopää, Jeannie Albrecht, David Irwin, and Barath Raghavan. Finding a "kneedle" in a haystack: Detecting knee points in system behavior. *Proceedings - International Conference on Distributed Computing Systems*, pages 166–171, 2011.

[167] Gillian J McDonald, Emmanuel Detournay, and Timothy M Kowalewski. [Submitted, in review] Modeling and Measurement of Pressure-Dependent Bending Stiffness for Soft Robotic Actuators via a Simple Free-Fold Test. *IEEE Robotics and Automation Letters*, 2021.

[168] I.M. Stuart and K. Baird. A new test for bending length. *Textile Research Journal*, 36(1):91–93, 1966.

[169] D. W. Lloyd, W. J. Shanahan, and M. Konopasek. The folding of heavy fabric sheets. *International Journal of Mechanical Sciences*, 20(8):521–527, jan 1978.

[170] L Mahadevan and Joseph B Keller. Periodic Folding of Thin Sheets. *Society for Industrial and Applied Mathematics*, 41(1):115–131, 1999.

[171] Naiyue Zhou and T.K. Ghosh. On-Line Measurement of Fabric Bending Behavior. *Textile Research Journal*, 68(7):533–542, jul 1998.

[172] T. Cassidy, C. Cassidy, S. Cassie, and M. Arkison. The stiffness of knitted fabrics: A new approach to the measurement of bending - part 1: Development. *International Journal of Clothing Science and Technology*, 3(5):14–19, may 1991.

[173] Loïc Blanc, Alain Delchambre, and Pierre Lambert. Flexible medical devices: Review of controllable stiffness solutions. *Actuators*, 6(3):1–31, 2017.

[174] Ian W. Hunter and Serge Lafontaine. A Comparison of Muscle with Artificial Actuators. *IEEE Technical Digest IEEE Solid-State Sensor and Actuator Workshop*, pages 178–185, 1992.

[175] B.A. Van den Horn and M. Kuipers. Strength and stiffness of a reinforced flexible hose. *Applied Scientific Research*, 45(3):251–281, 1988.

[176] Andrea Catinaccio. Pipes under internal pressure and bending. Technical report, Cern, 2009.

[177] B. G. Teng, L. Hu, and S. J. Yuan. Deformation behavior of thin-walled tube bending with internal pressure. *Reviews on Advanced Materials Science*, 33(5):436–441, 2013.

[178] Polymer Properties Database. Typical Poisson's Ratios of Polymers at Room Temperature. https://polymerdatabase.com/polymer physics/Poisson Table.html.

[179] Latex-tubing.com. Technical Specifications. http://www.latex-tubing.com/Technical.html.

[180] Bending Stiffness. Technical report, Scandinavian Pulp, Paper and Board Testing Committee, 1991.

[181] Y. Wyser, C. Pelletier, and J. Lange. Predicting and determining the bending stiffness of thin films and laminates. *Packaging Technology and Science*, 14(3):97–108, 2001.

[182] Raymond H. Plaut. Determining effective bending stiffness of fabrics and other materials from tests involving an added weight. *Textile Research Journal*, 90(1):101–109, 2020.

[183] Richard H. Gaylord. Fluid Actuated Motor System and Stroking Device, U.S. Patent 2844126, 1958.

[184] Hugh M. Herr and Roy D. Kornbluh. New horizons for orthotic and prosthetic technology: artificial muscle for ambulation. *Smart Structures and Materials 2004: Electroactive Polymer Actuators and Devices (EAPAD)*, 5385(July):1, 2004.

[185] Glen Brown, Roy Haggard, Richard Almassy, Richard Benney, and Scott Dellicker. The affordable guided airdrop system (AGAS). *15th Aerodynamic Decelerator Systems Technology Conference*, (c):316–325, 1999.

[186] M De Volder, A J M Moers, and D Reynaerts. Fabrication and control of miniature McKibben actuators. *Sensors and Actuators A: Physical*, 166:111–116, 2011.

[187] N. Dodds, A. G. Gibson, Y. H. Huang, R. Walker, A. Sharpe, and A. Porteous. Reinforced thermoplastic pipe using recycled PET reinforcement. *Plastics, Rubber and Composites*, 34(7):324–328, 2005.

[188] Bertrand Tondu and Pierre Lopez. Modeling and Control of McKibben Artificial Muscle Robot Actuators. *IEEE Control Systems*, 20(2):15–38, 2000.

[189] Curt S. Kothera, Mamta Jangid, Jayant Sirohi, and Norman M. Wereley. Experimental characterization and static modeling of McKibben actuators. *Journal of Mechanical Design, Transactions of the ASME*, 131(9):0910101–09101010, 2009.

[190] James M. Gere and Barry J. Goodno. *Mechanics of Materials*. Cengage Learning, eighth edition, 2012.

[191] Physik Instruments. Piezoelectric Actuators, 2020. www.piceramic.com.

[192] Timothy M. Kowalewski, James D. Van de Ven, Mark D. Gilbertson, Gabriel R.C. Korinek, and Gillian J. McDonald. Soft Robots, Soft Actuators, and Methods for Making the Same, U.S. Patent 10760597, 2020.

[193] Seyed Ali Amirshahi, Gregor Uwe Hayn-Leichsenring, Joachim Denzler, and Christoph Redies. Evaluating the Rule of Thirds in Photographs and Paintings. *Art and Perception*, 2(1-2):163–182, 2014.

[194] Robert J Webster III and Bryan A Jones. Design and Kinematic Modeling of Constant Curvature Continuum Robots: A Review. *The International Journal of Robotics Research*, 29(13):1661–1683, 2010.

[195] Pierre E. Dupont, Jesse Lock, Brandon Itkowitz, and Evan Butler. Design and control of concentric-tube robots. *IEEE Transactions on Robotics*, 26(2):209–225, 2010.

[196] S. Manini and L. Antiga. vmtk - The Vascular Modeling Toolkit. http://www.vmtk.org/.

Appendix A

Custom CNC Lathe for Constructing Fiber-Reinforced Actuators

This section includes work titled, "Automated Manufacturing of Fiber-Reinforced Elastomeric Enclosures for Patient Specific Catheter Robots" in the Proceedings of the 2019 Design of Medical Devices Conference [110].

A.1 Introduction and Background

The aim of the work presented in this section was to design a more automated manufacturing setup and methods to construct FREEs and evaluate their construction. Specifically, this section examines the capability of the proposed system to i) deposit fibers at desired angles as needed for a patient-specific design and ii) determine the accuracy of the deposited fibers' wrap angles using manual and computer vision means.

A.2 Methods

A.2.1 Construction

The manufacturing setup used a desktop Prazi lathe, stripped of its motors and electronics (Fig. 2.7). A belt drive system was designed to control both the central rotating axis of the lathe (the "Rotation Stage") and the worm gear driving the carriage (the "Linear Stage"). To drive this belt system, direct drive DC Motors (Maxon) were attached to laser-cut MXL pulleys and controlled with a Teensy 3.5 microcontroller and Pololu Dual VNH3SP30 motor driver. This gives a mechanical advantage of 27:1 in the belt pulley system. Encoders were used to measure the position of both stages throughout their motion. The rotation stage utilized a 22-bit absolute inductive encoder (NC-3-150-221001-SPI1-RFC4-5-AN Zettlex Systems, Inc). The linear stage used a transmissive optical linear encoder with 3000 counts per inch (CPI) from US Digital (EM2) (Fig. 2.7).

A thread spool holder and guide were designed for the linear stage. The thread was fed through a hole in the guide and then attached to the actuator being wrapped. This was typically accomplished by adhering the string to the tube with tape and then closing the lathe's chuck teeth on top of the tape.

A.2.2 Velocity Controller

The desired wrap angle was achieved by relating the linear stage's velocity (v_{lin}) to the circumferential velocity of the outer surface (v_{rot}) of the actuator being wrapped using eq. A.1.

$$v_{rot} = v_{lin} \tan(\theta_{wrap}) \tag{A.1}$$

The linear stage was set to run at a constant 4.5 mm/s. The circumferential velocity of the outer surface of the actuator being wrapped was calculated using eq. A.2.

$$v_{rot} = \frac{1}{2^{22}} \pi v D \tag{A.2}$$

Where v is the velocity of the rotation stage measured in counts per second from the absolute rotational encoder, D is the outer diameter (OD) of the actuator being wrapped, and 2^{22} is the number of counts per full revolution given by the absolute rotational encoder. v_{rot} was

controlled with a PID controller running at 1 kHz. Zeigler-Nichols and various step inputs were used to tune the gains, resulting in $K_p = 10$, $K_i = 12.5$, and $K_d = 0.09$.

A.2.3 Testing and Validation

The performance of the velocity controller was characterized by wrapping 20°, 45°, and 80° wrap angles, as the range of angles for actuator manufacturing is expected to be 20°- 80°. Per eq. A.1, v_{lin} of 1.64, 4.50 and 25.52 mm/s correspond to wrap angles of 20°, 45°, and 80°, respectively. Ten trials at the aforementioned v_{lin}, each trial making step changes from zero to the specified velocity, were conducted. The average velocity response over the ten trials for each v_{lin} was calculated. MATLAB's curve fitting toolbox was used to fit the average velocity response data for each target wrap angle to determine a 95% rise time (time from step to less than 5% error).

Generated wrap angles were qualitatively examined by overlaying a line at the desired wrap angle on a photo of the wrapped cylinder (Fig. A.1). This was accomplished by turning on the "rule of thirds" grid guide on a Pixel 2 XL phone camera [193]. One of those lines was aligned with the edge of the actuator, providing a ground truth for horizontal alignment of the actuator in the photo frame. The photo was then digitally cropped to align the actuator with the center of the image. A horizontal line was drawn from the left center of the image to the right center (white dashed lines in Fig. A.1). That line was duplicated, rotated in Microsoft Word to the specified wrap angle, and changed to solid red.

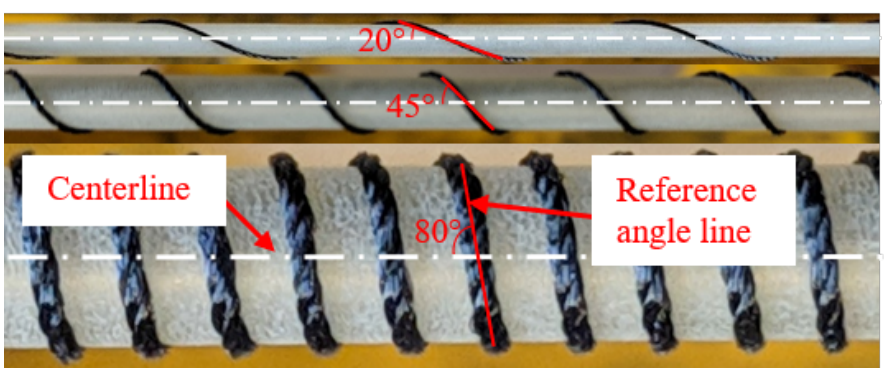

Figure A.1: 20°, 45° and 80° wrap angles on 2.8 mm OD actuator and corresponding overlaid angle reference lines.

Accuracy of wrap angles was quantitatively examined using OpenCV in Python (opencv-contrib-python library). A region of interest (ROI) was extracted from the center of the image. The ROI top and bottom bounds were approximately 20% smaller than the visible edge of the catheter and horizontal extents were clipped to where the visible fiber started to deviate from a straight line. A sample ROI around a single fiber is shown in Fig. A.2.

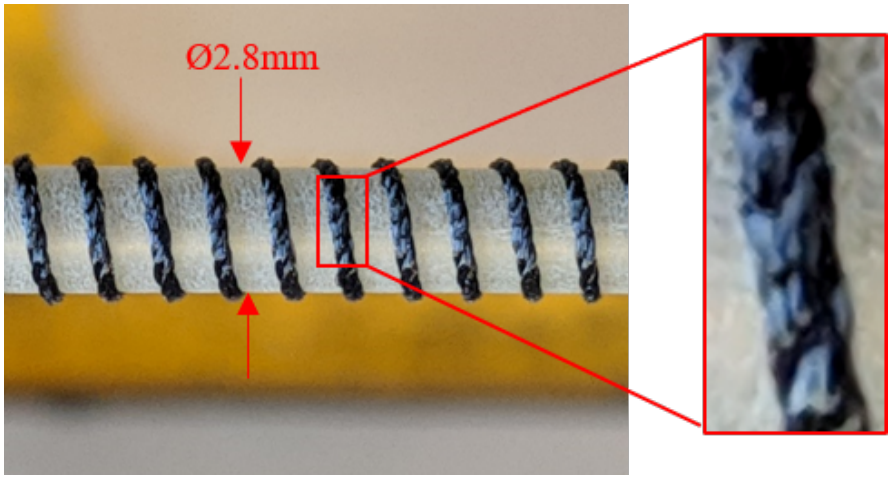

Figure A.2: Acquired image of 80° wrap angle, 2.8 mm OD shaft; Insert: sample extracted region of interest (ROI) for computer vision-based wrap angle measurement.

To extract fiber angle, the following steps were taken:

1. Median blur of 5 pixels & conversion to grayscale
2. Binary threshold at 50%
3. Canny edge extraction
4. Hough Transform line extraction (HoughLines) with 1-degree accuracy and threshold selected by decreasing from 100 until more than one line was returned. The angle of the two best lines was extracted from Hough parameters and averaged and reported as the angle of the thread derived from computer vision.

A.3 Results

Results for the control system are given in Fig. A.3 and Table A.1.

Table A.1: Time from 0 to <5% error from set point (95% rise time) and length of actuator with inaccurate wrap angles for 20, 45, and 80-degree wrap angles.

Wrap Angle (degrees)	$t_{95\%}$ **(seconds)**	$L_{inaccurate}$ **(mm)**
20	3.30	14.85
45	3.00	13.50
80	1.43	6.435

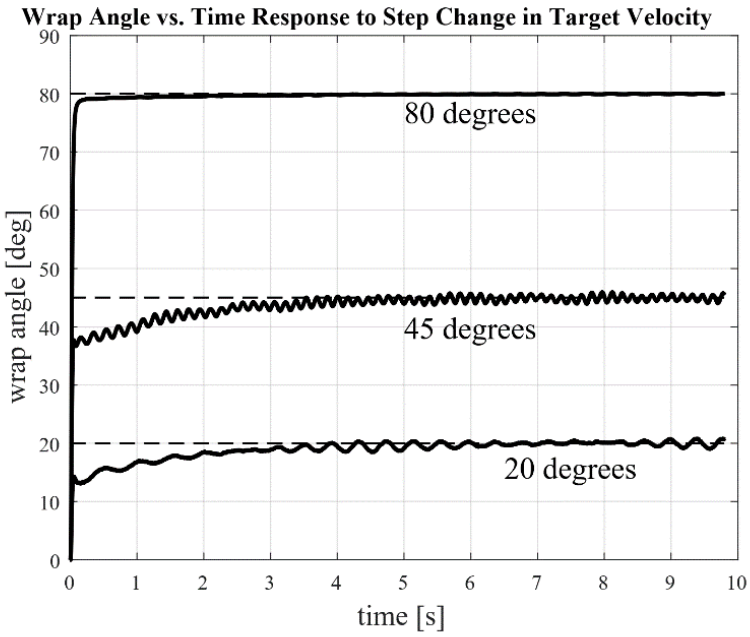

Figure A.3: Instantaneous wrap angle produced by controller in response to step inputs of 1.64, 4.5 and 25.52 mm/s (20°, 45°, and 80° wrap angles, respectively). Dashed lines are desired wrap angles and solid lines are actual wrap angles.

MATLAB's curve fitting toolbox minimized error with a double exponential function as shown in eqs. A.3-A.5 below.

$$v_{rot,20} = 1.64 - 1.42e^{\frac{-t}{0.017}} - 0.58e^{\frac{-t}{1.66}} \tag{A.3}$$

$$v_{rot,45} = 4.5 - 4.34e^{\frac{-t}{0.02}} - 1.17e^{\frac{-t}{1.79}} \tag{A.4}$$

$$v_{rot,80} = 25.54 - 28.72e^{\frac{-t}{0.05}} - 2.16e^{\frac{-t}{2.77}} \tag{A.5}$$

These fits were used to calculate the 95% rise time for each wrap angle (Table A.1).

The length of the actuator with wrap angle error greater than 5% was calculated by eq. A.6.

$$L_{inaccurate} = 4.5t_{95\%} \tag{A.6}$$

Where 4.5 was the constant velocity of the linear stage (mm/s) and $t_{95\%}$ was the 95% rise time (s) for that wrap angle (Table A.1).

Figs. A.1 and A.4 show the results of the manual and computer vision-based accuracy measurements, respectively. Fig. A.5 shows two actuators constructed with the automated process using pre-programmed wrap angles.

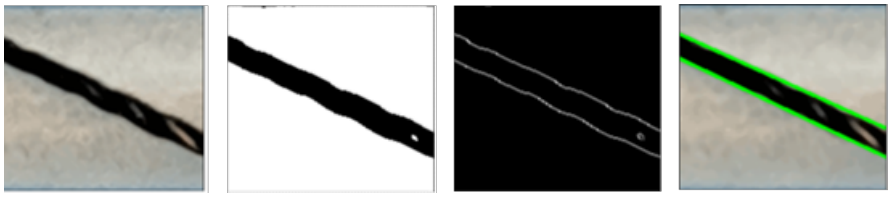

Figure A.4: Process from initial ROI to angle extraction for the 20° wrap angle. Stages are initial ROI, Binary thresholding in B&W, Canny edge extraction, Hough Transform line and angle extraction: 25°, at average processing duration of 3 ms.

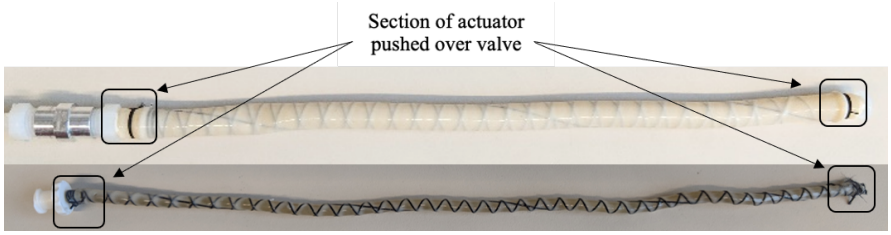

Figure A.5: Example of two actuators (top OD = 10.8 mm, bottom OD = 2.8 mm) manufactured on the custom platform each with three different thread fibers deposited at unique wrap angles followed by a dip-cast polyurethane overcoat (Polytek Elastomers, Polytek 74 Series Polyurethane).

A.4 Discussion

The control scheme presented was adequate for wrapping 10 mm and 2.8 mm OD actuators (Fig. A.5). Startup effects (Table A.1) were confined to one end of the actuator and are tolerable since these regions are pushed over a valve and do not inhibit final actuator performance (Fig. A.5). A 95% rise time was chosen instead of a settling time because the PID controller produced no overshoot for any wrap angle. Rise time was also chosen because the controller was found to not settle to within 2% of the setpoint for the 20° wrap angle during the 10-second trials. The controller did settle to within 2% of the setpoints for 45° and 80° wrap angles. This will be corrected in future work, possibly by tuning the controller at 20° and 80°.

Qualitatively, the accuracy of the deposited fibers seemed highest for the highest wrap angle (80°, Fig. A.1 bottom) and worst for the smallest wrap angle (20°, Fig. A.1 top). Computer vision (Fig. A.4) supported this observation quantitatively with a 5° discrepancy between desired and actual deposition for 20° wrap angle. It was unclear whether this perceived wrap angle error was due to inaccuracy in the control of motion, deposition, the thread sliding up the catheter after deposition, or was an optical effect resulting from projecting a 3D object (the fiber) onto a 2D plane (reference angle line) for the vision system.

The amplitude-modulated oscillation about the 20° wrap angle setpoint was likely due to non-concentricity in both the small upper and large lower MXL pulleys used in the manufacturing setup (Fig. 2.7). As each completed a full rotation, the tension in the belt (and as a result, the resistance felt by the motor) oscillated sinusoidally. This can be seen in the high-frequency oscillations on the 20° wrap angle line (from the small pulley) and the modulated amplitude of those high-frequency oscillations (from the large pulley). This hypothesis is supported by the increased frequency of these oscillations in the 45° wrap angle line in Figure 4. The same oscillations are present in the 80° wrap angle line but are much smaller in amplitude because of the higher rotational inertia in the system at that wrap angle (v_{rot} of 25.52 mm/s, as opposed to 4.5 and 1.64 mm/s for 45° and 20°, respectively). These velocity oscillations at low wrap angles may be corrected through more tuning of the PID controller and will be further investigated.

The 3ms delay from computer vision suggests online angle analysis is feasible. This will also be further investigated in future work on closed-loop deposition and control of fiber wrap angles. This would allow wrap angles to be varied dynamically, enabling more complex final geometries.

A.5 Conclusion

An automated method for programmable manufacturing of unique (possibly patient-specific) catheter robots was presented. The implemented velocity controller was found to settle between 1.4 and 3.3 seconds, depending on wrap angle. This produced accurate wrap angles for all but the first 6 to 15 mm of the actuator length. Custom 2.8 mm and 10 mm OD catheter actuators were successfully manufactured (Fig. A.5). With 3 ms latency, computer vision angle extraction for online control appears to be feasible. Further work could explore online computer vision angle tracking and varying wrap angle as a function of length.

Appendix B

Conceptual Mold Design for Casting Actuators

A conceptual drawing of the mold used to fabricate soft robot base tubing is shown in Fig. B.1. The illustration shows the inner rod (labeled as inner pipe) within a glass tube. The diameter of the inner rod designates the inner diameter of the base tubing being fabricated, and the inner diameter of the glass tube designates the outer diameter of the base tubing. An O-ring is used to keep the inner rod and glass tube concentric with one another. Liquid elastomer is injected into the space between the inner rod and glass tube using a barbed fitting.

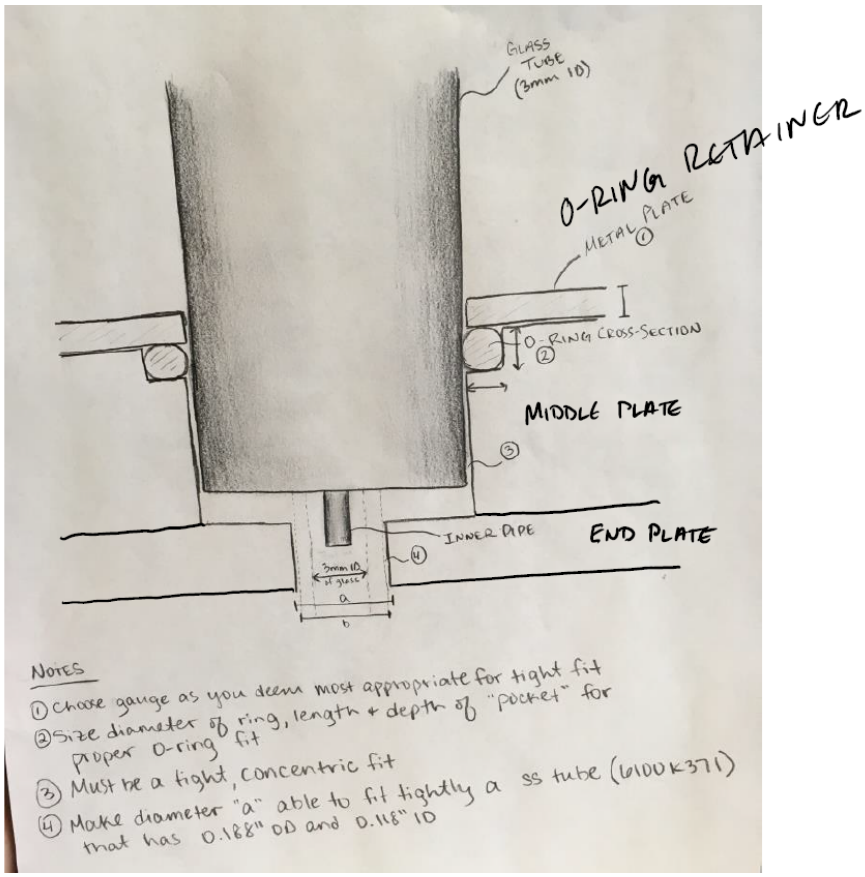

Figure B.1: Illustration of mold concept for fabricating soft robot base tubing.

Appendix C

Additional Anchoring Force Study

This section includes a poster titled, "Automated Manufacturing of Fiber-Reinforced Elastomeric Enclosures for Patient Specific Catheter Robots" from a workshop presentation at the 2017 IEEE IROS Full-day Workshop on Continuum Robots in Medicine - Design, Integration, and Applications [111] (Section 4.2).

Traction of Helical Soft Continuum Actuators for Endoluminal Robots

Gillian McDonald, Amer Safdari, and Timothy M. Kowalewski, PhD

University of Minnesota
Driven to Discover℠

Motivation

Background

Soft robots promise new types of endovascular access currently unattainable for traditional surgical robots. This includes novel locomotion through blood vessels as suggested in [1] and endovascular abdominal aortic aneurysm repair (EVAAR) which requires anchoring guidewires. Current methods (Fig. 1) include guidewires with curved ends that provide poor anchoring [2] or balloon anchors which block blood flow [3]. We propose soft, catheter-deployed, continuum spiral actuators inflated with saline to provide safe, compliant anchoring without blocking blood flow (Fig. 1 III). Specifically, we evaluate the traction forces of such spiral actuators as a function of typical intravascular actuation pressures compared to a control of a balloon actuator.

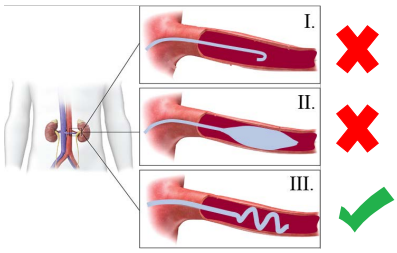

FIGURE 1: Guidewire with anchoring method of: **I.** curved end, **II.** balloon, **III.** our continuum helical actuator.

References and Acknowledgments

[1] M. D. Gilbertson, G. McDonald, G. Korinek, J. D. Van de Ven, and T. M. Kowalewski, "Serially actuated locomotion for soft robots in tube-like environments," IEEE Robotics and Automation Letters, vol. 2, no. 2, pp. 1140–1147, 2017.
[2] T. O. McNamara, B. A. Kirts, and E. J. Morris, "Preformed wire guide," Jul. 3 2001, united States Patent 6,254,550.
[3] M. H. Rosner and M. D. Okusa, "Acute kidney injury associated with cardiac surgery," Clin J Am Soc Nephrol, vol. 1, no. 1, pp. 19–32, 2006.
[4] J. Bishop-Moser and S. Kota, "Towards snake-like soft robots: Design of fluidic fiber-reinforced elastomeric helical manipulators," Proc. IEEE/RSJ Int. Conf. Intell. Robots and Syst. (IROS), pp. 5021–5026, Nov 2013.

Acknowledgments

This work was supported by the National Science Foundation Graduate Research Fellowship Program under Grant No. 00039202.

Methods

Experimental Setup

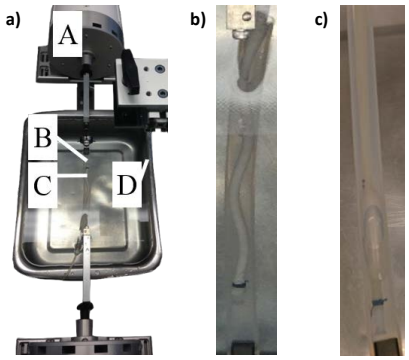

FIGURE 2: a) Experimental setup: A. ElectroForce TestBench B. surrogate artery C. anchored helical actuator D. water bath; **b)** Helical actuator in surrogate artery; **c)** Control balloon.

Methods

- Helical actuators (FREEs, [4], Fig. 3) were designed to anchor into a surrogate artery with 12.7 mm ID.
- A 4.76 mm OD, unwrapped latex tube was used as an experimental control of a traditional balloon (Fig. 1 II).
- Traction forces were measured in a water bath using an ElectroForce TestBench (Fig. 2a) with a 20 mm stroke length at a velocity of 0.2 mm/s (1mN accuracy).
- Actuators were inflated to a specified pressure inside the surrogate artery, then pulled apart.
- Pressure was increased by 0.5 atm until actuator burst.

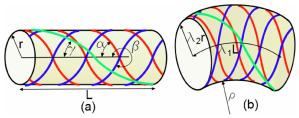

FIGURE 3: a) FREE actuator where α, β, and γ represent the wrap angles of each of the three fibers **b)** FREE where λ_1, λ_2, ρ, and L represent the axial stretch, radial stretch, radius of curvature, and overall length, respectively [4].

Results and Conclusion

Results

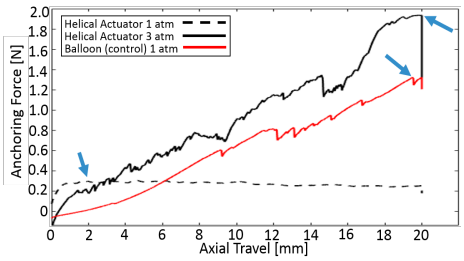

FIGURE 4: Representative transient data showing peak anchoring forces.

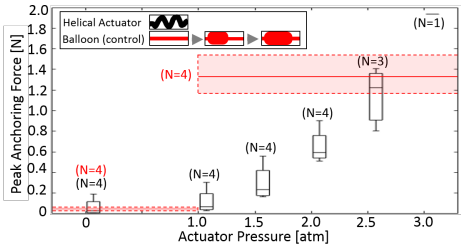

FIGURE 5: Peak actuator anchoring force. Once ballooning occurred, the overall length of the control balloon was maintained at 25 mm at a pressure of 1 atm. The engaged surface areas of the helical actuator and control balloon were 10.47 cm^2 and 20.27 cm^2, respectively.

Conclusion

- The results show that our helical actuator was capable of achieving comparable anchoring performance to the control balloon, yet did so with less engaged surface area and without occluding the surrogate artery (Fig. 5).
- Future work will include ex-vivo studies in porcine and human arteries, as well as an expansion into soft robot locomotion in tube-like environments.

Appendix D

Additional Actuator Designs

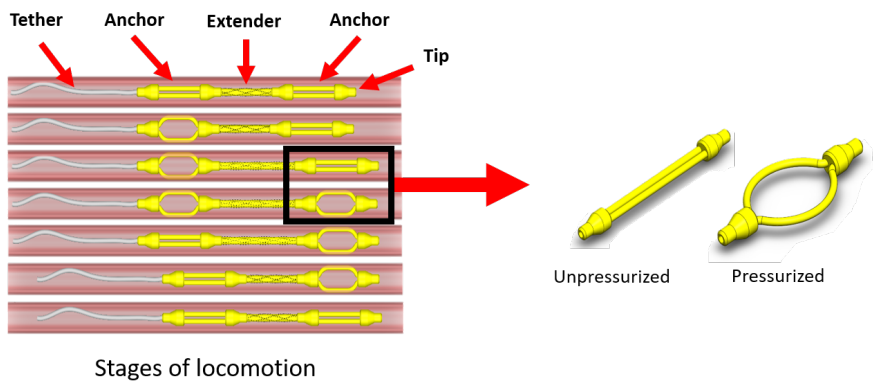

Figure D.1: Illustration of concept for an anchoring actuator comprised of two bending actuators.

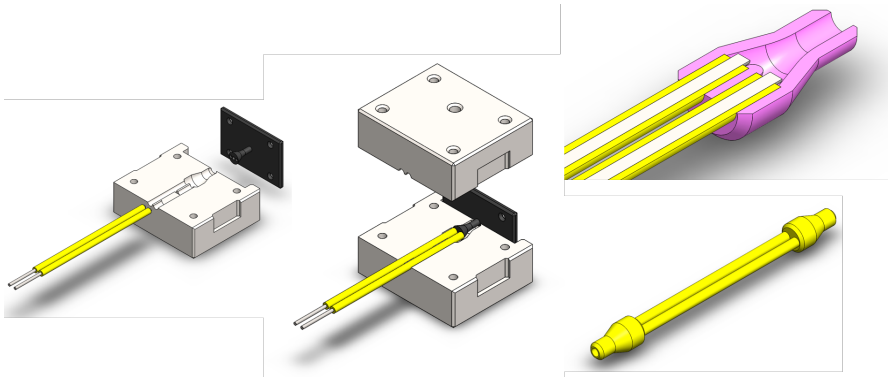

Figure D.2: Illustration of fabrication process for anchoring actuator comprised of two bending actuators.

Figure D.3: Prototype of anisotropic, scale-like skin to generate friction in desired direction.

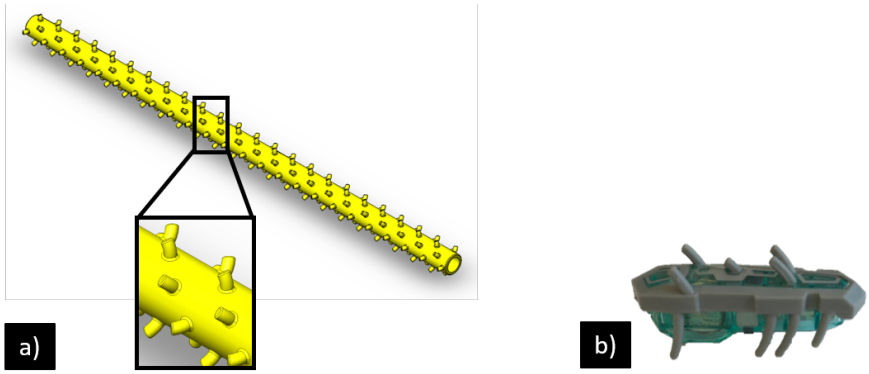

Figure D.4: a) Illustration of nubbed outer skin to generate anisotropic friction for actuators. b) The design was inspired by the ability of Hex Bugs to move on surfaces using angled legs.

Figure D.5: a) Polyurethane base tube (Polytek 74-20) and stainless steel extension spring (McMaster-Carr, 9665K53) used to create extending actuator. b) Resulting extending actuator after placing extension spring over base tube and casting in polyurethane (Polytek 74-20) bonding layer. The spring extending actuator achieves greater bending stiffness than with cotton fibers alone, but twists along its longitudinal axis as it extends because the spring is wound in only one direction, unlike the equal and opposite fiber angles with thread.

Appendix E

Inverse Design Contributions

This section includes a work titled, "Generalized Kinematics for Deformable Patient-Specific Soft Robots" presented at the IEEE IROS Full-day Workshop on Continuum Robots in Medicine - Design, Integration, and Applications [3] and a paper titled, "Computational inverse design of anatomy-specific soft robot actuators with physically-realizable material conditions" presented at The Hamlyn Symposium on Medical Robotics [4].

E.1 Generalized Kinematics for Deformable Patient-Specific Soft Robots [3]

E.1.1 Introduction

Cosserat modeling underpins the success of concentric tube robots [194, 195]. Unfortunately, neither concentric tubes nor Cosserat rods apply to fully deformable, stretchable soft actuators. This does not benefit patient-specific soft robots, particularly for under-served 'no option' patients requiring novel deformations (Fig. E.1a). This work introduces a general kinematic framework to model deformable soft actuators (as Cosserat rods model concentric tube robots). The requirement for the presented framework is that it generalizes traditional robot kinematics like Denavit-Hartenberg (D-H) and product of exponentials (POE). The framework is demonstrated with an application to patient-specific soft robot actuator design.

E.1.2 Methods

Similar to concentric tube robots, this model includes links with the traditional generalized joint angle $q : q_i \leq q \leq q_f \in \Re$ and a new link localization parameter $l : l_s \leq l \leq l_e \in \Re$, both scaled to $[0, 1]$. Given desired initial and final shapes as in Fig. E.1a with centerlines $c_i, c_f \in \Re^3$ and surfaces $\hat{S}_i, \hat{S}_f \in \Re^3$, the proposed method is as follows.

Define Link Centerline

Blend centerlines as $c(q, l) = (1-q)c_o(l)+qc_f(l)$. This may include intermediate steps. Compute tangent ($\mathbf{T}$), normal ($\mathbf{N}$), and binormal ($\mathbf{B}$) unit vectors using Frenet-Serret formulas along $c(q, l)$.

Define Link Start-End Frames

Attach start frame $\{S\}$ at $c_0(l_s)$ and end frame $\{E\}$ at $c_0(l_e)$ s.t. z-translation from $\{S\}$ is link length (Fig. E.1b). Choose final and intermediate $\{E\}$ frames to coincide with $c(q_f, l_e)$ and $c(q, l_e)$.

Express Link Ends with DH Parameters and POE

For DH Parameters, the translation from $\{S\}$ to $\{E\}$ at any $q \in [q_0, q_f]$ can be written as $c(q, l_e)$ and direction cosines provide the relative orientation ${}^sR_e$ of $\{E\}$ w.r.t $\{S\}$.

For POE formulation, decouple transformation from above as ${}^sT_e = e^{\widehat{\xi_1}\theta_1}e^{\widehat{\xi_2}\theta_2}$ where direction $\widehat{\xi_1}$ and magnitude θ_1 refer to prismatic translation, axis $\widehat{\xi_2}$ and magnitude θ_2 to rotation.

Construct Full Robot Kinematics

For each link j, project desired surface points $\hat{S}_j$ onto $c_j(q_j, l_j)$ via $(\mathbf{T}, \mathbf{N}, \mathbf{B})$. This may include a least squares fit and surface spline interpolants with end matching constraints for $S_j(q, l)$. Then, $S_{robot}(\bar{q}, \bar{l}) = \sum_{j=1}^{N} S_j(q_j, l_j) + c_{j-1}(q_{j-1}, l_{f,j-1})$.

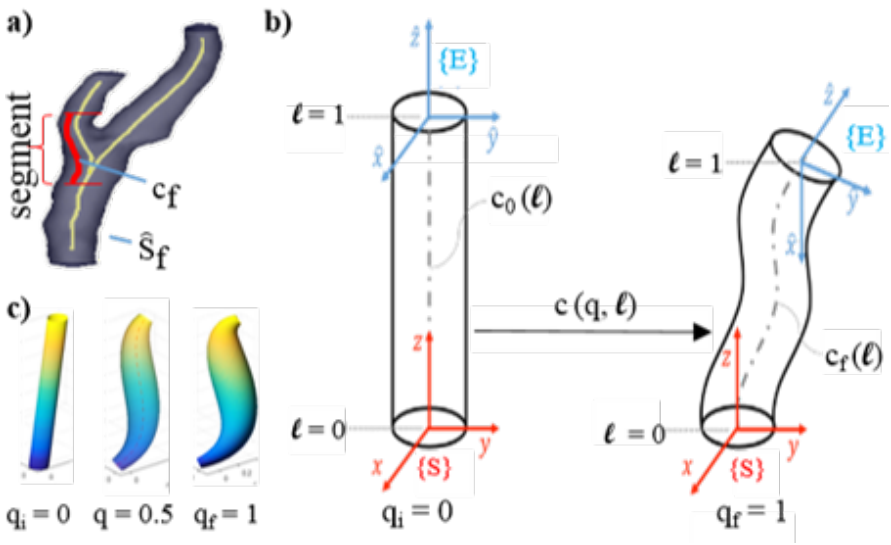

Figure E.1: (a) Sample centerline and surface $\hat{S}_f$ extracted from patient artery scan via VMTK [196]. (b) Labeling convention with initial q_i and final q_f where final link surface S matches $\hat{S}_f$. (c) Results of an axially-symmetric robot segment morphing from generalized joint angle $q_i = 0$ to $q_f = 1$.

E.1.3 Results

See Fig. E.1. The general DH parameters for each link are:

$$ {}^{s}T_e = \begin{bmatrix} \mathbf{N}(q,l) & \mathbf{B}(q,l) & \mathbf{T}(q,l) & c(q,l) \\ 0 & 0 & 0 & 1 \end{bmatrix}_{l=l_e} \tag{E.1} $$

The resulting general POE formulation results in:

$$ \theta_1 = \|c(q,l_e) - c(q,l_s)\| \tag{E.2} $$

$$ \theta_2 = acos[(\mathbf{N}_x + \mathbf{B}_y + \mathbf{T}_z - 1)/2] \tag{E.3} $$

and

$$\widehat{\xi}_1 = \begin{bmatrix} \overrightarrow{0_{3\times3}} & \frac{c(q,l_e)-c(q,l_s)}{\|c(q,l_e)-c(q,l_s)\|} \\ \overrightarrow{0_{1\times3}} & 0 \end{bmatrix} \tag{E.4}$$

$$\widehat{\xi}_2 = \frac{1}{2sin(\theta_2)} \begin{bmatrix} 0 & \mathbf{B}_x - \mathbf{N}_y & \mathbf{T}_x - \mathbf{N}_z & 0 \\ \mathbf{N}_y - \mathbf{B}_x & 0 & \mathbf{T}_y - \mathbf{B}_z & 0 \\ \mathbf{N}_z - \mathbf{T}_x & \mathbf{B}_z - \mathbf{T}_y & 0 & 0 \\ 0 & 0 & 0 & 0 \end{bmatrix}, \ \theta_2 \neq 0 \tag{E.5}$$

E.1.4 Discussion and Conclusion

The results (Fig. E.1c) show that the proposed method kinematically describes deformable robot links with stretchable surfaces that match desired shapes. It generalizes the kinematics of soft robots as a superset of both D-H and POE, providing intuitive use for roboticists. Future work will include incorporating realistic stress and strain metrics and automated design of multi-link soft robots from patient-specific data.

E.2 Computational Inverse Design of Anatomy-Specific Soft Robot Actuators with Physically-Realizable Material Conditions [4]

E.2.1 Introduction

Soft robotics has empowered robots to maneuver, traverse, and complete tasks where traditional rigid robots fall short [27]. Traditionally, soft robots rely on forward design. This limits robots' spectrum of potential actuator shapes [1], but what if a specific patient's anatomy requires a unique actuator shape not realizable by such methods? Inverse design, on the other hand, centers around the desired task and produces a robot geometry for that task. Currently, there exists no technique for the inverse design of a soft robot that can actuate from arbitrary anatomy-specified initial and final shapes. Worse, computational methods may easily result in designs that are physically impossible to realize with real-world materials (e.g. designs that violate volumetric compressibility properties of realistic elastomers).

This work introduces a method of computational inverse design of soft robot actuators that simultaneously achieves required arbitrary actuator shapes dictated by unique patient anatomy and ensures realistic volumetric compressibility throughout the actuator body. A three degrees of freedom (3 DOF) parameterization is presented. This work tests the hypothesis that partitioning 2 DOF to parameterize the required actuator surface shape and 1 DOF for volumetric compressibility provides computational designs that achieve desired shapes and meet compressibility requirements for typical hyperelastic elastomers.

E.2.2 Materials and Methods

The process for creating an anatomy-specific actuator consists of two steps. The first step involves segmenting medical scans to find anatomical centerlines from which the soft robotic actuator shapes are determined. The second step focuses on designing a soft actuator given the parametric representation of the anatomy (e.g. centerline, radius) and selecting the desired actuator shape.

The anatomy-specific soft actuator design method is applied to an abdominal vasculature scan as shown in Fig. E.2a. For a demonstration case, a spiral actuator in the renal artery is designed as outlined in Fig. E.2b. The renal artery was selected due to the need for vascular surgeons to anchor guidewires in the renal artery without obstructing blood flow. Moreover, the artery's small size and need for such shapes could not be achieved with the methods in [1].

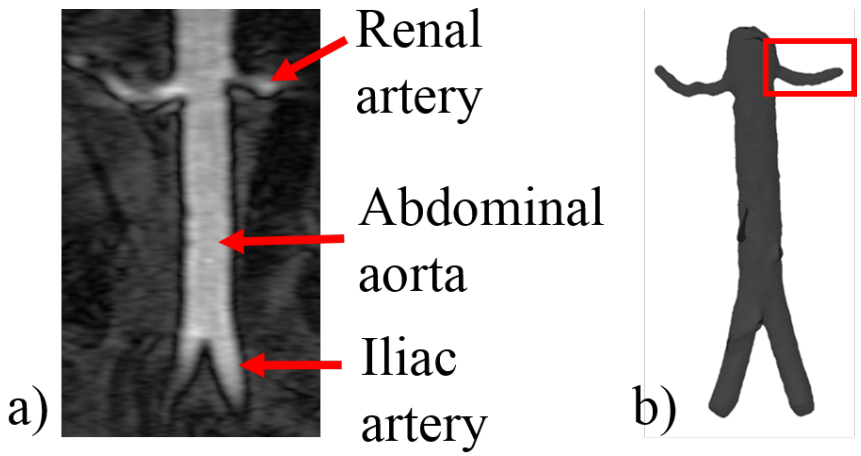

Figure E.2: a) MRI scan data of patient anatomy. b) 3D model, where the actuator is designed for the renal artery (boxed region).

Anatomy Segmentation and Centerline Creation

The process for creating an anatomy-specific actuator started with processing the abdominal medical image using the Vascular Modeling Toolkit Lab (VMTKLab) [196]. Thresholding and segmentation were performed on the image and a 3D model was created. The 3D model was uploaded into the centerline function in VMTKLab and the centerline data were exported.

The centerline points were loaded into MATLAB and fit with a cubic spline followed by a polynomial fitting as a function of the parametric variable for length, w. This resulted in a 3D parametric centerline with coefficients β and order N = 5 as written in eq. E.6.

$$\mathbf{c_a}(w) = \sum_{i=0}^{N} \beta_i w^i \tag{E.6}$$

The cubic spline and polynomial fit were also applied to the anatomical radius data, resulting in eq. E.7, with coefficients γ. Eqs. E.6-E.7 yield a continuously differentiable basis for an arbitrary robot actuator shape.

$$\mathbf{r_a} = \sum_{i=0}^{N} \gamma_i w^i \tag{E.7}$$

Soft Actuator Design

A helical spiraling actuator was selected for the renal artery as it can anchor in place without obstructing blood flow. The spiral actuator design was created by wrapping a helix about the anatomical centerline and extruding a cylinder about the obtained helical centerline. First, coordinate frames were assigned along the anatomical centerline which was parameterized by w. These frames were defined using Frenet-Serret method by computing the tangent, $\mathbf{T}$, normal, $\mathbf{N}$, and binormal, $\mathbf{B}$, vectors along the centerline $\mathbf{c_a}(w)$ as described by eqs. E.8-E.10.

$$\mathbf{T} = \frac{\frac{\partial c_a}{\partial w}}{\left|\frac{\partial c_a}{\partial w}\right|} \tag{E.8}$$

$$\mathbf{N} = \frac{\frac{\partial T}{\partial w}}{\left|\frac{\partial T}{\partial w}\right|} \tag{E.9}$$

$$\mathbf{B} = \mathbf{T} \times \mathbf{N} \tag{E.10}$$

With eqs. E.8-E.10 defined a helix was then fit around $\mathbf{c_a}(w)$ by applying modifications to the standard helix parameterization resulting in $\mathbf{c_f}(w)$ as shown in eq. E.11.

$$\mathbf{c_f}(w) = \mathbf{c_a}(w) + R_w \left[\cos\left(\frac{2\pi k w}{L}\right)\mathbf{N}\sin\left(\frac{2\pi k w}{L}\right)\mathbf{B}\right] + \rho\mathbf{T} \tag{E.11}$$

The radius of the helix was described by $R(w)$, described by eq. E.12, where $f_{env}(w)$, described by eq. E.13, was an envelope function that ensured the ends of the actuator centerline smoothly blended into the anatomical centerline.

$$R(w) = \frac{1}{2} f_{env}(w) r_a(w) \tag{E.12}$$

$$f_{env}(w) = \frac{1}{\sqrt{2}} \tan^{-1}(15w) \tag{E.13}$$

In eq. E.11, k represents the number of helical turns, ρ is the pitch of the spiral, and L is the length of the centerline. In this specific case, $L = 20.63$ mm, $k = 3.18$, $\rho = 0.8$ mm, inner radius $r_i = 0.99$ mm, and outer radius $r_o = 1.00$ mm. These can be modified to fit specific design criteria, such as occlusion ratio, actuator contact area with anatomy, or a combination of other objectives.

The next step was to create the actuator body about $c_f(w)$. Since the body was a volume, three parametric variables and a cylindrical coordinate basis were used, resulting in $X = [u,\ v,\ w]$, where $u = [r_i\ \ r_o]$ represented the radius of the cylindrical actuator, $v = [0\ \ 2\pi]$ represented the wrap angle, and $w = [0\ \ L]$ was the length along the centerline. A Frenet-Serret frame was then defined using $c_f(w)$, resulting in $(\mathbf{T}_f,\ \mathbf{N}_f,\ \mathbf{B}_f)$. The actuator body was then created as a function of parametric variables X as written in eqs. E.14-E.15. The function $f(u)$ was introduced to modify the local thickness of the actuator body at each point, as illustrated in Fig. E.3.

$$\boldsymbol{\varphi}(X) = \mathbf{c_f}(w)\,(u + f(u))\,\bar{n} \tag{E.14}$$

where

$$\bar{n} = [\mathbf{N}_f \cos(v) + \mathbf{B}_f \sin(v)] \tag{E.15}$$

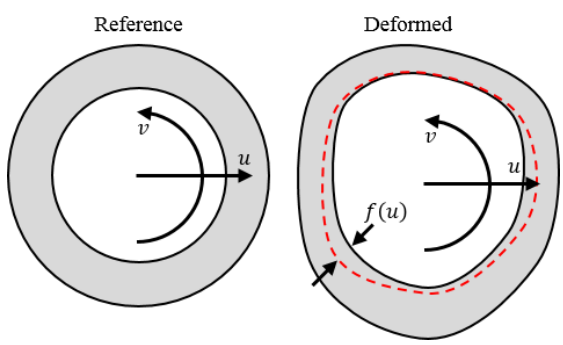

Figure E.3: The cross section of the soft robot is displayed in its initial undeformed cylindrical state and its deformed spiral state. The initial design focuses on creating a design over $[v,\ w]$ and does not directly account for u. The function $f(u)$ was created to modify the thickness to enforce incompressibility. The thickness adjusted by $f(u)$ is shown by the red dashed line.

To enforce material incompressibility of the design, the deformation gradient $\mathbf{F}$ was used as calculated by eq. E.16 with the reference basis being in cylindrical coordinates, X, and the deformed basis being in Cartesian coordinates, $\phi(X)$ [118]. If the determinant of $\mathbf{F}$ was sufficiently close to one, the design was considered incompressible.

When solving eq. E.17 for incompressibility, a first order differential equation was produced in terms of $f(u)$. It was assumed that $f(u)$ takes the form in eq. E.18, thus α_0 and α_1 could be

solved at every spatial location X.

$$\mathbf{F} = \begin{bmatrix} \frac{\partial \boldsymbol{\varphi}(X)}{\partial u} & \frac{1}{u}\frac{\partial \boldsymbol{\varphi}(X)}{\partial v} & \frac{\partial \boldsymbol{\varphi}(X)}{\partial w} \end{bmatrix} \tag{E.16}$$

$$\varepsilon = |det(\mathbf{F}) - 1| < 10^{-6} \tag{E.17}$$

$$f(u) = \alpha_0 + \alpha_1 uc \tag{E.18}$$

E.2.3 Results

The renal artery centerline and mesh are shown in Fig. E.4. Additionally, Fig. E.4 contains the soft robot's centerline and final computational design. The incompressibility constraint was numerically satisfied in eq. E.18 with all ε less than 10^{-6} over the whole range of $X = [u,\ v,\ w]$, 2000 spatial locations in all.

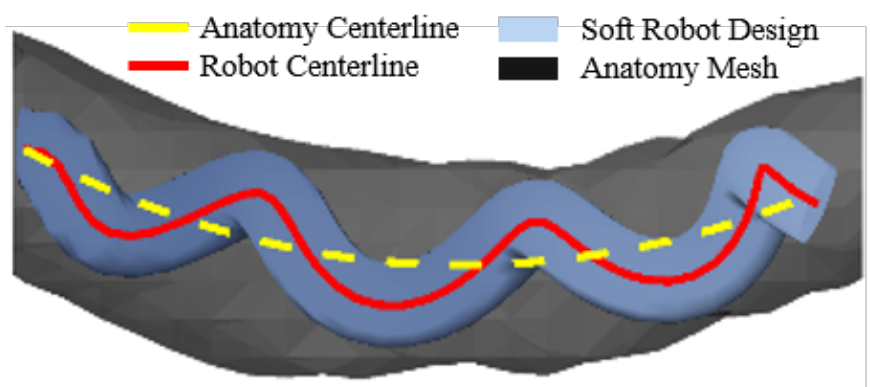

Figure E.4: Spiral actuator design inside the renal artery.

E.2.4 Discussion

The method produced a parametric soft robot actuator design for a specific renal artery while ensuring local volumetric compressibility by partitioning the DOF as hypothesized. This method is highly generalizable for nearly arbitrary shape requirements. It expands the possible design space of soft robots to new patients with unique anatomy. It also alleviates constraints such as those caused by wrap angles in fiber-reinforced actuators, and creates a design based upon the

task (specific patient-needs) and not the manufacturing method with which a soft robot designer begins. With the actuator shape created future work can continue on incorporating additional and anisotropic material properties into the computational design to realize a physical robot device.

Appendix F

Stress-Strain Curves

Tensile tests were conducted on dog bone samples (Fig. F.1) of Polytek 74-20 and Polytek 74-29 to determine material properties critical to the models throughout this work. The dog bones were cut from sheets of cured polyurethane and tested on an Instron machine (Fig. F.2). Tensile test parameters and results for each of the materials are shown in Tables F.1-F.4. Plots of the data for each material are shown in Figs. F.3 and F.4.

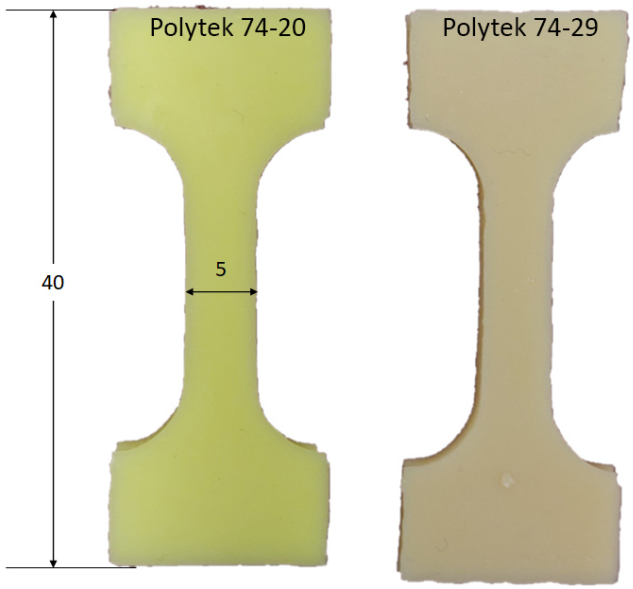

Figure F.1: Dog bone samples used in tensile tests. All dimensions in millimeters.

Figure F.2: Instron tensile tester.

Table F.1: Tensile test parameters for Polytek 74-20 dog bone samples.

Run	Material	Gauge Length (mm)	Cross-Sectional Geometry	Width (mm)	Thickness (mm)	Area (mm^2)
1	Polytek 74-20	26.50	Rectangular	5	2.89	14.45
2	Polytek 74-20	26.85	Rectangular	5	2.63	13.15
3	Polytek 74-20	26.75	Rectangular	5	2.94	14.70

Table F.2: Tensile test results for Polytek 74-20 dog bone samples.

Run	Material	Modulus [Automatic] (kPa)	Tensile Stress at Yield (MPa)	Tensile Strain (Extension) at Break (%)
1	Polytek 74-20	427.218	1.69	634.744
2	Polytek 74-20	488.868	—	664.604
3	Polytek 74-20	456.957	1.89	695.015
Avg.	N/A	457.681	1.79	664.788

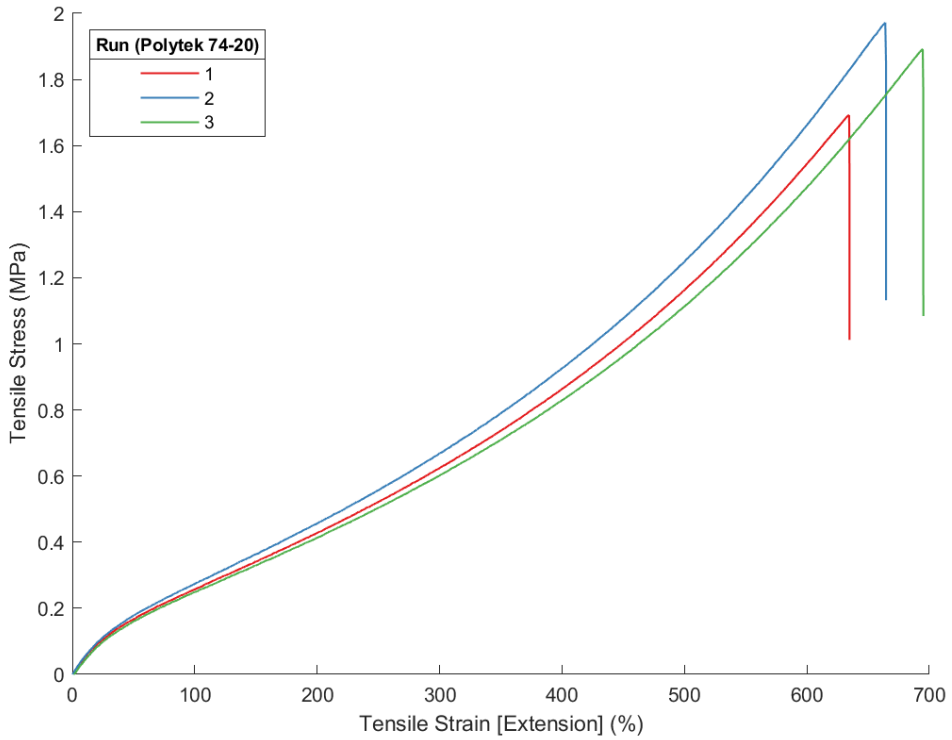

Figure F.3: Stress-strain data for Polytek 74-20 performed on an Instron tensile tester.

Table F.3: Tensile test parameters for Polytek 74-29 dog bone samples.

Run	Material	Gauge Length (mm)	Cross-Sectional Geometry	Width (mm)	Thickness (mm)	Area (mm^2)
1	Polytek 74-29	25.5	Rectangular	5	2.3	11.5
2	Polytek 74-29	25.39	Rectangular	5	2.25	11.25

Table F.4: Tensile test results for Polytek 74-29 dog bone samples.

Run	Material	Modulus [Automatic] (kPa)	Tensile Stress at Yield (MPa)	Tensile Strain (Extension) at Break (%)
1	Polytek 74-29	689.903	4.67	966.958
3	Polytek 74-29	597.299	5.13	1097.398
Avg.	N/A	643.601	4.90	1032.178

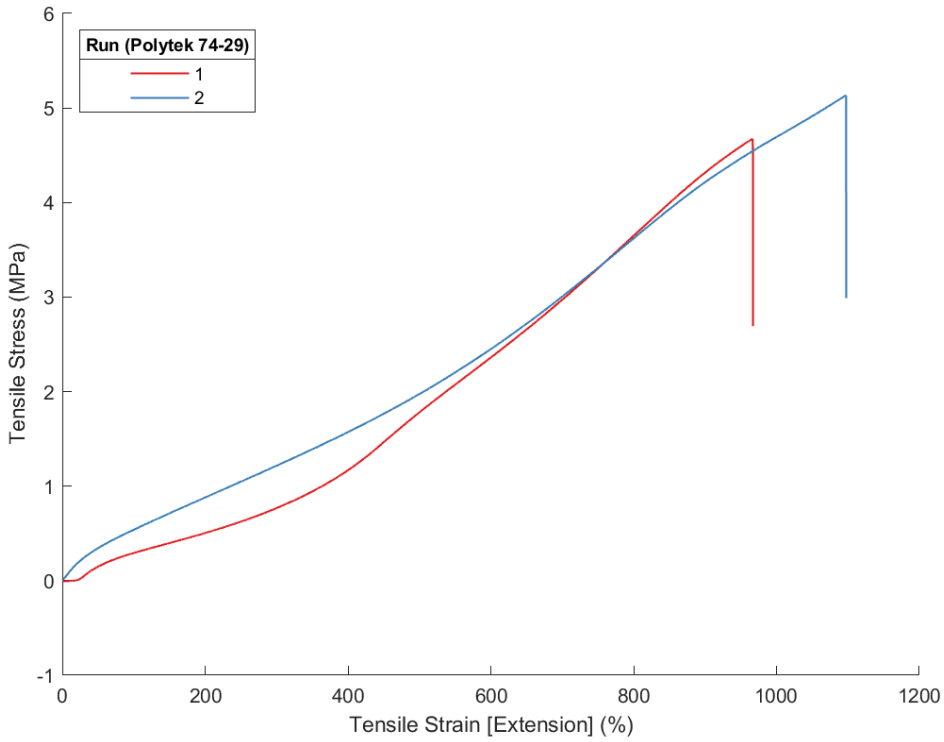

Figure F.4: Stress-strain data for Polytek 74-29 performed on an Instron tensile tester.